Overcoming Stress Singularities:
Combining Phase-Field Modelling of Fracture, Strain Gradient Theory, and Isogeometric Analysis

D I S S E R T A T I O N
zur Erlangung des akademischen Grades

Doktoringenieur
(Dr.-Ing.)

von M.Eng. Resam Makvandi
geboren am 26.06.1988 in Ahvaz, Iran

genehmigt durch die Fakultät für Maschinenbau
der Otto-von-Guericke-Universität Magdeburg

Gutachter:
1. Prof. Dr.-Ing. Daniel Juhre
2. Prof. Dr. Luca Placidi
3. Prof. Dr.-Ing. Andreas Öchsner

Promotionskolloquium am 05.11.2021

Kurzfassung

Klassische Theorien der Kontinuumsmechanik bestimmen Verformungen üblicherweise in Bereichen von Millimetern zu Metern, also auf der sogenannten makroskopischen Skala. Es handelt sich bei diesen Modellen um Annäherungen der physikalischen Realität, die die zugrundeliegende Mikrostruktur vernachlässigen. Beispielsweise kann ein Cauchy-Kontinuum, also ein Kontinuum mit einer elastischen Energie, die als Funktion der Gradienten seiner makroskopischen Verschiebung bestimmt wird, das Verhalten eines physikalischen Systems nur ausreichend annähern, solange die Mikrostruktur eine viel kleinere Längenskala als die Makrostruktur aufweist. Obwohl diese Modelle in theoretischen Studien für große und kleine Maßstäbe genutzt wurden, haben Experimente gezeigt, dass die klassischen Modelle nicht in der Lage sind, die kleineren Skalen richtig abzudecken; insbesondere werden häufig Probleme in Mikro- und Nanodimensionen beobachtet. Größeneffekte, die im Rahmen dieser Theorien nicht erfasst werden können, scheinen die Quelle dieses Problems zu sein. Darüber hinaus ist das Auftreten lokaler Singularitäten an den Rissspitzen (wie auch in Gegenwart von Punkt- und Linienlasten) eine der bekannten Grenzen der klassischen Theorie der Kontinuumsmechanik. Die Verallgemeinerung dieser Modelle durch die Einführung zusätzlicher kinematischer Zusammenhänge zur Berücksichtigung der zugrundeliegenden Mikrostruktureffekte auf makroskopischen Ebenen ist eine Möglichkeit, die oben genannten Probleme zu überwinden. 1964 veröffentlichte Mindlin seine bahnbrechende Arbeit über eine neue Elastizitätstheorie für Kontinua mit Mikrostrukturen. Dieses umfassende Werk vereinfacht die Dehnung von Gradientenelastizitätstheorien, indem es eine Beziehung zwischen den Mikroverformungen und Gradienten der Makroverformungen einführt. In der Dehnungsgradiententheorie enthält das Dehnungsenergiefunktional sowohl die Dehnungsterme als auch ihre Gradienten, was zu Spannungen in Abhängigkeit von höherwertigen Ableitungen des Verschiebungsfeldes führt. Man kann das Spannungsfeld regularisieren und somit die negativen Auswirkungen der Singularitäten beseitigen, indem man diese Dehnungsgradientenmodelle ausnutzt. In letzter Zeit erfreut sich die Phasenfeldmethode im Kontext von Rissausbreitungsvorgängen bei Forschern großer Beliebtheit, da die Verfolgung von Rissoberflächen nicht explizit erforderlich ist. Dies ist bereits eine signifikante Verbesserung bei der Untersuchung des Rissphänomens im Vergleich zu den herkömmlichen numerischen Werkzeugen, bei denen die Finite-Elemente-Methode in Verbindung mit der linear-elastischen Bruchmechanik verwendet wird und die Risse explizit eingeführt werden müssen, indem die Rissspitze verfolgt und während der numerischen Simulation neue interne Grenzen eingeführt werden. Alle aktuellen phasenfeldbasierten Modelle der Bruchmechanik basieren jedoch auf der klassischen Theorie der Kontinuumsmechanik, bei der an der Rissfront singuläre Spannungsspitzen unvermeidlich sind. Obwohl die sogenannte Phasenfeldfunktion das betrachtete Problem reguliert und damit die Auswirkungen einer Singularität mildert, ist das singuläre Verhalten im mathematischen Modell immer noch vorhanden und wirkt daher spürbar auf die Qualität der Endergebnisse.

Ziel des aktuellen Beitrags ist es zunächst, die nachteiligen Auswirkungen der auftretenden Singularitäten aufzuzeigen, die in vielen aktuellen Forschungsaktivitäten aus verschiedenen Gründen vernachlässigt zu werden scheinen. Zur Validierung bzw. Verifizierung der theoretischen Herleitungen werden in den meisten Fällen eindimensionale Beispiele untersucht und die beobachteten Funde anschließend auf höherdimensionale Fälle übertragen. Diesbezüglich ist festzuhalten, dass das klassische Cauchy-Kontinuum im eindimensionalen Fall keine Singularitäten aufweist. Daher ist die Annahme, dass die für den eindimensionalen Fall gezogenen Schlussfolgerungen auch für höherdimensionale Probleme vollständig wirksam sind, kritisch zu sehen. Ausschließlich bei zwei- und dreidimensionalen Fragestellungen tritt das Problem der Singularitäten bei der Nutzung von linien- und punktförmigen Randbedingungen auf. Kurz gesagt, gibt es in diesen Fällen keine Beiträge zur internen Arbeit zur Aufrechterhaltung von Linien- und Punktkräften. Das zweite Ziel dieser Arbeit ist es, ein Modell vorzustellen, das die Dehnungsgradiententheorie im Rahmen der Phasenfeldbruchmechanik nutzt, um diese nachteiligen Effekte zu beseitigen. Es werden in dieser Arbeit zwei Formulierungen für die Nutzung von Dehnungsgradienten in den Phasenfeldmodellen zweiter und vierter Ordnung vorgeschlagen. Es wird gezeigt, dass die erarbeiteten Gradientenmodelle die klassischen Modelle

verbessern, indem sie die Singularitäten regularisieren. Darüber hinaus deuten die numerischen Ergebnisse darauf hin, dass das Modell vierter Ordnung dem Modell zweiter Ordnung überlegen ist, da es realistischere Lösungsmerkmale bietet. Ein weiterer Vorteil der Formulierung vierter Ordnung ist die signifikante Reduzierung der Netzempfindlichkeit in numerischen Simulationen. Im Rahmen dieser Dissertation wird gezeigt, dass zukünftige Ansätze zur Phasenfeldmodellierung von Rissausbreitungsvorgängen die Auswirkungen von Spannungssingularitäten berücksichtigen müssen, um realistischere Ergebnisse zu erzielen.

Abstract

Originally, the classical continuum mechanics theories are supposed to determine deformations in ranges from millimeter to meter at the so-called macroscopic scales. In fact, these models are approximations of physical systems neglecting the underlying microstructure. For instance, a Cauchy continuum, i.e., a continuum with an elastic energy determined as a function of the gradients of its macroscopic displacement, can only approximate the behavior of a physical system sufficiently as long as the microstructure has a much smaller length-scale than the macrostructure. Although these models were exploited in studies for large and small scales, experiments have shown that the classical models are not able to properly cover the smaller scales; in particular, problems in micron- and nano-dimensions are frequently observed. Size effects, which cannot be captured exploiting these theories, seem to be the source of this issue. On top of that, the appearance of local singularities at the crack tips (or more broadly, in the presence of point and line loads) is one of the known limitations of the classical continuum mechanics theory. Generalizing these models by introducing additional kinematic terms to consider the underlying microstructure effects at macroscopic levels is one way of overcoming the aforementioned problems. In 1964, Mindlin published his seminal work on a new elasticity theory for continua with microstructures. This broad-spectrum framework simplifies to strain gradient elasticity theories by introducing the relation between the micro-deformations and gradients of the macro-deformations. In the strain gradient theory, the strain energy functional contains both the strain terms and their gradients, which leads to stresses depending on higher-order derivatives of the displacement field. One can regularize the stress field and therefore, remove the negative effects of the singularities by exploiting these strain gradient models.

Recently, the phase-field modelling of fracture is becoming very popular among researchers due to the fact that the tracking of crack surfaces is not explicitly required. This is already a significant improvement in studying the fracture phenomenon, compared to the conventional numerical tools where the finite element method is used in conjunction with linear elasticity fracture mechanics and the cracks must be introduced explicitly by tracking the crack tip and introducing new internal boundaries during the numerical simulation. However, all current phase-field based models of fracture mechanics are based on the classical continuum mechanics theory, where singular stress fields are inevitable at the crack front. Although the so-called degradation function regularizes the problem under consideration and thus, mitigates the effects of a singularity, the singular behavior is still present in the mathematical model and therefore, exerts a notable effect on the final results.

The goal of the current contribution is first to demonstrate the adverse effect of the singularity which seems to be neglected in current investigations for different reasons. In fact, to validate the theoretical derivations, more often than not one-dimensional examples are investigated and the observed finding are subsequently transferred to higher-dimensional cases. In that regard, it is important to realize that the classical Cauchy continuum does not suffer from any singularities in the one-dimensional case. Therefore, assuming that conclusions drawn for the one-dimensional case are also fully valid for higher-dimensional problems must be seen very critically. Only in two and three dimensions the problem of singularities arises when applying line and concentrated boundary conditions. Roughly speaking, in these cases, there are no contributions to the internal work to sustain line and point forces. The second goal of this work is to propose a model to integrate the strain gradient theory within the phase-field fracture mechanics framework in order to remove these spurious effects. Two strain gradient enhanced formulations are proposed based on the second-order and the fourth-order phase-field fracture models. It is shown that the proposed gradient models improve the performance of the classical models by regularizing the singular response. Moreover, the numerical results indicate that the proposed fourth-order model is superior to the second-order one in that it provides more realistic solution characteristics. Another advantage of the fourth-order formulation is the significant reduction of mesh sensitivity in numerical simulations. With this contribution, it has been demonstrated that future approaches directed towards phase-field fracture modelling need to take the effects of stress singularities into account to achieve more realistic results.

Contents

Nomenclature

Acronyms

B-Spline	Basis-Spline
CAD	Computer-Aided Design
CAGD	Computer-Aided Geometric Design
CDM	Continuum (Continuous) Damage Mechanics
CP	Control Point
DGE	Distortion Gradient Elasticity
DOF	Degree Of Freedom
FEA	Finite Element Analysis
FEAP	Finite Element Analysis Program
FEM	Finite Element Method
GFEM	Generalized Finite Element Method
IGA	Isogeometric Analysis
KKT	Karush-Kuhn-Tucker
LEFM	Linear Elastic Fracture Mechanics
NURBS	Non-Uniform Rational Basis-Splines
PD	PeriDynamics
PDE	Partial Differential Equation
PP	Post-Processing
PUFEM	Partition of Unity Finite Element Method
SGE	Strain Gradient Elasticity
XFEM	Extended Finite Element Method

Greek Symbols

$\alpha_\square^\square$	coefficients for B-Spline basis function derivatives
β_i	coefficients for knot-insertion technique
$\delta\Psi^{\text{ext}}$	external virtual work
$\delta\Psi^{\text{int}}$	internal virtual work
$\delta\Psi_{\text{grad}}^{\text{ext}}$	external virtual work (gradient material)
$\delta\Psi_{\text{grad}}^{\text{int}}$	internal virtual work (gradient material)
δ_{ij}	Kronecker delta
ϵ	length-scale parameter (crack)
ϵ_{ijk}	Levi-Civita tensor (alternating tensor)
Γ_{s}^n	n-th order crack density functional
Γ_{c}	internal-discontinuity boundary
Γ_{D}	Dirichlet boundary
Γ_{N}	Neumann boundary
Γ_i	bounding surfaces of Ω
λ	Lamé constant
λ_1	gradient material parameter (Reiher's model)
$\lambda_{1_{\text{real}}}$	gradient material parameter (Reiher's model)
μ	Lamé constant

ν	Poisson's ratio
Ω	material volume
$\phi_{(ij)}$	microscopic strain tensor
$\phi_{[ij]}$	microscopic rotation tensor
Ψ	total potential energy
Ψ	total potential energy of a body
ψ_{e}^{+}	tension part of stored elastic energy density
ψ_{e}^{-}	compression part of stored elastic energy density
$\Psi^{(2)}$	total energy of fracture (second-order phase-field model)
$\Psi_{\mathrm{grad}}^{(2)}$	total energy of fracture (second-order phase-field model) (gradient material)
$\psi_{\mathrm{grad}}^{(2)}$	degraded strain energy density (second-order phase-field model) (gradient material)
$\Psi^{(4)}$	total energy of fracture (fourth-order phase-field model)
$\Psi_{\mathrm{grad}}^{(4)}$	total energy of fracture (fourth-order phase-field model) (gradient material)
$\psi_{\mathrm{grad}}^{(4)}$	degraded strain energy density (fourth-order phase-field model) (gradient material)
ψ_{crit}	critical fracture energy density (Pham's model)
Ψ_{c}	fracture energy
Ψ_{e}	stored elastic energy
ψ_{e}	stored elastic energy density
Ψ_{grad}	potential (stored) energy of a gradient material
ψ_{grad}	potential energy density of a gradient material
$\Psi_{\mathrm{grad}}^{\mathrm{DGE}}$	potential (stored) energy of a gradient material (DGE)
$\psi_{\mathrm{grad}}^{\mathrm{DGE}}$	potential energy density of a gradient material (DGE)
$\Psi_{\mathrm{grad}}^{\mathrm{SGE}}$	potential (stored) energy of a gradient material (SGE)
$\psi_{\mathrm{grad}}^{\mathrm{SGE}}$	potential energy density of a gradient material (SGE)
ρ	density
σ_{crit}	critical tensile strength (Pham's model)
θ	angle
$\boldsymbol{\chi}$	microscopic deformations gradient tensor
$\bar{\eta}$	numerical parameter
η	second parametric direction
$\boldsymbol{\gamma}$	relative deformations tensor
$\boldsymbol{\mu}$	double-stress tensor (Mindlin's theory)
$\boldsymbol{\phi}$	microscopic deformations tensor
$\boldsymbol{\sigma}$	relative stress tensor
Ξ	NURBS knot vector in ξ-direction
ξ	first parametric direction
ξ_i	NURBS knot values in ξ-direction
ζ	third parametric direction

Roman Symbols

A	area
$\mathbb{A}, A_{ijklmn}$	sixth-order material stiffness tensor
$\mathbf{a}$	acceleration vector
$\tilde{a}_1 - \tilde{a}_{15}$	gradient material coefficient (Mindlin's theory)
$a_1 - a_5$	gradient material coefficient (DGE)
$\mathbb{B}, B_{ijkl}$	fourth-order material stiffness tensor

$\mathbf{b}$	body forces vector
$\mathbf{B^u}$	strain-displacement matrix
$\mathbf{B}^s$	matrix of gradients for the phase-field variable
$\tilde{b}_1 - \tilde{b}_3$	gradient material coefficient (Mindlin's theory)
$b_1 - b_5$	gradient material coefficient (SGE)
$B_i^p(\square)$	Bernstein polynomials in ξ-direction
$\mathbb{C}, C_{ijkl}$	fourth-order material stiffness tensor
$\mathbf{C}$	global Bézier extraction operator
$\tilde{c}_1 - \tilde{c}_3$	classical material coefficient (Mindlin's theory)
$\underline{\mathbf{C}}$	material stiffness tensor(Voigt notation)
d	dimensionality of the problem
$\mathbb{D}, D_{ijklm}$	fifth-order material stiffness tensor
$\hat{\mathbf{D}}$	damping matrix
d_{ij}	time integrator coefficients
E	Young's modulus
e	edge
$\mathbf{E}$	linear strain tensor
$\underline{\mathbf{E}}$	linear strain tensor (Voigt notation)
$\mathbb{F}, F_{ijklm}$	fifth-order material stiffness tensor
$\mathbf{f}$	force vector
$\mathbb{G}, G_{ijkl}$	fourth-order material stiffness tensor
$\mathbf{G}$	microscopic deformation gradient tensor (DGE)
$\mathcal{G}_\mathrm{c}$	critical energy release rate (crack thoughness)
$\tilde{g}_1 - \tilde{g}_3$	gradient material coefficient (Mindlin's theory)
$g(s)$	energy degradation function
$\mathbf{H}$	microscopic deformation gradient tensor (SGE)
$\mathcal{H}^{d-1}$	Hausdorff measure
$\underline{\mathbf{H}}$	microscopic deformation gradient tensor (SGE) (Voigt notation)
k	dummy variable
$\hat{\mathbf{K}}$	stiffness matrix
K_I	stress intensity factor
L	length
l	length-scale parameter (GRADELA)
$\mathbf{L}$	macroscopic displacement gradient (distortion tensor)
$L_k^r(\square)$	B-Spline basis functions in ζ-direction
M	kinetic coefficient (mobility)
m	mass
$\bar{m}$	initial slope of the degradation function (Pham's model)
$\mathbf{m}$	outward unit vector to Σ
$\tilde{m}$	multiplicity of a knot in a NURBS knot vector
$M_j^q(\square)$	B-Spline basis functions in η-direction
n	total number of NURBS control points
$\bar{N}_i^p(\square)$	first derivative of B-Spline basis functions in ξ-direction with respect to ξ
$\mathbf{n}$	outward unit vector to Γ_1
$N_i^p(\square)$	B-Spline basis functions in ξ-direction
$\bar{p}$	initial slope of the softening curve (Pham's model)
$\bar{\mathbf{P}}_i$	Bézier mesh control points
$\hat{\mathbf{P}}$	residuum matrix

$\mathbf{P}^{\mathrm{DGE}}$	double-stress tensor (DGE)
$\mathbf{P}^{\mathrm{frac}}$	effective double-stress tensor
$\mathbf{P}^{\mathrm{SGE}}$	double-stress tensor (SGE)
$\mathbf{P}_i$	NURBS control points
p	NURBS degree in ξ-direction
q	NURBS degree in η-direction
r	NURBS degree in ζ-direction
$R_{ijk}(\square)$	tri-variate NURBS basis functions
$R_{ij}(\square)$	bi-variate NURBS basis functions
$R_i(\square)$	univariate NURBS basis functions
$\hat{\mathbf{S}}$	tangent matrix
$\mathbf{S}$	classical Cauchy stress tensor
$\mathbf{S}^{\mathrm{frac}}$	effective classical Cauchy stress tensor
s	phase-field order parameter (crack)
S^i	surface i
t	time
$\bar{\mathbf{t}}^1$	surface tractions
T	NURBS curve
$\mathbf{u}$	macroscopic displacement vector
$\mathbf{u}'$	microscopic displacement vector
V	volume
$\mathbf{v}$	velocity vector
$\bar{W}(\square)$	first derivative of NURBS weighting function with respect to $\square$
$\mathbf{W}$	NURBS weights matrix
$W(\square)$	NURBS weighting function
$w(s)$	geometric crack function
$W^{\mathrm{b}}(\square)$	Bézier weighting function
w_i^{b}	weights associated to Bézier control points
w_i	weights associated to NURBS control points
$\mathbf{X}$	material position vector of a macroscopic volume
$\mathbf{x}$	spatial position vector of a macroscopic volume
$\mathbf{X}'$	material position vector of a microscopic volume
$\mathbf{x}'$	spatial position vector of a microscopic volume

Operators

$\delta\square$	differential operator (variation)
$\Delta\square, \nabla^2\square$	Laplace operator
$\nabla\square$	gradient operator
$\nabla_{\mathrm{n}}\square$	normal derivative
$\nabla_{\mathrm{s}}\cdot\square$	surface divergence operator
$\square\otimes\square$	Kronecker product
$\square\times\square$	cross product
$\square^{\mathrm{T}}$	transpose operator
$\square_{(ij)}$	symmetric part of a second-order tensor
$\square_{[ij]}$	anti-symmetric part of a second-order tensor
$\mathrm{tr}\,\square$	trace operator
$\square:\square$	double contraction between tensors
$\square\cdot\square$	scalar product between tensors
$\square\,\vdots\,\square$	triple contraction between tensors

1 Introduction

This chapter provides essential information regarding the main topics discussed in this thesis. After a short history of generalized continua, a summary of the efforts done to predict the fracture in brittle materials is provided with a focus on the phase-field method. Thereafter, the motivation behind the current work is discussed, and an outline of the remaining chapters is provided.

1.1 Generalized Continua

The classical continuum mechanics theories were initially supposed to determine deformations ranging from millimeter to meter, the so-called macroscopic scales. These models are approximations of physical systems neglecting the underlying microstructure. A Cauchy continuum, i.e., a continuum equipped with an elastic energy that depends on the gradients of its macroscopic displacements, can only approximate the behavior of a physical system sufficiently provided that the microstructure has a much smaller length-scale than the macrostructure [1]. Although these models have been exploited in studies for large and small scales, experiments show that the classical models cannot adequately cover the smaller scales; in particular, problems in micron- and nano-dimensions are frequently observed [2]. Size-effects, which cannot be captured exploiting these theories, seem to be the source of this issue. Although showing considerable complexity in their structure and interior architecture, a diverse range of materials can be modeled at a small length scale by a classical Cauchy medium. Such a model can be characterized by a considerable number of degrees of freedom, even for a small sample. On the one hand, this choice allows us to use standard numerical tools based on finite element methods (FEM) which are optimized for this kind of models. On the other hand, the complexity of the considered continua makes the use of such a model unsuitable from the point of view of computational costs. Gradient models allow to obtain sufficiently accurate solutions comparable with those of the Cauchy theory, but at much smaller computational expenses (see e.g., [3–5]). There are many examples for materials where the corresponding continuum models are obtained by a homogenisation procedure which leads to micromorphic generalized continua. Gradient materials are a very particular case of such micromorphic continua (see e.g., [6–13] for generalized continua with microstructure and [14–17]). Gradient models involve an increase of material parameters necessary to describe the more detailed characterization of deformations. Therefore, specific tests, both experimental and numerical, can be designed to identify such parameters as proposed in [18–23].

The appearance of local singularities in the presence of point and line loads is one of the known limitations of the classical continuum mechanics theory [24]. Point forces and force distributions along lines are fundamental concepts in mechanics; however, in classical continuum mechanics where a Cauchy continuum is used, these concepts are not included. It has been shown in the literature that exploiting strain gradient models helps with overcoming this problem, as a continuum body in these theories can sustain contributions from point and line loads [24–27].

The idea of using higher-order spatial derivatives in the continuum equations goes back to the early 1850s to Piola [28–30] and Cauchy [31–33], who proposed exploiting them to approximate the behavior of discrete lattice models using an additional constitutive parameter representing the elementary volume's size. The early attempts to generalize the theory in this direction were either only physically motivated, lacking a concise mathematical theory (like the works of Cauchy), or were involving complicated mathematical concepts resulting in complex models that could only be solved making use of severe simplifications (see, for instance, the studies by Voigt [34–36]). In 1909, the Cosserat brothers added micro-rotations as additional degrees of freedom and included the corresponding couple-stresses into the classical theory [37]. Their model considers the size-effect; namely, a small sample of the same material shows a stiffer behavior compared to a larger one. This theory was later developed by Eringen [38], who added the micro-inertia terms and renamed the theory to Micropolar elasticity. After Cosserats' work, this research area did not receive much attention until the early 1960s, where the seminal works of Toupin and Mindlin [39–41] picked up on the topic. Mindlin published his article on a new elasticity theory for continua with microstructures in 1964 [42]. This broad-spectrum framework simplifies to strain gradient elasticity theories by introducing the relation between the micro-deformations and gradients of the macro-deformations. In gradient elasticity, the strain energy function contains both the strain terms and their gradients, which leads to stresses depending on higher-order derivatives of the displacement field. Mindlin's original paper only included the first gradients of the strain, while in a later article, he expanded his theory to second gradients [43]. Mindlin categorized the gradient theory into three forms: Form I where the microscopic deformation gradients are defined as the second (and third) gradients of the macroscopic displacement, Form II where the microscopic deformation gradients are replaced with the gradients of the macroscopic strain, and Form III where the microscopic deformation is split into gradients of the macroscopic displacements and rotations. The resulting boundary value problems, written in terms of the displacement field, are identical for all three forms. However, the notions and characteristics of double- and triple-stresses are different among them (see [44–50]).

The strain gradient models have recently been shown to be applicable for the homogenization of the micro-structure of metamaterials of any scale for different types of lattices [51–53]. One of the motivations of proposing the gradient elasticity theory for solid mechanics is to overcome the problem of singular fields in the vicinity of crack fronts and dislocation cores. The existence of singular stress fields in front of the crack tip in linear elastic fracture mechanics (LEFM) has been shown analytically in the literature (see, for instance, [54–56]). In short, in LEFM, the stress field possesses an $\mathcal{O}(1/\sqrt{r})$ singularity at the tip of a crack, with r being the distance from the crack tip. In reality, however, there is no stress singularity at the crack tip as confirmed by atomistic simulations [57, 58]. The source of the problem causing stress singularities is presumably related to the incapability of the classical Cauchy model in sustaining line and point forces acting on a continuum. The effect of these kinds of forces is similar to the effects resulting from the crack front. It has been shown that this fundamental problem can be solved using appropriate gradient models [25, 59–63]. In this context, it is well known that the first and second strain gradient theories are sufficient to remove the singularities caused by line and point loads, respectively (see [25–27]). In the context of strain gradient models, many contributions in the literature show that exploiting the gradient models results in a non-singular solution for the crack tip and dislocation lines, among which we name [59, 60, 64–67]. For an extensive review, the interested reader can consult [2] and [68] and the references therein.

The involvement of higher-order derivatives in the partial differential equations of gradient

elasticity theories makes it difficult to solve them directly using conventional numerical tools such as Lagrangian finite elements. The finite element method is mostly used in engineering to study problems with moving boundaries. The FEM is a numerical tool to solve partial differential equations and obtain the unknown field by discretizing the domain into a finite number of smaller elements. A series of points, called nodes, defines these elements. Shape functions are used to approximate any field (such as geometry and displacement) between these nodal points. In general, the unknown field is assumed to be C^0-continuous across element boundaries resulting in globally discontinuous derivatives. In contrast, gradient theories require higher-order derivatives to be continuous all over the discretized domain. That is to say, first and second strain gradient theories need C^1- and C^2-continuous elements, respectively. One possible workaround to circumvent this problem is to split the higher-order equation into multiple lower-order equations using a so-called operator split method [69, 70]. Another approach would be to use Lagrange multipliers to fulfill additional constraints in a weak sense [25, 27]. These methods reduce the computational efficiency drastically as they introduce additional equations/unknowns to the original problem. Yet another way of tackling this issue is to utilize numerical methods that naturally support higher-order continuities inside the computational domain. One primary example among these methods is the isogeometric analysis (IGA) introduced by Hughes et al. [71] in 2005. IGA integrates computer-aided design (CAD) into the scientific simulation pipeline by using spline basis functions to describe both the geometry and the numerical solution. Initially, it was introduced for non-uniform rational basis splines (NURBS), but shortly after, other spline technologies were also implemented into the framework. Since then, several studies have been done exploiting the IGA in commercial and non-commercial analysis software packages. In the area of gradient elasticity, many researchers have exploited IGA and showed its robustness and efficiency compared to conventional approaches [26, 63, 72–76].

1.2 Fracture Mechanics

Until the end of the 19th century, cracks were not considered to play a significant role in the failure of massive structures. In the early years of the 20th century, a series of sudden failures in large structures like ships and aircraft drew several researchers' attention to the importance of these small, seemingly irrelevant defects. In 1921, Griffith [77], inspired by the work of Inglis [78], proposed an energy-based failure criterion taking into account the energy required to break atomic bonds and the strain energy released as the crack propagates. This is considered to be the first attempt to derive a mathematical model for fracture mechanics and is widely used today. However, his model had some limitations; namely, it could not predict the crack nucleation and branching. We refer the interested reader to [77] and [79] for more discussions on the topic.

Fracture occurs when, as a result of external loadings, multiple micro-defects in an object merge and form a crack, sometimes leading to its failure. In continuum mechanics, modelling crack initiation and propagation requires exploiting specific criteria to determine whether the crack can propagate. For brittle and quasi-brittle materials, these criteria are provided within the framework of LEFM. Studies with the focus on LEFM can be divided into two major groups: fracture mechanics and continuous/continuum damage mechanics (CDM) [80, 81]. In fracture mechanics, the crack is recognized as a discrete topological discontinuity, which in terms of finite elements means that considering this framework, a separation should occur between element edges [82]. Consequently, LEFM requires the crack to be (a priori) present in the model. CDM, on the other hand, works with smeared cracks. Smeared (or distributed)

cracks are the counterpart of discrete cracks where the cracked structure is still assumed to be a continuum. In terms of micro/macro dimensions, one can say that in fracture mechanics, the focus is on macroscopic cracks, while microscopic cracks are considered in CDM.

The finite element method is a candidate to solve fracture mechanics problems numerically. However, as mentioned before, using classical elements and shape functions, the unknown field is assumed to be continuous throughout the domain, and therefore, studying fracture and cracks, where a discontinuity in the displacement field is expected, becomes challenging. Using the conventional FEM, one needs to track the crack tip position and re-mesh the domain whenever the crack propagates. This procedure involves introducing internal boundaries to the problem and gets very complicated for sophisticated crack paths.

There are more suitable developments of the FEM available where studying discontinuous unknown fields has been made easier. One of the most famous approaches is the extended finite element method (XFEM) [83–86]. The idea here is to improve the finite element approximation using known characteristics of the solution field utilizing the enrichment concepts from the partition of unity finite element method (PUFEM) [87]. This enrichment makes the approach capable of approximating non-smooth features such as the discontinuous displacement field in a cracked structure by introducing additional degrees of freedom associated with the enrichment functions to the problem. For fracture mechanics problems, XFEM uses two different sets of enrichment functions to represent the discrete crack independent of the finite element mesh: (1) discontinuous enrichment functions to handle the jumps in the displacement field along the crack path, and (2) singularity enrichment functions in the vicinity of the crack front [88]. In XFEM, the crack's direction is obtained using stress intensity factors and various criteria for each step [89–91], while the length of each propagation increment is usually constant during the simulation. The crack path is always straight within each increment. Numerical integration in the framework of XFEM becomes tricky as the classical Gaussian schemes cannot be used because of the non-smooth functions [83, 92–94]. Also, ill-conditioning caused by the potential linear dependence of the shape functions used for the standard and enriched parts of the approximation, both for jump and tip enrichments, is another source of complexity with XFEM [95–100]. Moreover, the extension to three-dimensional problems and particularly the definition of the crack propagation increment in three dimensions is cumbersome [88]. It is worth noticing that XFEM is very close in definition to the generalized finite element method (GFEM) [87, 101, 102], with the difference that the XFEM was originally developed to handle discontinuities using local enrichments keeping the sparsity of the final matrices for the problems involving localized phenomena, while the enrichment was global in the classical GFEM. With the later advances in GFEM, the local enrichment was also used, and currently, XFEM and GFEM are virtually indistinguishable [103, 104].

Another approach to fracture which has gained momentum in recent years and is worth mentioning here is the peridynamics (PD) theory which discretizes the structure into a cloud of points. The theory is motivated by molecular dynamics and involves integral equations (integro-differential equations) instead of the usual differential equations of the classical continuum mechanics. This formulation has the advantage that no spatial derivatives are involved in the governing equations, making it very appealing to handle problems with discontinuities (see [105–112]). Moreover, in contrast to XFEM, the fracture criterion is embedded in the theory and no extra criteria is needed to simulate the crack propagation. PD performs very well in simulating the crack branching phenomenon, for instance when studying fracture in shattered glasses [113, 114]. For the sake of brevity, other numerical methods being capable of handling fracture problems are only mentioned at this point, e.g., phantom node method [115, 116], meshless methods [117, 118], scaled boundary finite element

method [119–121], and cohesive zone [122, 123] and segment [124] models among others. Decades after Griffith's pioneering works, Ginzburg, and Landau [125, 126], based on the idea of diffuse interfaces, used a so-called order parameter to expand the thermodynamic state functions in their remarkable theory of phase transitions. The prospect of seeing the interface between two phases as diffusive goes back to van der Waals [127] who believed that it is more natural to assume the interface between material phases to be diffusive rather than sharp. Cahn and Hilliard [128, 129] exploited the same idea to develop a spinodal decomposition model by using the alloy concentration as the order parameter. Aifantis and Serrin [130] later revisited the idea in 1983 in their mechanical theory of vapor-liquid phase transitions.

The term phase-field was introduced in the 1980s by Fix et al. [131] and Langer [132]. The phase-field method circumvents the problem of tracking the interface boundary by adding a phase-field parameter (order parameter) defined in the whole computational domain. This new parameter is restricted between two distinct states (0 and 1 in scientific papers) where the transition between these values takes place smoothly in a so-called interphase region. For instance, in terms of phase transition problems, one can define the phase-field as 1 where a specific phase exists and 0 where it vanishes. The crucial assumption here is that the phase-field diffuseness exists on a scale that is below the microstructure scale of interest [125, 132].

In 1998, Francfort et al. [133], proposed an energy minimization variational approach to develop a continuum theory that can predict the crack nucleation and propagation phenomena. Two years later, Bourdin et al. [134] regularized this variational formulation and introduced a scalar-valued phase-field parameter s to distinguish the intact material from the crack. The proposed formulation was capable of predicting both the crack nucleation and propagation. They also proposed a new parameter for the interphase ϵ, which defines the width of transition region between the damaged and undamaged material states. The Griffith energy analog to a sharp crack will be recovered in the limit case when the value of ϵ goes to zero. These studies paved the way for a classical FEM implementation of fracture mechanics. Miehe and his group [135, 136] developed an alternative phase-field fracture mechanics model based on continuum mechanics and showed its thermodynamic consistency. Built on this framework, many researchers proposed different variations to the original model [137]; among them, we mention [138–140] for dynamic fractures, and [141–143] for fracture in polymers, piezoelectric ceramics, and multi-physics problems, respectively. A successful implementation in the IGA framework was achieved in [140, 144–147] for different spline technologies such as NURBS, T-Splines, and (Truncated-) Hierarchical Basis Splines. A fourth-order phase-field formulation is used in some of these studies, which requires C^1-continuity and benefits from the higher continuity of IGA shape functions.

1.3 Motivation

From a computational point of view, the simulation of crack propagation has always been a challenging task. In the past, many mathematical and mechanical assumptions had to be taken into account to simulate this process successfully. The problem of tracking the sharp crack surface was among the first issues which was alleviated by introducing phase-field models. The appearance of stress singularities near the crack tip in classical continuum mechanics theory is considered to be another source of problem which makes selecting proper mesh sizes for numerical models very cumbersome and may lead to unphysical results. In the presence of a singularity, the crack propagation starts earlier in problems

with a finer discretization, which is only natural, considering that the strain energy density is higher and increases faster for smaller mesh sizes. Likewise, a loading that generally could not cause a crack to nucleate or propagate inside a structure will do so in the numerical simulation due to over-estimated stresses. Therefore, it stands to reason that removing this singular field from the results is a very crucial step in achieving physically meaningful results. The overarching goal of this thesis is twofold: first, existing phase-field models are shown to exhibit a singular stress behavior. This is important as the problem seems to be neglected in the community of phase-field fracture. One reason for this could be that the original phase-field fracture formulation already does a fine job of regularizing the stress field. However, solely using the idea of phase-field modelling is not sufficient to overcome the problem as singularities are inherent in the fundamental equations of continuum mechanics used in the current formulations. A series of concise numerical studies are needed to see the remaining effects of the singular field. Moreover, it is very common to use linear elements in studies of phase-field problems. Most of the time, the discretizations used for such models are already fine because of the requirement that the mesh size should be smaller than the interphase width of the order parameter. Here, using meshes with small distances between adjacent nodes is somehow forced, and higher-order interpolations do not significantly improve the results. Therefore, higher-order elements are usually avoided to decrease the computational effort. The problem is that the effects of the singularity (e.g., oscillations in the results because of a sudden jump between the values of two adjacent computational points) can be concealed when using linear elements. It is only when using higher-order elements that one notices the effects of the existence of a singular field. Finally, there are analytical solutions to the problem available, which do not show any signs of a singular response. Almost all of these analytical solutions are derived for the one-dimensional case (e.g., a space truss element), and the classical Cauchy theory does not exhibit singularities in one dimension, as a line body can sustain line and point boundary conditions. It is only in two and three dimensions that this specific problem emerges. The second goal of the current work is to propose a possible remedy to this problem based on the application of higher-order displacement gradients. For this purpose, two formulations for phase-field modelling of fracture mechanics based on strain gradient theory will be proposed and their performance in regularizing the singularities in the solution field will be investigated.

1.4 Structure of the Work

This thesis is organized in the following way: after this introduction, Chapter 2 provides an introduction to continuum mechanics and strain gradient theories. Two simplified strain gradient models based on Form I and Form II of Mindlin's theory are also introduced ,which will be exploited in the following chapters. Chapter 3 provides the governing equations of phase-field fracture models. Here also two models based on the standard formulation are introduced and the main components of these models are discussed in detail. In the final section of Chapter 3, the ideas of strain gradient elasticity and phase-field modelling of fracture are subsequently combined into two strain gradient elasticity enhanced phase-field fracture models, exploiting the advantages of both theories. Afterwards, Chapter 4 introduces the numerical method being used to discretize the problem; namely the isogeometric analysis. Some essential information regarding the employed shape functions are provided, and a complete representation of the residual and tangent matrices is given for all the previously discussed models. The numerical models are discussed in Chapter 5, where the material and geometric properties that are used in the benchmark tests are also reported. The

results section starts with showing the ability of the simplified strain gradient models in regularizing the singular fields for static problems, i.e., without considering fracture. The results are demonstrated for two strain gradient models for two- and three-dimensional settings verifying the performance of the models as well as the numerical method exploited to discretize the governing equations. Next, the problems associated with using the classical phase-field fracture models are shown and discussed for a benchmark test. After that, the performance of the proposed strain gradient enhanced phase-field fracture models is investigated. A comprehensive discussion on the results is provided by comparing the strain energy density and individual stress fields from the classical phase-field fracture and the proposed formulations. Finally, conclusions, as well as an outlook on ongoing research activities and the future research direction are presented in Chapter 6.

2 Strain Gradient Elasticity

We start the chapter by briefly providing the necessary background on continuum mechanics, following by an introduction to Mindlin's theory of elasticity with microstructures. Different notions of double-stresses in Forms I and II of Mindlin's theory are discussed afterward. In the final sections of this chapter, two simplified strain gradient models are provided, which will be our gradient models of choice for the studies done in the following chapters.

2.1 Classical Continuum Mechanics

Classical continuum mechanics is based on two important assumptions: (1) considering only the macroscopic scales and ignoring the discontinuities in the microstructure level, objects are continuous in space, and (2) the material properties can be characterized by averaged values in this space, where they can change continuously within this space [148].

2.1.1 Force and Stress

We start with Newton's second law of motion,

$$\mathbf{f} = m\,\mathbf{a} = m\,\frac{\mathrm{d}\mathbf{v}}{\mathrm{d}t}, \tag{2.1}$$

where $\mathbf{f}$ is a vector and represents the summation of all forces acting on the continuum, m is the total mass of the body, t represents time, and $\mathbf{v}$ and $\mathbf{a}$ denote the velocity vector and its first derivative with respect to time, the acceleration vector, respectively. In continuum mechanics, we mostly deal with two different kinds of forces. Body forces which act on every material element in the object and surface forces (also known as traction or contact forces) that act on the object boundaries. Body forces acting on a body are proportional to its mass, while surface forces are proportional to the total area of the region where the forces are applied. Figure 2.1 provides a graphical representation of these forces for a material volume Ω bounded by a surface Γ. In this figure, $\mathbf{b}$ and $\mathbf{t}$ represent body and surface forces, respectively, while $\mathbf{n}$ is the unit normal vector of the infinitesimal area $\mathrm{d}A$. The reliance of surface forces on the area on which they are applied makes it difficult to quantify and compare them without taking the size of this area into account. Therefore, we tend to normalize the quantity of surface forces using the size of the area leading to the introduction of the concept of stresses [148]. In general, stress is defined as the surface force per unit area. From a continuum mechanics point of view, we usually look for stresses at a material point, i.e., in the limit of the size of the area going to zero [149]. A material point is referred to an infinitesimal volume with an infinitesimal mass. Classical stresses can be divided into two major types. Normal stresses caused by force vectors normal to the surface, and shear stresses where the force vector is parallel to the surface. When a force vector is neither parallel nor normal to the surface, one can extract the normal and tangential components of it with respect to the surface and then calculate the corresponding normal and shear stresses.
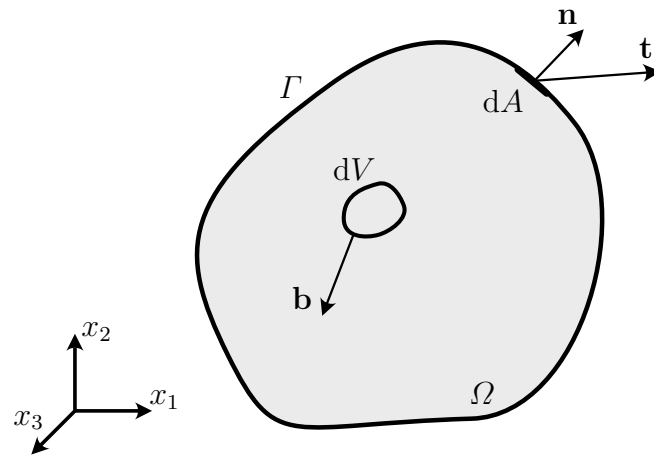
Figure 2.1: Surface and body forces acting on a body

The full stress tensor can be represented by the coefficient matrix,

$$S_{ij} = \begin{bmatrix} S_{11} & S_{12} & S_{13} \\ S_{21} & S_{22} & S_{23} \\ S_{31} & S_{32} & S_{33} \end{bmatrix},$$ (2.2)

where and henceforth, we use Einstein's summation convention. In this form, the diagonal terms represent the normal stress components, while the non-diagonal terms are the shear stresses. To keep the element volume in equilibrium, the shear stress components must fulfill $S_{ij} = S_{ji}$, a result of the principle of conservation of angular momentum, cf. Sect. 2.1.3.2. Figure 2.2 shows the full stress state acting on an elemental volume. Components of the stress tensor are denoted by S_{ij} where i and j denote the direction normal to the surface and the direction of stress component, respectively.
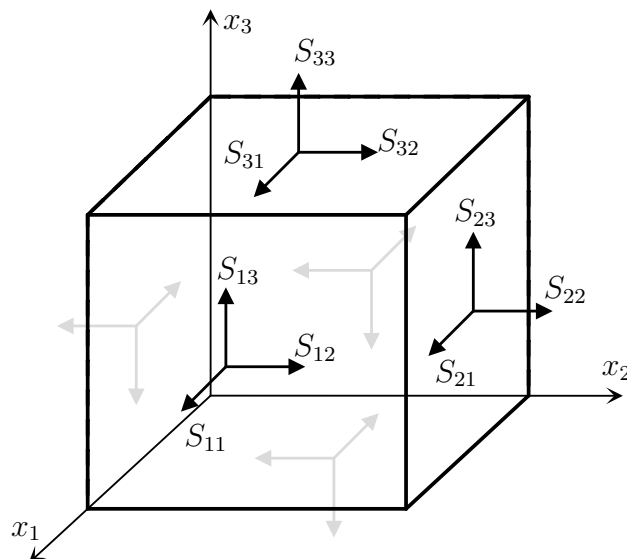
Figure 2.2: Stress state of an infinitesimal volume in a continuum

2.1.2 Deformation and Strain

The continuum deforms under the applied body and surface forces (stresses) as shown in Fig. 2.3. Deformation can be measured using a vector connecting the positions of the element of the body before and after deformation. Displacement components of a material particle can be determined by

$$u_i := x_i - X_i, \tag{2.3}$$

where X_i and x_i $(i = 1, 2, 3)$ are the material and spatial position vectors with respect to the fixed origin of a Cartesian coordinate system.

In what follows, we assume only small deformations, i.e., the displacement gradients are assumed to be very small compared to unity,

$$\frac{\partial u_j}{\partial X_i} \ll 1. \tag{2.4}$$

Consequently, one can assume

$$\frac{\partial u_j}{\partial X_i} \approx \frac{\partial u_j}{\partial x_i}, \quad u_j = u_j(x_i, t). \tag{2.5}$$

Moreover, neglecting the rigid body deformations, i.e., translations and rotations, the deformations caused by body forces and stresses produce distortions (strains) in the body. We define the symmetric part of the displacement gradient, the linear strain tensor E_{ij},

$$E_{ij} := \frac{u_{j,i} + u_{i,j}}{2}, \tag{2.6}$$

where the comma notation denotes partial derivative in space. The stress tensor shown in
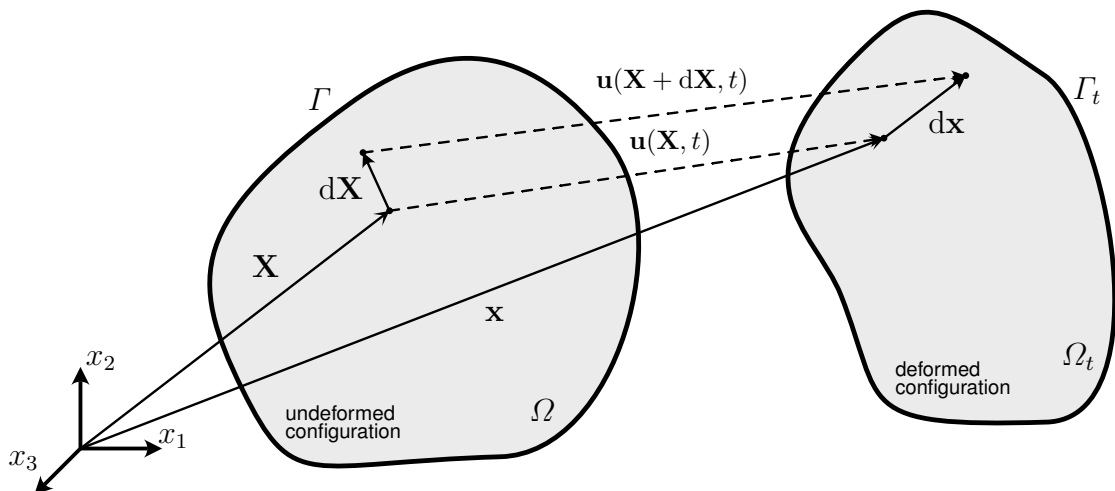
Figure 2.3: Undeformed and deformed (at time t) configurations of a material volume bounded by its surface

Eq. (2.2) is the work-conjugate of

$$E_{ij} = \begin{bmatrix} E_{11} & E_{12} & E_{13} \\ E_{21} & E_{22} & E_{23} \\ E_{31} & E_{32} & E_{33} \end{bmatrix} . \tag{2.7}$$

The variable E_{ij} denotes a deformation determined by the displacement u_j varying linearly in the direction of x_i. In the same way, the stress component S_{ij}, the work-conjugate of E_{ij}, corresponds to a force vector in the direction x_j acting on a plane with a normal in the x_i direction. Figure 2.4 shows an example where a strain E_{22} of magnitude k (a constant value) is applied on a unit cube. Considering E_{22}, we have $u_2 = kx_2$ and $u_1 = u_3 = 0$.
In the same way, for the case of pure shear stress (no normal stresses) in the x_2-x_3 plane, a strain $E_{23} = E_{32} = k$ is applied on the same unit cube. Considering E_{23} and E_{32}, we have $u_3 = kx_2$, and $u_2 = kx_3$, respectively, while $u_1 = 0$ (see Fig. 2.5).

2.1.3 Conservation Laws

Every physical system can evolve with the condition that certain measurable physical quantities, such as energy, remain conserved. In this section, we go through the conservation laws in the context of continuum mechanics.

2.1.3.1 Conservation of Mass

Conservation of mass states that the total mass of an object does not change. In terms of continuum mechanics, for a stationary elemental volume, mass is neither generated nor consumed inside the volume. In other words, the only way to change the mass of the volume is to flow mass across its boundaries. We define the material density ρ to be the amount of mass per unit volume. Considering the infinitesimal elemental volume shown in Fig. 2.6,
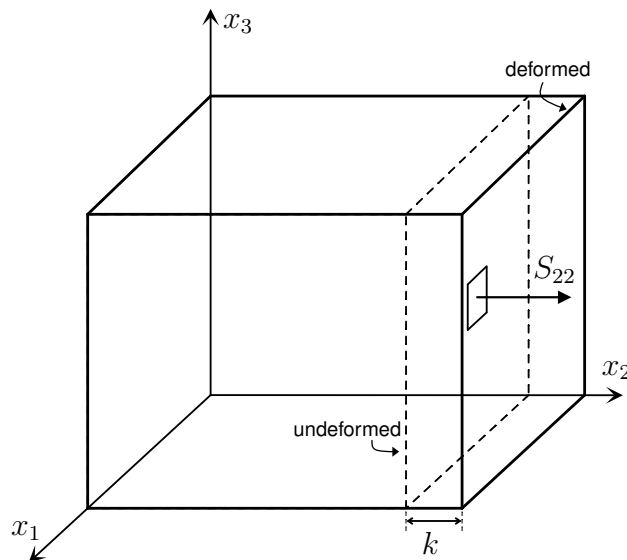
Figure 2.4: A cubic volume of unit edges under constant strain $E_{22} = k$ and related work-conjugate stress S_{22}
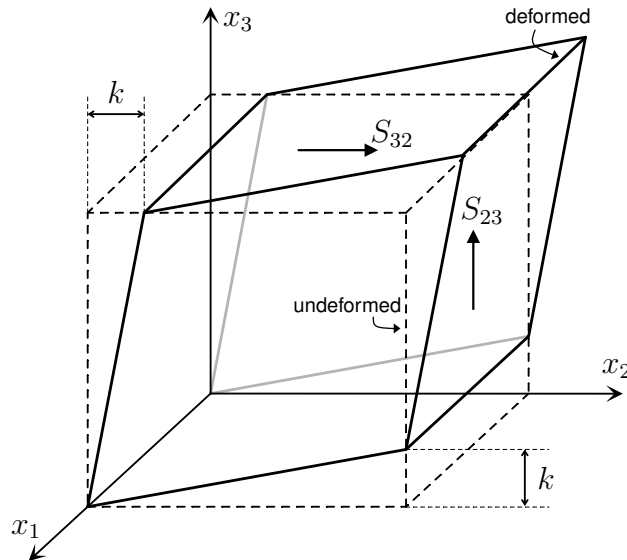
Figure 2.5: A cubic volume of unit edges under constant strain $E_{23} = E_{32} = k$ and related work-conjugate stress $S_{23} = S_{32}$
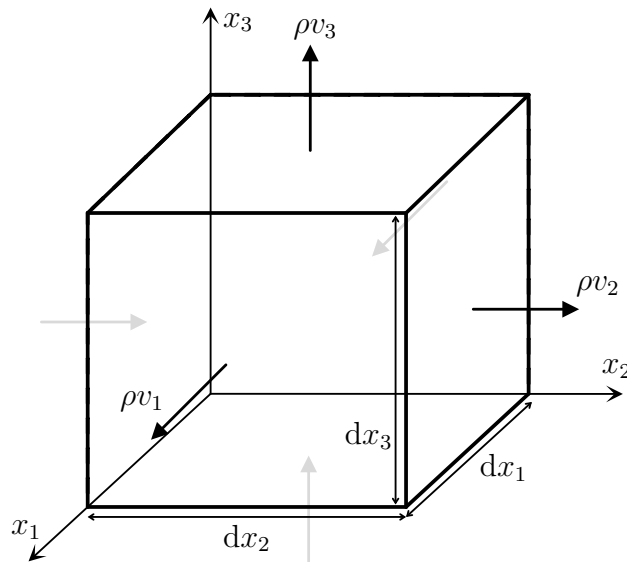
Figure 2.6: Mass flux across boundaries of an elemental volume

$$\rho = \frac{m}{V} \qquad m = \rho\, V = \rho\, dx_1\, dx_2\, dx_3. \tag{2.8}$$

According to the law of conversation of mass, the rate of changes in the mass should be equaled to the flux of mass entering the volume minus the flux of mass leaving the volume. For the shown elemental volume, we can consider the flux of mass on each face and accumulate the values to find the total rate of changes in the mass. The flow of a mass entering a face can be calculate by taking the product of density, velocity and the area of the

face. For instance, for the elemental volume shown in Fig. 2.6,

$$
\begin{aligned}
\frac{\partial}{\partial t}\left(\rho\, \mathrm{d}x_1\, \mathrm{d}x_2\, \mathrm{d}x_3\right) = {} & \left[\left(\rho v_1 \mathrm{d}x_2\, \mathrm{d}x_3\,\right)_{x_1} - \left(\rho v_1 \mathrm{d}x_2\, \mathrm{d}x_3\,\right)_{x_1+\mathrm{d}x_1}\right] \\
& + \left[\left(\rho v_2 \mathrm{d}x_1\, \mathrm{d}x_3\,\right)_{x_2} - \left(\rho v_2 \mathrm{d}x_1\, \mathrm{d}x_3\,\right)_{x_2+\mathrm{d}x_2}\right] \\
& + \left[\left(\rho v_3 \mathrm{d}x_1\, \mathrm{d}x_2\,\right)_{x_3} - \left(\rho v_3 \mathrm{d}x_1\, \mathrm{d}x_2\,\right)_{x_3+\mathrm{d}x_3}\right],
\end{aligned}
\tag{2.9}
$$

where v_i represent the components of the velocity vector. Considering the stationarity of the elemental volume and subdividing both sides of Eq. (2.9) by $\mathrm{d}x_1\, \mathrm{d}x_2\, \mathrm{d}x_3$, in the limit of $\mathrm{d}x_1$, $\mathrm{d}x_2$, and $\mathrm{d}x_3$ going to zero, we have:

$$
\frac{\partial \rho}{\partial t} = -\left(\frac{\partial \rho v_1}{\partial x_1} + \frac{\partial \rho v_2}{\partial x_2} + \frac{\partial \rho v_3}{\partial x_3}\right) = -\frac{\partial \rho v_j}{\partial x_j}.
\tag{2.10}
$$

Eq. (2.10) is known as the continuity equation [148, 150]. The negative sign means that a decrease in the net gradient of the mass flux along the spatial coordinates results in accumulation of mass in the volume. Using the divergence operator, Eq. (2.10) can be written in the compact form of

$$
\frac{\partial \rho}{\partial t} = -\nabla \cdot (\rho \mathbf{v}).
\tag{2.11}
$$

which states the principle of conservation of mass. Carrying out the derivation in Eqs. (2.10) and (2.11) yields

$$
\frac{\partial \rho}{\partial t} + v_j \frac{\partial \rho}{x_j} = -\rho \frac{\partial v_j}{x_j}.
\tag{2.12}
$$

The term on the left-hand side is called the "special" or "material" derivative [150],

$$
\frac{D\rho}{Dt} = \frac{\partial \rho}{\partial t} + v_j \frac{\partial \rho}{x_j}.
\tag{2.13}
$$

We can re-write Eq. (2.11) as

$$
\frac{D\rho}{Dt} = -\rho \frac{\partial v_j}{x_j}.
\tag{2.14}
$$

For materials in which the density is constant in time, $D\rho/Dt = 0$, Eq. (2.14) leads to the divergence of the velocity field to be zero as well.

2.1.3.2 Conservation of Linear Momentum

Conservation of linear momentum (also known as balance of linear momentum) is an essential concept in continuum mechanics. According to this principle, for an elemental volume, the rate of changes in momentum is equal to the flow of momentum entering the volume minus the flow of momentum leaving the volume plus the sum of forces acting on the volume [151]. Momentum is a vector quantity and can be determined from the product of mass and velocity. Using Eq. (2.8), we can relate momentum to density and volume, and then, the flow of momentum can be calculated by taking the product of density, the velocity at which the momentum flows, and the area of the face across which the momentum flows. For instance, for the elemental volume shown in Fig. 2.7, one can write the following relation
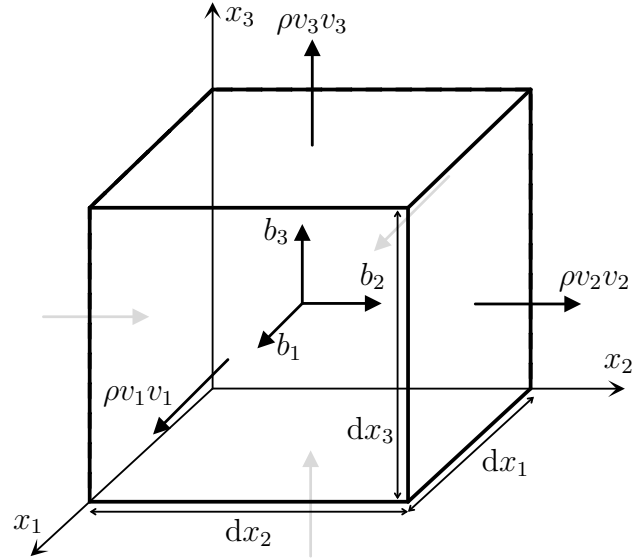
Figure 2.7: Momentum flux across boundaries of an elemental volume

for the flux of the x_i-direction component of momentum [148]:

$$
\begin{aligned}
\text{momentum flux} =\ & \left(\rho\, v_i\, v_1\, \mathrm{d}x_2\, \mathrm{d}x_3\right)_{x_1} - \left(\rho\, v_i\, v_1\, \mathrm{d}x_2\, \mathrm{d}x_3\right)_{x_1+\mathrm{d}x_1} \\
& + \left(\rho\, v_i\, v_2\, \mathrm{d}x_1\, \mathrm{d}x_3\right)_{x_2} - \left(\rho\, v_i\, v_2\, \mathrm{d}x_1\, \mathrm{d}x_3\right)_{x_2+\mathrm{d}x_2} \\
& + \left(\rho\, v_i\, v_3\, \mathrm{d}x_1\, \mathrm{d}x_2\right)_{x_3} - \left(\rho\, v_i\, v_3\, \mathrm{d}x_1\, \mathrm{d}x_2\right)_{x_3+\mathrm{d}x_3}.
\end{aligned}
\tag{2.15}
$$

In addition to the above relation, we should consider the changes in the rate of momentum caused by the body and surface forces (consider an elemental volume $\mathrm{d}x_1\,\mathrm{d}x_2\,\mathrm{d}x_3$ such as the one shown in Fig. 2.2):

$$
\begin{aligned}
\frac{\Delta\,(mV)}{\Delta t} =\ & -\left(S_{1i}\,\mathrm{d}x_2\,\mathrm{d}x_3\right)_{x_1} + \left(S_{1i}\,\mathrm{d}x_2\,\mathrm{d}x_3\right)_{x_1+\mathrm{d}x_1} + \\
& -\left(S_{2i}\,\mathrm{d}x_1\,\mathrm{d}x_3\right)_{x_2} + \left(S_{2i}\,\mathrm{d}x_1\,\mathrm{d}x_3\right)_{x_2+\mathrm{d}x_2} + \\
& -\left(S_{3i}\,\mathrm{d}x_1\,\mathrm{d}x_2\right)_{x_3} + \left(S_{3i}\,\mathrm{d}x_1\,\mathrm{d}x_2\right)_{x_3+\mathrm{d}x_3} + \rho\,b_i\,\mathrm{d}x_1\,\mathrm{d}x_2\,\mathrm{d}x_3,
\end{aligned}
\tag{2.16}
$$

where ρb_i is the body force density and Δ denotes changes of the quantity. With this, we can write the principle of conservation of linear momentum for the i-th direction:

$$
\begin{aligned}
\frac{\partial}{\partial t}\left(\rho\, v_i\, \mathrm{d}x_1\, \mathrm{d}x_2\, \mathrm{d}x_3\right) =\ & \left(\rho\, v_i\, v_1\, \mathrm{d}x_2\, \mathrm{d}x_3\right)_{x_1} - \left(\rho\, v_i\, v_1\, \mathrm{d}x_2\, \mathrm{d}x_3\right)_{x_1+\mathrm{d}x_1} \\
& + \left(\rho\, v_i\, v_2\, \mathrm{d}x_1\, \mathrm{d}x_3\right)_{x_2} - \left(\rho\, v_i\, v_2\, \mathrm{d}x_1\, \mathrm{d}x_3\right)_{x_2+\mathrm{d}x_2} \\
& + \left(\rho\, v_i\, v_3\, \mathrm{d}x_1\, \mathrm{d}x_2\right)_{x_3} - \left(\rho\, v_i\, v_3\, \mathrm{d}x_1\, \mathrm{d}x_2\right)_{x_3+\mathrm{d}x_3} \\
& - \left(S_{1i}\,\mathrm{d}x_2\,\mathrm{d}x_3\right)_{x_1} + \left(S_{1i}\,\mathrm{d}x_2\,\mathrm{d}x_3\right)_{x_1+\mathrm{d}x_1} \\
& - \left(S_{2i}\,\mathrm{d}x_1\,\mathrm{d}x_3\right)_{x_2} + \left(S_{2i}\,\mathrm{d}x_1\,\mathrm{d}x_3\right)_{x_2+\mathrm{d}x_2} \\
& - \left(S_{3i}\,\mathrm{d}x_1\,\mathrm{d}x_2\right)_{x_3} + \left(S_{3i}\,\mathrm{d}x_1\,\mathrm{d}x_2\right)_{x_3+\mathrm{d}x_3} \\
& + \rho\,b_i\,\mathrm{d}x_1\,\mathrm{d}x_2\,\mathrm{d}x_3.
\end{aligned}
\tag{2.17}
$$

Dividing Eq. (2.17) by $\mathrm{d}x_1\,\mathrm{d}x_2\,\mathrm{d}x_3$, in the limit case when the dimensions $\mathrm{d}x_1$, $\mathrm{d}x_2$, and $\mathrm{d}x_3$ go to zero, we have

$$\frac{\partial}{\partial t}\left(\rho\,v_i\right) = -\frac{\partial}{\partial x_j}\left(\rho\,v_j\,v_i\right) + \frac{\partial S_{ij}}{\partial x_j} + \rho\,b_i. \tag{2.18}$$

Carrying out the differentiation of the left-hand side and the first term of the right-hand side of Eq. (2.18), we have

$$\rho\left(\frac{\partial v_i}{\partial t} + v_j\frac{\partial v_i}{\partial x_j}\right) + v_i\left(\frac{\partial \rho}{\partial t} + v_j\frac{\partial \rho}{\partial x_j} + \rho\frac{\partial v_j}{x_j}\right) = \frac{\partial S_{ij}}{\partial x_j} + \rho\,b_i. \tag{2.19}$$

Considering the principle of conservation of mass (Eqs. (2.17) and (2.18)), and the definition of special derivatives introduced in the previous section, we end up with the equations for the conservation of linear momentum [148]:

$$\rho\frac{Dv_i}{Dt} = S_{ij,j} + \rho\,b_i, \tag{2.20}$$

or, in matrix notation

$$\rho\frac{D\mathbf{v}}{Dt} = \nabla\cdot\mathbf{S} + \rho\,\mathbf{b}. \tag{2.21}$$

In this work, we only consider static and quasi-static models, and with this assumption, Eq. (2.20) can be simplified to

$$\nabla\cdot\mathbf{S} + \rho\,\mathbf{b} = \mathbf{0}. \tag{2.22}$$

2.1.3.3 Conservation of Angular Momentum

Let us write the equations for balance of angular momentum in our elemental volume [152]

$$\int_{\Gamma_1} \mathbf{x}\,\times\,\bar{\mathbf{t}}^1\,\mathrm{d}A + \int_{\Omega} \mathbf{x}\,\times\,\mathbf{b}\,\rho\,\mathrm{d}V = \frac{d}{dt}\left(\int_{\Omega} \mathbf{x}\,\times\,\mathbf{v}\,\rho\,\mathrm{d}V\right), \tag{2.23}$$

or, in index notation,

$$\int_{\Gamma_1} \epsilon_{ijk}\,x_j\,\bar{t}_k^1\,\mathrm{d}A + \int_{\Omega} \epsilon_{ijk}\,x_j\,b_k\,\rho\,\mathrm{d}V = \frac{d}{dt}\left(\int_{\Omega} \epsilon_{ijk}\,x_i\,v_k\,\rho\,\mathrm{d}V\right), \tag{2.24}$$

where $\bar{t}_i^1$ and x_i denote the prescribed surface tractions and the position vector, respectively, and ϵ_{ijk} is the alternating tensor [1]. The left-hand side is the resultant moment exerted by surface tractions and body forces, while in the right-hand side we have the total angular momentum of the elemental volume. Writing the equation in terms of S_{ij}, after some transformations and consideration of the principles of conservation of mass and linear

---

[1] The superscript $\square^1$ in $\bar{t}_i^1$ is to distinguish between surface tractions and double-tractions as well as edge tractions, which will be introduced in the following sections.

momentum, we end up with the following equations:

$$S_{12} - S_{21} = 0,$$
$$S_{23} - S_{32} = 0, \qquad\qquad (2.25)$$
$$S_{13} - S_{31} = 0.$$

In other words, the principle of conservation of angular momentum requires the Cauchy stress to be symmetric, i.e.,

$$S_{ij} = S_{ji}. \qquad\qquad (2.26)$$

2.1.4 Constitutive Law

The discussions provided in the previous sections were independent of the material properties of the body. The constitutive laws provide the relation between stresses and strains. In other words, they tell us how the body will behave under the applied stresses. In the current work, we will only focus on homogeneous linear elastic isotropic materials and small deformations. We can use Hooke's law to study the behavior of these materials. The general formulation for Hooke's law is

$$\mathbf{S} = \mathbb{C} : \mathbf{E}, \qquad\qquad (2.27)$$

or, in index notation,

$$S_{ij} = C_{ijkl} E_{kl}, \qquad\qquad (2.28)$$

where $\mathbb{C}$ is a fourth-order tensor and is called the material stiffness tensor or the tensor of elastic moduli [152],

$$C_{ijkl} = \lambda\, \delta_{ij}\delta_{kl} + \mu\left(\delta_{ik}\delta_{jl} + \delta_{il}\delta_{jk}\right), \qquad\qquad (2.29)$$

with λ and μ being the Lamé constants and δ_{ij} the Kronecker delta.

2.1.5 Principle of Virtual Work

Variational principles based on weak formulations, and in particular the principle of virtual work, form the basis for the finite element solution of continuum mechanics equations. We begin the derivation by multiplying the balance of linear momentum equation, cf. Eq. (2.22), by a test function $\delta\mathbf{u}$, and then will integrate the resulting equation over the whole domain,

$$\int_{\Omega} (-\nabla \cdot \mathbf{S} - \rho\,\mathbf{b}) \cdot \delta\mathbf{u}\, dV = 0, \qquad\qquad (2.30)$$

or, in index notation,

$$\int_{\Omega} (-S_{ij,j} - \rho\,b_i)\, \delta u_i\, dV = 0. \qquad\qquad (2.31)$$

In Eqs. (2.30) and (2.31), δ is a linear operator and can be treated as a differential operator. The test function is chosen to be arbitrary, but should vanish in regions where Dirichlet (essential) boundary conditions are applied. Moreover, its value should be always trivial,

independent of the value of the actual displacement, which is our primary unknown field. Applying the divergence theorem yields

$$- \int_{\Omega} S_{ij,j} \, \delta u_i \, \mathrm{d}V = \int_{\Omega} S_{ij} \, \delta E_{ij} \, \mathrm{d}V - \int_{\Gamma_1} S_{ij} \, n_j \, \delta u_i \, \mathrm{d}A, \qquad (2.32)$$

where we have used the symmetry of the Cauchy stresses, i.e.,

$$S_{ij} \, \delta E_{ij} = S_{ij} \left(\frac{\delta u_{i,j} + \delta u_{j,i}}{2} \right) = \frac{1}{2} \left(S_{ij} \, \delta u_{i,j} + S_{ji} \, \delta u_{i,j} \right) = S_{ij} \, \delta u_{i,j}. \qquad (2.33)$$

Replacing Eq. (2.32) in Eq. (2.31) yields

$$\int_{\Omega} S_{ij} \, \delta E_{ij} \, \mathrm{d}V = \int_{\Gamma_1} S_{ij} \, n_j \, \delta u_i \, \mathrm{d}A + \int_{\Omega} b_i \, \delta u_i \, \rho \, \mathrm{d}V. \qquad (2.34)$$

The left-hand side of Eq. (2.34) represents the work of internal forces, $\delta\Psi^{\mathrm{int}}$. In the absence of dynamic forces, the principle of virtual work states

$$\delta\Psi^{\mathrm{int}} = \delta\Psi^{\mathrm{ext}}. \qquad (2.35)$$

For Eq. (2.35) to be valid, the external forces $\delta\Psi^{\mathrm{ext}}$ should have the form

$$\delta\Psi^{\mathrm{ext}} = \int_{\Gamma_1} \bar{t}_i^1 \, \delta u_i \, \mathrm{d}A + \int_{\Omega} b_i \, \delta u_i \, \rho \, \mathrm{d}V, \qquad (2.36)$$

which yields the weak formulation

$$\int_{\Omega} S_{ij} \, \delta E_{ij} \, \mathrm{d}V = \int_{\Gamma_1} \bar{t}_i^1 \, \delta u_i \, \mathrm{d}A + \int_{\Omega} b_i \, \delta u_i \, \rho \, \mathrm{d}V. \qquad (2.37)$$

At this point, it should be noted that the same outcome can be achieved by considering the stored energy as the starting point and taking its first variation with respect to the displacements [153, 154]. This will be discussed in more detail in the following sections.

2.2 Mindlin's Theory of Elasticity with Micro-Structures

2.2.1 Introduction

We base our formulation on the theory of elasticity with micro-structures introduced by Mindlin [42]. This theory provides a comprehensive framework, considering both the macro- and micro-deformations, to study the behavior of materials taking their internal structure into account. Mindlin's theory is based on the idea of unit cells and therefore a continuum in this sense has some characteristics of lattice crystals. A crystal is created by repetitive translations of the unit cells. This means that a unit cell is the smallest portion of a crystal which can be repeated to construct the whole structure. Figure 2.8 shows a simple cubic unit cell of a lattice crystal. According to Mindlin, the unit cell in his theory can also be regarded as a molecule of a polymer, a crystallite of a polycrystal or a grain of a granular material [42]. Before we continue, we need to define some new variables related to the microstructure of the material, such as micro-displacements and micro-rotations. As this is the only section in this work which deals with variables in micro-scales and to make it easier for the reader to
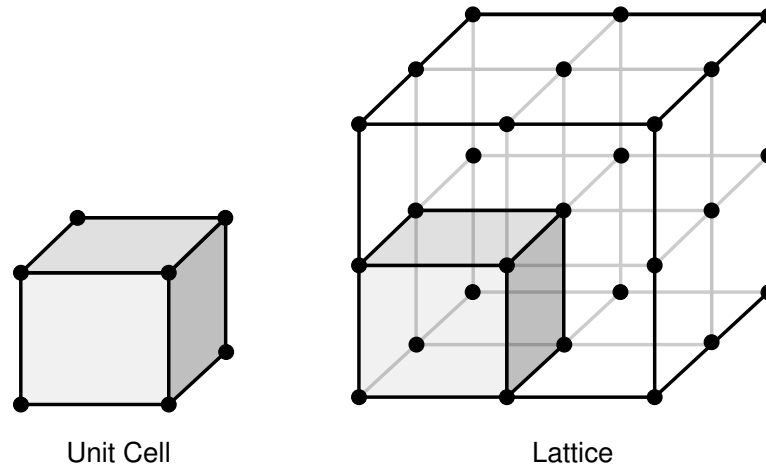
Unit Cell   Lattice

Figure 2.8: A simple cubic unit cell of a crystal lattice. The black circles denote the so-called lattice points which represent crystalline solid particles, such as atoms, molecules, or ions.

distinguish between macro- and micro-fields, we will use Greek letters and "prime" symbols to represent the microscopic fields such as micro-rotations and relative deformation.
We have already introduced the macro-displacements, u_i in the previous sections, cf. Eq. (2.3). We further define the micro-displacements,

$$u_i' := x_i' - X_i', \tag{2.38}$$

where it is assumed that a micro-volume is embedded in each material point, and $\mathbf{x}'$ and $\mathbf{X}'$ are the spatial and material position vectors of this micro-volume, respectively. The axes of the coordinate system corresponding to the new position vectors are parallel to the original Cartesian coordinate system of the macro-volume, but its origin moves with the macro-displacement u_i (see Fig. 2.9). Considering small deformations, one can write
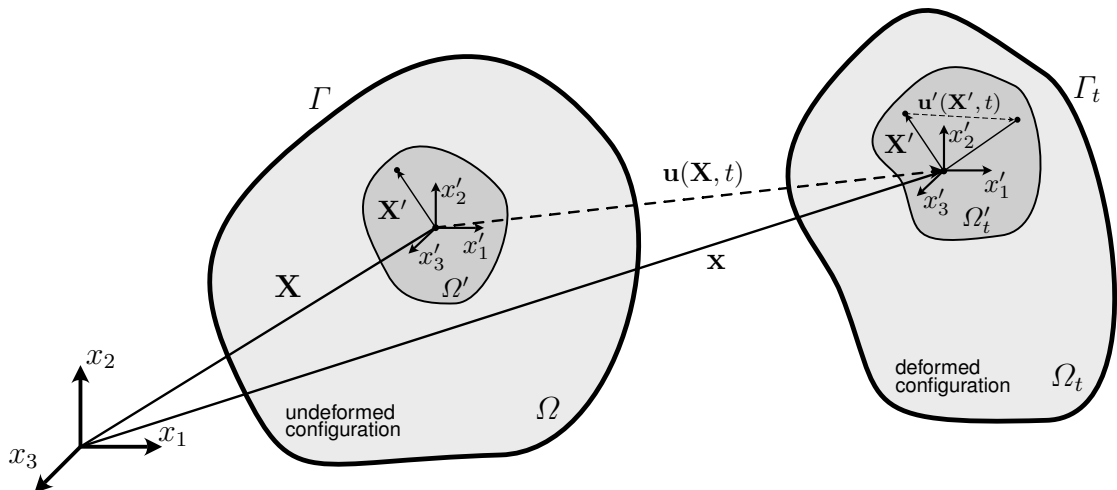
Figure 2.9: Undeformed and deformed (at time t) configurations of a material volume bounded by its surface, and a micro-volume embedded to a material point for Mindlin's theory of elasticity with microstructures

$$\frac{\partial u'_j}{\partial X'_i} \ll 1, \tag{2.39}$$

and therefore,

$$\frac{\partial u'_j}{\partial X'_i} \approx \frac{\partial u'_j}{\partial x'_i}, \quad u'_j = u_j(x_i, x'_i, t). \tag{2.40}$$

Let us further define the displacement gradient in the microscopic volume, the so-called micro-deformation,

$$\phi_{ij} = u'_{j,i'}. \tag{2.41}$$

The micro-deformations can be divided into a symmetric part, micro-strain,

$$\phi_{(ij)} = \frac{\phi_{ij} + \phi_{ji}}{2}, \tag{2.42}$$

and an anti-symmetric part, micro-rotation,

$$\phi_{[ij]} = \frac{\phi_{ij} - \phi_{ji}}{2}. \tag{2.43}$$

Moreover, one can define two new variables, the relative deformation,

$$\gamma_{ij} = L_{ij} - \phi_{ij}, \tag{2.44}$$

and the micro-deformation gradient,

$$\chi_{ijk} = \phi_{jk,i}, \tag{2.45}$$

where $L_{ij} = u_{j,i}$ is the macroscopic-displacement gradient (the distortion tensor). For a better understanding of the meaning of these new variables, the reader is referred to Figs. 2.10–2.12. We define the potential energy density to be a quadratic function of E_{ij} (6 independent components), γ_{ij} (9 independent components), and χ_{ijk} (27 independent components),

$$\psi_{\text{grad}} = \psi_{\text{grad}}\left(E_{ij}, \gamma_{ij}, \chi_{ijk}\right) = \frac{1}{2}C_{ijkl}E_{ij}E_{kl} + \frac{1}{2}B_{ijkl}\gamma_{ij}\gamma_{kl} + \frac{1}{2}A_{ijklmn}\chi_{ijk}\chi_{lmn}$$
$$+ D_{ijklm}\gamma_{ij}\chi_{klm} + F_{ijklm}\chi_{ijk}E_{lm} + G_{ijkl}\gamma_{ij}E_{kl}, \tag{2.46}$$

where the density is considered with respect to the macroscopic volume, and we have the following symmetries:

$$
\begin{aligned}
C_{ijkl} = C_{klij} = C_{jikl} \quad &\text{resulting in 21 independent coefficients,}\\
B_{ijkl} = B_{klij} \quad &\text{resulting in 45 independent coefficients,}\\
A_{ijklmn} = A_{lmnijk} \quad &\text{resulting in 378 independent coefficients,}\\
D_{ijklm} \quad &\text{resulting in 243 independent coefficients,}\\
F_{ijklm} = F_{ijkml} \quad &\text{resulting in 162 independent coefficients, and}\\
G_{ijkl} = G_{ijlk} \quad &\text{resulting in 54 independent coefficients.}
\end{aligned}
\tag{2.47}
$$

Figure 2.10: Components of relative stress σ_{ij}, macro-displacement gradient L_{ij}, micro deformation ϕ_{ij}, and relative deformation γ_{ij} (adapted from [42])

The energy-conjugate of E_{ij} is the Cauchy stress S_{ij}. We further define the relative stress,

$$\sigma_{ij} = \frac{\partial \psi_{\text{grad}}}{\partial \gamma_{ij}}, \tag{2.48}$$

the energy-conjugate of γ_{ij}, and the double stress,

$$\mu_{ijk} = \frac{\partial \psi_{\text{grad}}}{\partial \chi_{ijk}}, \tag{2.49}$$

the energy-conjugate of χ_{ijk}. Equation (2.46) has $42 \times 42 = 1764$ coefficients, 903 of which are independent. In other words, the generality of Mindlin's theory results in 903 independent coefficients to define a specific material. Certainly, it is almost impossible to determine all these material coefficients, therefore simplification is meant to be done. Considering a centrosymmetric isotropic material (applicable to all the materials which we use in the current work), we can simplify Eq. (2.46) as the odd-order tensors vanish. Centrosymmetry in crystal structures refers to the existence of a centre of symmetry about which for each particle (for example, an atom) at (x, y, z) there exists a particle at $(-x, -y, -z)$ [155]. The simplified Eq. (2.46) can be written as

$$\psi_{\text{grad}} = \frac{1}{2}C_{ijkl}E_{ij}E_{kl} + \frac{1}{2}B_{ijkl}\gamma_{ij}\gamma_{kl} + \frac{1}{2}A_{ijklmn}\chi_{ijk}\chi_{lmn} + G_{ijkl}\gamma_{ij}E_{kl}. \tag{2.50}$$

The material tensors in Eq. (2.50) can be defined in terms of products of Kronecker delta:

$$
\begin{aligned}
C_{ijkl} &= c_1\delta_{ij}\delta_{kl} &&+ c_2\delta_{ik}\delta_{jl} &&+ c_3\delta_{il}\delta_{jk}, \\
B_{ijkl} &= b_1\delta_{ij}\delta_{kl} &&+ b_2\delta_{ik}\delta_{jl} &&+ b_3\delta_{il}\delta_{jk}, \\
G_{ijkl} &= g_1\delta_{ij}\delta_{kl} &&+ g_2\delta_{ik}\delta_{jl} &&+ g_3\delta_{il}\delta_{jk},
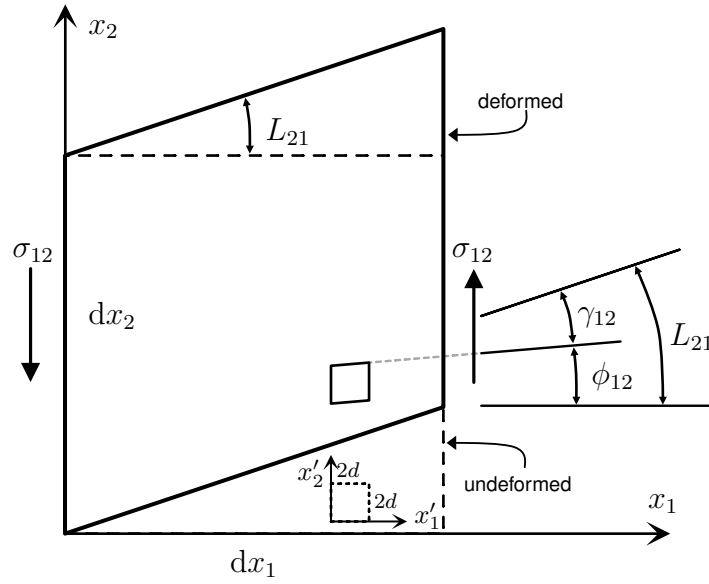\end{aligned}
$$

Figure 2.11: Components of relative stress σ_{ij}, macro-displacement gradient L_{ij}, micro deformation ϕ_{ij}, and relative deformation γ_{ij} (adapted from [42])

$$A_{ijklmn} = a_1\delta_{ij}\delta_{kl}\delta_{mn} + a_2\delta_{ij}\delta_{km}\delta_{nl} + a_3\delta_{jk}\delta_{in}\delta_{lm} + a_4\delta_{ij}\delta_{il}\delta_{mn} + a_5\delta_{jk}\delta_{im}\delta_{nl}$$
$$+ a_6\delta_{jk}\delta_{in}\delta_{lm} + a_7\delta_{ki}\delta_{jl}\delta_{mn} + a_8\delta_{ki}\delta_{jm}\delta_{nl} + a_9\delta_{ki}\delta_{jn}\delta_{lm} + a_{10}\delta_{il}\delta_{jm}\delta_{kn}$$
$$+ a_{11}\delta_{jl}\delta_{km}\delta_{in} + a_{12}\delta_{kl}\delta_{im}\delta_{jn} + a_{13}\delta_{il}\delta_{jn}\delta_{km} + a_{14}\delta_{jl}\delta_{kn}\delta_{im} + a_{15}\delta_{kl}\delta_{in}\delta_{jm}, \quad (2.51)$$

where, because of the symmetries described in Eq. (2.47), we should consider the following requirements:

$$c_2 = c_3,$$
$$g_2 = g_3, \quad (2.52)$$
$$a_1 = a_6, \quad a_2 = a_9, \quad a_5 = a_7, \quad a_{11} = a_{12}.$$

Using these relations, and replacing $c_1 = \lambda$, and $c_2 = c_3 = \mu$ where λ and μ are the so-called Lamé constants (cf. Eq. (2.29)) and are well-known with the measurement details [156], yields

$$\psi_{\mathrm{grad}} = \frac{1}{2}\lambda E_{ii}E_{jj} + \mu E_{ij}E_{ij} + \frac{1}{2}b_1\gamma_{ii}\gamma_{jj} + b_2\gamma_{ij}\gamma_{ij} + b_3\gamma_{ij}\gamma_{ji} + g_1\lambda_{ii}E_{jj}$$
$$+ g_2\left(\gamma_{ij} + \gamma_{ji}\right)E_{ij} + a_1\chi_{iik}\chi_{kjj} + a_2\chi_{iik}\chi_{jkj} + \frac{1}{2}a_3\chi_{iik}\chi_{jjk} + \frac{1}{2}a_4\chi_{ijj}\chi_{ikk}$$
$$+ a_5\chi_{ijj}\chi_{kik} + \frac{1}{2}a_8\chi_{iji}\chi_{kjk} + \frac{1}{2}a_{10}\chi_{ijk}\chi_{ijk} + a_{11}\chi_{ijk}\chi_{jki} + \frac{1}{2}a_{13}\chi_{ijk}\chi_{ikj}$$
$$+ \frac{1}{2}a_{14}\chi_{ijk}\chi_{jik} + \frac{1}{2}a_{15}\chi_{ijk}\chi_{kji}, \quad (2.53)$$

which results in 18 independent material coefficients. However, compared to the only two coefficients (e.g., the Lamé constants) needed for the classical theory, this number is still too large. In an attempt to reduce the number of required material properties, Mindlin himself has
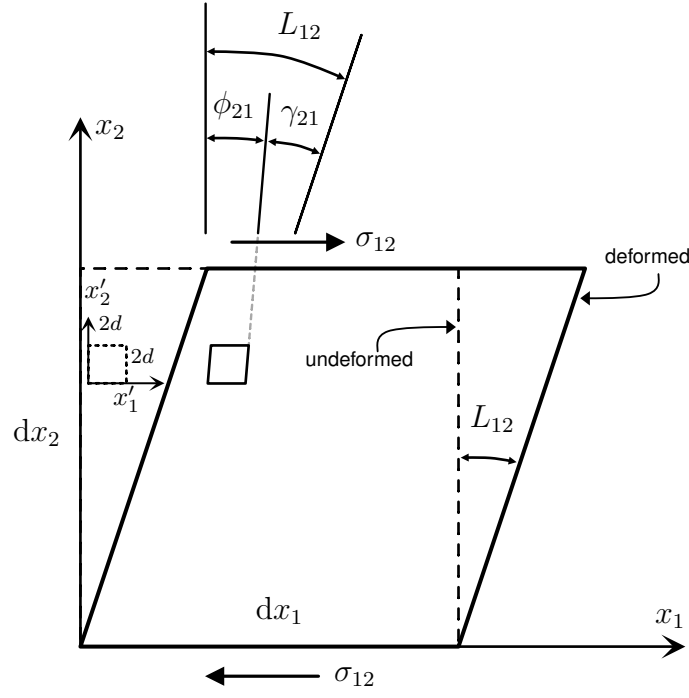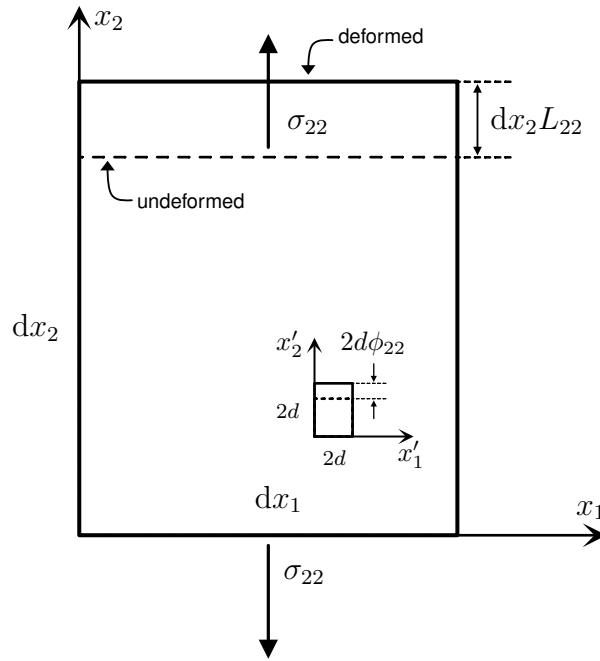
Figure 2.12: Components of relative stress σ_{ij}, macro-displacement gradient L_{ij}, micro deformation ϕ_{ij} (adapted from [42])

suggested some simplifications to relate the macroscopic deformations and their microscopic counterparts. These simplifications can be categorized into three separate forms:

- Form I: also known as Distortion Gradient Elasticity (DGE), where the microscopic deformation gradient is defined using the second gradient of the macroscopic displacement (the first gradient of the distortion tensor),
- Form II: also known as Strain Gradient Elasticity (SGE), where the microscopic deformation gradient is defined as the first gradient of the macroscopic strain, and,
- Form III: where the microscopic effect is split into gradients of the macroscopic rotation and displacement.

In the literature, Forms I and II are frequently referred to as strain gradient elasticity [45]. It is crucial to note that all three forms lead to the same boundary-value problem in terms of the (macroscopic) displacement field, but the notion of the so-called hyper-stresses, i.e., double-stresses for the first-strain gradient models, is different among them [42, 43, 157]. In the following sections, we first go through the general formulation of Mindlin's theory for a linear elastic isotropic material, and then we will focus on two more simplified models derived from this formulation, i.e., the model introduced in Reiher et al. [25] (Form I) and the model from Aifantis and his co-workers (GRADELA) [66].

2.2.2 Distortion Gradient Elasticity (Form I)

Assuming only small deformations, cf. Eq. (2.39), we can define the third-order microscopic deformation gradient tensor as

$$G_{ijk} := u_{k,ji}, \tag{2.54}$$

which is symmetric with respect to its first two indices. Assuming centrosymmetry, a quadratic form for the stored elastic energy of a homogeneous linear isotropic material can be defined as

$$\Psi_{\text{grad}}^{\text{DGE}} := \int_{\Omega} \psi_{\text{grad}}^{\text{DGE}} \mathrm{d}V = \int_{\Omega} \left(\frac{1}{2} E_{ij} C_{ijkl} E_{kl} + \frac{1}{2} G_{ijk} D_{ijklmn} G_{lmn} \right) \mathrm{d}V, \tag{2.55}$$

where $\psi_{\text{grad}}^{\text{DGE}}$ is the strain energy density, and C_{ijkl} and D_{ijklmn} are the fourth-order and the sixth-order material tensors, respectively.
Under the previously mentioned assumptions, the stored energy density can be simplified to

$$\begin{aligned}
\psi_{\text{grad}}^{\text{DGE}} := \frac{1}{2}\lambda E_{ii} E_{jj} + \mu E_{ij} E_{ij} \\
+ a_1 G_{iik} G_{kjj} + a_2 G_{ijj} G_{ikk} + a_3 G_{iik} G_{jjk} + a_4 G_{ijk} G_{ijk} + a_5 G_{ijk} G_{kji}.
\end{aligned} \tag{2.56}$$

Accordingly, the energy formulation consists of seven independent material coefficients.

$$\lambda = \frac{\nu E}{(1 - 2\nu)(1 + \nu)}, \quad \mu = \frac{E}{2(1 + \nu)}, \tag{2.57}$$

and a_1 to a_5 are the gradient material parameters. In Eq. (2.57), E and ν are the Young's modulus and Poisson's ratio, respectively. Next, we can define the stresses and double-stresses

$$S_{ij} := \frac{\partial \psi_{\text{grad}}^{\text{DGE}}}{\partial E_{ij}} = \lambda E_{pp} \delta_{ij} + 2\mu E_{ij} \tag{2.58}$$

and,

$$\begin{aligned}
P_{ijk}^{\text{DGE}} := \frac{\partial \psi_{\text{grad}}^{\text{DGE}}}{\partial G_{ijk}} = \frac{1}{2} a_1 \left(\delta_{jk} G_{ppi} + 2\delta_{ij} G_{kpp} + \delta_{ik} \delta_{ppj} \right) \\
+ a_2 \left(\delta_{jk} G_{ipp} + \delta_{ik} G_{jpp} \right) \\
+ 2a_3 \delta_{ij} G_{ppk} + 2a_4 G_{ijk} + a_5 \left(G_{kji} + G_{kij} \right),
\end{aligned} \tag{2.59}$$

where δ_{ij} denotes the Kronecker delta. This completes the derivation of the required fields for Form I formulation.

2.2.3 Strain Gradient Elasticity (Form II)

For Form II where the higher-order terms depend on the gradient of the strain tensor, we define

$$H_{ijk} := E_{jk,i} = \frac{u_{k,ji} + u_{j,ki}}{2}, \tag{2.60}$$

where the microscopic deformation gradient H_{ijk} is a third-order tensor and is symmetric with respect to its last two indices. The variable H_{ijk} denotes a deformation determined by a strain E_{jk} varying linearly in the direction of x_i. In this case, the quadratic stored elastic energy becomes

$$\Psi_{\text{grad}}^{\text{SGE}} := \int_{\Omega} \psi_{\text{grad}}^{\text{SGE}} \mathrm{d}V = \int_{\Omega} \left(\frac{1}{2} E_{ij} C_{ijkl} E_{kl} + \frac{1}{2} H_{ijk} D_{ijklmn} H_{lmn} \right) \mathrm{d}V. \tag{2.61}$$

The strain energy density $\psi_{\text{grad}}^{\text{SGE}}$ can be simplified to

$$
\begin{aligned}
\psi_{\text{grad}}^{\text{SGE}} := & \frac{1}{2}\lambda E_{ii}E_{jj} + \mu E_{ij}E_{ij} \\
& + b_1 H_{iik}H_{kjj} + b_2 H_{ijj}H_{ikk} + b_3 H_{iik}H_{jjk} + b_4 H_{ijk}H_{ijk} + b_5 H_{ijk}H_{kji}.
\end{aligned}
\tag{2.62}
$$

with b_1 to b_5 being the gradient material parameters. Accordingly, the double-stresses will be defined as

$$
\begin{aligned}
P_{ijk}^{\text{SGE}} := \frac{\partial \psi_{\text{grad}}^{\text{SGE}}}{\partial H_{ijk}} = & \frac{1}{2}b_1 \left(\delta_{ij}H_{kpp} + 2\delta_{jk}H_{ppi} + \delta_{ki}H_{jpp}\right) \\
& + 2b_2\delta_{jk}H_{ipp} + b_3 \left(\delta_{ij}H_{ppk} + \delta_{ik}H_{ppj}\right) \\
& + 2b_4 H_{ijk} + b_5 \left(H_{kij} + H_{jki}\right),
\end{aligned}
\tag{2.63}
$$

while the stresses remain the same as in Eq. (2.58). At this point, it is worth noting that there is a relation between the gradient material parameters of Form I and Form II; namely,

$$
\begin{aligned}
b_1 &= 2a_1 - 4a_3, \\
b_2 &= -a_1 + a_2 + a_3, \\
b_3 &= 4a_3, \\
b_4 &= 3a_4 - a_5, \\
b_5 &= -2a_4 + 2a_5.
\end{aligned}
\tag{2.64}
$$

Moreover, obviously, the hyper-stresses (double-stresses) of DGE and SGE are not the same, i.e., $\mathbf{P}^{\text{DGE}} \neq \mathbf{P}^{\text{SGE}}$. In the next two sections, we briefly go through the differences between these two (hyper-stress) notions.

2.2.4 Hyper-Stresses in Distortion Gradient Elasticity

In DGE, we use the distortion h_{jk} and its gradient G_{ijk} for the higher-order terms of the stored elastic energy. The variable G_{ijk} denotes a deformation determined by the distortion h_{jk} varying linearly in the direction of x_i. In the same way, the double-stress P_{ijk}^{DGE}, the work-conjugate of G_{ijk}, corresponds to a double-force in direction of x_k acting on a plane with a normal in the x_j direction, having a lever arm of direction x_i. Figure 2.13 shows an example, where a first distortion gradient $G_{211} = G_{121} = k$ of magnitude k (a constant value) is applied on a unit cube. Considering G_{211}, we have a dilatation $L_{11} = kx_2$. In the same way, considering G_{121}, one obtains the distortion $L_{21} = kx_1$. Combining the two, the displacements can be determined as $u_1 = kx_1x_2$, and $u_2 = u_3 = 0$. In this figure, the double-forces are shown using arrows starting from the surface on which the force is applied. A transversal stroke is used to show the lever arm, which is determined from the first index of the corresponding double-stress.

To help getting a better comprehension of the three-dimensional case, Fig. 2.14 shows the same unit cube, this time for an applied distortion of $G_{213} = G_{123} = k$. Following the previous procedure, we will get to a distortion of $L_{13} = kx_2$ for G_{213} and a distortion of $L_{23} = kx_1$ for G_{123}. Therefore, one can determine the displacements $u_1 = u_2 = 0$ and $u_3 = kx_1x_2$.

Figure 2.13: A cubic volume element of unit edges under constant distortion gradient $G_{121} = G_{211} = k$ and related work-conjugate double stresses $P_{121} = P_{211}$. The superscript "DGE" is omitted for brevity (adapted from [45]).

Figure 2.14: A cubic volume element of unit edges under constant distortion gradient $G_{213} = G_{123} = k$ and related work-conjugate double stresses $P_{213} = P_{123}$. The superscript "DGE" is omitted for brevity (adapted from [45]).

2.2.5 Hyper-Stresses in Strain Gradient Elasticity

In SGE, we use the strain E_{jk} and its gradient H_{ijk} for the gradient terms of the stored elastic energy. The variable H_{ijk} denotes a deformation determined by a strain E_{jk} varying linearly

in the direction of x_i. In the same way, the double-stress P_{ijk}^{SGE}, the work-conjugate of H_{ijk} corresponds to a double-force in direction of x_k acting on a plane with a normal in the x_j direction, having a lever arm of direction x_i. Figure 2.15 shows an example, where a first distortion gradient $H_{121} = H_{112} = k$ of magnitude k (a constant value) is applied on a unit cube. Here, the displacements can be determined as $u_1 = kx_1x_2$, $u_2 = \frac{1}{2}k\left(x_1\right)^2$ and $u_3 = 0$, leading to $E_{11} = kx_2$, $E_{12} = kx_1$, $E_{22} = E_{33} = 0$, and $E_{13} = E_{23} = 0$.

To illustrate the three-dimensional case, Fig. 2.16 shows the same unit cube, this time for an applied strain gradient of $H_{132} = H_{123} = k$. Following the previous procedure, one obtains a displacement field of $u_1 = 0$, $u_2 = kx_1x_3$, and $u_3 = kx_1x_2$.

2.3 Simplified Models

Although Mindlin's theory is compellingly describing the behavior of a first-strain gradient material using seven independent material coefficients, one has to point out that finding these material properties is in no way a trivial task [2, 158–160]. Therefore, many researchers have tried to simplify the model even further to reduce the number of material coefficients required, among which we consider the models proposed by Reiher et al. [25] and Aifantis et al. [61, 66]. The former is based on Form I of Mindlin's theorem, while the latter can be considered a Form II type.

2.3.1 Reiher's Model

The elastic energy is defined as a function of the first- (∇) and the second- ($\nabla(\nabla)$) gradients of the displacement field as in Sec. 2.2.2 (Form I). The second-gradient strain energy in [25]
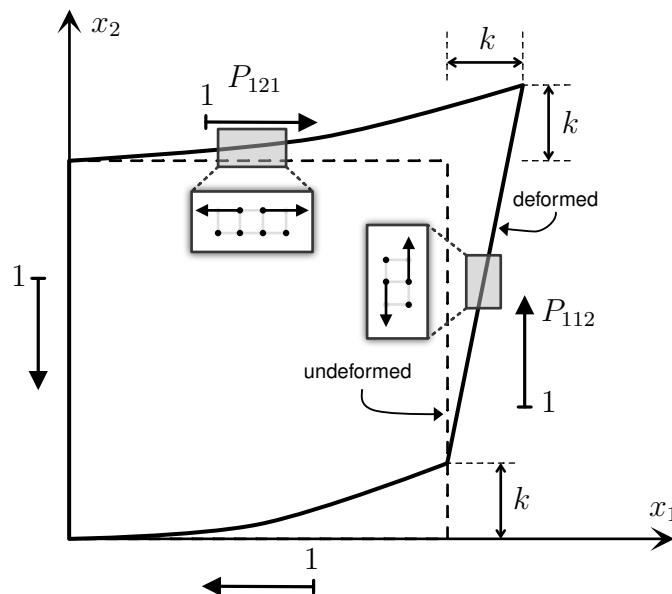
Figure 2.15: A cubic volume element of unit edges under constant strain gradient $H_{121} = H_{112} = k$ and related work-conjugate double stresses $P_{121} = P_{112}$. The superscript "SGE" is omitted for brevity (adapted from [45]).
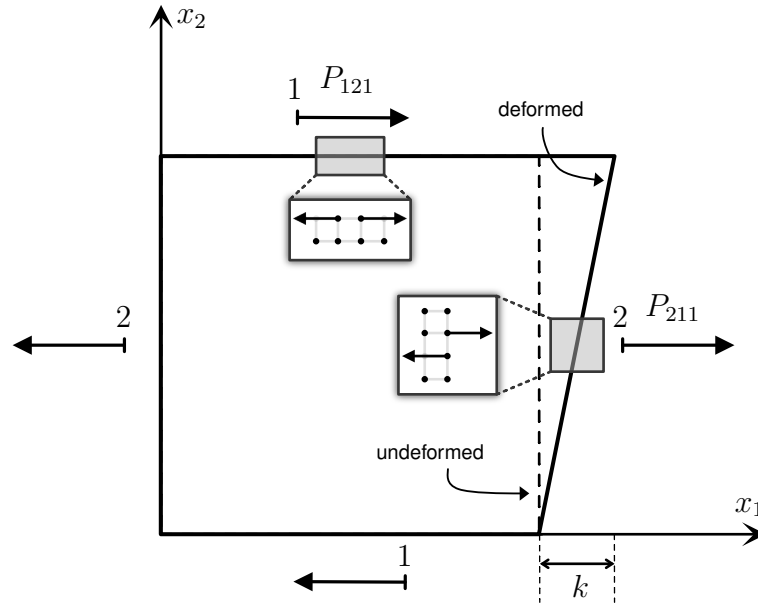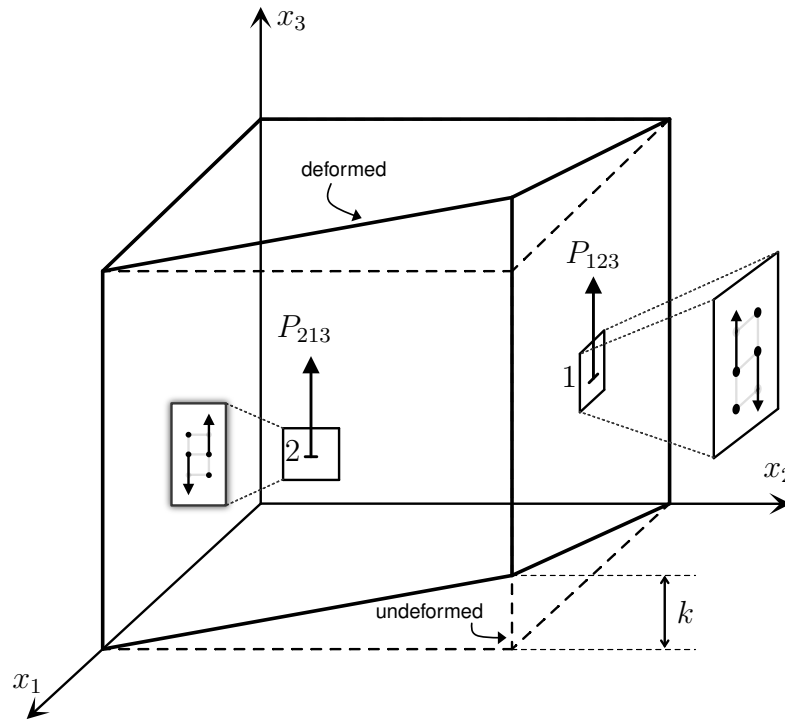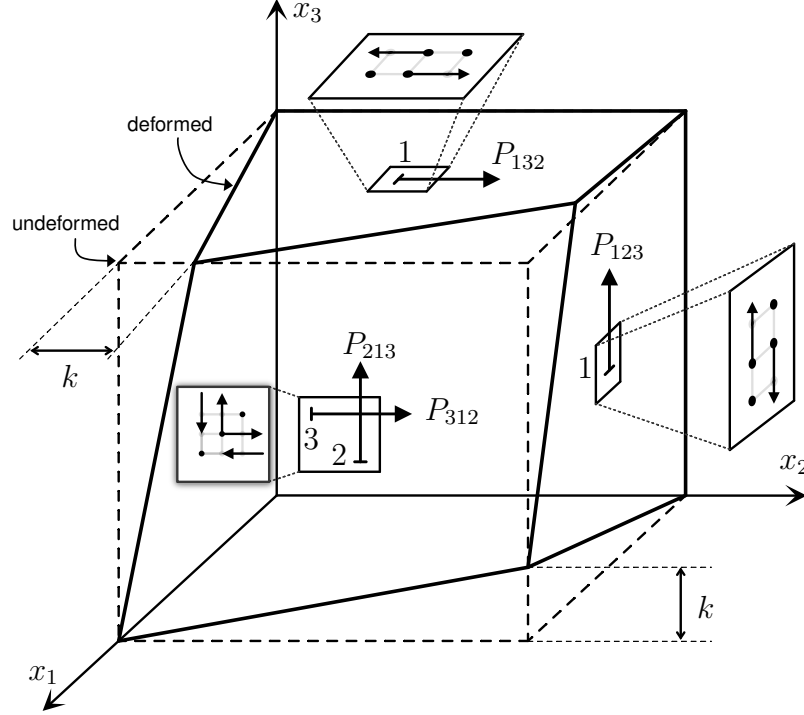
Figure 2.16: A cubic volume element of unit edges under constant strain gradient $H_{132} = H_{123} = k$ and related work-conjugate double stresses $P_{132} = P_{123}$. The superscript "SGE" is omitted for brevity (adapted from [45]).

is defined by,

$$\Psi_{\mathrm{grad}} := \int_{\Omega} \psi_{\mathrm{grad}} \mathrm{d}V = \int_{\Omega} \left(\frac{1}{2} \left(2\mu' \mathbf{E} : \mathbf{E} + \lambda' \operatorname{tr}\left(\mathbf{E}\right)^2 \right) + \frac{1}{2} \left(\lambda_1 \nabla(\nabla \mathbf{u}) \therefore \nabla(\nabla \mathbf{u}) \right) \right) \mathrm{d}V, \quad (2.65)$$

where λ_1 is called the second-gradient stiffness parameter. In Eq. (2.65), $:$ and $\therefore$ represent the scalar product of second-order ($\mathbf{A} : \mathbf{B} := A_{ij} B_{ij}$) and third-order tensors ($\mathbf{A} \therefore \mathbf{B} := A_{ijk} B_{ijk}$), respectively. A reference length-scale l_{ref} and a reference Lamé constant λ_{ref} are introduced to make the energies independent of the problem dimensions,

$$\lambda' = \frac{\lambda}{\lambda_{\mathrm{ref}}}, \quad \mu' = \frac{\mu}{\lambda_{\mathrm{ref}}}, \quad \lambda_1 = \frac{\lambda_{1_{\mathrm{real}}}}{\lambda_{\mathrm{ref}} \, l_{\mathrm{ref}}^2}. \quad (2.66)$$

In the current work, to avoid unnecessary confusion and to keep consistency with the rest of the thesis, we will not use these dimensionless material coefficients, i.e., in what follows, we will use the real Lamé constants and the real second-gradient stiffness parameter.
Taking $\delta \mathbf{E} = \operatorname{sym}\left(\nabla \delta \mathbf{u}\right)$, the first variation of the elastic energy becomes,

$$\delta \Psi_{\mathrm{grad}} = \int_{\Omega} \left(\mathbf{S} : \delta \mathbf{E} + \mathbf{P} \therefore \nabla\left(\nabla \mathbf{u}\right) \right) \mathrm{d}V. \quad (2.67)$$

Deriving the weak form by applying the principle of virtual work yields,

$$\delta\Psi_{\text{grad}}^{\text{int}} = \delta\Psi_{\text{grad}}^{\text{ext}}$$

$$\int_{\Omega} \left((2\mu\mathbf{E}:\delta\mathbf{E} + \lambda\operatorname{tr}(\mathbf{E})\operatorname{tr}(\delta\mathbf{E})) + \lambda_{1_{\text{real}}}\nabla(\nabla\mathbf{u}) \because \nabla(\nabla\delta\mathbf{u}) \right) \mathrm{d}V =$$

$$\int_{\Omega} \mathbf{b}\cdot\delta\mathbf{u}\,\mathrm{d}V + \int_{\Gamma_1} \bar{\mathbf{t}}^1\cdot\delta\mathbf{u}\,\mathrm{d}A + \int_{\Gamma_1} \bar{\mathbf{t}}^2\cdot\delta\nabla_{\mathbf{n}}\mathbf{u}\,\mathrm{d}A, + \int_{\Sigma} \bar{\mathbf{t}}^3\cdot\delta\mathbf{u}\,\mathrm{d}L,$$
(2.68)

where $\mathbf{b}$ is the vector of body forces, and $\bar{\mathbf{t}}^1$, $\bar{\mathbf{t}}^2$, and $\bar{\mathbf{t}}^3$ are the prescribed surface tractions, surface double-tractions and edge tractions, respectively. Moreover, the intersections of the surface boundary Γ_1 segments define a network of boundary curves (edges) e, the union of which describes the boundary Σ. We will discuss these boundary terms in more detail in the next section.

2.3.2 Aifantis' Model

This model is mostly referred to as GRADELA in the literature. Assuming a linear elastic isotropic material and taking into account the assumption that the stress-strain symmetry of the elastic energy should also be valid for the gradient terms (see [49, 61, 62, 69]), the Helmholtz free energy provided in Mindlin's theory reduces to

$$\Psi_{\text{grad}}(\mathbf{E},\mathbf{H}) := \int_{\Omega} \psi_{\text{grad}}\mathrm{d}V$$

$$= \int_{\Omega} \left(\frac{1}{2}\lambda(\operatorname{tr}\mathbf{E})^2 + \mu\mathbf{E}:\mathbf{E} + l^2\left(\frac{1}{2}\lambda(\operatorname{tr}\mathbf{H}\cdot\operatorname{tr}\mathbf{H}) + \mu\mathbf{H}\because\mathbf{H}\right) \right)\mathrm{d}V,$$
(2.69)

which is a function of the first and the second gradients of the displacement. In Eq. (2.69), l denotes the length-scale parameter for the gradient elasticity theory, and the first two terms of the right-hand side are equal to the classical strain energy density, ψ_{e}. Moreover, the trace of $\mathbf{H}$ is a vector and is defined by

$$\operatorname{tr}\mathbf{H} := \nabla\left[\operatorname{tr}\mathbf{E}\right].$$
(2.70)

It should be noted that setting $l = 0$ recovers the classical Cauchy continuum model. We define the stress, $\mathbf{S}$ and the double-stress, $\mathbf{P}$ as

$$\mathbf{S} := \frac{\partial\psi_{\text{grad}}}{\partial\mathbf{E}} = \lambda\left(\operatorname{tr}\mathbf{E}\right)\mathbf{I} + 2\mu\mathbf{E},$$
(2.71)

and

$$\mathbf{P} := \frac{\partial\psi_{\text{grad}}}{\partial\mathbf{H}} = l^2\nabla\left(\lambda\left(\operatorname{tr}\mathbf{E}\right)\mathbf{I} + 2\mu\mathbf{E}\right),$$
(2.72)

where $\mathbf{I}$ is the second-order identity tensor. Considering $\delta\mathbf{E} := \nabla_{\text{sym}}(\delta\mathbf{u})$ and $\delta\mathbf{H} := \nabla(\delta\mathbf{E})$, and calculating the first variation of the work of the internal forces yield

$$x.$$
(2.73)

Applying the divergence theorem, the first term of the right-hand side of Eq. (2.73) is simplified to

$$\int_{\Omega} \mathbf{S} : \delta\mathbf{E}\,\mathrm{d}V = -\int_{\Omega} (\nabla\cdot\mathbf{S})\cdot\delta\mathbf{u}\,\mathrm{d}V + \int_{\Gamma_1} (\mathbf{S}\cdot\mathbf{n})\cdot\delta\mathbf{u}\,\mathrm{d}A, \tag{2.74}$$

where Ω and Γ_1 represent the whole volume and its surface, respectively, and $\mathbf{n}$ denotes the outer normal to the surface. In the same way, the second term of the right-hand side of Eq. (2.73) is transformed

$$\int_{\Omega} \mathbf{P} \mathbin{\vdots} \delta\mathbf{H}\,\mathrm{d}V = -\int_{\Omega} (\nabla\cdot\mathbf{P}) : \delta\mathbf{E}\,\mathrm{d}V + \int_{\Gamma_1} (\mathbf{P}\cdot\mathbf{n}) : \delta\mathbf{E}\,\mathrm{d}A. \tag{2.75}$$

Applying again the surface divergence theorem on both terms of the right-hand side of Eq. (2.75) results in

$$\int_{\Omega} (\nabla\cdot\mathbf{P}) : \delta\mathbf{E}\,\mathrm{d}V = -\int_{\Omega} \nabla^2\mathbf{P}\cdot\delta\mathbf{u}\,\mathrm{d}V + \int_{\Gamma_1} [(\nabla\cdot\mathbf{P})\cdot\mathbf{n}]\cdot\delta\mathbf{u}\,\mathrm{d}A, \tag{2.76}$$

$$\begin{aligned}
\int_{\Gamma_1} (\mathbf{P}\cdot\mathbf{n}) : \delta\mathbf{E}\,\mathrm{d}A = & \int_{\Gamma_1} [\mathbf{P} : [\mathbf{n}\otimes\mathbf{n}]]\cdot\delta\nabla_{\mathbf{n}}\mathbf{u}\,\mathrm{d}A \\
& + \int_{\Gamma_1} \left[\nabla_s\cdot\mathbf{n}\,\mathbf{P}_2 : [\mathbf{n}\otimes\mathbf{n}] - \nabla_s\cdot [\mathbf{P}_2\cdot\mathbf{n}]^T \right]\cdot\delta\mathbf{u}\,\mathrm{d}A \\
& + \int_{\Sigma} \sum_e [\mathbf{P}_2 : [\mathbf{m}\otimes\mathbf{n}]]\cdot\delta\mathbf{u}\,\mathrm{d}L,
\end{aligned} \tag{2.77}$$

where $\nabla_s\cdot\square := [[\nabla\square]\cdot[\mathbf{I}-\mathbf{n}\otimes\mathbf{n}]] : \mathbf{I}$ represents the surface divergence, $\mathbf{n}$ is the outward normal vector to Γ_1, and $\mathbf{m}$ is the outward normal vector to Ψ and is perpendicular to $\mathbf{n}$ (see Fig. 2.17). In the last term of the right-hand side of Eq. (2.77), the contributions of the stresses $\mathbf{P}$ on each edge e correlated to the volume are summed up. Finally, substituting Eqs. (2.76) and (2.77) into Eq. (2.75) provides the internal energy contribution of the gradient part,

$$\begin{aligned}
\int_{\Omega} \mathbf{P} \mathbin{\vdots} \delta\mathbf{H}\,\mathrm{d}V = & \int_{\Omega} \nabla^2\mathbf{P}\cdot\delta\mathbf{u}\,\mathrm{d}V \\
& + \int_{\Gamma_1} \left[-(\nabla\cdot\mathbf{P})\cdot\mathbf{n} + \nabla_s\cdot\mathbf{n}\,\mathbf{P} : [\mathbf{n}\otimes\mathbf{n}] - \nabla_s\cdot [\mathbf{P}\cdot\mathbf{n}]^T \right]\cdot\delta\mathbf{u}\,\mathrm{d}A \\
& + \int_{\Gamma_1} [\mathbf{P} : [\mathbf{n}\otimes\mathbf{n}]]\cdot\delta\nabla_{\mathbf{n}}\mathbf{u}\,\mathrm{d}A + \int_{\Sigma} \sum_e [\mathbf{P} : [\mathbf{m}\otimes\mathbf{n}]]\cdot\delta\mathbf{u}\,\mathrm{d}L.
\end{aligned} \tag{2.78}$$

For a more detailed derivation of the boundary terms, we refer to [24, 74, 161]. Considering only the classical vector of body forces $\mathbf{b}$ and neglecting the contributions of the so-called body double-forces, Eqs. (2.74) and (2.78) yield the following form for the work of the external forces

$$\delta\Psi_{\mathrm{grad}}^{\mathrm{ext}} = \int_{\Omega} \mathbf{b}\cdot\delta\mathbf{u}\,\mathrm{d}V + \int_{\Gamma_1} \bar{\mathbf{t}}^1\cdot\delta\mathbf{u}\,\mathrm{d}A + \int_{\Gamma_1} \bar{\mathbf{t}}^2\cdot\delta\nabla_{\mathbf{n}}\mathbf{u}\,\mathrm{d}A + \int_{\Sigma} \bar{\mathbf{t}}^3\cdot\delta\mathbf{u}\,\mathrm{d}L. \tag{2.79}$$
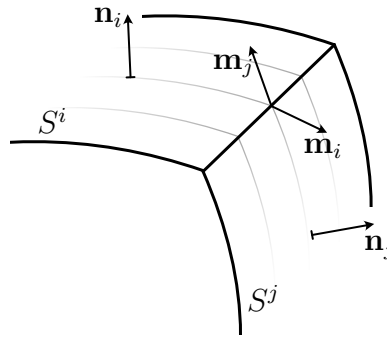
Figure 2.17: Illustration of vectors $\mathbf{n}$ and $\mathbf{m}$ for surfaces S^i and S^j (adapted from [24])

Finally, we can introduce the weak form of the governing equations via the principle of virtual work as:

$$\delta\Psi_{\text{grad}}^{\text{int}} = \delta\Psi_{\text{grad}}^{\text{ext}},$$

$$\int_\Omega \mathbf{S} : \delta\mathbf{E}\,\mathrm{d}V + \int_\Omega \mathbf{P} \mathbin{\vdots} \delta\mathbf{H}\,\mathrm{d}V =$$

$$\int_\Omega \mathbf{b} \cdot \delta\mathbf{u}\,\mathrm{d}V + \int_{\Gamma_1} \bar{\mathbf{t}}^1 \cdot \delta\mathbf{u}\,\mathrm{d}A + \int_{\Gamma_1} \bar{\mathbf{t}}^2 \cdot \delta\nabla_\mathbf{n}\,\mathbf{u}\,\mathrm{d}A + \int_\Sigma \bar{\mathbf{t}}^3 \cdot \delta\mathbf{u}\,\mathrm{d}L.$$

(2.80)

An alternative representation of the above equations in index notation is provided in [42] (see Eqs. (9.15)–(9.23) and the paragraph below, cf. Eq. (11.7)).

It ought to be remarked at this point that the existence of internal energy contributions at the edges in Eqs. (2.78) and (2.80) shows that a body must be equipped at least with second-gradient elastic energy to sustain concentrated line tractions at its edges. Note that the internal energy in the classical Cauchy theory only includes the contribution in volumes and surfaces, leading to the fact that the theory does not show any singular behavior in the presence of external volume and surface forces, but encounters problems with handling edge and point loads. In the same way, exploiting the third-gradient theory results in internal energy contribution at points and ensures that the body can sustain concentrated point tractions at its vertices (see also [24, 25]). The latter can be exploited when studying crack propagation phenomena in a three-dimensional structure. In those cases, a third displacement gradient model similar to the one introduced in [67] can be used following the same reasoning which leads to exploiting the first-strain gradient models to overcome the problem of singularity for the two-dimensional cases of fracture.

3 Phase-Field Modelling of Fracture

Tracking the crack surface (internal-discontinuity boundaries, Γ_c) is well-known to be numerically a challenging task. This, in particular, becomes difficult if one considers multiple cracks propagating in two- or three-dimensional settings, for instance. Before we start discussing phase-field models for fracture mechanics, a summary of linear elasticity fracture mechanics is given.

3.1 Linear Elasticity Fracture Mechanics

What follows is a quick review of topics related to fracture mechanics which mostly follow the book by Gross and Seelig [162]. Fracture mechanics can be classified into linear and non-linear theories. Linear (elastic) fracture mechanics is mostly used to study fracture processes in brittle materials. This is in particular because the theory is based on linear elasticity and is sufficient to study the behavior of brittle materials. On the other hand, the so-called non-linear fracture mechanics considers the fracture processes in inelastic materials. During fracture, the body separates into two or more parts, causing the formation of new surfaces. LEFM is based on the ideas of continuum mechanics, which only considers a body's macrostructure, neglecting the microstructure. From a macroscopic point of view, one can consider the crack to be a cut in a body. The surfaces created in the body because of crack propagation are called crack surfaces (or faces). The end of a crack is called the crack tip or the crack front. Figure 3.1 provides a graphical representation of these concepts.

The loading of a crack can be categorized into three different types of crack opening (see Fig. 3.2):

- Mode I: also known as the opening mode is a symmetric crack opening normal to the crack face and occurs because of a tensile type of loading. It is the most common mode and usually receives the highest attention in research and practical applications as it causes the major part of damage,

- Mode II: also known as the shearing mode, as the name suggests, occurs when a shear type of loading is applied in the in-plane direction, and the crack faces slide on each other relatively normal to the crack front. Mode II is of second place in terms of the attention from the scientific community, as the problem is still considered to be two-dimensional, and,

- Mode III: also known as the tearing mode, is the same as the shearing mode, but this time the shear loading is applied on the out-of-plane direction, and the crack faces slide on each other in a direction parallel to the crack front. Mode III of crack opening is very rare.

It is very well established that even metals that are classified as brittle material undergo some inelastic deformations close to the crack front in the so-called yielding zone. This zone causes non-singular finite stresses (and strains) around the crack tip, and the behavior of the
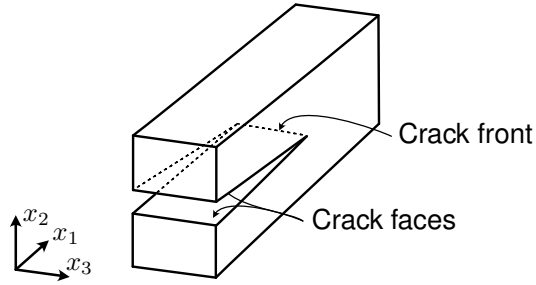
Figure 3.1: Representation of a cracked body
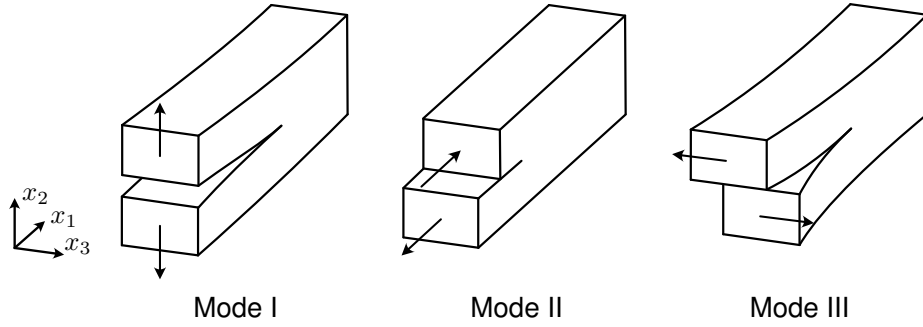
Figure 3.2: Crack opening modes

material in this region cannot be studied by classical linear elasticity. Nevertheless, assuming that the yielding zone is a small region, the theory of linear elasticity can be exploited very well in the other regions of the body. Using the method of complex variables, assuming a plane strain state and Mode I of crack opening, we end up with the analytical solution and the following expressions for the stress field [162],

$$
\begin{bmatrix} S_{11} \\ S_{22} \\ S_{12} \end{bmatrix} = \frac{K_{\mathrm{I}}}{\sqrt{2\pi r}} \cos\left(\frac{\theta}{2}\right) \begin{bmatrix} 1 - \sin\left(\frac{\theta}{2}\right)\sin\left(\frac{3\theta}{2}\right) \\ 1 + \sin\left(\frac{\theta}{2}\right)\sin\left(\frac{3\theta}{2}\right) \\ \sin\left(\frac{\theta}{2}\right)\cos\left(\frac{3\theta}{2}\right) \end{bmatrix},
\tag{3.1}
$$

where K_{I} is the stress intensity factor for Mode I crack opening. The stress intensity factor can be recognized as a measure for the strength of the crack. In Eq. (3.1), the stress field clearly posseses a singularity of order $\mathcal{O}(1/\sqrt{r})$ (in the limit of r going to zero, the stresses go to infinity; see Fig. 3.3).

In the rest of this chapter, we will exploit a numerical approach, namely the phase-field method of fracture, which can circumvent the problem of tracking the crack surfaces by defining the crack as a continuous field over the whole domain. The idea is to use a scalar-valued variable s, ranging from zero to one to distinguish between the damaged and the intact material states. This change significantly helps approximating the crack surface at the cost of introducing an extra degree of freedom to the problem. Another advantage of using the phase-field method is that, since a variational approach is used to study the cracks, investigating the crack nucleation, branching, and propagation is possible without any extra efforts.

The total potential energy of the body (also known as the Griffith functional) can be considered as

$$
\Psi = \Psi_{\mathrm{e}} + \Psi_{\mathrm{c}} = \int_{\Omega} \psi_{\mathrm{e}}\mathrm{d}V + \int_{\Gamma_{\mathrm{c}}} \mathcal{G}_{\mathrm{c}}\mathrm{d}A,
\tag{3.2}
$$
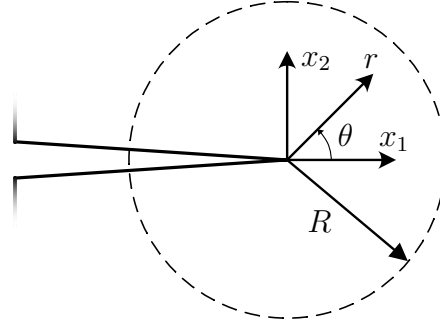
Figure 3.3: Representation of the crack tip field in 2D
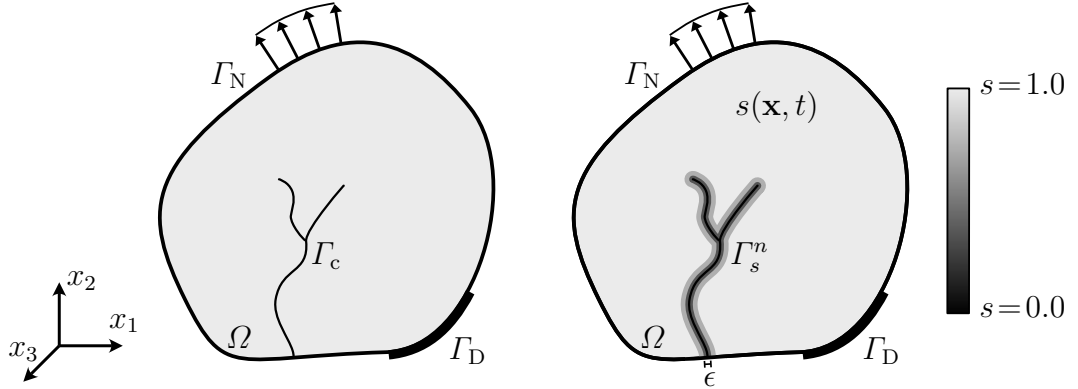
Figure 3.4: Representation of a body with a sharp (left) and a diffusive crack (right) under Dirichlet and Neumann boundary conditions

where Ψ_e and Ψ_c are the elastic energy and the fracture energy of the body, respectively. In Eq. (3.2), $\mathcal{G}_c$ corresponds to the energy required to create a unit area crack surface and is called the critical energy release rate or the crack thoughness in the literature. Moreover, the integration $\int_{\Gamma_c} \mathrm{d}A$ is equivalent to $\mathcal{H}^{d-1}(\Gamma_c)$, the $(d-1)-$Hausdorff measure (where d represents the dimensionality of the problem) giving the surface area of the crack. In the phase-field modelling of fracture, the second term of the right-hand side of Eq. (3.2) is approximated by a volume integral, namely

$$\Psi_c = \int_{\Gamma_c} \mathcal{G}_c \mathrm{d}A \approx \int_{\Omega} \mathcal{G}_c \Gamma_s^n \mathrm{d}V, \tag{3.3}$$

where Γ_s^n is an n-th order crack density functional depending on derivatives of the phase-field parameter s up to order n [163], and a crack length-scale parameter ϵ which governs the width of the crack (see Fig. 3.4). Whether to treat the length-scale ϵ as a numerical parameter or material properties is still an open debate. While it was initially considered to be merely a numerical parameter, the idea of considering it as a material parameter is gaining popularity and some studies have shown that it is possible to determine it through experiments [164–167].

In the next section, we will discuss two well-known classical phase-field fracture models with second-order and fourth-order derivatives of s.

3.2 Classical Phase-Field Fracture Models

In this section, the derivation of the governing equations of fracture using the linear elasticity fracture mechanics and the phase-field method is discussed. We separate our discussions to two main categories based on the order of the final governing equations. It should be emphasized that both the formulations in Sects. 3.2.1 and 3.2.2 are based on the classical continuum mechanics theory, i.e., no higher-order displacement derivatives are involved in the formulation. In other words, the order of the equations is based on the approximation functions used to describe the phase-field crack parameter.

3.2.1 Second-Order Phase-Field Fracture Model

Considering a one-dimensional setting and following the approach used by Miehe et al. [135], let us first assume an exponential function $s(x)$ with the properties

$$s(x = 0) = 0 \quad \text{and} \quad s(x = \pm\infty) = 1 \, (\text{or } s'(x = \pm\infty) = 0) \, . \tag{3.4}$$

One suitable candidate for such a function would be

$$s(x) = 1 - \exp\left(-\frac{|x|}{2\epsilon}\right) . \tag{3.5}$$

Figure 3.5 depicts the non-smooth function described by Eq. (3.5). Clearly, in the limit of ϵ going to zero, the classical Griffith's theory with sharp cracks is recovered. We would like our final crack profile to look like this, that is we are looking for a differential equation with such a solution field. Considering the boundary conditions introduced in Eq. (3.4), we end up with the following homogeneous differential equation

$$1 - s + 4\epsilon^2 s'' = 0, \tag{3.6}$$

where the double-prime symbol is used to show the second-derivate with respect to the only spatial direction, x. Equation (3.6) has the same solution as the minimization problem

$$\operatorname*{argmin}_{s} \left(I\left(s\right) \right), \quad I\left(s\right) = \int \Gamma_s^2 \, \mathrm{d}x, \tag{3.7}$$
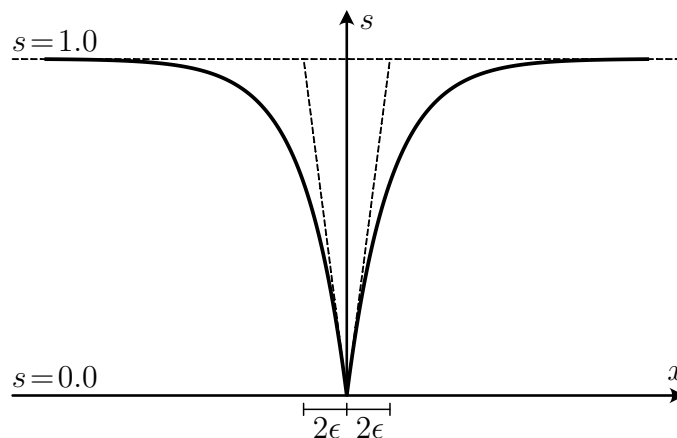
Figure 3.5: Crack profile for the second-order phase-field fracture model

where

$$\Gamma_s^2 = \frac{(1-s)^2}{4\epsilon} + \epsilon|\nabla s|^2, \tag{3.8}$$

which can be obtained by constructing the Galerkin-type weak form of the Euler equation, cf. Eq. (3.6). In the general case (multi-dimensional settings), for the second-order phase-field fracture model, we use

$$\int_\Gamma \mathcal{G}_\mathrm{c}\,\mathrm{d}A \approx \int_\Omega \mathcal{G}_\mathrm{c}\left(\frac{(1-s)^2}{4\epsilon} + \epsilon|\nabla s|^2\right)\,\mathrm{d}V. \tag{3.9}$$

The model is based on the linear elasticity theory, and neglecting the contributions of external forces, the total energy of the fracture model is represented by

$$\Psi^{(2)} = \int_\Omega \left[g(s)\,\psi_\mathrm{e} + \mathcal{G}_\mathrm{c}\left(\frac{(1-s)^2}{4\epsilon} + \epsilon|\nabla s|^2\right)\right]\,\mathrm{d}V. \tag{3.10}$$

where the superscript $\square^{(2)}$ refers to the second-order phase-field model, and ψ_e is the strain energy density of a linear elastic material in the classical Cauchy theory. In Eq. (3.10), $g(s)$ is the so-called degradation function (e.g., $g(s) = s^2$) whose role is to reduce the elastic strength of the material. We will discuss this function in the following sections.

Considering the classical stresses, Eq. (2.71), and applying the principle of virtual work, cf. Sect. 2.1.5, the weak form of the mechanical part yields

$$\int_\Omega \left(g\left(s\right)\mathbf{S}:\delta\mathbf{E}\right)\,\mathrm{d}V = \int_\Omega \mathbf{b}\cdot\delta\mathbf{u}\,\mathrm{d}V + \int_{\Gamma_1} \bar{\mathbf{t}}^1\cdot\delta\mathbf{u}\,\mathrm{d}A. \tag{3.11}$$

For the phase-field part, the evolution of s is governed by a Ginzburg-Landau type evolution equation [168, 169],

$$\dot{s} = -M\frac{\delta\Psi^{(2)}(\mathbf{E},s)}{\delta s}, \tag{3.12}$$

where $\dot{s} := \partial s/\partial t$ is the partial derivative of the phase-field with respect to time, and $M \geq 0$ is a kinetic coefficient and is called the mobility constant [170]. It is worth to note here that the kinetic coefficient can be defined as a function as well, but it is considered to be constant in the standard Ginzburg-Landau formulation [169]. The limit of M going to infinity leads to the quasi-static case. Therefore, it can be assumed that finite values of M resemble a viscous approximation of the quasi-static case.

In Eq. (3.12), $\delta\Psi/\delta s$ represents a functional derivative. Given a functional

$$F[p(r)] = \int f\left(r, p(r), \nabla p(r), \nabla^{(2)}p(r)\right)\,\mathrm{d}r, \tag{3.13}$$

the functional derivative would be

$$\frac{\delta F[p]}{\delta p} = \frac{\partial f}{\partial p} - \nabla\cdot\frac{\partial f}{\partial(\nabla p)} + \nabla^{(2)}\cdot\frac{\partial f}{\partial\left(\nabla^{(2)}p\right)}. \tag{3.14}$$

Inserting Eq. (3.14) into Eq. (3.12) yields

$$\dot{s} = -M \left(g'(s)\psi_\mathrm{e} - 2\mathcal{G}_\mathrm{c}\epsilon\Delta s + \frac{\mathcal{G}_\mathrm{c}(s-1)}{2\epsilon} \right),$$ (3.15)

which is the strong form of the phase-field. Multiplying Eq. (3.15) with a weighting function and applying integration by parts results in the weak form of the phase-field

$$\int_\Omega \left[\frac{\dot{s}}{M}\delta s + 2\,\mathcal{G}_\mathrm{c}\epsilon\,\nabla s\,\delta\nabla s + \left(g'(s)\psi_\mathrm{e} + \frac{\mathcal{G}_\mathrm{c}(s-1)}{2\epsilon} \right)\delta s \right] \mathrm{d}V = \int_{\Gamma_2} q_\mathrm{n}\,\delta s\,\mathrm{d}A,$$ (3.16)

where q_n is the normal flux acting on Γ_2 and is usually assumed to be zero [171].

3.2.2 Fourth-Order Phase-Field Fracture Model

Equation (3.15) is a second-order phase-field model for crack propagation. Borden et al. [172] introduced a fourth-order model, including the Laplacian of the order parameter (Δs), which is supposed to improve the accuracy of the obtained results in the case of anisotropic materials [173, 174], and also relaxes the mesh size requirements of the second-order theory [174]. In what follows, we derive the weak form for this model.

Let us introduce an exponential function $s(x)$ with the properties

$$s(x = 0) = 0,\ s'(x = 0) = 0,\ \text{and}\quad s(x = \pm\infty) = 1,$$ (3.17)

which has an extra constraint on the gradient of s at $x = 0$ compared to the second-order case. One suitable candidate for such a function would be [172]

$$s(x) = 1 - \left(1 + \frac{|x|}{\epsilon} \right) \exp\left(-\frac{|x|}{\epsilon} \right).$$ (3.18)

Figure 3.6 depicts the smooth function described in Eq. (3.18). We would like to find a differential equation with such a solution field. Considering the boundary conditions introduced in Eq. (3.17), we end up with the following homogeneous differential equation

$$1 - s + 2\epsilon^2 s'' + \epsilon^4 s'''' = 0.$$ (3.19)
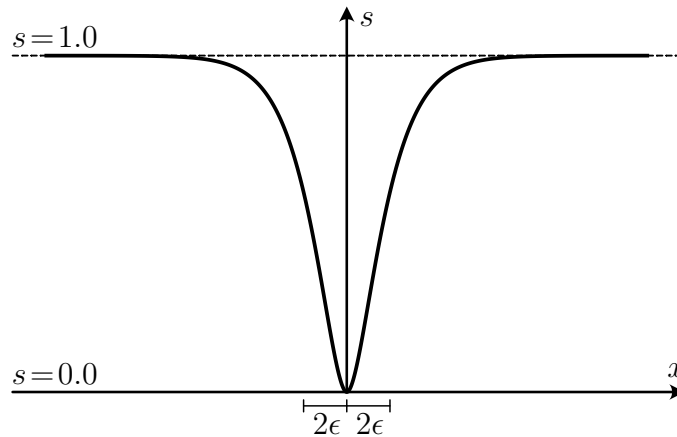
Figure 3.6: Crack profile for the fourth-order phase-field fracture model

Equation (3.6) has the same solution as the minimization problem

$$\underset{s}{\mathrm{argmin}}\left(I\left(s\right)\right), \quad I\left(s\right) = \int \Gamma_s^4 \, \mathrm{d}x, \tag{3.20}$$

where

$$\Gamma_s^4 = \frac{(1-s)^2}{4\epsilon} + \frac{1}{2}\epsilon|\nabla s|^2 + \frac{1}{4}\epsilon^3\left(\Delta s\right)^2, \tag{3.21}$$

which can be obtained by constructing the Galerkin-type weak form of the Euler equation, cf. Eq. (3.19).
In the general case, for the fourth-order phase-field fracture model, we use

$$\int_\Gamma \mathcal{G}_\mathrm{c}\,\mathrm{A} \approx \int_\Omega \mathcal{G}_\mathrm{c}\left(\frac{(1-s)^2}{4\epsilon} + \frac{1}{2}\epsilon|\nabla s|^2 + \frac{1}{4}\epsilon^3\left(\Delta s\right)^2\right)\mathrm{d}V. \tag{3.22}$$

The model introduced in [172] is also based on the classical theory of linear elasticity. The total fracture energy for the fourth-order formulation is therefore

$$\Psi^{(4)} = \int_\Omega \left[g(s)\,\psi_\mathrm{e} + \mathcal{G}_\mathrm{c}\left(\frac{(1-s)^2}{4\epsilon} + \frac{1}{2}\epsilon|\nabla s|^2 + \frac{1}{4}\epsilon^3\left(\Delta s\right)^2\right)\right]\mathrm{d}V, \tag{3.23}$$

where the superscript $\square^{(4)}$ refers to the fourth-order phase-field model. Following the same procedure as in Sect. 3.2.1 leads to the weak-form of the fourth order model,

$$\int_\Omega \left[\frac{\dot{s}}{M}\delta s + \mathcal{G}_\mathrm{c}\left(\epsilon\,\nabla s\,\delta\nabla s + \frac{\epsilon^3}{2}\Delta s\,\delta\Delta s\right) + \left(g'(s)\psi_\mathrm{e} + \frac{\mathcal{G}_\mathrm{c}(s-1)}{2\epsilon}\right)\delta s\right]\mathrm{d}V$$
$$= \int_{\Gamma_2} q_\mathrm{n}\,\delta s\,\mathrm{d}A. \tag{3.24}$$

Applications of the fourth-order model can be found in [175, 176]. The phase-field fracture models introduced in Sects. 3.2.1 and 3.2.2 are usually referred in the literature as the standard models; however, they are not the only phase-field formulations to study the crack. In the following sections we will briefly discuss the points of departure and differences between the available models.

3.2.3 Geometric Crack Function

In the introduced formulations we always use a quadratic potential or geometric crack function

$$w(s) = (1-s)^2, \tag{3.25}$$

which determines the distribution of the crack field. In some sources, it is referred to as the local dissipated energy density function [177]. In general, the geometric crack function $w(s)$ should fulfill the conditions [167]

$$w(0) = 0, \quad \text{and} \quad w(1) = k, \tag{3.26}$$

for monotonic functions, with k being a finite positive value. Clearly, Eq. (3.25) is not the only possible choice and alternatives are proposed in the literature, such as the profile introduced in Pham et al. [178] where gradient damage models are incorporated. Two broadly used functions with these properties are

$$w(s) = (1 - s),\tag{3.27}$$

and Eq. (3.25) which we will refer to as linear [177, 179] and quadratic [134, 135, 140, 170] geometric crack functions, respectively. The equivalent to Eq. (3.8) for the linear function is

$$\Gamma_s^2 = \frac{3}{8\epsilon}\left(1 - s + \epsilon^2|\nabla s|^2\right).\tag{3.28}$$

Although double-well potentials such as [180, 181]

$$w(s) = 16s^2\left(1 - s\right)^2,\tag{3.29}$$

are very popular in the community of phase-field modelling, for phase-field modelling of fracture, usually monotonic functions are preferred. The problem with using double-well potentials is two-fold: first, there is no mathematical proof that the surface energy approximated by these functions converges to the one from the variational formulation; second, since the peak of the function is at $s = 0.5$ the phase-field tends to evolve away from the actual crack $s = 0$ [134, 167, 182]. All three functions are demonstrated in Fig. 3.7. For the second-order phase-field formulation, the resulting crack profile for the linear case is given by

$$s(x) = \begin{cases} 1 - \left(\dfrac{|x|}{2\epsilon} - 1\right)^2 & \text{if } -2\epsilon \leq x \leq 2\epsilon, \\ 0 & \text{otherwise,} \end{cases}\tag{3.30}$$

while for the quadratic case the profile is given by Eq. (3.5). Figure 3.8 compares the crack
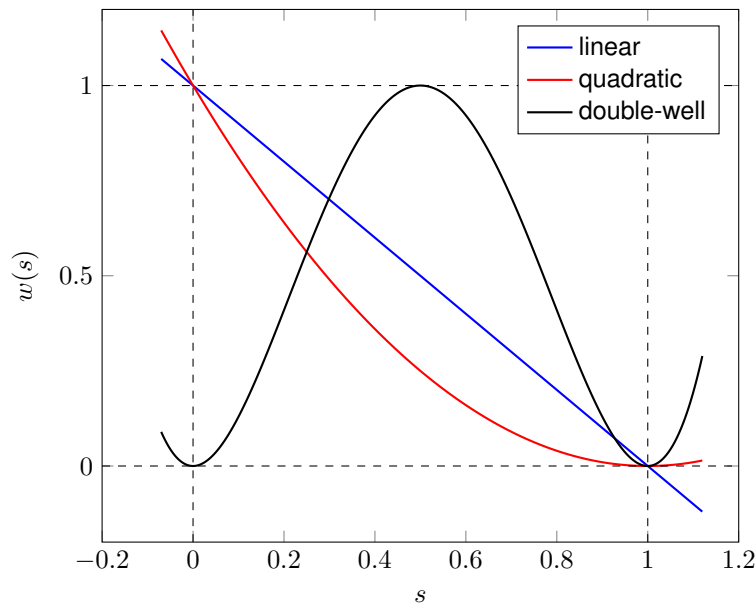
Figure 3.7: Graphical representation of different types of geometric crack functions
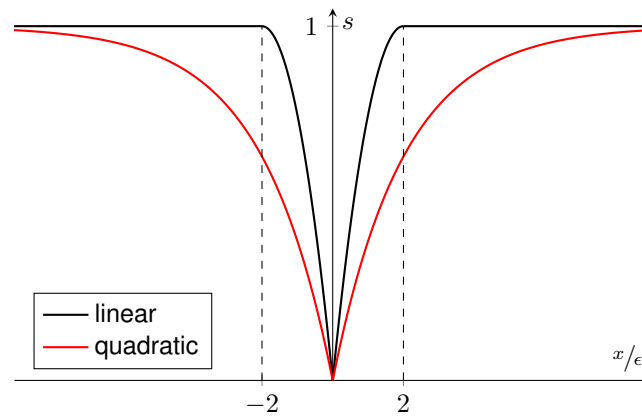
Figure 3.8: Graphical representation of the phase-field profile for different types of geometric crack functions for a normalized domain

profile of the given functions for a normalized domain. As it is shown in this figure, the quadratic geometric crack function results in a localization band with an infinite support causing the phase-field variable and consequently the degradation function to start evolving as soon as a load is applied to the structure. This is in contrast with the expected behavior of brittle materials where the response is assumed to be linear elastic until a crack is initiated. On the other hand, the linear approximation has a finite support of 4ϵ providing the basis for a purely elastic behavior appearance of damage [88, 167, 177].

That being said, the quadratic function still has benefits over its linear counterpart; namely, using the quadratic function, the boundedness of the phase-field crack parameter is automatically guaranteed; that is, the phase-field parameter always remains between zero and one during the simulation. It can also be seen in Fig. 3.7 that the quadratic function has a local minimum at $s = 1$, i.e., the undamaged state, meaning that in the absence of mechanical loadings, $s = 1$ is a minimizer of the total energy. The linear function, on the other hand, needs extra treatment, and additional constraints must be added to the problem using the penalty method or the Lagrange multipliers method to ensure the boundedness of the phase-field parameter, which results in an increase in the computational costs. The final system of equations with these extra constraints needs to be solved using staggered iterative schemes [183] (see Sect. 3.2.6.2 for more information on staggered solvers). Using the quadratic function, in the case of a staggered solution, the phase-field part of the problem is linear (compared to a non-linear system for the linear function due to the additional constraints), which gives this formulation an extra advantage. Apart from these, using the linear approximation, a different kind of degradation function is needed, which adds an upper bound to the value of the crack length-scale parameter ϵ [177]. This will be discussed in the next section. We, therefore, decide to stick with the quadratic function in our formulations. It should be noted here that using the double-well function has the advantage of having a local minimum as well; however, as mentioned earlier, these functions do not coincide very well with Griffith's theory.

3.2.4 Energy Degradation Function

The form of the equation for the total potential energy of the body, cf. Eq. (3.2), implies that to maintain the total energy of the system conserved, any changes in the fracture energy must be compensated by the elastic energy. In other words, if the fracture energy increases due to an increase in the crack surface resulting from crack propagation, we should

compensate this increase by decreasing the elastic energy. To achieve this, a coupling between the crack phase-field variable and the stored elastic energy must be established. In Eqs. (3.10) and (3.23), $g(s)$ is the so-called energy degradation function whose task is to model the loss of stiffness in the material during fracture and determines how the elastic energy is released in relation to the evolution of the phase-field. This function is required to be non-negative in the interval $[0, 1]$, with $g(s = 1) = 1$ and $g(s = 0) = 0$, representing the intact and cracked material states, respectively. Moreover, to avoid the so-called damage widening where the damage zone becomes very wide after the localization of deformation is completed [184], we add an extra constraint, requiring the function to fulfill $g'(s = 0) = 0$ as well [167]. We also demand the degradation function to be monotonically increasing, i.e., in no point between the two material states can the function decrease. The original degradation function used in Bourdin et al. [134] was

$$g(s) = s^2; \tag{3.31}$$

a quadratic function which was originated by Ambrosio and Tortorelli [185]. This function is mostly used in the literature and is sometimes referred to as the classical degradation function. Higher-order functions are also available in the literature, for instance, cubic [144, 186]

$$g(s) = 3s^2 - 2s^3, \tag{3.32}$$

and quartic [181, 187, 188]

$$g(s) = 4s^3 - 3s^4, \tag{3.33}$$

degradation functions. Figures 3.9 and 3.10 show the graphical representation of these functions and their derivative with respect to the crack phase-field variable. The advantage of having a zero derivative at $s = 1$, $g'(1) = 0$, is that in conjunction with the quadratic geometric crack function, the degradation of the material does not occur immediately in the initial loading steps as $s = 1$ remains an admissible solution of the evolution equation [186].
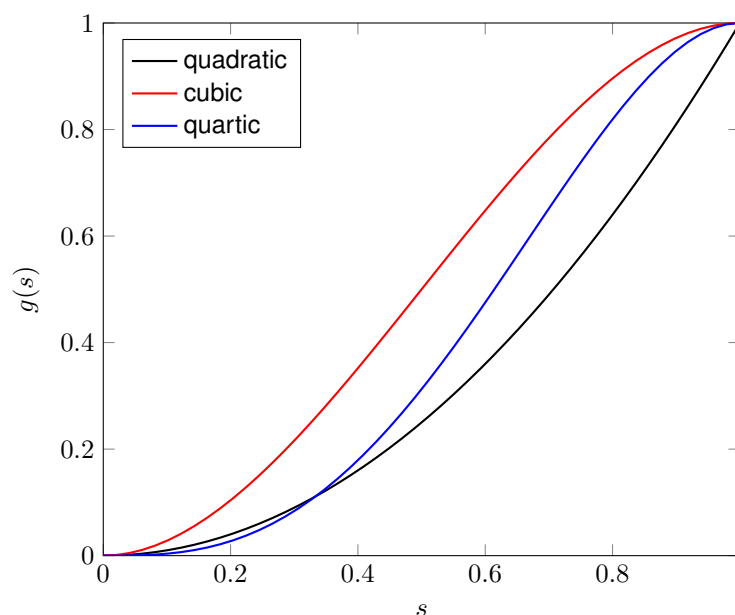
Figure 3.9: Graphical representation of different types of degradation functions
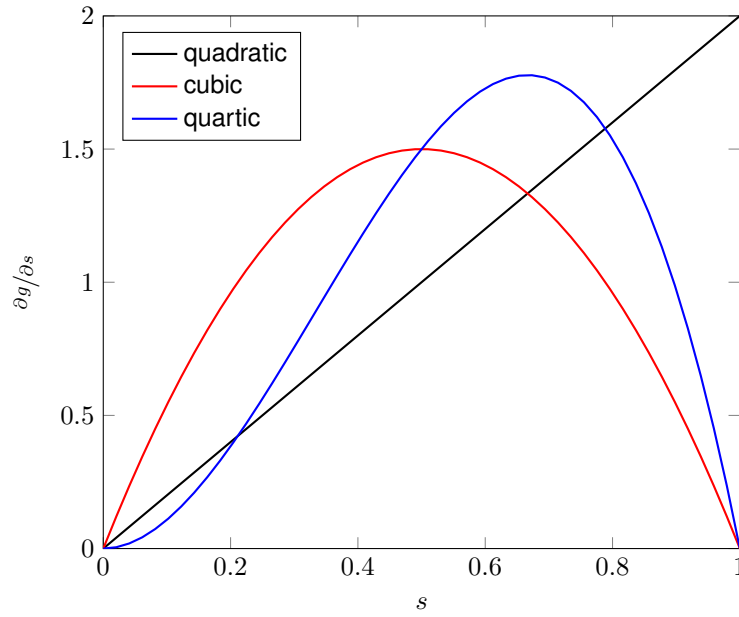
Figure 3.10: Graphical representation of the first derivative of different types of degradation functions with respect to the phase-field value

All the above mentioned degradation functions are compatible with the quadratic geometric crack approximation discussed in Sect. 3.2.3. The cubic and quartic degradation functions show a more reliable stress-strain relation to model brittle materials before reaching the maximum stress response. These functions provide a stiffer behavior of the material and therefore the resulting maximum stress is higher in comparison with the quadratic function [186]. However, as also discussed in [186], due to the existence of multiple admissible solutions (because of $g'(s = 1) = 0$), using these higher-order functions needs introducing numerical treatments to the problem by adding a perturbation of the crack field for the first Newton's method iteration of each load step, and even with this the final results still do not match the expectations from the analytical solutions. It should be also pointed out that for the linear geometric crack approximation discussed in the previous section, Geelen et al. [177] have proposed a degradation function of form

$$g(s) = \frac{s^2}{s^2 + \bar{m}\,(1-s)\,(1 + \bar{p}\,(1-s))} \quad \text{with} \quad \bar{p} \geq 1 \quad \text{and} \quad \epsilon < \frac{3E\mathcal{G}_c}{4\,(\bar{p}+2)\,\sigma_c^2}, \tag{3.34}$$

where $\bar{m}$ denotes the initial slope of the degradation function

$$\bar{m} = g'(s_0) = \frac{3\mathcal{G}_c}{8\epsilon\psi_{\text{crit}}}, \tag{3.35}$$

and $\bar{p}$ is the initial slope of the softening curve assuming the initial phase-field $s_0 = 1$. Moreover, σ_c and ψ_{crit} represent the critical tensile strength and the critical fracture energy density, respectively,

$$\psi_{\text{crit}} = \frac{\sigma_c^2}{2E}. \tag{3.36}$$

As mentioned before, this formulation restricts the value of the length-scale parameter [167]. For a review on more sophisticated degradation functions available in the literature we refer

to [167, 174, 186].

The choice of degradation function especially becomes crucial when dealing with the crack nucleation phenomenon, i.e., when the material is intact all over the domain at the beginning of the loading, which is not the case in the studies carried out in the current work. It is also reported that the influence of the type of the degradation function becomes trivial after the crack nucleation [186]. As our aim here is to study the effects of the singular stress field on the simplest model possible, and the quadratic degradation function is most broadly used in the community, we choose to remain with this standard formulation. Moreover, the author is not aware of any studies with the fourth-order model with degradation functions different than the quadratic form. While using different degradation functions is interesting for future investigations, introducing new changes to the model could raise further questions that the results shown in the next chapters could result from one of these changes. Another reason for choosing this formulation is that the results obtained by Borden et al. [144] show that using the higher-order degradation functions leads to a smaller process zone for the phase-field parameter in front of the crack tip compared to the one from the original quadratic formulation. Later in Chapter 5, we show that merely changing the formulation for the elastic energy to the strain gradient theory results in smaller process zones without changing the degradation function.

3.2.5 Irreversibility

In macroscopic scales, the crack is irreversible. Irreversibility of a crack means that the crack does not heal, i.e.,

$$\Gamma_{\mathrm{c}}(t) \subseteq \Gamma_{\mathrm{c}}(t + \Delta t). \tag{3.37}$$

This restriction ensures as well that the crack does not move. A disadvantage of using a Ginzburg-Landau type evolution equation for the phase-field parameter is that the irreversibility is not automatically fulfilled. In other words, the phase-field parameter changes freely based on the loading condition. Choosing a double-well function as the local fracture energy can make the formulation to some extent irreversible; however, we use a quadratic potential in our formulation, $w(s) = (1 - s)^2$, which does not add any constraints in favor of the irreversibility [186].

Different methods have been proposed to overcome the problem of reversible cracks in the literature, from using history variables to using Dirichlet type boundary conditions, or using damage-like constraints on $\dot{s}$ [134, 136, 182]. The idea behind using Dirichlet boundary conditions is to add a constraint that ensures once the phase-field value at a computational point is reduced to a certain value close to zero, from that moment on, it cannot increase anymore and will be fixed to zero. Obviously, before reaching that specific amount of damage, the phase-field value can still recover and increase due to unloading cases. Furthermore, one can define a history variable based on the strain energy density and put a set of Karush-Kuhn-Tucker (KKT) [189, 190] conditions to ensure that the history variable on each point always represents the maximum value reached on that point during the procedure. The damage-like condition $\dot{s} < 0$ can be deduced from the same idea [88, 186].

The examples considered in the current work are limited to tensile tests and the Mode I crack opening for isotropic materials (see also Sect. 3.2.6.3), and consequently, the implementation of irreversibility is not necessary. Therefore, it is not considered in the numerical implementations described in the next chapters for the sake of simplicity and clarity.

3.2.6 Remarks

In the previous sections, we discussed some of the most important aspects to consider when modelling fracture using the phase-field approach. In the current section, we make some remarks about the other elements of the formulation, and try to justify our choices for the final model used in the following sections.

3.2.6.1 Model Parameter $\bar{\eta}$

One point of debate in the formulation is the presence of an additional model parameter, $\bar{\eta}$, in the literature (see, for instance, [135, 170]), which was first used by Ambrosio and Tortorelli [185] to avoid ill-posedness and to guarantee well-conditioning of the problem. The idea is to use $g(s) = s^2 + \bar{\eta}$ (sometimes also $g(s) = (1 + \bar{\eta}) s^2 + \bar{\eta}$) instead of $g(s) = s^2$ as the degradation function where $\bar{\eta}$ has a very small value. Following Borden et al. [172], we set $\bar{\eta} = 0$ as we could not recognize any significant differences in our numerical results between using a minimal value of $\bar{\eta}$ or zero. Wu et al. [167] have also reported the same observation (see "Remark 16" therein).

3.2.6.2 Monolithic vs. Staggered Solvers

After assembling the system matrices for the phase-field fracture, we end up with a system of equations where we have coupling terms in the stiffness matrix (see Chapter 4). These terms include both mechanical and phase-field degrees of freedom. Two major solution techniques are used in the literature to solve such a system of equations. The monolithic solver is the first approach which deals with the whole system in the same time, i.e., the system is solved for displacements and the phase-field variable simultaneously. Although it seems to be the most natural and accurate way of solving this system of equations, it turns out that because of the non-convexity of the main energy functional, the performance of Newton-Raphson method is not satisfactory and, especially for more complex problems, occasionally the convergence cannot be achieved. Roughly speaking, the solver gets trapped in local minima and cannot find the correct global minimum. Among the attempts to tackle this issue, we name Gerasimov and De Lorenzis [191] where the authors have used a line search method to improve the results, and May et al. [192] where an arc-length method has been used to achieve the same goal.

Alternatively, there are the so-called staggered solvers, also known as alternate minimization solvers in the literature [164, 193]. The idea here is that first, the solver handles the system of equations for the displacement field assuming the phase-field parameter to be constant, and then in the second step, using the solution from the previous step, the system is solved for the phase-field variable with the displacement field considered to be constant during the solution step. The Newton-Raphson method can be used for this solution strategy as well. The advantage here is that the complexity of these subproblems are much less in comparison to the original problem since the coupling components in the stiffness matrix vanish. For instance, for the case of a standard formulation [134], a simple linear problem needs to be solved for the displacement field. However, using the staggered solvers comes with the problem of slower convergence rate. It is therefore very crucial to choose a proper time (load) step size for these solutions. A large step size can result in inaccurate results, while choosing very small step sizes is computationally expensive. Moreover, since each field is solved separately and the coupling between the mechanical and phase-field parameters is removed, a termination scheme is required to stop the simulation after the crack has reached

the domain boundaries [134, 137]. The same as with the monolithic approach, many studies have been done to increase the convergence rate for the staggered solvers [194–196]. Although it has been shown in the literature that choosing the right load step size and termination criterion, the staggered solutions can produce acceptable results, we still believe that using the monolithic solution scheme gives a more accurate result and it is more natural to use it for the current study as we try to keep the effect of the other factors which can possibly influence the final results as low as possible.

3.2.6.3 Energy Split

Another topic to be discussed here is the choice between isotropic and anisotropic phase-field formulations. Our degradation function $g(s)$ of choice acts on the whole stored elastic energy potential Ψ_{e} which means that in our formulation, we do not distinguish between the tension and compression forces. In the literature, this form is usually referred to as the isotropic or the standard formulation of the phase-field fracture (see, for instance, [134, 137, 167]). Using this formulation, the crack will grow under both compression and tension forces. Obviously, this is not a realistic behavior for the fracture of brittle material where no fracture should occur under pure compression forces. Using this formulation, it is also not possible to study fatigue problems where cyclic loads are applied to the structure. Due to these shortcomings, the so-called anisotropic phase-field models are introduced where the material stiffness is degraded based on a split of the stored energy into the energies coming from tension and compression, where fracture is only caused by tension forces, i.e.,

$$\Psi_{\mathrm{e}} = g(s)\Psi_{\mathrm{e}}^{+} + \Psi_{\mathrm{e}}^{-}. \tag{3.38}$$

This approach is very common in gradient damage mechanics. Unfortunately, there is no reference way of splitting the energy in fracture mechanics, and therefore, how to define Ψ_{e}^{+} is different based on the type of energy split approach exploited. Among the most common approaches in the literature, we can name the model by Lancioni et al. [197] where the energy split is based on the shear fracture and only the deviatoric part of the stored energy is assumed to be responsible for crack propagation. Amor et al. [164] also used a volumetric/deviatoric decomposition to keep the negative part of the stored energy undegraded. We should also mention the contrbutions of Miehe et al. [135, 136] and Wu et al. [198] where, respectively, spectral decompositions of strain and stress tensors are used to achieve the same goal. All the mentioned formulations are variationally consistent. The problem with these models, apart from the lack of a reference energy split approach, is that using these formulations, the equilibrium equation to solve for the displacement field becomes non-linear leading to an increase in the complexity of the problem and the computational costs.

There are also the so-called hybrid approaches, which are a combination of the isotropic and anisotropic models where the equilibrium equation remains the same as in the isotropic case, and the evolution of the crack field is only influenced by the positive part of the stored energy [137]. The resulting formulation is of course variationally not consistent anymore as it is not possible to obtain the evolution equations for the displacement field and the crack field from a single energy functional. Finally, in contrast to the previously mentioned models which have mathematical backgrounds, we can also mention the fracture mechanics driven models to split the energy [199]. In Bilgen et al. [199], the authors discuss the inevitability of using a hybrid formulation to capture the correct behavior of quasi-brittle fracture when using mathematically driven models, however they also emphasize that such a hybrid formulation

is neither unique nor evident from the physical point of view. They suggest using ad-hoc physically driven models based on fracture mechanics to tackle practical examples. For discussions and comparisons of the anisotropic models, we refer the interested reader to [137, 167, 199].

Clearly, the discussion is still open and there is no "universal" energy split formulation on which everyone agrees. From the results shown in the previously mentioned literature, even slight changes in the model can produce different crack paths, which is only obvious because of the different ways that the crack driving forces are determined in each model. It should be noted that all the presented formulations are still based on the classical Cauchy theory, and will nevertheless exhibit the stress singularity which is the main concern of the current contribution. Apart from that, as mentioned above, by introducing the energy split, the mechanical part of the problem becomes non-linear and it becomes almost impossible to use a monolithic solver. This is not the case for the hybrid formulations, however they are not variationally consistent. Therefore, we believe that, at this stage, introducing an energy split in the formulation not only adds unnecessary computational complexities, but it also affects the generality of the conclusions to be made. That being said, in this work, we do not split the elastic energy contributions concerning tension and compression. We are aware that choosing this configuration restricts our choices in applying the formulation for models with various loading cases, however it should be emphasized again that an isotropic formulation together with Mode I crack opening of a body with a homogeneous isotropic material will suffice (and somehow facilitate the process, as it will be evident in Chapter 5) to perform a thorough investigation on the stored energy density and stress fields in the damaged material and in front of the crack tip, as the crack path is expected to be a straight line in this case.

3.2.7 Summary

Here, we summarize the previous sections and list the characteristics of the phase-field fracture model formulation exploited in the next section. Two different models based on the second-order and the fourth-order formulations, respectively, will be introduced (Sects. 3.2.1 and 3.2.2). A quadratic function will be used as the geometric crack function (Sect. 3.2.3), together with a quadratic degradation function (Sect. 3.2.3) acting on the whole stored energy of the model, i.e., no energy split (Sect. 3.2.6.3). No extra constraints for the irreversibility of the crack will be applied to keep the numerical results intact (Sect. 3.2.5). We also do not add any model parameters to improve/guarantee well-conditioning of the problem (Sect. 3.2.6.1). Finally, for all the numerical models studied in the current work, a monolithic solver together with the Newton-Raphson method will be used (Sect. 3.2.6.2).

3.3 Strain Gradient Enhanced Phase-Field Fracture Models

This section discusses the integration of the strain gradient elasticity into the phase-field modelling of fracture mechanics. The classical phase-field fracture model only considers strains, and no higher-gradients of the displacement field are involved in the formulation, which may lead to a singular response near the crack tip. In the current work, we propose an energy functional for the fracture that is a function of strain and its gradients as well as the phase-field parameter and its gradients. In contrast to this model, there are other fracture models based on the strain gradient elasticity available in the literature where the energy functional is based on the strains and higher gradients of the displacement field, together with a damage parameter, but without any contributions from the gradients of this damage field.

We refer to the formulations based on this approach as strain gradient enhanced damage models [193, 200].

The section is separated into two main parts: first, a second-order phase-field fracture model based on the first strain gradient elasticity is proposed. We will focus mainly on Aifantis' model (GRADELA, cf. Sect. 2.3.2) as it is indeed a prevalent model in the strain gradient community, and many studies have shown its effectiveness despite the inherent simplicity. The last section of this chapter is devoted to a fourth-order model integrating the fourth-order phase-field model with the fourth-order strain gradient formulation.

For the sake of conciseness, in what follows, we adopt the following terminology:

- Second-order formulation: the second-order phase-field model based on gradient elasticity.
- Fourth-order formulation: the fourth-order phase-field model based on gradient elasticity.

In other words, we formally distinguish the two formulations only based on the order of the phase-field model, which is the decisive difference between both approaches.

3.3.1 Second-Order Phase-Field Fracture Model

In Chapter 2, we went through the fundamentals of strain gradient elasticity and introduced some simplified models. In this chapter, we modify the phase-field models introduced in Sect. 3.2 and replace the classical elastic energy with the ones from the strain gradient models.

In Section 3.2.1, we ended up with the following expression for the total energy of fracture, cf. Eq. (3.10):

$$
\Psi^{(2)} = \int_{\Omega} \left[g(s)\,\psi_{\mathrm{e}} + \mathcal{G}_{\mathrm{c}} \left(\frac{(1-s)^2}{4\epsilon} + \epsilon |\nabla s|^2 \right) \right] \mathrm{d}V.
$$

Using a quadratic degradation function and the strain energy density expression from the classical theory of continuum mechanics leads to

$$
\Psi^{(2)}(\mathbf{E}, s) = \int_{\Omega} \left[s^2 \left(\frac{1}{2} \lambda (\mathrm{tr}\,\mathbf{E})^2 + \mu \mathbf{E} : \mathbf{E} \right) + \mathcal{G}_{\mathrm{c}} \left(\frac{(1-s)^2}{4\epsilon} + \epsilon |\nabla s|^2 \right) \right] \mathrm{d}V. \tag{3.39}
$$

Replacing the strain energy density contribution in Eq. (3.39) with the one from Eq. (2.69)

$$
\psi_{\mathrm{grad}} = \frac{1}{2} \lambda (\mathrm{tr}\,\mathbf{E})^2 + \mu \mathbf{E} : \mathbf{E} + l^2 \left(\frac{1}{2} \lambda \left(\mathrm{tr}\,\mathbf{H} \cdot \mathrm{tr}\,\mathbf{H} \right) + \mu \mathbf{H} \because \mathbf{H} \right), \tag{3.40}
$$

in the presence of external forces, yields

$$
\Psi^{(2)}_{\mathrm{grad}}(\mathbf{E}, \mathbf{H}, s) = \int_{\Omega} \left[\psi^{(2)}_{\mathrm{grad}} + \mathcal{G}_{\mathrm{c}} \left(\frac{(1-s)^2}{4\epsilon} + \epsilon |\nabla s|^2 \right) \right] \mathrm{d}V - \int_{\Omega} \mathbf{b} \cdot \mathbf{u}\, \mathrm{d}V, \tag{3.41}
$$

where

$$
\begin{aligned}
\psi^{(2)}_{\mathrm{grad}} &= \frac{1}{2} s^2 \left(\mathbf{E} : [\mathbb{C}\,\mathbf{E}] + l^2 \mathbf{H} \because \nabla [\mathbb{C}\,\mathbf{E}] \right) \\
&= s^2 \left(\frac{1}{2} \lambda (\mathrm{tr}\,\mathbf{E})^2 + \mu \mathbf{E} : \mathbf{E} + l^2 \left(\frac{1}{2} \lambda (\mathrm{tr}\,\mathbf{H} \cdot \mathrm{tr}\,\mathbf{H}) + \mu \mathbf{H} \because \mathbf{H} \right) \right)
\end{aligned} \tag{3.42}
$$

is called the effective (degraded) strain energy density. The corresponding effective stresses, $\mathbf{S}^{\mathrm{frac}}$ and $\mathbf{P}^{\mathrm{frac}}$, are consequently defined as

$$\mathbf{S}^{\mathrm{frac}} := \frac{\partial \psi_{\mathrm{grad}}^{(2)}}{\partial \mathbf{E}} = s^2 \left(\lambda(\operatorname{tr} \mathbf{E})\mathbf{I} + 2\mu\mathbf{E} \right), \tag{3.43}$$

$$\mathbf{P}^{\mathrm{frac}} := \frac{\partial \psi_{\mathrm{grad}}^{(2)}}{\partial \mathbf{H}} = s^2 \left(l^2 \nabla \left(\lambda(\operatorname{tr} \mathbf{E})\mathbf{I} + 2\mu\mathbf{E} \right) \right). \tag{3.44}$$

Applying the principle of virtual work, the weak form of the mechanical part yields an expression which is very similar to Eq. (2.80)

$$\int_\Omega \left(\mathbf{S}^{\mathrm{frac}} : \delta\mathbf{E} + \mathbf{P}^{\mathrm{frac}} \vdots \delta\mathbf{H} \right) \mathrm{d}V = \int_\Omega \mathbf{b} \cdot \delta\mathbf{u}\, \mathrm{d}V + \int_{\Gamma_1} \bar{\mathbf{t}}^1 \cdot \delta\mathbf{u}\, \mathrm{d}A$$
$$+ \int_{\Gamma_1} \bar{\mathbf{t}}^2 \cdot \delta\nabla_{\mathbf{n}}\mathbf{u}\, \mathrm{d}A + \int_\Sigma \bar{\mathbf{t}}^3 \cdot \delta\mathbf{u}\, \mathrm{d}L. \tag{3.45}$$

For the phase-field counterpart, the evolution of s is governed by

$$\dot{s} = -M \left(s \left(\mathbf{E} : [\mathbb{C}\,\mathbf{E}] + l^2 \mathbf{H} \vdots \nabla [\mathbb{C}\,\mathbf{E}] \right) - 2\mathcal{G}_{\mathrm{c}}\epsilon\Delta s + \frac{\mathcal{G}_{\mathrm{c}}(s-1)}{2\epsilon} \right). \tag{3.46}$$

Multiplying Eq. (3.46) with a weighting function and applying integration by parts results in the weak form of the phase-field

$$\int_\Omega \left[\frac{\dot{s}}{M}\delta s + 2\,\mathcal{G}_{\mathrm{c}}\epsilon\,\nabla s\,\delta\nabla s + \left(s \left(\mathbf{E} : [\mathbb{C}\,\mathbf{E}] + l^2\mathbf{H} \vdots \nabla [\mathbb{C}\,\mathbf{E}] \right) + \frac{\mathcal{G}_{\mathrm{c}}(s-1)}{2\epsilon} \right) \delta s \right] \mathrm{d}V$$
$$= \int_{\Gamma_2} q_{\mathrm{n}}\,\delta s\, \mathrm{d}A. \tag{3.47}$$

3.3.2 Fourth-Order Phase-Field Fracture Model

In our numerical approach, we employ a linear elastic constitutive model based on a Laplacian formulation, see Eq. (3.41). Therefore, one could consider combining it with the corresponding fourth-order phase-feld model. Following the same procedure as Sect. 3.3.1, the total fracture energy (analogous to Eq. (3.23)) for the fourth-order phase-field model

$$\Psi^{(4)} = \int_\Omega \left[g(s)\,\psi_{\mathrm{e}} + \mathcal{G}_{\mathrm{c}} \left(\frac{(1-s)^2}{4\epsilon} + \frac{1}{2}\epsilon|\nabla s|^2 + \frac{1}{4}\epsilon^3\left(\Delta s\right)^2 \right) \right] \mathrm{d}V.$$

Considering strain gradient elasticity and replacing the degradation function with a quadratic type, the total fracture energy is

$$\Psi_{\mathrm{grad}}^{(4)}(\mathbf{E}, \mathbf{H}, s) = \int_\Omega \left[\frac{1}{2}s^2 \left(\mathbf{E} : [\mathbb{C}\,\mathbf{E}] + l^2\mathbf{H} \vdots \nabla[\mathbb{C}\,\mathbf{E}] \right) \right.$$
$$\left. + \mathcal{G}_{\mathrm{c}} \left(\frac{(1-s)^2}{4\epsilon} + \frac{1}{2}\epsilon|\nabla s|^2 + \frac{1}{4}\epsilon^3(\Delta s)^2 \right) \right] \mathrm{d}V - \int_\Omega \mathbf{b} \cdot \mathbf{u}\, \mathrm{d}V, \tag{3.48}$$

where the effective strain energy density and stresses are defined as before, cf. Eqs.(3.43) and (3.44). Equation (3.48) leads to the following weak form for the fully fourth-order formulation,

$$
\int_{\Omega} \left[\frac{\dot{s}}{M} \delta s + \mathcal{G}_{\mathrm{c}} \left(\epsilon \, \nabla s \, \delta \nabla s + \frac{\epsilon^3}{2} \, \Delta s \, \delta \Delta s \right) \right. \\
\left. + \left(s \big(\mathbf{E} : [\mathbb{C}\,\mathbf{E}] + l^2 \mathbf{H} \mathbin{\vdots} \nabla[\mathbb{C}\,\mathbf{E}] \big) + \frac{\mathcal{G}_{\mathrm{c}}(s-1)}{2\epsilon} \right) \delta s \right] \mathrm{d}V = \int_{\Gamma_2} q_{\mathrm{n}} \, \delta s \, \mathrm{d}A.
$$

(3.49)

At this point, all the required weak forms for the pure strain gradient elasticity models, as well as the strain gradient enhanced phase-field fracture models have been derived successfully. In the next chapter, we will go through the numerical implementation of these models.

4 Numerical Implementation

In this chapter, the discretization of the governing equations in the framework of isogeometric analysis is discussed. For the sake of completeness, we will first briefly introduce the concept of NURBS, which are used as shape functions in our numerical approach. After that, we start with the discrete forms of pure strain gradient models (i.e., without a coupled phase-field variable) introduced in Chapter 2 for three- and two-dimensional settings. Finally, the discrete forms of the system matrices for the strain gradient enhanced phase-field fracture models (Chapter 3) in two dimensions are presented.

4.1 Isogeometric Analysis

Concerning the numerical method to discretize the governing equations, Isogeometric Analysis, one of the recent developments of the finite element method, will be used. Introduced to fill the gap between computer-aided geometric design and analysis worlds, IGA has recently attracted the interest of many researchers. Hughes et al. [71] introduced the concept in 2005, where they proposed to use non-uniform rational B-splines as the basis function both for the geometry and the analysis. NURBS are the industry standard in Computer-Aided Geometric Design (CAGD), and using them as the basis of the analysis will eliminate the need to approximate the geometry to have an analysis-suitable model such that one obtains more accurate results. Consequently, further refinements to the analysis model can be performed without the need of going back to the original geometry in CAGD. Besides, using NURBS shape functions will provide a smoother solution field, i.e., higher continuity (regularity).

4.1.1 Non-Uniform Rational Basis-Splines

NURBS are a rational generalization of Basis splines (B-splines) and the result of projecting B-splines from $\mathbb{R}^{d+1}$ into $\mathbb{R}^d$ where d represents the dimensionality of the problem. A NURBS entity can be defined using knot vectors and a series of control points. The name "knot vector" can be deceiving as a knot vector is in fact a list of non-decreasing entries called knots, i.e., it does not possess a direction like a real vector. A knot vector

$$\Xi = \begin{bmatrix} \xi_1 & \xi_2 & \cdots & \xi_{n+p+1} \end{bmatrix} \tag{4.1}$$

defines the parametric space of a univariate (curve) NURBS entity. In Eq. (4.1), p and n represent the degree of the NURBS and the number of control points, respectively. A knot vector can range between any two real numbers, however it is very common to choose 0 and 1 as the lower- and upper-bounds of the parameteric space, respectively. The space between two adjacent knots is called a knot span. Non-zero knot spans can be compared to elements in classical FEM.

Knot vectors control the discretization of the geometry and the continuity across elements, whereas the control points are responsible for all the changes in the geometry. NURBS

patches are geometrically simple domains within which the element type and material are presumed to be uniform. As a rule, a degree p NURBS has $C^{p-\tilde{m}}$-continuity across the knot spans inside a patch, where $\tilde{m}$ is the knot multiplicity in the knot vector. The first and the last knots in the knot vectors of "open" NURBS considered in this study have a multiplicity of $p+1$, making their ends C^{-1}-continuous.

Figure 4.1 demonstrates an example of a univariate B-spline. The knot vector for this curve is:

$$\Xi = \begin{bmatrix} 0 & 0 & 0 & 0 & 0.2 & 0.2 & 0.2 & 0.5 & 0.8 & 0.8 & 0.8 & 1 & 1 & 1 & 1 \end{bmatrix}. \tag{4.2}$$

Since the first and the last knots are repeated 4 times, we can conclude that the curve is cubic, $p = 3$. Moreover, there are 15 knots listed in the knot vector, therefore one should expect $n = 15 - 3 - 1 = 11$ control points. The basis is $C^{3-3} = C^0$ on knots 0.2 and 0.8, although it is not visually apparent for the former knot by merely looking at the geometry. The control points are interpolatory to the curve on these locations. The continuity on the middle knot, 0.5 is $C^{3-1} = C^2$. An open NURBS/B-spline is always parallel to its control polygon at the start and end knots. The knot vector in Eq. (4.2) consists of four non-zero knot spans, resembling four elements for the numerical simulation in the sense of FEM.

A univariate NURBS is a rational generalization of a B-spline curve. Provided the knot vector and the control points, a NURBS curve can be determined using the interpolation relation,

$$\mathbf{T}(\xi) = \sum_{i=1}^{n} R_i(\xi)\mathbf{P}_i, \tag{4.3}$$

where $R_i(\xi)$ is the i-th NURBS basis function.
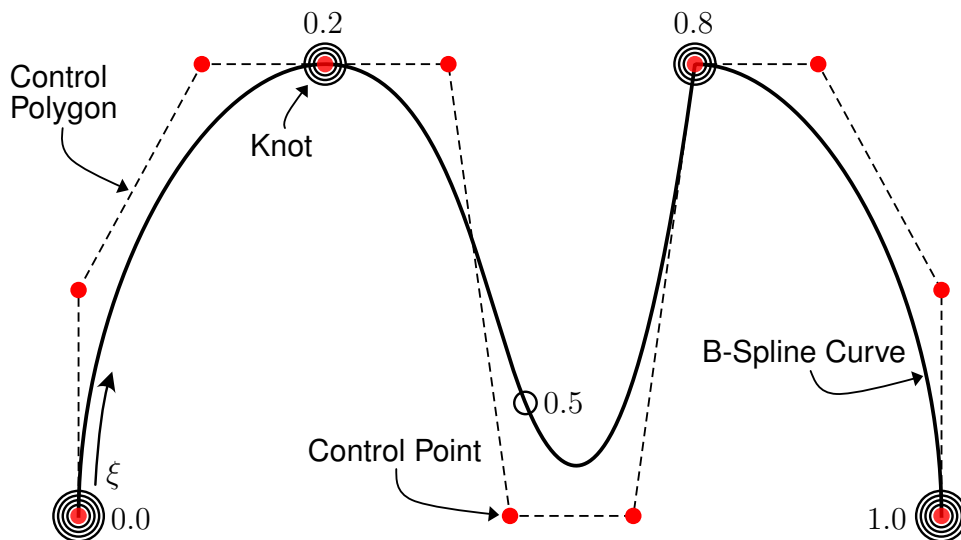
Figure 4.1: Example of a univariate B-spline. The control polygon is responsible for all the changes in the geometry, while the knot vector controls the discretization. The circles around each knot represent its multiplicity in the knot vector.

4.1.1.1 Basis Functions

For a degree p NURBS curve, the basis function is given by

$$R_i(\xi) = \frac{N_i^p(\xi)w_i}{W(\xi)} = \frac{N_i^p(\xi)w_i}{\sum_{\hat{i}=1} N_{\hat{i}}^p(\xi)w_{\hat{i}}}, \tag{4.4}$$

where $W(\xi)$ is the weighting function, w_i are the weights associated to the control points, and $N_i^p(\xi)$ are the standard B-spline basis functions in the parametric space. B-spline basis functions are linearly independent, always non-negative, and benefit from the partition of unity property. It is worth to note that in the case where all the weights associated to the NURBS control points have the same value, the NURBS and B-spline basis functions become indistinguishable:

$$R_i(\xi) = \frac{N_i^p(\xi)w_i}{\sum_{\hat{i}=1} N_{\hat{i}}^p(\xi)w_{\hat{i}}} = \frac{N_i^p(\xi)w_i}{w_i} = N_i^p. \tag{4.5}$$

This means that the B-spline curve demonstrated in Fig. 4.1 can be considered as a NURBS curve where the weight associated to each control point is 1.0. Considering the diagonal matrix of weights,

$$\mathbf{W} = \begin{bmatrix} w_1 & & & \\ & w_2 & & \\ & & \ddots & \\ & & & w_n \end{bmatrix}, \tag{4.6}$$

one can rewrite Eq. (4.4) in matrix-form as,

$$\mathbf{R}(\xi) = \frac{1}{W(\xi)}\mathbf{W}\mathbf{N}(\xi). \tag{4.7}$$

Figure 4.2 shows the basis functions of the curve given in Fig. 4.1. Shape functions of the
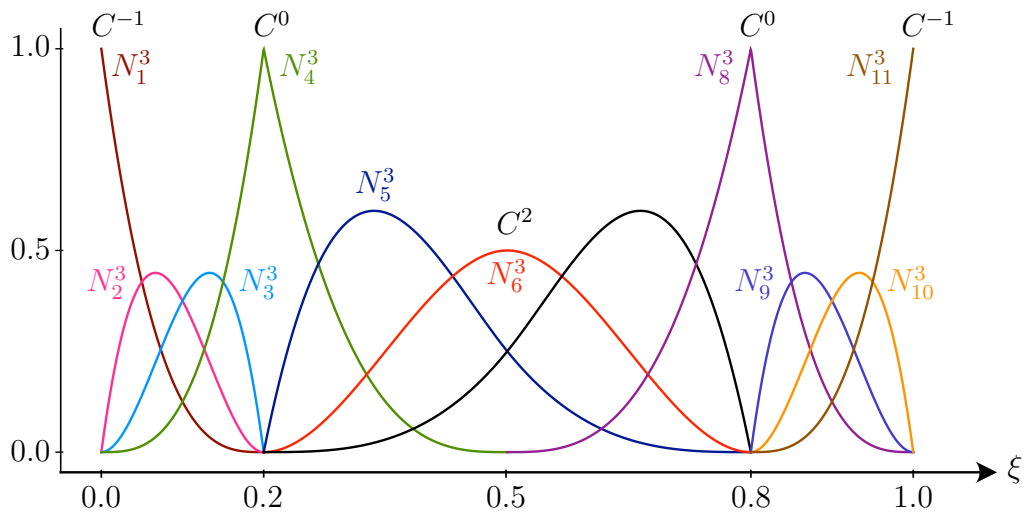
Figure 4.2: Basis functions of the B-spline demonstrated in Fig. 4.1. The basis functions are plotted only on the region of their local support, i.e., when their value is non-zero.

basis splines are defined by the Cox-de Boor recursion formula [201]. We have

$$
N_i^0(\xi) = \begin{cases} 1 & \text{if } \xi_i \leq \xi < \xi_{i+1} \\ 0 & \text{otherwise,} \end{cases} \quad \text{for } p = 0, \tag{4.8}
$$

and

$$
N_i^p(\xi) = \frac{\xi - \xi_i}{\xi_{i+p} - \xi_i} N_i^{p-1}(\xi) + \frac{\xi_{i+p+1} - \xi}{\xi_{i+p+1} - \xi_{i+1}} N_{i+1}^{p-1}(\xi) \quad \text{for } p = 1, 2, 3, \ldots. \tag{4.9}
$$

A bivariate (surface) NURBS is a rational generalization of a tensor-product B-spline surface which itself is created from tensor-products of univariate B-splines. In two dimensions, the NURBS basis functions are

$$
R_{ij}(\xi, \eta) = \frac{N_i^p(\xi) M_j^q(\eta) w_{i,j}}{W(\xi, \eta)} = \frac{N_i^p(\xi) M_j^q(\eta) w_{i,j}}{\sum_{\hat{i}=1} \sum_{\hat{j}=1} N_{\hat{i}}^p(\xi) M_{\hat{j}}^q(\eta) w_{\hat{i},\hat{j}}}, \tag{4.10}
$$

where p and q are the degrees of the univariate B-splines in ξ and η, respectively, $W(\xi, \eta)$ is the weighting function, $w_{i,j}$ are the weights associated to the control points, and finally, $N_i^p(\xi)$ and $M_j^q(\eta)$ are the standard B-spline basis functions in the parametric space [202]. In the same way, the shape functions of the trivariate (volume) NURBS are provided by

$$
R_{ijk}(\xi, \eta, \zeta) = \frac{N_i^p(\xi) M_j^q(\eta) L_k^r(\zeta) w_{ijk}}{W(\xi, \eta, \zeta)} = \frac{N_i^p(\xi) M_j^q(\eta) L_k^r(\zeta) w_{i,j}}{\sum_{\hat{i}=1} \sum_{\hat{j}=1} \sum_{\hat{k}=1} N_{\hat{i}}^p(\xi) M_{\hat{j}}^q(\eta) L_{\hat{k}}^r(\eta) w_{\hat{i}\hat{j}\hat{k}}}. \tag{4.11}
$$

4.1.1.2 Derivatives of Basis Functions

Applying the quotient rule on the NURBS shape functions, one can derive the local derivatives of the shape functions in the parametric space

$$
\frac{\mathrm{d}}{\mathrm{d}\xi} R_i(\xi) = \frac{W(\xi) \bar{N}_i^p(\xi) - \bar{W}(\xi) N_i^p(\xi)}{(W(\xi))^2} w_i, \tag{4.12}
$$

where

$$
\bar{N}_i^p(\xi) = \frac{\mathrm{d}}{\mathrm{d}\xi} N_i^p(\xi) = \frac{p}{\xi_{i+p} - \xi_i} N_i^{p-1}(\xi) + \frac{p}{\xi_{i+p+1} - \xi_{i+1}} N_{i+1}^{p-1}(\xi) \tag{4.13}
$$

and

$$
\bar{W}(\xi) = \sum_{\hat{i}=1} \bar{N}_{\hat{i}}^p(\xi) w_{\hat{i}}. \tag{4.14}
$$

There is also a generalized expression for higher-derivatives of the NURBS shape functions available [202, 203]

$$
\frac{\mathrm{d}^k}{\mathrm{d}\xi^k} R_i(\xi) = \frac{A_i^{(k)}(\xi) - \sum_{j=1}^k \binom{k}{j} W^{(j)}(\xi) \frac{\mathrm{d}^{(k-j)}}{\mathrm{d}\xi^{(k-j)}} R_i(\xi)}{W(\xi)}, \tag{4.15}
$$

where

$$\binom{k}{j} = \frac{k!}{j!(k-j)!},$$

(4.16)

$$A_i^{(k)}(\xi) = \frac{\mathrm{d}^k}{\mathrm{d}\xi^k} N_i^p(\xi) w_i,$$

(4.17)

$$\frac{\mathrm{d}^k}{\mathrm{d}\xi^k} N_i^p(\xi) = \frac{p!}{(p-k)!} \sum_{j=0}^{k} \alpha_j^k N_{i+j}^{p-k}(\xi),$$

(4.18)

with

$$\alpha_0^0 = 1,$$
$$\alpha_0^k = \frac{\alpha_0^{k-1}}{\xi_{i+p-k+1} - \xi_i},$$
$$\alpha_j^k = \frac{\alpha_j^{k-1} - \alpha_{j-1}^{k-1}}{\xi_{i+p+j-k+1} - \xi_{i+j}} \quad j = 1, ..., k-1,$$
$$\alpha_k^k = \frac{-\alpha_{k-1}^{k-1}}{\xi_{i+p+1} - \xi_{i+k}}.$$

(4.19)

Whenever the denominator of any $\alpha_\square^\square$ coefficient is zero, that coefficient is considered to be zero. These expressions yield the derivatives of the shape functions in local coordinates. A different mapping between the parametric and physical spaces is required to calculate the global derivatives which is discussed in Appendix A.

4.1.1.3 Refinement Techniques

Refinement of NURBS entities is usually achieved by modifying the underlying B-spline (in R^{d+1}). There are three methods to refine a B-spline/NURBS entity:

- knot insertion, where as the name suggests more knots are added to the knot vector, consequently increasing the number of control points and basis functions. Knot insertion is very close to the concept of h-refinement in the classical FEM,
- degree elevation, where the polynomial degree of the NURBS entity is increasing preserving the continuity of the curve. Degree elevation is the equivalent of p-refinement in the classical FEM, and
- the so-called k-refinement which is a combination of the knot insertion and degree elevation techniques. k-refinement makes it possible to increase the polynomial degree of the NURBS object while increasing its continuity, and does not have any equivalents in the conventional FEM.

It is important to note that none of the above mentioned refinement techniques changes the original geometry of the NURBS object. For a more detailed introduction to NURBS, the interested reader is referred to the seminal monograph by Piegl and Tiller [203].

4.1.2 Bézier Extraction Method

Although exploiting higher-order NURBS shape functions in a simulation provides the benefit of a smoother solution field, it comes at a price to pay, i.e., it is not possible easily to adapt already developed finite element software packages to support isogeometric analysis techniques. In other words, as the structure of the discretized domain is different than the conventional FEM models, new software must be developed to perform IGA. In IGA, the parametric space which is defined using knot vectors can contain several elements. This is of course in contrast with the classical FEM, where the parametric space is defined over one parent element. Therefore, an extra mapping from the parametric space to the parent element is needed. Moreover, the conventional numerical integration methods, such as Gauss-Legendre quadrature rules, cannot be used for NURBS domains with higher regularities. Another difficulty would be to handle models with multi-patch settings (i.e., analysis models which are created from more than one NURBS patch); in these cases, an extra loop over the patches should be added to the global assembly routine.

To overcome the problems listed above, Borden et al. [204] proposed a new data structure for IGA based on Bézier extraction of NURBS. They showed that using their method allows for the implementation of the IGA concept in already-developed finite element codes at the cost of calculating an extraction operator. Following their approach, numerical integration of smooth functions will be carried out on C^0-continuous Bézier elements using the extraction operator. It also enables the use of other spline technologies (such as T-Splines) as the analysis basis without much difficulty. In fact, any spline technology for which a Bézier extraction operator can be derived is possible to be employed in this framework.

The basic idea here is to decompose NURBS objects and construct the so-called Bézier elements. Hence, in the literature, this method is sometimes referred to as Bézier decomposition. One can think of a Bézier element as a B-spline with no inner knots in its knot vector. Bézier elements are usually defined in the domain from 0 to 1 in the parametric space. However, to be able to facilitate using the numerical integration approaches, we will define them over the interval $[-1, 1]$, the same as the classical finite elements. This will save us from mapping the parent element to the parametric space, as the mapping, in this case, would be one-to-one. Moreover, although it is possible to use the Cox-de Boor recursion formula to calculate basis functions of Bézier elements, using the interval $[-1, 1]$, we can determine the basis functions by explicit relations:

$$B_i^p(\xi) = \frac{1}{2}\left(1 - \xi\right) B_i^{p-1}(\xi) + \frac{1}{2}\left(1 + \xi\right) B_{i-1}^{p-1}(\xi), \tag{4.20}$$

where

$$B_1^0(\xi) = 1. \tag{4.21}$$

These functions are defined to be zero for i values smaller than 1 and higher than $p + 1$. The basis functions of Bézier elements are called Bernstein polynomials. They have the same properties as B-spline basis functions, such as the partition of unity and non-negativity. Calculating the local derivatives is also straightforward; for instance, the first derivatives can be determined by

$$\frac{\mathrm{d}}{\mathrm{d}\xi}B_i^p(\xi) = \frac{1}{2}\left(B_{i-1}^{p-1}(\xi) - B_i^{p-1}(\xi)\right). \tag{4.22}$$

The process of decomposing a NURBS entity to its Bézier elements involves using the knot

insertion technique. The idea is to insert inner knots into the knot vector of the NURBS object until the multiplicity of each inner knot is p. This produces a set of Bézier elements which are connected to each other because of the C^0-continuity achieved by the knot insertion. In theory, we should achieve $p + 1$ multiplicity for each knot to have entirely separated Bézier elements, but it suffices to have the multiplicity of p; it is computationally less expensive as well. The information required for this mapping will be stored in the so-called extraction operators. One should remember that this procedure does not change the original geometry and its parametrization.

Let us explain the procedure using the NURBS curve considered in the previous section, cf. Eq. (4.2),

$$\Xi = \begin{bmatrix} 0 & 0 & 0 & 0 & 0.2 & 0.2 & 0.2 & 0.5 & 0.8 & 0.8 & 0.8 & 1 & 1 & 1 & 1 \end{bmatrix},$$

as the original knot vector. The knot vector has three inner knots: 0.2, 0.5, and 0.8. The multiplicities of knots 0.2 and 0.8 are already $\tilde{m} = p = 3$. For knot 0.5, the multiplicity is one and therefore we need to insert two knots into our knot vector, $\{0.5, 0.5\}$.

At this point, let us look closer into the knot insertion procedure. In order to preserve the geometry and its parametariaztion, special care must be taken when adding the new control points resulting from adding the new knots.

Let $\Xi = [\xi_1, \xi_2, \ldots, \xi_{n+p+1}]$ be a given knot vector. Inserting a new knot $\bar{\xi} = [\xi_k, \xi_{k+1}[$ with $k > p$ into the knot vector requires $\bar{m} = n + 1$ new basis functions to be defined using the Cox-de Boor recursion formula (see Sect. 4.1.1.1). To preserve the geometry, the new set of control points, $\bar{\mathbf{P}}$, must be defined from the original set of control points, $\mathbf{P}$, [203, 204]

$$\bar{\mathbf{P}}_\mathbf{i} = \begin{cases} \mathbf{P}_1, & i = 1, \\ \beta_i \mathbf{P}_i + (1 - \beta_i) \mathbf{P}_{i-1}, & 1 < i < \bar{m}, \\ \mathbf{P}_n, & i = \bar{m}, \end{cases} \tag{4.23}$$

where

$$\beta_i = \begin{cases} 1, & 1 \leq i \leq k - p, \\ \dfrac{\bar{\xi} - \xi_i}{\xi_{i+p} - \xi_i}, & k - p + 1 \leq i \leq k, \\ 0, & i \geq k + 1. \end{cases} \tag{4.24}$$

The Bézier extraction operator will be determined using the relations given in Eqs. (4.23) and (4.24). Let $\{\bar{\bar{\xi}}_j\}$ with $j = 1, \underline{m}$ be a set of knots required to produce C^0 continuity on the inner knots of the B-spline object. Let us define β_i^j with $i = 1, n + j$ to be the ith β for the jth knot inserted. Then, one can define the new control variables $\bar{\mathbf{P}}^{j+1}$ created after inserting $\bar{\bar{\xi}}_j$ into the knot vector as

$$\bar{\mathbf{P}}^{j+1} = \left(\mathbf{C}^j\right)^{\mathrm{T}} \bar{\mathbf{P}}^j, \tag{4.25}$$

with $\bar{\mathbf{P}}^1 = \mathbf{P}$, i.e., the set of original B-spline control points. In Eq. (4.25), $\mathbf{C}^j$ can be defined

as

$$\mathbf{C}^j = \begin{bmatrix} \beta_1 & 1-\beta_2 & 0 & \cdots & & & 0 \\ 0 & \beta_2 & 1-\beta_3 & 0 & \cdots & & 0 \\ 0 & 0 & \beta_3 & 1-\beta_4 & 0 & \cdots & 0 \\ \vdots & & & \ddots & \ddots & & \\ 0 & \cdots & & & 0 & \beta_{n+j-1} & 1-\beta_{n+j} \end{bmatrix}. \tag{4.26}$$

It can be shown that the last set of control points $\bar{\mathbf{P}}^{\underline{m}+1}$ gives us the set of control points for Bézier elements [204]. The relation between the control points of the Bézier elements and the B-spline object can be written as

$$\mathbf{P}^b = \mathbf{C}^{\mathrm{T}}\mathbf{P}, \tag{4.27}$$

where,

$$\mathbf{C}^{\mathrm{T}} = \left(\mathbf{C}^{\underline{m}}\right)^{\mathrm{T}} \left(\mathbf{C}^{\underline{m}-1}\right)^{\mathrm{T}} \cdots \left(\mathbf{C}^1\right)^{\mathrm{T}}, \tag{4.28}$$

and $\mathbf{C}$ is the global Bézier extraction operator. The B-spline basis functions can be written in terms of Bézier basis functions (Bernstein polynomials),

$$\mathbf{N}(\xi) = \mathbf{C}\mathbf{B}(\xi). \tag{4.29}$$

The equivalent to Eq. (4.27) for NURBS is

$$\mathbf{P}^b = \left(\mathbf{W}^b\right)^{-1} \mathbf{C}^{\mathrm{T}}\mathbf{W}\mathbf{P}, \tag{4.30}$$

where $\mathbf{W}^b$ is the diagonal matrix of weights associated to the control points of Bézier elements,

$$\mathbf{W}^b = \begin{bmatrix} w_1^b & & & \\ & w_2^b & & \\ & & \ddots & \\ & & & w_{n+\underline{m}}^b \end{bmatrix}. \tag{4.31}$$

Taking the NURBS weight vector $\mathbf{w} = \{w_i\}$ with $i = 1, n$, the components of $\mathbf{w}^b$ for the Bézier entity can be determined through $\mathbf{w}^b = \mathbf{C}^{\mathrm{T}}\mathbf{w}$. Moreover, using the Bézier extraction operator, NURBS basis functions can be written as,

$$\mathbf{R}(\xi) = \frac{1}{W^b(\xi)}\mathbf{W}\mathbf{C}\mathbf{B}(\xi), \tag{4.32}$$

where $W^b(\xi) = W(\xi)$ [204]. Finally, the NURBS curve can be determined in terms of C^0-continuous Bézier elements,

$$T(\xi) = \frac{1}{W^b(\xi)}\mathbf{P}^{\mathrm{T}}\mathbf{W}\mathbf{C}\mathbf{B}(\xi). \tag{4.33}$$

Figures 4.3 and 4.4 demonstrate the Bézier elements and their basis functions for the B-spline curve presented in Sect. 4.1.1.1. Considering that the Bézier extraction process creates a Bézier element for each non-zero knot interval, it is possible to localize the process
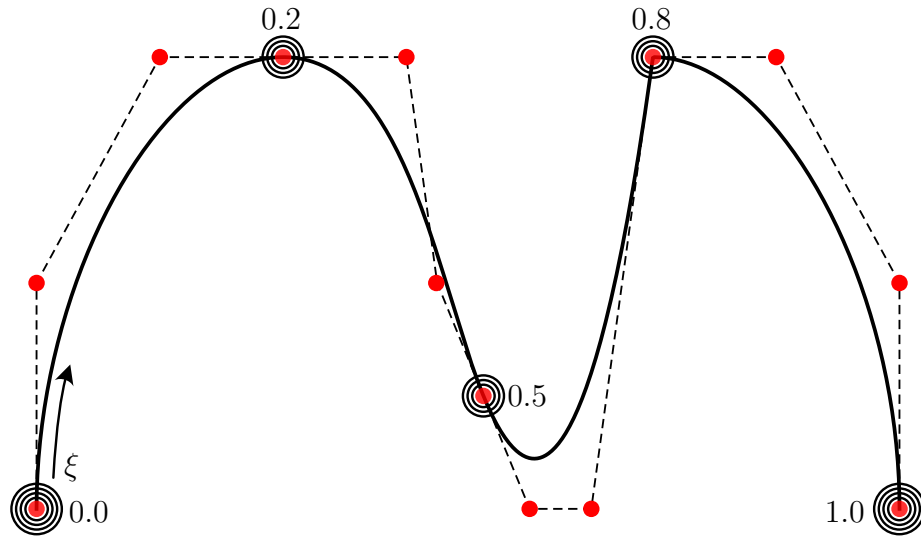
Figure 4.3: Bézier curve equivalent to the B-Spline curve represented in Fig. 4.1. The circles around each knot represent its multiplicity in the knot vector.
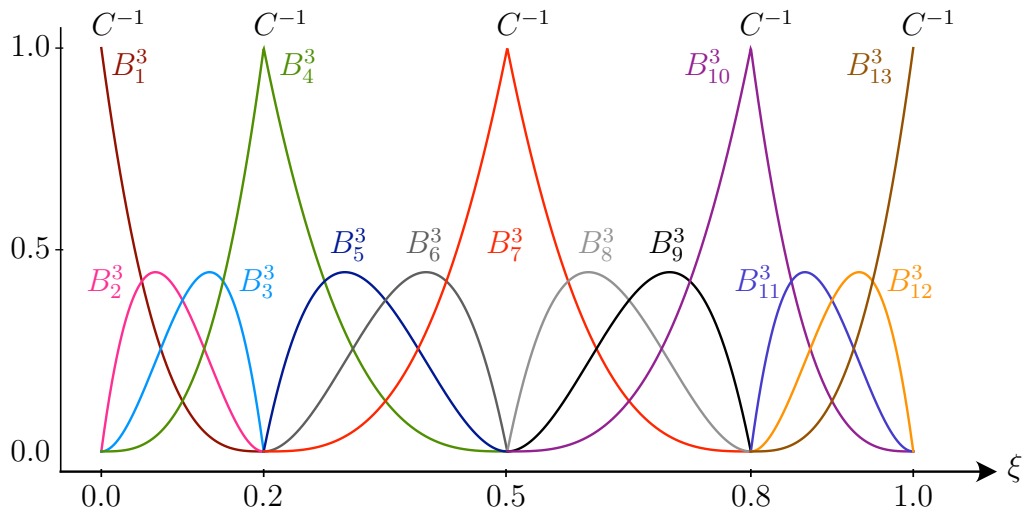
Figure 4.4: Basis functions of the Bézier curve demonstrated in Fig. 4.3. The basis functions are plotted only on the region of their local support, i.e., when their value is non-zero.

and handle the mapping in the element level [204]. There are efficient algorithms to handle the knot insertion and Bézier decomposition available in the literature [204, 205]. The Bézier extraction operators corresponding to the elements of our example are:

$$
\mathbf{C}^1 = \begin{bmatrix} 1 & 0 & 0 & 0 \\ 0 & 1 & 0 & 0 \\ 0 & 0 & 1 & 0 \\ 0 & 0 & 0 & 1 \end{bmatrix}, \quad
\mathbf{C}^2 = \begin{bmatrix} 1 & 0 & 0 & 0 \\ 0 & 1 & 0.5 & 0.25 \\ 0 & 0 & 0.5 & 0.5 \\ 0 & 0 & 0 & 0.25 \end{bmatrix},
$$
$$
\mathbf{C}^3 = \begin{bmatrix} 0.25 & 0 & 0 & 0 \\ 0.5 & 0.5 & 0 & 1 \\ 0.25 & 0.5 & 1 & 0 \\ 0 & 0 & 0 & 1 \end{bmatrix}, \quad
\mathbf{C}^4 = \begin{bmatrix} 1 & 0 & 0 & 0 \\ 0 & 1 & 0 & 0 \\ 0 & 0 & 1 & 0 \\ 0 & 0 & 0 & 1 \end{bmatrix},
$$

(4.34)

where $\mathbf{C}^e$ represents the extraction operator for element e. As it can be seen in Eq. (4.34),

the extraction operator for the knot intervals where no knot insertion is required is the identity matrix.

Kronecker products will be used to establish the extraction operators for bi-variate and tri-variate B-splines and NURBS. Defining $\mathbf{C}_\xi^i$, $\mathbf{C}_\eta^j$, and $\mathbf{C}_\zeta^k$ to be the ith, jth, and kth univariate element extraction operators in the ξ, η, and ζ directions, respectively, we can define the surface (bi-variate) and solid (tri-variate) element extraction operators as,

$$\mathbf{C}^e = \mathbf{C}_\eta^j \otimes \mathbf{C}_\xi^i, \tag{4.35}$$

and,

$$\mathbf{C}^e = \mathbf{C}_\zeta^k \otimes \mathbf{C}_\eta^j \otimes \mathbf{C}_\xi^i, \tag{4.36}$$

where, for two matrices $\mathbf{A}$ and $\mathbf{B}$ we have

$$\mathbf{A} \otimes \mathbf{B} = \begin{bmatrix} A_{11}\mathbf{B} & A_{12}\mathbf{B} & \cdots \\ A_{21}\mathbf{B} & A_{22}\mathbf{B} & \\ \vdots & & \ddots \end{bmatrix}. \tag{4.37}$$

In practice, only the elemental extraction operators are needed to perform IGA using the Bézier extraction method. All the other information, such as the knot vectors and the control points are transferred from the original NURBS model. As we are dealing with C^0-continuous elements like the ones from the classical finite elements, it is possible to slightly modify the shape function routines and calculate the basis functions for each NURBS element by multiplying the extraction operator with the corresponding Bézier basis functions (cf. Eq. (4.20)) or their derivatives for that specific element. Consequently, there is no need to, for instance, determine the control points of the Bézier elements for IGA.

4.2 Strain Gradient Elasticity

The numerical solution of gradient elasticity equations needs higher continuities of the solution field. This is one of the issues where the advantages of the IGA method become evident. Fischer et al. [73] used IGA to solve the problem of gradient elasticity in two dimensions and exploited the higher continuity nature of the NURBS basis functions to overcome the need of introducing auxiliary degrees of freedom. Since then, many studies have been performed based on the IGA and its application in gradient elasticity theory, among which we name [26, 74, 76, 206].

In this section, we provide the numerical implementation of the strain gradient models introduced in Chapter 2. Our focus will be on the two simplified models (Reiher's and Aifantis') as the derivation of the required system matrices is more straightforward for these cases, and in the same way the implementation is easier. However, as mentioned before, these models can be considered as special cases of Mindlin's model with five gradient parameters. Therefore, for the sake of completeness, the full representation of the system matrices of the discrete form for the general theory and the three-dimensional setting is provided in Appendix B for the interested reader.

4.2.1 Reiher's Model

In Sect. 2.3.1, we have derived the weak form for the simplified model introduced in [25], which is repeated here, cf. Eq. (2.68),

$$\int_\Omega \left((2\mu \mathbf{E} : \delta\mathbf{E} + \lambda \operatorname{tr}(\mathbf{E}) \operatorname{tr}(\delta\mathbf{E})) + \lambda_{1_{\text{real}}} \nabla(\nabla\mathbf{u}) \because \nabla(\nabla\delta\mathbf{u}) \right) dV =$$

$$\int_\Omega \mathbf{b} \cdot \delta\mathbf{u} \, dV + \int_{\Gamma_1} \bar{\mathbf{t}}^1 \cdot \delta\mathbf{u} \, dA + \int_{\Gamma_1} \bar{\mathbf{t}}^2 \cdot \delta\nabla_\mathbf{n}\mathbf{u} \, dA, + \int_\Xi \bar{\mathbf{t}}^3 \cdot \delta\mathbf{u} \, dL.$$

The approximation of the displacement field $\mathbf{u}$ and its variation $\delta\mathbf{u}$ using NURBS shape functions can be obtained from

$$\mathbf{u} := \sum_{ijk} \bar{\mathbf{u}}_{ijk} R_{ijk}, \qquad \delta\mathbf{u} := \sum_{ijk} \delta\bar{\mathbf{u}}_{ijk} R_{ijk}. \tag{4.38}$$

In Eq. (4.38), $\bar{\mathbf{u}}_{ijk}$ represents the displacement vector of the control point ijk. For the sake of clarity, we will use a single index $I = 1, \ldots, n_{\text{cp}}$ where n_{cp} is the total number of control points, instead of the triple index ijk, i.e., $\bar{\mathbf{u}}_I = \bar{\mathbf{u}}_{ijk}$ and $R_I = R_{ijk}$.

The weak form is composed of first- and second-gradient terms of the displacement field. Using Voigt notation (denoted by underlined letters in the following) in three dimensions, we define the linear strain $\underline{\mathbf{E}}$ as

$$\underline{\mathbf{E}} = \begin{bmatrix} E_{11} & E_{22} & E_{33} & 2E_{12} & 2E_{23} & 2E_{13} \end{bmatrix}^{\text{T}} := \sum_{I=1}^n [\boldsymbol{B}_I^{\mathbf{u}}] \, \bar{\boldsymbol{u}}_I, \tag{4.39}$$

where $n = (p+1)(q+1)(r+1)$ is the number of control points generating each element. In Eq. (4.39), $[\boldsymbol{B}_I^{\mathbf{u}}]$ represents the strain-displacement matrix for the Ith control point and is defined as

$$[\boldsymbol{B}_I^{\mathbf{u}}] := \begin{bmatrix} R_{I,1} & 0 & 0 \\ 0 & R_{I,2} & 0 \\ 0 & 0 & R_{I,3} \\ R_{I,2} & R_{I,1} & 0 \\ 0 & R_{I,3} & R_{I,2} \\ R_{I,3} & 0 & R_{I,1} \end{bmatrix}, \tag{4.40}$$

where $R_{I,k} = \frac{\partial R_I}{\partial x_k}$. The discretized form of the second-gradient terms, for instance in the x_1-direction is

$$(\nabla(\nabla\mathbf{u}))_{11} := \sum_I \frac{\partial^2 R_I}{\partial x_1^2} \bar{\mathbf{u}}_I, \tag{4.41}$$

which clearly requires the second-derivatives of the shape functions to exist throughout the domain, i.e., continuous first-derivatives (at least C^1-continuity).

For a static analysis, in the absence of external forces, the residual matrix is given by

$$\hat{\mathbf{P}}_I^{\mathbf{u}} = \int_{\bar{\Omega}} \left([\boldsymbol{B}_I^{\mathbf{u}}]^{\text{T}} \underline{\boldsymbol{C}}\underline{\boldsymbol{E}} + \lambda_{1_{\text{real}}} \nabla(\nabla R_I) \nabla(\nabla\, \mathbf{u}) \right) dV, \tag{4.42}$$

Therefore, we end up with the following system of equations

$$\hat{\mathbf{P}} = \hat{\mathbf{K}}\bar{\mathbf{u}},\tag{4.43}$$

where $\hat{\mathbf{K}}$ denotes the stiffness matrix, and $\bar{\mathbf{u}}$ represents the discretized field of unknowns, i.e., the displacement field. For the sake of clarity, the stiffness matrix will be decomposed into two main parts, the classical part $\hat{\mathbf{K}}^1$ and the second-gradient part $\hat{\mathbf{K}}^2$. The total stiffness matrix is the sum of these two expressions, i.e., $\hat{\mathbf{K}} = \hat{\mathbf{K}}^1 + \hat{\mathbf{K}}^2$.
The classical theory contribution for the pair of control points IJ is

$$\hat{\mathbf{K}}^1_{IJ} = \int_{\bar{\Omega}} [\boldsymbol{B}^{\mathbf{u}}_I]^{\mathrm{T}} \, \underline{\boldsymbol{C}} \, [\boldsymbol{B}^{\mathbf{u}}_J] \, \mathrm{d}V.\tag{4.44}$$

In the same way, $\mathbf{K^2}$ consists of the second-gradient terms

$$\hat{\mathbf{K}}^2_{IJ} = \int_{\bar{\Omega}} \lambda_1 \, \nabla(\nabla R_I) \, \nabla(\nabla R_J) \, \mathrm{d}V.\tag{4.45}$$

For a more detailed derivation, the interested reader is referred to [26] and the discussions therein.

4.2.2 Aifantis' Model

The weak form for this model was derived in Sect. 2.3.2 and is repeated here, cf. Eq. (2.80),

$$\int_{\Omega} \mathbf{S} : \delta\mathbf{E} \, \mathrm{d}V + \int_{\Omega} \mathbf{P} \mathbin{\vdots} \delta\mathbf{H} \, \mathrm{d}V =$$
$$\int_{\Omega} \mathbf{b} \cdot \delta\mathbf{u} \, \mathrm{d}V + \int_{\Gamma_1} \bar{\mathbf{t}}^1 \cdot \delta\mathbf{u} \, \mathrm{d}A + \int_{\Gamma_1} \bar{\mathbf{t}}^2 \cdot \delta\nabla_{\mathbf{n}} \mathbf{u} \, \mathrm{d}A, + \int_{\Xi} \bar{\mathbf{t}}^3 \cdot \delta\mathbf{u} \, \mathrm{d}L,$$

which can be re-written as

$$\int_{\Omega} \left(2\mu\mathbf{E} : \delta\mathbf{E} + \lambda \operatorname{tr}(\mathbf{E}) \operatorname{tr}(\delta\mathbf{E})\right) \mathrm{d}V + \int_{\Omega} \left(2\mu\mathbf{H} \mathbin{\vdots} \delta\mathbf{H} + \lambda \operatorname{tr}(\mathbf{H}) \cdot \operatorname{tr}(\delta\mathbf{H})\right) \mathrm{d}V$$
$$= \int_{\Omega} \mathbf{b} \cdot \delta\mathbf{u} \, \mathrm{d}V + \int_{\Gamma_1} \bar{\mathbf{t}}^1 \cdot \delta\mathbf{u} \, \mathrm{d}A + \int_{\Gamma_1} \bar{\mathbf{t}}^2 \cdot \delta\nabla_{\mathbf{n}} \mathbf{u} \, \mathrm{d}A, + \int_{\Xi} \bar{\mathbf{t}}^3 \cdot \delta\mathbf{u} \, \mathrm{d}L.\tag{4.46}$$

From this point on, we change the problem setting to a two-dimensional one assuming plane strain (this will be discussed further in Chapter 5). In the same way as the previous section, we use NURBS shape functions to approximate the displacement field and its variation

$$\mathbf{u} := \sum_{ij} \bar{\mathbf{u}}_{ij} R_{ij} \qquad \delta\mathbf{u} := \sum_{ij} \delta\bar{\mathbf{u}}_{ij} R_{ij}.\tag{4.47}$$

We replace the double index ij with a single index I (i.e., $\mathbf{u}_I = \mathbf{u}_{ij}$, and $R_I = R_{ij}$).

Using Voigt notation in two dimensions, we define the strain $\underline{\boldsymbol{E}}$ and its first gradient $\underline{\boldsymbol{H}}$ as

$$\underline{\boldsymbol{E}} = [E_{11} \quad E_{22} \quad 2E_{12}]^{\mathrm{T}} := \sum_{I=1}^{n} [\boldsymbol{B}_I^{\mathbf{u}}] \, \bar{\boldsymbol{u}}_I \,,$$

$$\underline{\boldsymbol{H}}_k = [E_{11,k} \quad E_{22,k} \quad 2E_{12,k}]^{\mathrm{T}} := \sum_{I=1}^{n} \left[\frac{\partial \boldsymbol{B}_I^{\mathbf{u}}}{\partial x_k} \right] \bar{\boldsymbol{u}}_I, \tag{4.48}$$

where x_k represents the kth component of the Cartesian coordinates. In Eq. (4.48), $\left[\boldsymbol{B}_I^{\mathbf{u}} \right]$ represents the strain-displacement matrix for the Ith control point, and is defined as

$$[\boldsymbol{B}_I^{\mathbf{u}}] := \begin{bmatrix} R_{I,1} & 0 \\ 0 & R_{I,2} \\ R_{I,2} & R_{I,1} \end{bmatrix}, \quad \left[\frac{\partial \boldsymbol{B}_I^{\mathbf{u}}}{\partial x_1} \right] := \begin{bmatrix} R_{I,11} & 0 \\ 0 & R_{I,21} \\ R_{I,21} & R_{I,11} \end{bmatrix},$$

$$\left[\frac{\partial \boldsymbol{B}_I^{\mathbf{u}}}{\partial x_2} \right] := \begin{bmatrix} R_{I,12} & 0 \\ 0 & R_{I,22} \\ R_{I,22} & R_{I,12} \end{bmatrix}, \tag{4.49}$$

where $R_{I,kl} = \frac{\partial^2 R_I}{\partial x_k \partial x_l}$. For a static analysis, in the absence of external forces, the residual matrix is given by

$$\hat{\mathbf{P}}_I^{\mathbf{u}} = \int_{\Omega} \left([\boldsymbol{B}_I^{\mathbf{u}}]^{\mathrm{T}} \underline{\boldsymbol{C}} \underline{\boldsymbol{E}} + l^2 \sum_{k=1}^{2} \left(\left[\frac{\partial \boldsymbol{B}_I^{\mathbf{u}}}{\partial x_k} \right]^{\mathrm{T}} \underline{\boldsymbol{C}} \underline{\boldsymbol{H}}_k \right) \right) \mathrm{d}V, \tag{4.50}$$

and we end up with the following system of equations

$$\hat{\mathbf{P}} = \hat{\mathbf{K}} \bar{\mathbf{u}}, \tag{4.51}$$

where, the same as before, $\hat{\mathbf{K}}$ denotes the stiffness matrix, and $\bar{\mathbf{u}}$ represents the discretized unknown field. For the sake of clarity, the stiffness matrix will be decomposed into two main parts, the classical part $\hat{\mathbf{K}}^1$ and the second-gradient part $\hat{\mathbf{K}}^2$. The total stiffness matrix is the sum of these two expressions, i.e., $\hat{\mathbf{K}} = \hat{\mathbf{K}}^1 + \hat{\mathbf{K}}^2$.
The contribution of the classical theory for the pair of control points IJ is the same as before, cf. Eq. (4.44). $\mathbf{K}^2$ is different, though,

$$\hat{\mathbf{K}}_{IJ}^2 = \int_{\bar{\Omega}} l^2 \left(\sum_{k=1}^{2} \left[\frac{\partial \boldsymbol{B}_I^{\mathbf{u}}}{\partial x_k} \right]^{\mathrm{T}} \underline{\boldsymbol{C}} \left[\frac{\partial \boldsymbol{B}_J^{\mathbf{u}}}{\partial x_k} \right] \right) \mathrm{d}V. \tag{4.52}$$

4.3 Strain Gradient Enhanced Phase-Field Fracture Models

In the previous sections, we provided the residual and stiffness matrices required to establish the system of equation for pure strain gradient models. Since we are dealing with static problems for those cases, the tangent matrix required for the Newton-Raphson method consists only of the stiffness matrix. For the phase-field fracture problems, we assume a quasi-static mechanical problem together with a weak form for the phase-field variable evolution which consists of transient terms as well. For this reason, in the current section, in addition to the residual and stiffness matrices, the so-called damping matrix is also required for the phase-field part of the solution. In what follows, we provide the representation of

these matrices for the second-order and the fourth-order formulations.

4.3.1 Second-Order Phase-Field Fracture Model

We start by considering the second-order model. From Chapter 3, we have, cf. Eq. (3.45),

$$\int_\Omega \left(\mathbf{S}^{\text{frac}} : \delta\mathbf{E} + \mathbf{P}^{\text{frac}} \mathbin{\vdots} \delta\mathbf{H} \right) \mathrm{d}V$$
$$= \int_\Omega \mathbf{b} \cdot \delta\mathbf{u}\, \mathrm{d}V + \int_{\Gamma_1} \bar{\mathbf{t}}^1 \cdot \delta\mathbf{u}\, \mathrm{d}A + \int_{\Gamma_1} \bar{\mathbf{t}}^2 \cdot \delta\nabla_{\mathbf{n}}\mathbf{u}\, \mathrm{d}A, + \int_\Xi \bar{\mathbf{t}}^3 \cdot \delta\mathbf{u}\, \mathrm{d}L$$

which can be re-written as

$$\int_\Omega s^2 \left((2\mu\mathbf{E} : \delta\mathbf{E} + \lambda\operatorname{tr}(\mathbf{E})\operatorname{tr}(\delta\mathbf{E})) + (2\mu\mathbf{H} \mathbin{\vdots} \delta\mathbf{H} + \lambda\operatorname{tr}(\mathbf{H}) \cdot \operatorname{tr}(\delta\mathbf{H})) \right) \mathrm{d}V$$
$$= \int_\Omega \mathbf{b} \cdot \delta\mathbf{u}\, \mathrm{d}V + \int_{\Gamma_1} \bar{\mathbf{t}}^1 \cdot \delta\mathbf{u}\, \mathrm{d}A + \int_{\Gamma_1} \bar{\mathbf{t}}^2 \cdot \delta\nabla_{\mathbf{n}}\mathbf{u}\, \mathrm{d}A, + \int_\Xi \bar{\mathbf{t}}^3 \cdot \delta\mathbf{u}\, \mathrm{d}L, \tag{4.53}$$

and represents the weak form of the mechanical part. Furthermore, cf Eq. (3.47),

$$\int_\Omega \left[\frac{\dot{s}}{M}\delta s + 2\,\mathcal{G}_{\text{c}}\epsilon\,\nabla s\,\delta\nabla s + \left(s\left(\mathbf{E} : [\mathbb{C}\,\mathbf{E}] + l^2\mathbf{H} \mathbin{\vdots} \nabla[\mathbb{C}\,\mathbf{E}] \right) + \frac{\mathcal{G}_{\text{c}}(s-1)}{2\epsilon} \right)\delta s \right] \mathrm{d}V$$
$$= \int_{\Gamma_2} q_{\text{n}}\,\delta s\, \mathrm{d}A,$$

provides the weak form for the phase-field parameter. The approximation of the displacement field $\mathbf{u}$ and its variation $\delta\mathbf{u}$ were defined in the last section. Keeping the single notation introduced in the previous section, for the scalar-valued phase-field s and its variation δs, we have

$$s := \sum_I \bar{s}_I R_I, \qquad \delta s := \sum_I \delta\bar{s}_I R_I, \tag{4.54}$$

where s_I represents the phase-field value of the control point I. We further define the gradient of the phase-field by

$$\nabla s := \sum_{I=1}^n [\boldsymbol{B}_I^s]\,\bar{s}_I, \qquad [\boldsymbol{B}_I^s] := \begin{bmatrix} R_{I,1} \\ R_{I,2} \end{bmatrix}. \tag{4.55}$$

In the absence of external forces, the residual matrix for the control point I derived from Eqs. (3.45) and (3.47) is

$$\left[\hat{\mathbf{P}}_I\right] = \begin{bmatrix} \hat{\mathbf{P}}_I^{\mathbf{u}} \\ \hat{P}_I^s \end{bmatrix} = \int_\Omega \begin{bmatrix} s^2\left([\boldsymbol{B}_I^{\mathbf{u}}]^{\mathrm{T}}\,\underline{\boldsymbol{C}\boldsymbol{E}} + l^2\sum_{k=1}^2 \left(\left[\frac{\partial\boldsymbol{B}_I^{\mathbf{u}}}{\partial x_k}\right]^{\mathrm{T}}\underline{\boldsymbol{C}\boldsymbol{H}}_k \right) \right) \\ R_I\frac{\dot{s}}{M} + 2\mathcal{G}_{\text{c}}\epsilon\,[\boldsymbol{B}_I^s]^{\mathrm{T}}\,\nabla s + \\ R_I\left(s\left(\underline{\boldsymbol{E}}^{\mathrm{T}} \cdot (\underline{\boldsymbol{C}\boldsymbol{E}}) + l^2\sum_{k=1}^2 (\underline{\boldsymbol{H}}_k^{\mathrm{T}} \cdot \underline{\boldsymbol{C}\boldsymbol{H}}_k) \right) + \frac{\mathcal{G}_{\text{c}}(s-1)}{2\epsilon} \right) \end{bmatrix} \mathrm{d}V. \tag{4.56}$$

As we use the Newton-Raphson method to solve the problem (see Sect. 3.2.6.2), linearization of the residual is required. We define the tangent matrix for the control point pair IJ to be

$$\hat{\mathbf{S}}_{IJ} = d_1 \hat{\mathbf{K}}_{IJ} + d_2 \hat{\mathbf{D}}_{IJ} = d_1 \left(\frac{\partial \hat{\mathbf{P}}_I}{\partial \boldsymbol{\alpha}_J} \right) + d_2 \left(\frac{\partial \hat{\mathbf{P}}_I}{\partial \dot{\boldsymbol{\alpha}}_J} \right), \tag{4.57}$$

where $\hat{\mathbf{K}}_{IJ}$ denotes the stiffness matrix, $\hat{\mathbf{D}}_{IJ}$ is the damping matrix, d_1 and d_2 represent the multipliers derived from the time integrator (in our case, the Backward Euler scheme), and $\boldsymbol{\alpha}_J$ and $\dot{\boldsymbol{\alpha}}_J$ are the vectors of degrees of freedom and their derivatives with respect to time for the control point J, respectively. Consequently, the stiffness matrix can be written as

$$\left[\hat{\mathbf{K}}_{IJ} \right] = \int_\Omega \begin{bmatrix} \hat{\mathbf{K}}_{IJ}^{\mathbf{uu}} & \hat{\mathbf{K}}_{IJ}^{\mathbf{us}} \\ \hat{\mathbf{K}}_{IJ}^{\mathbf{su}} & \hat{K}_{IJ}^{ss} \end{bmatrix} \mathrm{d}V, \text{ with}$$

$$\hat{\mathbf{K}}_{IJ}^{\mathbf{uu}} = s^2 \left([\boldsymbol{B}_I^{\mathbf{u}}]^{\mathrm{T}} \underline{\boldsymbol{C}} \, [\boldsymbol{B}_J^{\mathbf{u}}] + l^2 \left(\sum_{k=1}^2 \left[\frac{\partial \boldsymbol{B}_I^{\mathbf{u}}}{\partial x_k} \right]^{\mathrm{T}} \underline{\boldsymbol{C}} \left[\frac{\partial \boldsymbol{B}_J^{\mathbf{u}}}{\partial x_k} \right] \right) \right),$$

$$\hat{\mathbf{K}}_{IJ}^{\mathbf{us}} = 2s \left([\boldsymbol{B}_I^{\mathbf{u}}]^{\mathrm{T}} \underline{\boldsymbol{C}} \boldsymbol{E} + l^2 \left(\sum_{k=1}^2 \left[\frac{\partial \boldsymbol{B}_I^{\mathbf{u}}}{\partial x_k} \right]^{\mathrm{T}} \underline{\boldsymbol{C}} \boldsymbol{H}_k \right) \right) R_J, \tag{4.58}$$

$$\hat{\mathbf{K}}_{IJ}^{\mathbf{su}} = 2s R_I \left((\underline{\boldsymbol{C}} \boldsymbol{E})^{\mathrm{T}} [\boldsymbol{B}_J^{\mathbf{u}}] + l^2 \left(\sum_{k=1}^2 (\underline{\boldsymbol{C}} \boldsymbol{H}_k)^{\mathrm{T}} \left[\frac{\partial \boldsymbol{B}_J^{\mathbf{u}}}{\partial x_k} \right] \right) \right),$$

$$\hat{K}_{IJ}^{ss} = 2\mathcal{G}_{\mathrm{c}} \epsilon \, [\boldsymbol{B}_I^s]^{\mathrm{T}} [\boldsymbol{B}_J^s] + R_I \left(\underline{\boldsymbol{E}}^{\mathrm{T}} \cdot \underline{\boldsymbol{C}} \boldsymbol{E} + l^2 \sum_{k=1}^2 (\underline{\boldsymbol{H}}_k^{\mathrm{T}} \cdot \underline{\boldsymbol{C}} \boldsymbol{H}_k) + \frac{\mathcal{G}_{\mathrm{c}}}{2\epsilon} \right) R_J.$$

Finally, the damping matrix has the form

$$\left[\hat{\mathbf{D}}_{IJ} \right] = \int_\Omega \begin{bmatrix} \mathbf{0} & \mathbf{0} \\ \mathbf{0} & \frac{1}{M} R_I R_J \end{bmatrix} \mathrm{d}V. \tag{4.59}$$

4.3.2 Fourth-Order Phase-Field Fracture Model

Considering the weak form derived in Chapter 3, we have, cf. Eq. (3.49)

$$\int_\Omega \left[\frac{\dot{s}}{M} \delta s + \mathcal{G}_{\mathrm{c}} \left(\epsilon \nabla s \, \delta \nabla s + \frac{\epsilon^3}{2} \Delta s \, \delta \Delta s \right) \right.$$
$$\left. + \left(s \big(\mathbf{E} : [\mathbb{C} \, \mathbf{E}] + l^2 \mathbf{H} \therefore \nabla [\mathbb{C} \, \mathbf{E}] \big) + \frac{\mathcal{G}_{\mathrm{c}}(s-1)}{2\epsilon} \right) \delta s \right] \mathrm{d}V = \int_{\Gamma_2} q_{\mathrm{n}} \, \delta s \, \mathrm{d}A,$$

which needs to be discretized. Taking the same steps as presented in Sect. 4.3.1, we obtain the discretized form of the fourth-order formulation. Indeed, most of the terms are similar to the case of the second-order model. Therefore, we only repeat selected steps that are different from the previous derivation. We define the Laplacian of s as

$$\Delta s := \sum_{I=1}^n \sum_{k=1}^2 \left[\frac{\partial^2 R_I}{\partial x_k^2} \right] \bar{s}_I, \tag{4.60}$$

and the residual matrix becomes

$$
\left[\hat{\mathbf{P}}_I\right] = \begin{bmatrix} \hat{\mathbf{P}}^{\mathbf{u}}_I \\ \hat{P}^s_I \end{bmatrix} = \int_\Omega \left[\begin{array}{c} s^2 \left([\boldsymbol{B}^{\mathbf{u}}_I]^{\mathrm{T}}\,\underline{\boldsymbol{C}}\underline{\boldsymbol{E}} + l^2 \left(\sum_{k=1}^2 \left[\frac{\partial \boldsymbol{B}^{\mathbf{u}}_I}{\partial x_k}\right]^{\mathrm{T}}\underline{\boldsymbol{C}}\underline{\boldsymbol{H}} \right) \right) \\[2ex] R_I \frac{\dot{s}}{M} + \mathcal{G}_{\mathrm{c}} \left(\epsilon\,[\boldsymbol{B}^s_I]^{\mathrm{T}}\,\nabla s + \frac{\epsilon^3}{2} \left(\sum_{k=1}^2 \frac{\partial^2 R_I}{\partial x_k^2} \right) \Delta s \right) \\[2ex] + R_I \left(s \left(\boldsymbol{E}^{\mathrm{T}}\cdot (\underline{\boldsymbol{C}}\underline{\boldsymbol{E}}) + l^2 \sum_{k=1}^2 \left(\underline{\boldsymbol{H}}_k^{\mathrm{T}}\cdot\underline{\boldsymbol{C}}\underline{\boldsymbol{H}}_k \right) \right) + \frac{\mathcal{G}_{\mathrm{c}}(s-1)}{2\epsilon} \right) \end{array} \right] \mathrm{d}V.
$$

(4.61)

For the stiffness matrix, only the K^{ss}_{IJ} component in Eq. (4.58) changes:

$$
\hat{K}^{ss}_{IJ} = \mathcal{G}_{\mathrm{c}} \left(\epsilon\,[\boldsymbol{B}^s_I]^{\mathrm{T}}\,[\boldsymbol{B}^s_J] + \left(\sum_{k=1}^2 \frac{\partial^2 R_I}{\partial x_k^2} \right) \left(\sum_{k=1}^2 \frac{\partial^2 R_J}{\partial x_k^2} \right) \right)
$$
$$
+ R_I \left(\underline{\boldsymbol{E}}^{\mathrm{T}}\cdot\underline{\boldsymbol{C}}\underline{\boldsymbol{E}} + l^2 \sum_{k=1}^2 \left(\underline{\boldsymbol{H}}_k^{\mathrm{T}}\cdot\underline{\boldsymbol{C}}\underline{\boldsymbol{H}}_k \right) + \frac{\mathcal{G}_{\mathrm{c}}}{2\epsilon} \right) R_J\,.
$$

(4.62)

With this, we are done with deriving the discrete forms of the governing equations. In the next chapter, the performance of the aforementioned models will be investigated using different geometries and loading conditions.

5 Results and Discussion

In this section, the numerical results obtained using the different models introduced in the previous chapters are presented. All the models are implemented as user elements into the Finite Element Analysis Program (FEAP) and its IGA add-on (igaFEAP) [207], which is developed based on the Bézier extraction method [204]. For the three-dimensional strain gradient model, an additional subroutine was written to determine the global second-order derivatives of the basis functions. The details for the calculation of global second- and third-order derivatives of the basis functions can be be found in [26] and in Appendix A of the current work.

This chapter is structured as follows: In the first section, the ability of the strain gradient elasticity models to regularize the strain energy density field near the singular zones is investigated. We first start with a three-dimensional model (Reiher's model) and show that a first-strain gradient model is indeed sufficient to overcome the stress singularity caused by line displacements (or loads). Moreover, the superiority and higher efficiency of the isogeometric analysis over the conventional finite element approaches in solving higher-order problems is demonstrated. Then, the same conclusion will be achieved for the GRADELA model by Aifantis in a two-dimensional plane strain case, this time for a point displacement boundary condition. After that, the phase-field fracture models, coupled with the strain gradient theory, are investigated in the second section of this chapter. The results obtained from the classical phase-field models of fracture are compared with the ones from the proposed enhanced models and a detailed discussion on the strain energy density and individual stress components is provided.

5.1 Strain Gradient Elasticity

5.1.1 Reiher's Model

We start the section by simulating the behavior of a cube under an edge displacement boundary condition. In such a case, as discussed in the previous chapters, a first-strain gradient stored elastic energy is sufficient to overcome the problem of singularity of the strain energy density. Figure 5.1 shows the model size and the applied boundary conditions. The bottom surface is completely fixed in all directions. A uniform line displacement of magnitude $0.05\,\mathrm{mm}$ in x_1-direction has been prescribed, while the movement in x_3-direction is suppressed (producing a kind of shear test). In all the following studies, the material properties from Reiher et al. [25] have been used: $\lambda = 1.0\,\mathrm{MPa}, \mu = 0.08\,\mathrm{MPa}$, and $\lambda_{1_\mathrm{real}} = 0.04\,\mathrm{N}$.

A mesh convergence study has been done to verify the method and determine its robustness compared to the conventional finite element method. The results are presented in Fig. 5.2. Trivariate cubic (tri-cubic, i.e., $p = q = r = 3$) NURBS elements (C^2-continuous across elements/knot spans) and hexahedral cubic Lagrangian elements are chosen for the isogeometric analysis and the finite element method, respectively. Uniform meshes are used for the study, starting from only one element for the first model, then two elements in each
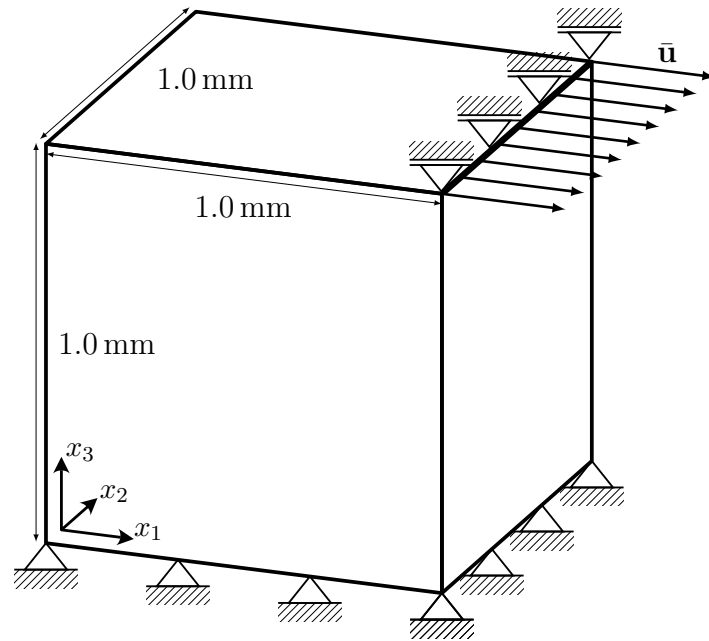
Figure 5.1: Model size and applied boundary conditions for Reiher's model
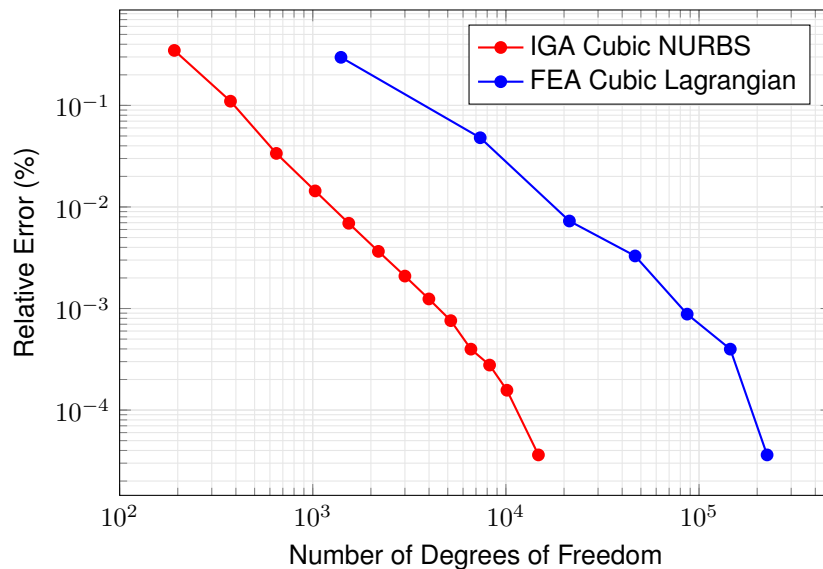
Figure 5.2: Mesh convergence study results for Reiher's model. The plot shows the strain energy relative error for the case of cubic NURBS and Lagrangian finite elements.

direction (i.e., total number of 8 elements), and so on. The significant difference between the total number of degrees of freedom (DOFs) of one NURBS element ($=192$) versus one hexahedral cubic Lagrange element ($=1400$) is because of the usage of Lagrange multipliers in the finite element simulation. In IGA, there are only three degrees of freedom, belonging to the displacement field, per control point, whereas, in the finite element analysis (FEA), apart from the primary displacement field, auxiliary degrees of freedom are involved. Since the classical cubic finite elements are C^0-continuous, additional degrees of freedom need to be introduced for each second-gradient term, i.e., components of the third-order tensor $\mathbf{H}$, per node. Moreover, another set of degrees of freedom are required for the Lagrange multipliers to establish constraints between the displacement and the second-gradient DOFs,

i.e., $\mathbf{H} - \nabla(\nabla \mathbf{u}) = 0$, which leads to a significant increase in the number of DOF of the final element in comparison to a classical cubic Lagrange element. Moreover, comparing the discretizations with more than one element, tri-cubic C^2-continuous NURBS models will always have less number of DOFs than their C^0-continuous FEM counterparts.

Looking at the results in Fig. 5.2, IGA shows a slightly better convergence rate, probably because of the higher regularity. There is an offset between IGA and FEM results, which is due to the less number of DOFs per element for the NURBS discretizations. Figure 5.3 depicts the strain energy density for a $13 \times 13 \times 13$ model. Taking a very fine tri-quartic NURBS mesh results as the reference value for the total elastic strain energy of the body, Table 5.1 compares the results for different kinds of basis functions. IGA results show significantly shorter analysis times compared to the FEM. Although the number of degrees of freedom is significantly lower using tri-quartic NURBS elements, the elapsed time is almost the same as the tri-cubic NURBS. The reason appears to be the difference in the quadrature order. While the required quadrature order for the cubic NURBS basis is 4 (64 quadrature points per element), 5 is needed for the quartic mesh (thus, 125 quadrature points per element), which considerably increases the computational time. The non-efficiency of the higher-order elements due to the cost of quadrature is a well-known problem in the FEM community and many researchers have proposed approaches to overcome this issue (see, for instance, [208] and [209]). Since dealing with the quadrature methods is out of the present work's scope, we refer the interested reader to the mentioned articles and [210].

Although the obtained results are promising, the problem with Reiher's model is that there is no straightforward way to calculate the gradient material parameter $\lambda_{1_{\mathrm{real}}}$. A thorough parameter study based on the classical and gradient strain energies is needed for each set of geometry and material to find the proper material coefficients, making it difficult to exploit the
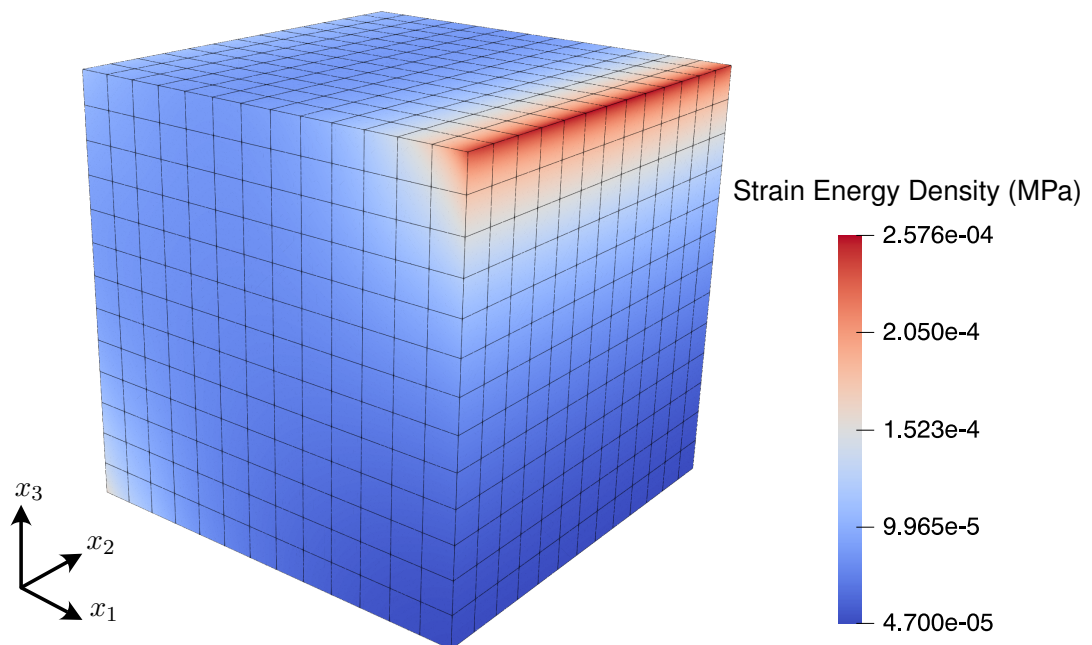
Figure 5.3: Results for a cube under an applied line displacement (deformed shape). A $13 \times 13 \times 13$ elements cube (cubic NURBS)

Table 5.1: Comparison between IGA and FEA results

Basis	Order	Elapsed Time	No. of DOF	Total Elastic Strain Energy
Lagrangian (FEA)	Cubic	$430.0\,\text{s}$	225104	$8.291583\text{e}{-}05\,\text{N.mm}$
NURBS (IGA)	Cubic	$20.0\,\text{s}$	14739	$8.291579\text{e}{-}05\,\text{N.mm}$
NURBS (IGA)	Quartic	$20.3\,\text{s}$	3993	$8.291577\text{e}{-}05\,\text{N.mm}$

[†] The CPU times are calculated on an Intel® Core™ i7-4790 at $3.60\,\text{GHz}$ clock speed with $32.0\,\text{GB}$ of memory (DDR3-$1600\,\text{MHz}$) running Microsoft Windows 10 Pro (64-bit) for the finite element method results and Ubuntu 16.04 LTS (64-bit) for the isogeometric analysis results.
[†] The Intel® Pardiso sparse solver has been used for all the simulations.

model for general purposes. Nevertheless, it is a very simple model showing the efficiency of the strain gradient theories to overcome the problem of singular stress fields, considering only one of the five gradient material coefficients of the original theory.

5.1.2 Aifantis' Model

The simplified model proposed by Aifantis and co-workers, on the other hand, makes the usage of the gradient theory much simpler by defining a length-scale parameter and using the Lamé constants for the gradient part of the stored energy as well. In this section, we first show this model's ability to regularize the singular stress fields in two-dimensional settings. This reduction of the problem's dimensionality is to validate our assumption that the first-strain gradient model is capable of regularizing the singular stress fields caused by application of point load/displacement boundary conditions. In the final section of this chapter, we will exploit the same model to investigate the fracture process in brittle materials.

Let us take the $1 \times 1\,\text{mm}^2$ square shown in Fig. 5.4 as the geometry. The displacement in x_1-direction is constrained on the right edge of the model. On the bottom edge, from $x_1 = 0.25\,\text{mm}$ to $x_1 = 1.0\,\text{mm}$, all the displacements in x_2-direction are constrained as well. For the material properties, we adopt the Lamé constants from [211], namely we have $\lambda = 50727.5\,\text{MPa}$ and $\mu = 46825.4\,\text{MPa}$. Moreover, a displacement boundary condition with the magnitude of $u_2 = 0.01\,\text{mm}$ is applied on the top edge. As we will see in the next chapter, this amount of applied displacement is enough for a crack to start propagating in this model. The discontinuous Dirichlet boundary condition in the bottom of Fig. 5.4 resembles a crack tip in the structure. Therefore, we predict to have a singular response on this point using the classical continuum mechanics theory. Our goal here is to show that a first-strain gradient model, such as the one introduced by Aifantis and his co-workers, is sufficient to overcome the problem of singularity in this case. Since we have reduced our model from a three-dimensional one to a two-dimensional plane strain model, in the same way, one can assume that the line displacements/loads will be reduced to point displacement/loads. Therefore a body equipped with second displacement gradients should be able to sustain this kind of loading.

Figure 5.5 shows the results for different values of the length-scale parameter l. All the studies are done on a bi-quadratic C^1-continuous NURBS surface, i.e., $p = q = 2$. Three different discretizations have been considered for this study. A relatively coarse mesh consisting of $84 \times 85\,(h \approx 0.012\,\text{mm})$ control points. A finer $193 \times 194\,(h \approx 0.005\,\text{mm})$ control points mesh
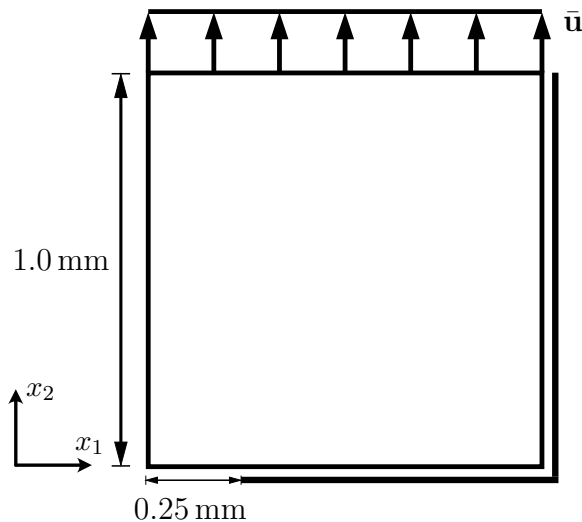
Figure 5.4: Geometry and boundary conditions for the pure gradient elasticity (without phase-field fracture) simulation model

and finally we have the finest mesh with $408 \times 409 \, (h \approx 0.002 \, \text{mm})$ control points, where h denotes the mesh size defined as the maximum distance between two adjacent control points in each parametric direction. For the strain gradient models, a mesh is sufficiently fine if the mesh size is smaller than the length-scale parameter so that the mesh can capture the so-called size effects. This requirement is fulfilled for all the studies performed, except for the case of $l = 0.01$ with the 84×85 mesh. Here, we focus on the classical part of the strain energy density (ψ_e) and study the convergence of its maximum and minimum values, which always occur in front of the crack tip, i.e., the region close to the point $(0.25, 0)$. Before we start with discussing the results, it should be noted that we expect the strain energy density to be always positive for this material throughout the computational domain. However, since we are using NURBS as basis functions, whenever a sudden jump in the results happen, it results in the Gibbs phenomenon [212, 213], causing oscillations and, consequently, negative values in the interpolated results. This behavior is discussed in more detail in the following sections. Moreover, $l = 0$ recovers the classical Cauchy theory. For this case, as expected, the results show an exponential growth for finer meshes, and no convergence is in prospect which is an obvious sign of singularity. There is also a significant amount of negative strain energy density that is unacceptable and increases exponentially for the refined meshes. On the other hand, the strain gradient models ($l > 0$) show a different behavior; namely, all the results tend to converge even for minimal values of the length-scale parameter. It is also to conclude that all the chosen discretizations are fine enough and in the converged zone, following the results from the previous chapter (see Fig. 5.2). Moreover, the minimum strain energy density is positive and close to zero for all models, which shows that there are no sudden jumps in the results. There is one exception here, where the minimum strain energy density is negative for $l = 0.01$ and the 84×85 mesh, but one should note that this mesh is not sufficiently fine for this value of the length-scale parameter. Figures 5.6 and 5.7 depict the strain energy density fields for two different values of the length-scale parameter. Based on these results, it can be concluded that the simplified model introduced by Aifantis can be used to overcome the problem of singularity for the plane strain two-dimensional case. It should be noted that the same conclusion was proposed by Niiranen et al. [63].
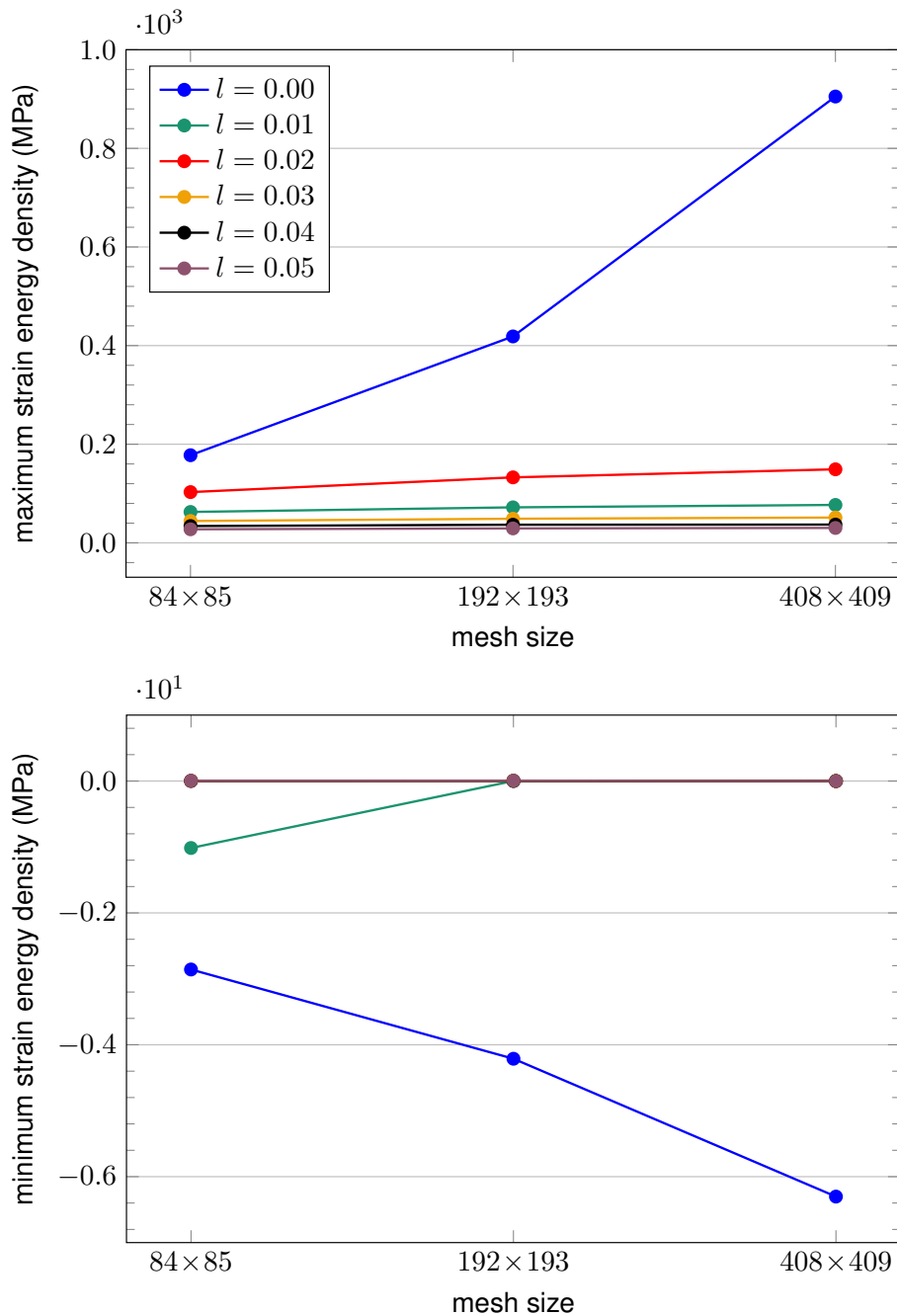
Figure 5.5: Mesh convergence study results for Aifantis' model (above: maximum strain energy density, below: minimum strain energy density)

5.2 Phase-Field Fracture Models

For all the following numerical simulations, we use a square geometry and plane strain assumptions. Keep in mind that we have chosen this academic benchmark problem on purpose to clearly observe the effects of the singularity, which are not fully eliminated by the phase-field approach alone. The size of the model is $1\,\mathrm{mm} \times 1\,\mathrm{mm}$. We take the left-bottom corner of the square as the origin of the coordinate system. As for boundary conditions, the movement of the control points at the bottom edge of the plane is constrained in x_2-direction. Moreover, the control points belonging to the right edge are fixed in x_1-direction, and a uniform line displacement of $\bar{u}_y = 0.1\,\mathrm{mm}$ is acting on the top edge and is applied in a
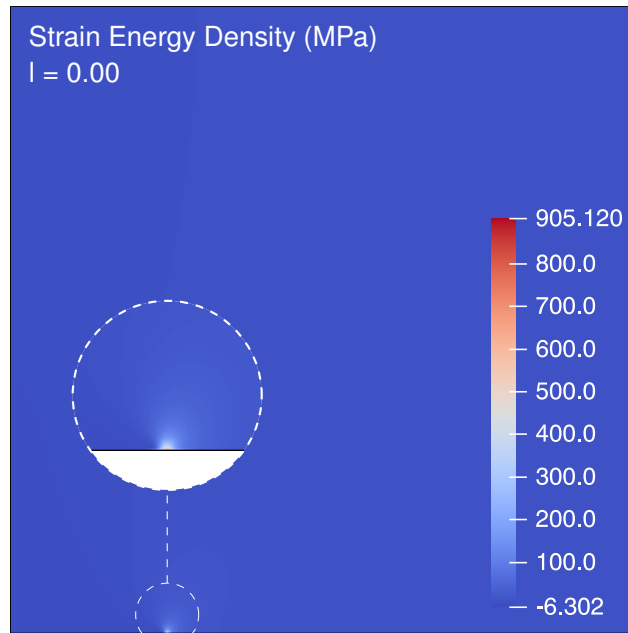
Figure 5.6: Classical strain energy density (ψ_e) distribution for the classical continuum mechanics theory ($l = 0$)
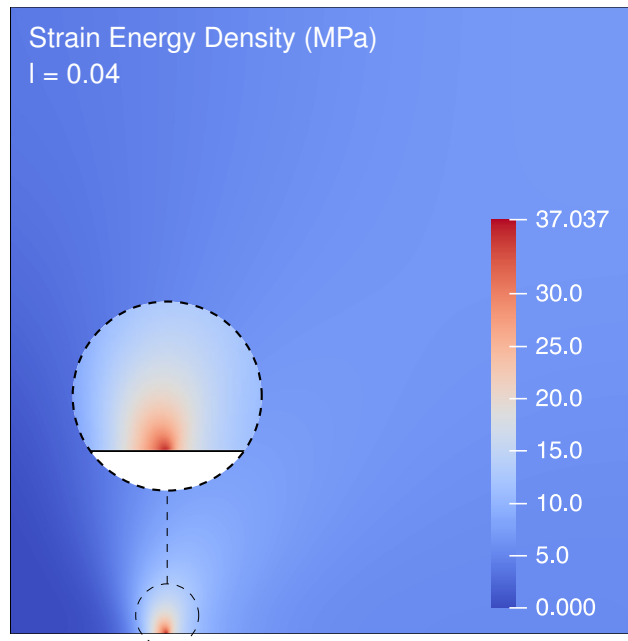
Figure 5.7: Classical strain energy density (ψ_e) distribution for the strain gradient theory ($l = 0.04$)

quasi-static manner. We introduce a pre-existing crack by initializing the phase-field itself. The initial crack length is $0.25\,\mathrm{mm}$ and is located in the middle of the plane, starting from the left edge (see Fig. 5.8). The material properties used are the same as in the previous chapter, i.e., $\lambda = 50727.5\,\mathrm{MPa}$, $\mu = 46825.4\,\mathrm{MPa}$, $\mathcal{G}_c = 2.0\,\mathrm{N/mm}$, and $M = 2000.0\,\mathrm{^1/_{MPa \cdot s}}$ [211]. The interphase width (the length-scale parameter for the phase-field) is chosen as $\epsilon = 0.02\,\mathrm{mm}$. Bi-quadratic NURBS with full integration (9 quadrature points per element) are used as it is the lowest degree which provides C^1-continuity needed for the fourth-order formulations. There are three different meshes with uniform subdivisions (equidistant inner
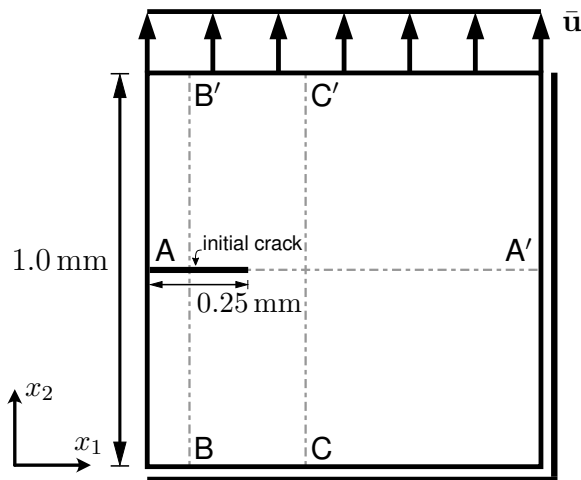
Figure 5.8: Boundary conditions and the initial crack for the phase-field fracture simulations

knots) of 84×85, 192×193, and 408×409 control points chosen as coarse, normal, and fine meshes, respectively. The number of control points in each parametric direction is chosen so that there will always be a control point at the position $(x_1, x_2) = (0.25, 0.50)$ where the initial crack tip is located. The results are verified using a similarly refined (i.e., almost with the same number of control points as the fine quadratic mesh) bi-quartic ($p = q = 4$) C^3-continuous NURBS model. At this point, we remind the reader that the same discretizations were used in the previous section, and therefore it is safe to assume that all the meshes are sufficiently fine for the upcoming simulations.

For each model, we define the initial crack as a Dirichlet boundary condition. This procedure ensures that the initial crack does not heal and, at the same time, reduces the total number of equations to be solved. At the beginning of the simulation, a static-analysis step is performed in the absence of mechanical loads to regularize the crack phase-field (see [170]).

In order to facilitate the comparability of the results, we evaluate them when the peak of the strain energy density (near the crack front) reaches the line $x = 0.65\,\mathrm{mm}$. Figure 5.9 shows the contour plots for the phase-field parameter s for the second- and the fourth-order crack models at this state, side by side.

5.2.1 Post-Processing of NURBS Results

Before we continue, a short remark on the visualization of NURBS results ought to be given. Most of the widely-used post-processing (FEM) software tools do not support splines to visualize the results, and ParaView [214], which is our software of choice for post-processing, is not an exception. One popular workaround to visualize IGA results using current post-processing tools is to first construct a standard FE mesh based on low-order Lagrange elements and to map the results on this visualization mesh (see, for instance, [215]). This FE model is usually based on a *linear* approximation of the geometry, and each isogeometric element is subdivided into a number of these linear elements depending on the desired accuracy. Although this method has been proven to yield an acceptable approximation of the original mesh, because of the dissimilar positions of the control points/nodes, and also different continuities of the original and the visualization mesh, most often, it is not possible to obtain the exact values in the post-processing stage (the projected values are very close, but not exactly the same as the values on the NURBS entity). That being said,
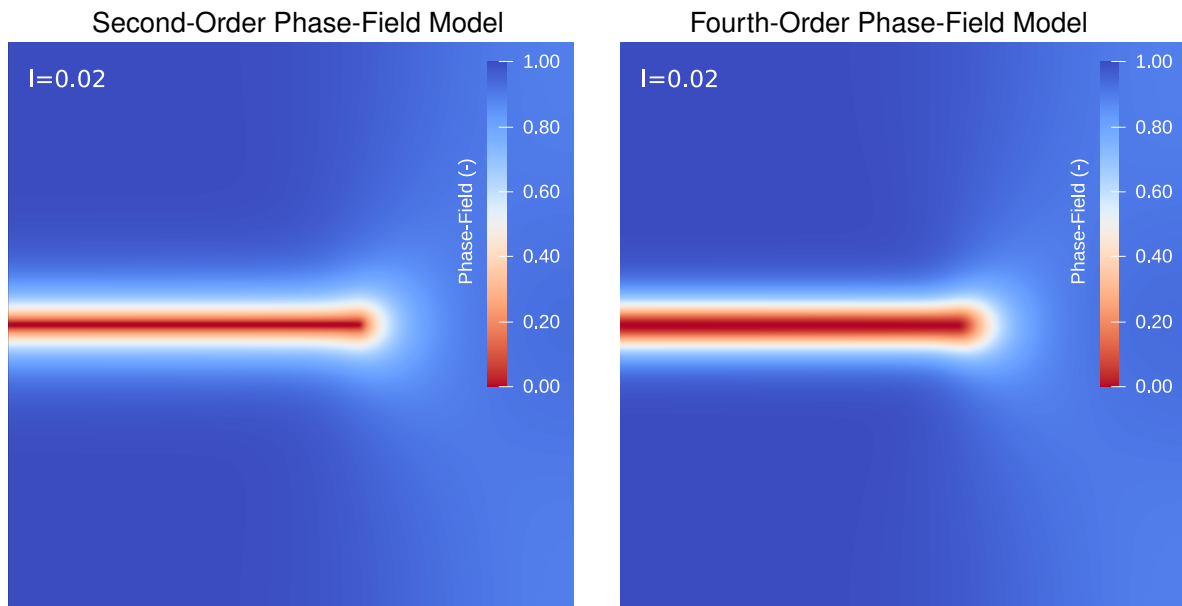
Figure 5.9: Phase-field contours for the second- and the fourth-order crack models based on gradient elasticity

we have extended this approximation to *quadratic* FE elements in order to be closer to the original NURBS models [216]. There is still a problem of non-matching continuity, i.e., our quadratic NURBS model is C^1-continuous while the FEM model exhibits only C^0-continuity, which results in different positions of the control points/nodes. Therefore, it is not surprising that in the following figures, although we are plotting the values on the line $y = 0.5\,\mathrm{mm}$, and we expect the strain energy density and the phase-field to be exactly zero at least in the region of the initial crack, this is not the case. In fact, there is almost no point in the projected mesh where the phase-field has a value of exactly zero (even at the beginning of the analysis). Here, one should note the non-interpolatory nature of NURBS control variables as well. Fortunately, this does not result in difficulties in post-processing as we always use the same meshes (NURBS/FEM) to visualize the results for classical and gradient theories, and we *compare* these projected results. For better comprehension, the reader is referred to Fig. 5.10, where the results from ParaView (PP data) and the control points (CP data) are illustrated. Moreover, the effective strain energy density ($s^2\,\psi_\mathrm{e}$) at $y = 0.5\,\mathrm{mm}$ is not zero even in the NURBS data (control variables). It is due to another projection error (local least squares method [217]), where the energy values and the phase-field are projected from quadrature points to the NURBS control points.

5.2.2 Strain Energy Density Analysis

5.2.2.1 Classical Model

We start by studying the results of the classical Cauchy continuum theory ($l = 0.0$). Figures 5.11 and 5.12 depict the simulation results based on the second- and the fourth-order formulations, respectively. The results are plotted along the three paths illustrated in Fig. 5.8. Path A-A′ is along the initial crack direction and shows the path that we expect the crack to grow in. Paths B-B′ and C-C′ are perpendicular to the path A-A′, and they are located at the distances $0.1\,\mathrm{mm}$ and $0.4\,\mathrm{mm}$ from the left edge, respectively. The difference between B-B′ and C-C′ is that the first path is located where we constrain the crack using Dirichlet
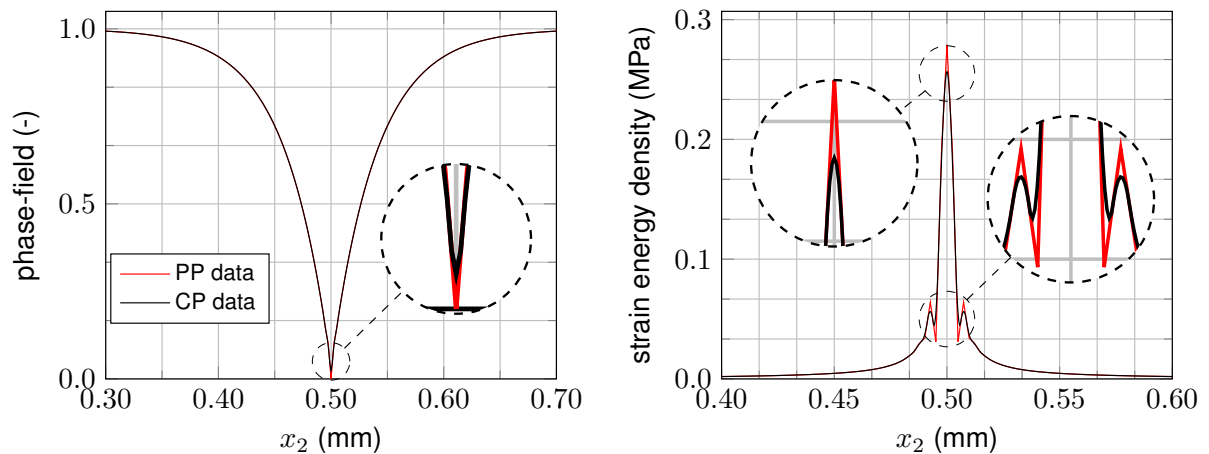
Figure 5.10: Comparison between the visualization mesh (post-processing data) and the direct results from the IGA mesh (control points data) for the phase-field (left), and the strain energy density (right). The results are shown for a quadratic NURBS with $408{\times}409$ control points and demonstrate the values for the second-order formulation on the line $x = 0\,\mathrm{mm}$ at the time $0.005\,\mathrm{s}$ with $l = 0.0$.

boundary conditions (resulting in exactly zero values for the phase-field, initial crack position) while the latter path does not intersect a region with prescribed values. The left column depicts the phase-field values, while the right one displays the degraded strain energy density $s^2\,\psi_{\mathrm{e}}$. The results are shown for three different meshes. Studying the results presented in Fig. 5.11, the coarse mesh (green dashed line) certainly does not perform well. Along Path A-A$'$, the oscillations in the phase-field and the energy plots are due to a zigzag behavior in the crack movement at the beginning of the propagation (the mesh is simply not fine enough). It coincides with the shifts observed along Paths B-B$'$ and C-C$'$. The value we are most interested in is the value of the energy at the crack tip, roughly $15.0\,\mathrm{MPa}$ for the coarse mesh. The finer meshes perform much better and exhibit some kind of convergence for the phase-field values (see the left column of Fig. 5.11). However, studying the results for Path A-A$'$, it is clear that refining the mesh increases the maximum strain energy density value. This particular behavior is usually considered to be a sign of the existence of a singularity in the results. Evaluating the results for Paths B-B$'$ and C-C$'$, three crucial observations are made:

- The results are plotted when the crack has passed both Paths B-B$'$ and C-C$'$, meaning that the material is broken. Consequently, the existence of relatively high energy density values (roughly $2.0\,\mathrm{MPa}$) does not have a physical meaning.

- Refining the mesh changes the distribution of the energy density in the vicinity of the crack zone, leading to a high concentration of strain energy density for finer meshes suggesting that the anomalies are mesh sensitive.

- There are considerable negative strain energy density values because of oscillations in the crack zone's vicinity. Here, Runge's phenomenon (similar to Gibbs' phenomenon in Fourier-series approximations) is observed because of a sudden jump in the value of the strain energy density. It is shown in [212] and [213] that the phenomenon also appears for splines with equidistant interpolation points, which is the case in our examples. It should be noted that the implemented user element in igaFEAP always checks the value of the (effective) strain energy density on the quadrature point level for positivity, i.e., the simulation will be aborted if the subroutine finds negative values
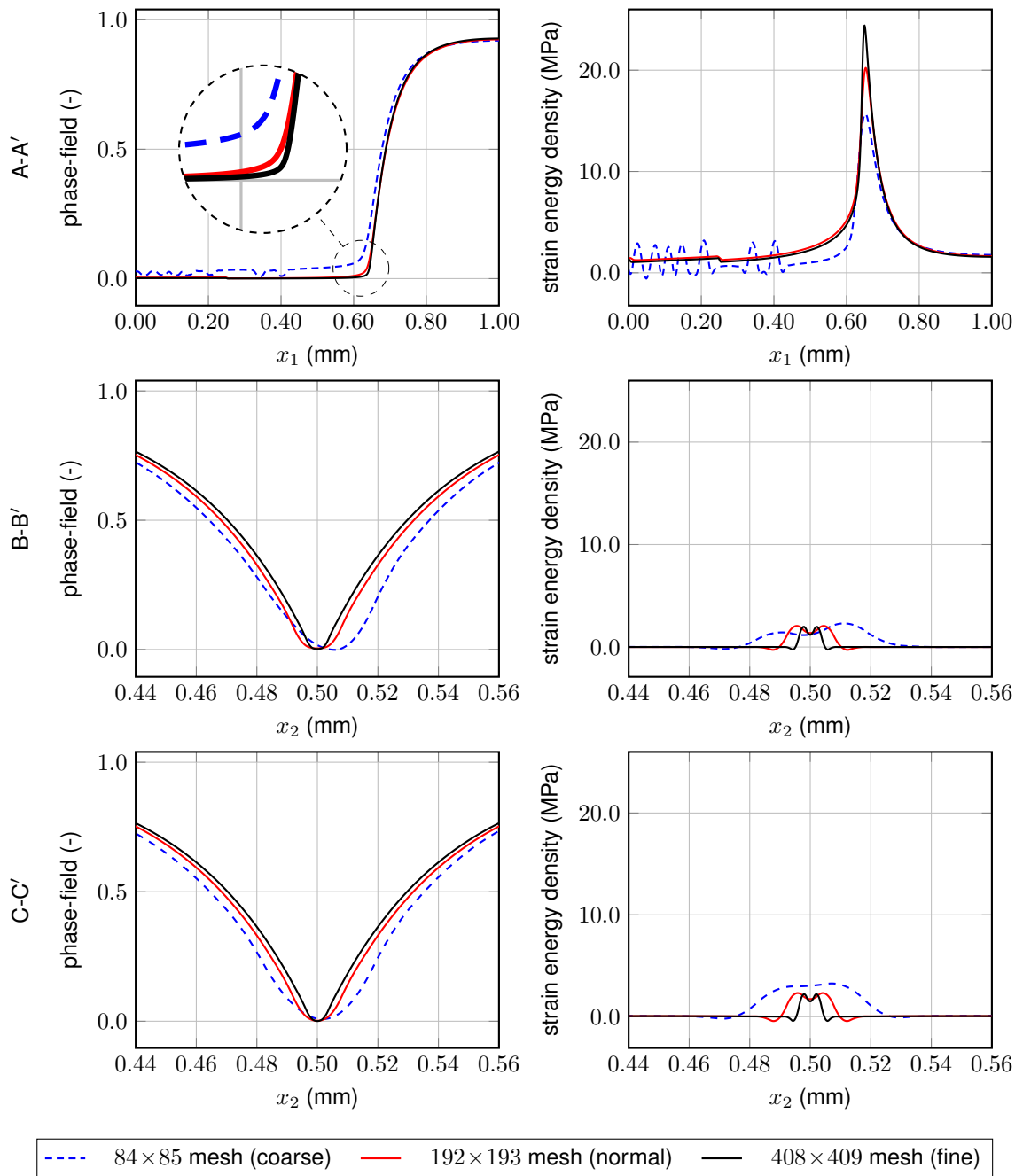
Figure 5.11: Results for the classical second-order phase-field theory (coupled with linear elasticity) for different mesh sizes. Distributions of the phase-field (left), and the strain energy density (right) along three different cross-sections in the plane.
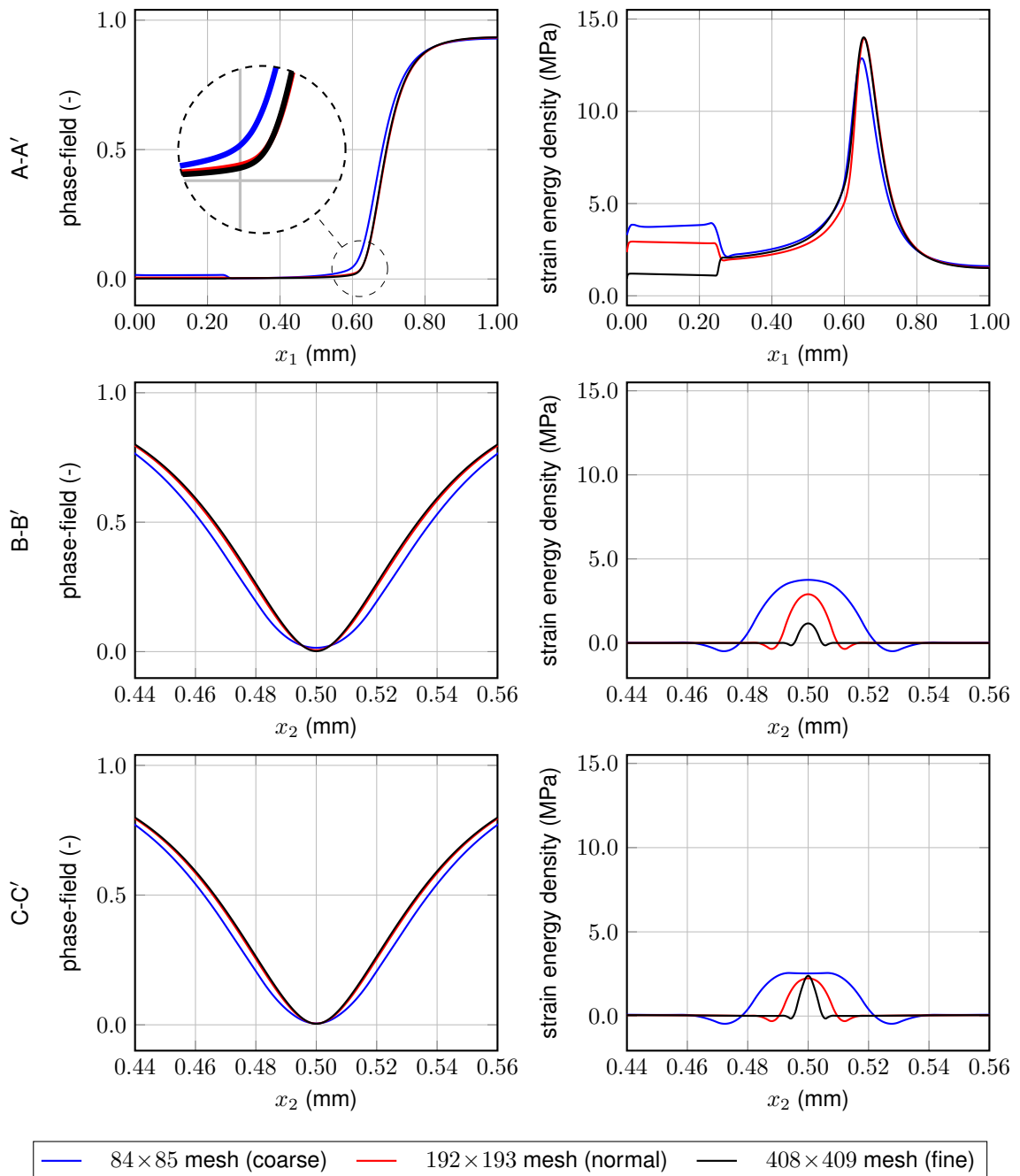
Figure 5.12: Results for the classical fourth-order phase-field theory (coupled with linear elasticity) for different mesh sizes. Distributions of the phase-field (left), and the strain energy density (right) along three different cross-sections in the plane.

of energy density on the quadrature points. This means that the negative values on the strain energy density plots are merely because of the interpolation procedure and existence of sudden jumps in the results.

We have already observed a similar behavior around the pointwise boundary conditions in three-dimensional problems in the existence of a singularity (see [26], Fig. 9). The effect of this phenomenon can be mitigated by refining the mesh, which is, in fact, the reason why the domain of oscillation reduces in finer meshes in Fig. 5.11. The crucial message that needs to be highlighted here is that the existence of this jump in the energy is unphysical in the first place. Almost all of the above assertions also hold for the results depicted in Fig. 5.12 for the fourth-order formulation. Although the results for Path A-A' show a kind of convergence for the maximum strain energy density, the behavior is different behind the crack tip for different mesh sizes. Moreover, the localization of the strain energy density is observable in the results for Paths B-B' and C-C'. It is also interesting to mention that although the material properties have not been changed, the maximum strain energy density in the case of $l = 0.0$ drops severely, going from the second-order to the fourth-order theory (from $24.33\,\mathrm{MPa}$ to $14.01\,\mathrm{MPa}$). One could argue that this is because the fourth-order theory is less mesh dependent, and the fact that the value in the second-order theory is much higher because the considered mesh is not fine enough. While we do acknowledge that this might be the case, we doubt if there will be any convergence in the presence of singularity. At this point, we remind the reader that the results presented in Fig. 5.11 depict a completely different trend where a more refined mesh has an even larger maximum energy density. Therefore, due to the described behavior, we can conclude that singularities are present in the numerical phase-field fracture model based on the classical theory of elasticity developed by Cauchy.

5.2.2.2 Strain Gradient Enhanced Model

The current section investigates the same model and merely exchanges the classical theory of elasticity by the strain gradient theory. In the following, the influence of different values of the gradient material length-scale l, on the results is studied in detail. We consider three cases: $l = 0.0$ which is equivalent to the non-gradient model (representing the same results already provided in Sect. 5.2.2.1 for comparison purposes), $l = \epsilon$ which takes the same value for the crack and the gradient length-scales, and finally, $l = 2\epsilon$. It should be emphasized that, in general, higher values of the gradient length-scale parameter result in a stiffer material behavior. According to our numerical results, we assume a relation between the phase-field crack-width ϵ and the gradient elasticity length-scale l. By taking length-scale values much higher than ϵ ($l > 3\,\epsilon$), the computed crack width significantly increases. In the current simulations, the value $\epsilon = 0.02$ is chosen for the phase-field (see [135, 170]), and the gradient elasticity length-scales are adapted accordingly. Figure 5.13 illustrates the simulation data for the second-order formulation. Note that all simulations have been executed for the finest mesh (408×409 control points), and the results are plotted on the paths introduced in the previous section. From the obtained results, we can conclude:

- There is a clear difference between the classical ($l = 0.0$) and the gradient theories in the results depicted for Path A-A'. In the visualization of the phase-field parameter, a wider transition zone between the cracked and intact material is observed for the classical theory. This transition is much sharper for the two gradient results, and accordingly, it is easier to determine the crack tip position. In other words, the rate of changes of the phase-field parameter in the crack-growth direction for the classical

Figure 5.13: Results for the second-order formulation for different values of l and the $408{\times}409$ mesh. Distributions of the phase-field (left), and the strain energy density (right) along three different cross-sections in the plane.

theory is rather slow compared to the behavior in the normal direction (see the phase-field values in Paths A-A′ and B-B′). This is not the case for the other two values of l.

- The results for $l = \epsilon$ are more localized (exhibit a faster rate of change) than the ones for $l = 2\epsilon$, making the distance between the energy density peak and the crack tip smaller.

- Considering the energy density, Paths B-B′ and C-C′ show no oscillations around the crack zone for the gradient theory results, and the strain energy density is zero in the vicinity of the crack zone.

- The energy density in the results for Paths B-B′ and C-C′ is more uniformly distributed for the gradient theory in comparison to the classical theory where it is strongly localized.

There is, however, one problem with these results. Although not easily noticeable at first, the phase-field for the $l = \epsilon$ simulations is slightly deviated from the expected path resulting in a slightly non-symmetric phase-field distribution on Paths B-B′ and C-C′. The effect is better seen in Fig. C.1 in the Appendix, where the results for $l = \epsilon$ are depicted individually for different mesh sizes. According to our numerical results, the source of this is expected to originate from using a second-order formulation for the phase-field in conjunction with a fourth-order one for the mechanical part. On the other hand, using non-matching formulations for the phase-field and the displacements where a second-order elasticity model is coupled to a fourth-order formulation for the crack field does not result in deteriorated solutions. Similar behavior is also seen if the length-scale parameter is increased to $l = 2\epsilon$.

Finally, Fig. 5.14 shows the numerical solutions for the fourth-order formulation. The results for the two cases $l = \epsilon$ and $l = 2\epsilon$ illustrate all advantages of the previous case, plus, this time there is no deviation of the phase-field values, i.e., the phase-field distributions for different meshes almost completely match, and the energy is settled in the crack zone. It should also be emphasized that the severe drop of the maximum strain energy density from the second-order to the fourth-order theory, which is observed in the classical theory and was discussed in the previous section, does not happen in the gradient elasticity models and the difference between the maximum energy values, comparing the second-order to the fourth-order formulation, is relatively small.

5.2.2.3 Finite Element Analysis Results

The numerical results provided so far have been obtained using the isogeometric analysis approach in conjunction with quadratic NURBS shape functions. These shape functions exhibit C^1-continuity and are therefore, ideal when using first strain gradient models. In the wide body of literature, the standard finite element method is favoured for numerical simulations based on the classical second-order phase-field fracture model. Therefore, we additionally provide the results for the model described in Sect. 3.2.1 using bi-linear finite elements (4-node quadrilaterals) which are shown in Fig. 5.15. The results are illustrated for three different mesh sizes h which are significantly finer than the ones used in the IGA simulations. The first model consists of 501×501 equidistant nodes which results in a mesh size of $h = 0.002\,\mathrm{mm}$, while the second and third refinement steps feature models consisting of 1001×1001 ($h = 0.001\,\mathrm{mm}$) and 2001×2001 ($h = 0.0005\,\mathrm{mm}$) nodes. All the mesh sizes are far smaller than the assumed phase-field length-scale parameter $\epsilon = 0.02\,\mathrm{mm}$. Note that the same results as discussed in Sect. 5.2.2.1 can be observed. Although the phase-field plots for different meshes coincide with each other, the maximum strain energy density in
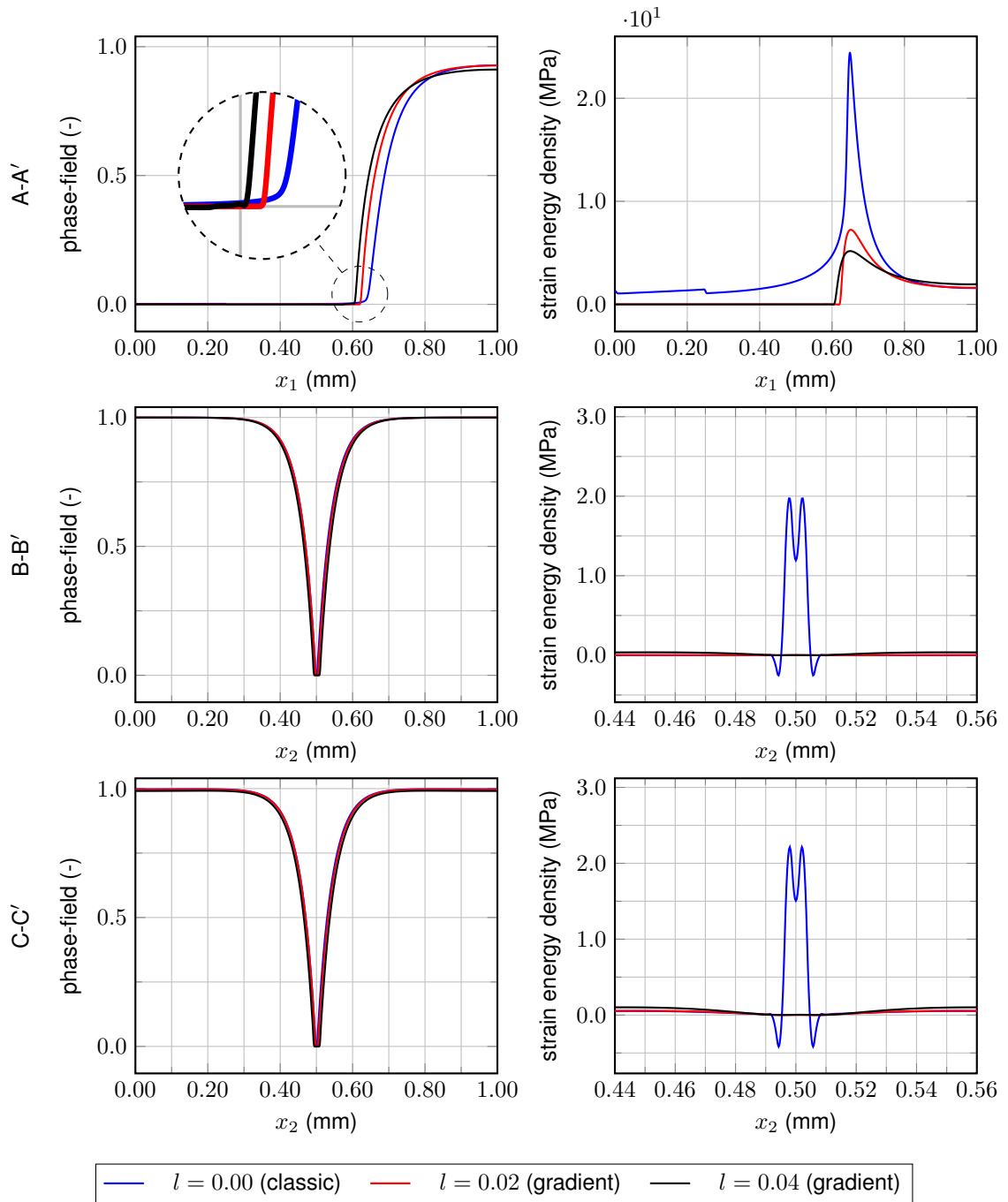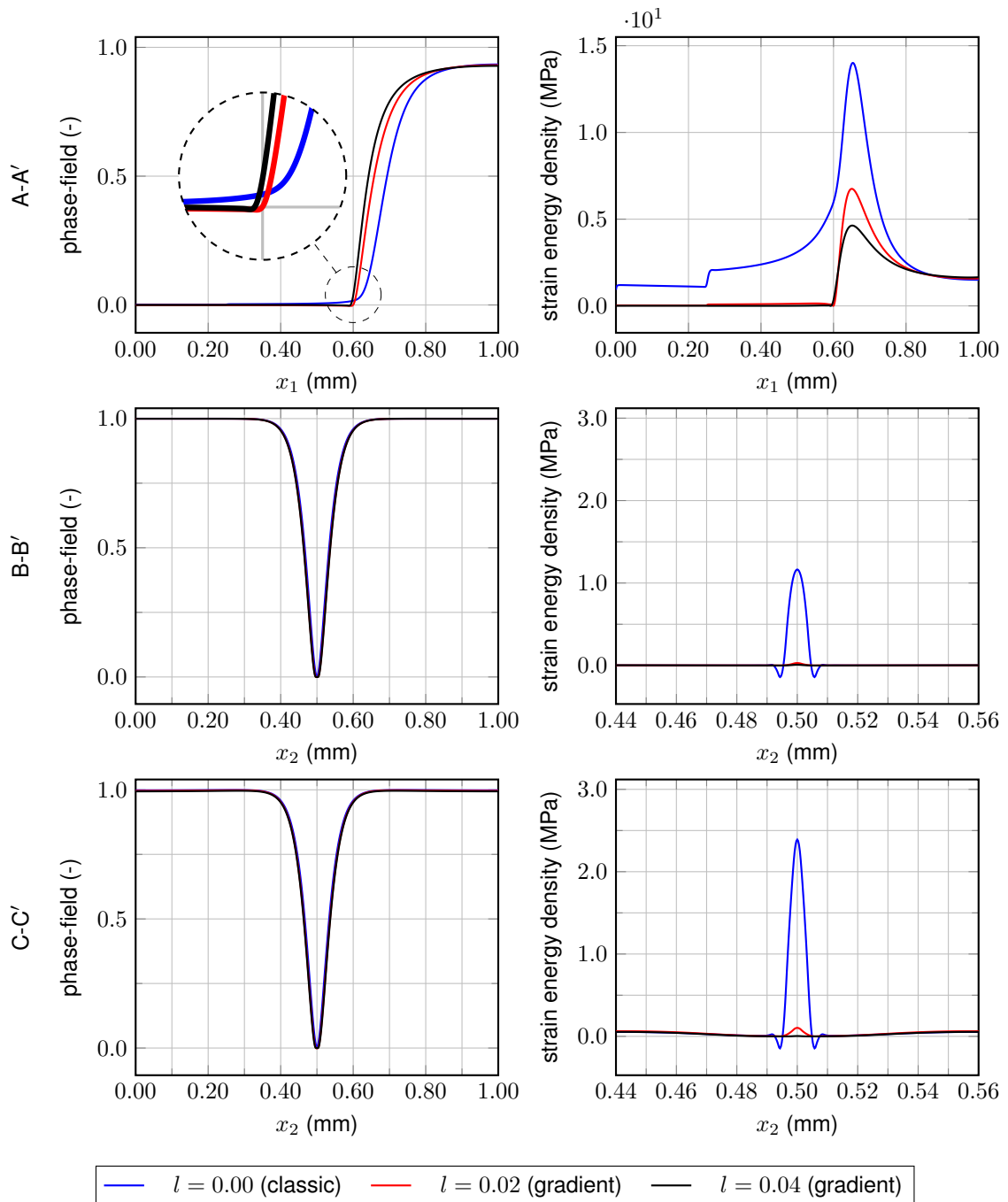
Figure 5.14: Results for the fourth-order formulation for different values of l and the 408×409 mesh. Distributions of the phase-field (left), and the strain energy density (right) along three different cross-sections in the plane.

front of the crack tip is different and does not seem to converge. Moreover, the strain energy density in the broken material behind the crack tip remains non-zero showing no signs of mitigation for finer meshes. Since linear elements are used in the studies and a sudden jump in the results do not produce oscillations in this case, there are no negative strain energy density values present in the plots shown in Fig. 5.15. It is worth mentioning that we also executed these simulations using the same number of nodes but quadratic Lagrangian shape functions (tensor product space). Increasing the polynomial order did not alleviate the observed problems, instead the maximum strain energy density values in front of the crack for the models with quadratic interpolation were higher than the corresponding linear ones. Therefore, we can only conclude that influence of the singularity inherited from the classical Cauchy continuum theory also prevails when the classical finite element method is applied, although the signs of a singular behavior are not as evident as in the case with IGA elements with higher regularity.

5.2.2.4 Summary

To summarize our findings, we concentrate on a comparison between the strain energy density contour plots for different values of the gradient material length-scale l. In fact, Fig. 5.16 combines all results from Sects. 5.2.2.1 and 5.2.2.2. The values for the second- and the fourth-order models are depicted side-by-side. To facilitate the comparison of the graphs, the data ranges for the color maps are regularized to the results presented in the second-order model with $l = \epsilon$ as it has the widest range of strain energy density values among the gradient models. The following remarks ought to be provided:

- We observe the existence of non-zero energy values in the broken material in the top row where the results for the classical second-order and fourth-order theories are compared ($l = 0.0$). There is a change in the value of these non-zero points in the transition area from the initial to the propagated crack for the fourth-order formulation. In fact, all these (unphysical) values are relatively high in both cases. We should stress that the gradient theory results ($l > 0$) do not exhibit this behavior and the strain energy density tends to vanish in the broken material.

- Far away from the crack tip, both the classical and the gradient theories predict the same strain energy density distribution. It is only around the crack tip that the classical theory drastically overestimates the stresses, which may cause problems such as predicting the failure of the structure due to cracks under loadings that normally could not cause a crack to nucleate or propagate.

In the results represented in Fig. 5.16, there are strain energy density values that marginally differ from zero (roughly $0.1\,\mathrm{MPa}$) behind the crack tip for the $l = \epsilon$ case in the fourth-order formulation. This is not the case at the initial crack region, which implies that the non-zero value of the energy is related to the numerically non-zero values of the phase-field s in those regions. Because of numerical limitations, it is not possible to obtain an exactly zero value in the solution region, and the phase-field has very small (close to zero) values in those areas. We should also note that, though very small, there are still some negative energy values for the second-order theory with $l = \epsilon$ and $l = 2\epsilon$ even with the gradient theory, which suggests that there are still small jumps of the strain energy density value in the broken material. It could be a motivation for considering other (more sophisticated) gradient models for future studies. One should note that the GRADELA model used in the current work is a simple strain gradient elasticity model involving only one internal length parameter instead of the originally proposed five parameters of [42]. Therefore, although in theory first strain gradient
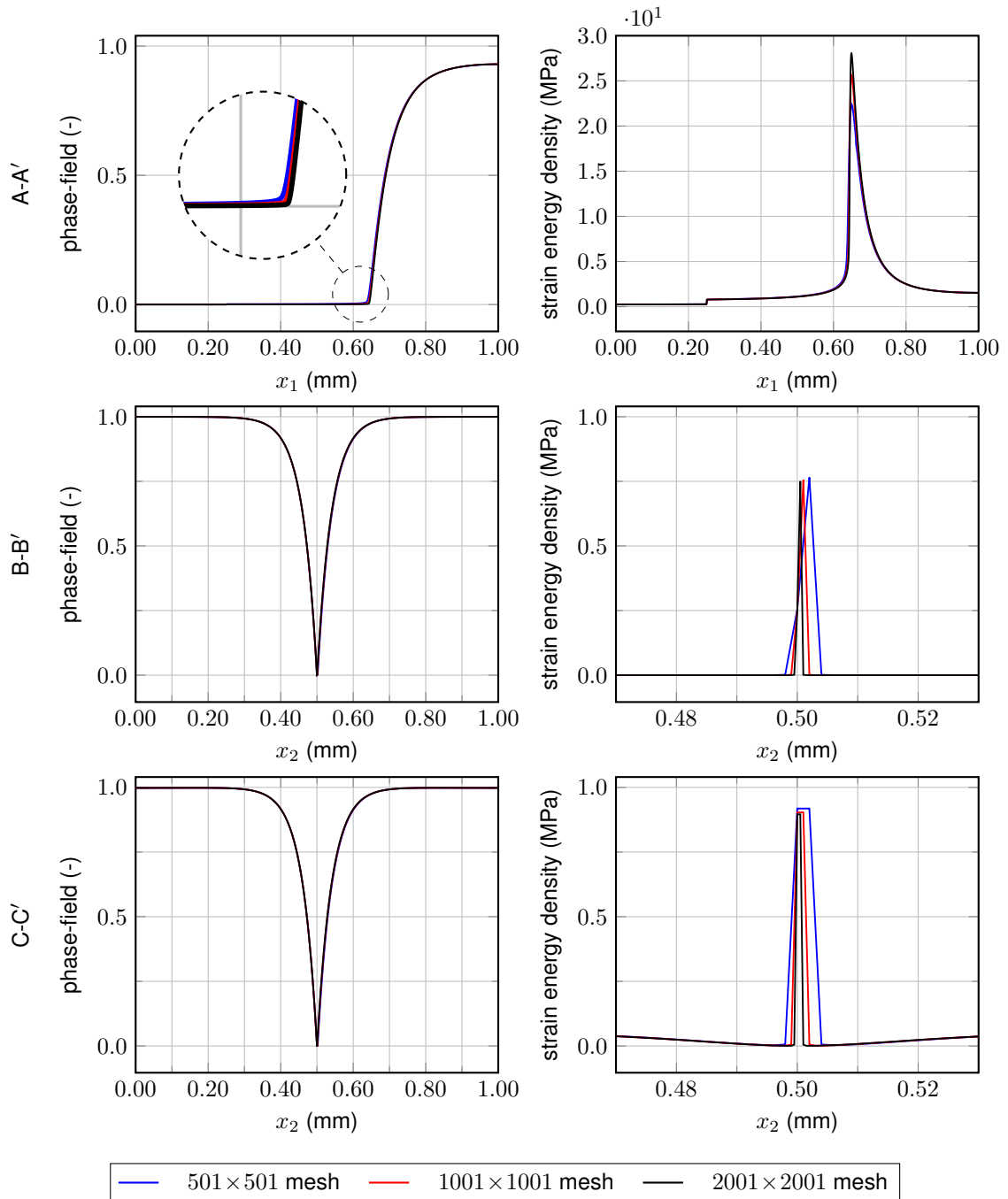
Figure 5.15: FEM results for the classical second-order phase-field theory (coupled with linear elasticity) for different mesh sizes with linear elements. Distributions of the phase-field (left), and the strain energy density (right) along three different cross-sections in the plane.

models are sufficient to remove the singularities caused by line loads (i.e., point loads in the two-dimensional cases) [24], this seems not to be the case for the simplified model exploited in the present study. Higher-order theories, involving the third-gradients of the displacement field, can be considered for further investigations on this topic, cf. [53, 67, 218].

To conclude, the outcome of the fourth-order formulation seems to be in better agreement with the theoretical considerations than the second-order model. Moreover, the different choices of the length-scale parameter $l = \epsilon$ and $l = 2\epsilon$ produce outstanding results concerning the removal of the crack tip singularity. Using $l = 2\epsilon$, the results are less mesh sensitive and already converged for the 192×193 control points grid (see Fig. C.4). However, using the finest mesh with $l = \epsilon$ also gives acceptable results. Therefore, we recommend setting the length-scale parameter $\epsilon \leq l \leq 2\epsilon$ to obtain meaningful results.

5.2.3 Stress Analysis

We finished the previous section by showing problems associated with using classical phase-field fracture formulations, and we used plots of strain energy density to show these shortcomings. The strain energy density is a cumulative measure, meaning that it is influenced by all the stress and strain components in the problem. Although it is indeed a good measure to show the overall problem because of the mentioned property, the source of the problem remains ambiguous. In other words, the questions of "which strain/stress components are responsible for this behavior?" and "how adding strain gradient terms can help to solve the problem?" have not been entirely addressed yet. This section tries to clarify and help find answers to the mentioned questions by studying individual stress components. Although the patterns which are going to be discussed are observable as well when studying the strain energy density, it comes out that the effects are more pronounced when looking at the individual stress components. All the results in this section are for the 408×409 mesh and show the state where the maximum strain energy density reaches the line $x_1 = 0.65 \, \text{mm}$ as was the case in the previous section.

5.2.3.1 Classical Model

We start with the classical phase-field fracture models. Figure 5.17 shows the contour plots for the primary degrees of freedom (displacements and the phase-field variable) and the effective stress components for the second-order model. Looking at the results for the displacement in x_1-direction, the maximum displacement occurs in a small region in the left side of the model where the initial crack is supposed to start. Apparently, we have a considerable value of the displacement in x_1-direction in that region comparing to the rest of the domain which is not expected. This could lead to high gradients and therefore high strains on that specific point. The maximum displacement in x_1-direction is expected to occur close to the top and bottom edges where the displacements in x_2-direction are restricted. The same results can be seen for the classical fourth-order theory in Fig. 5.18. On the other hand, the displacements in the x_2-direction look as expected in both figures. The minimum displacement in this direction happens in the lower half of the model, which is natural due to the fracture and the applied displacement boundary conditions. High changes of the displacement field is noticeable around the crack, while the transition is smoother in the undamaged region. The minimum value for the displacement in this direction is slightly affected on the region where maximum u_1 displacements is observed. The figures also show the phase-field contour plot in that state. Again, as expected, the phase-field looks a bit
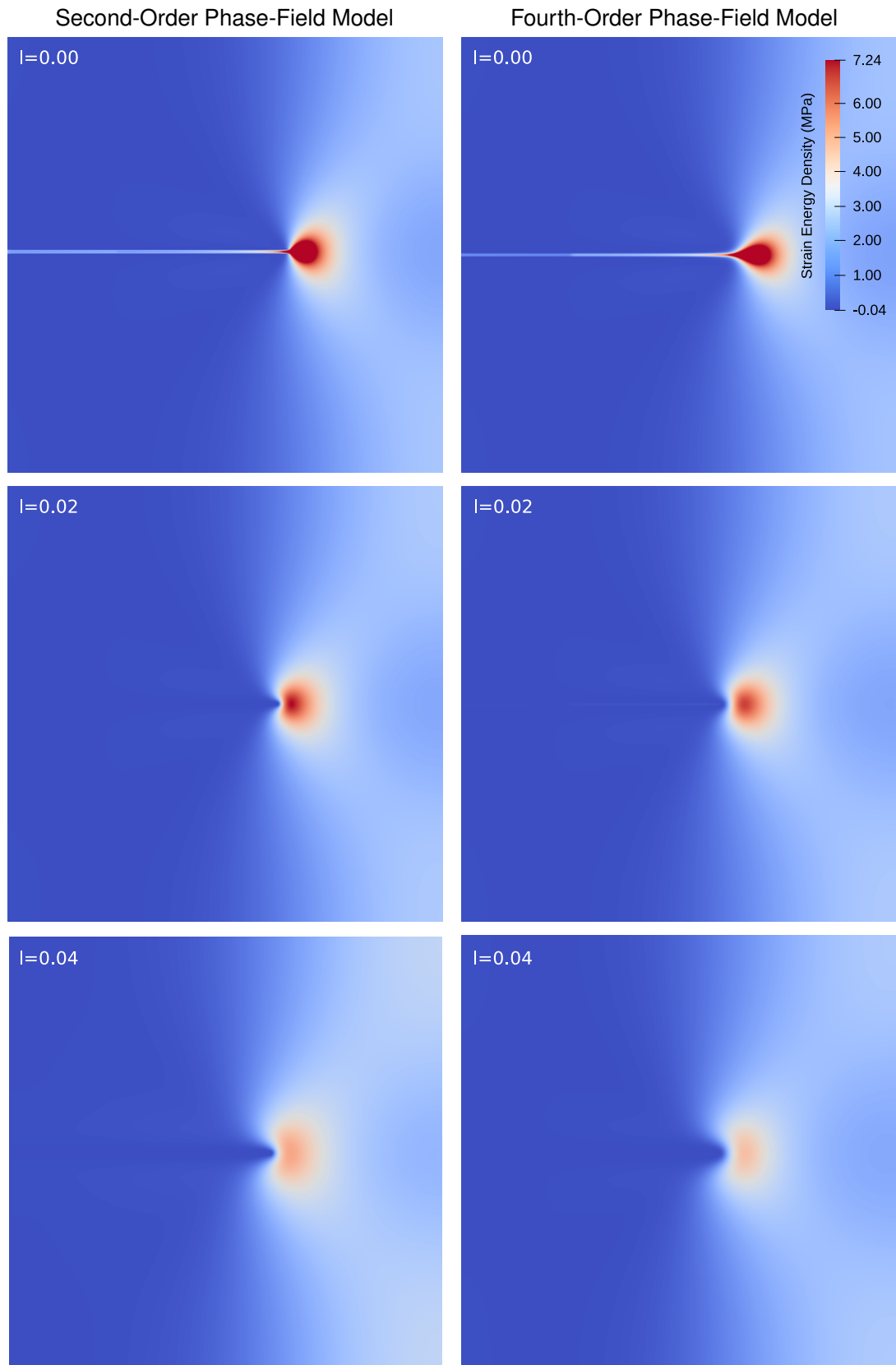
Figure 5.16: Comparison between contour plots of the strain energy density (left: second-order, and right: fourth-order phase-field model) for different values of l for the 408×409 mesh

wider for the fourth-order model. On the right side of both the figures, the stress components are plotted. As it was the case with the strain energy density plots, here also using the fourth-order model leads to smaller maximum stress values for all the components. At first glance there is no sign of any potential problems with these plots, and it is likely that this is the reason that other studies done using the phase-field modelling of fracture have not reported any anomalies with the results. Before looking more closely into these plots, let us review the results for the strain gradient theory.

5.2.3.2 Strain Gradient Enhanced Model

Now, let us look at the results produced by the phase-field fracture models tuned with the strain gradient elasticity. Figure 5.19 shows the contour plots for the primary degrees of freedom (displacements and the phase-field variable) and the effective stress components for the second-order model. We will focus on the results for the case with the strain gradient elasticity length-scale parameter of $l = \epsilon = 0.02$ as it was shown in the previous section that it produces acceptable results with the 408×409 mesh while keeping the extra regularization of the strain gradient fields in a moderate level. Here, because of the integration of the strain gradient theory, double-stresses are also involved in the simulation. Figure 5.20 depicts the plots for these stress components. Note that P_{ijk} is the energy conjugate of H_{ijk} which denotes the linear changes of E_{kj} in x_i-direction (see Sect. 2.2.5). Looking at the results provided in Fig. 5.19, at first glance, there is a tangible difference in the plot for the displacements in x_1-direction compared to the ones from the classical theory. It is because that singular point on the left edge does not appear in the results obtained from the strain gradient theory, although the same boundary conditions have been applied to the model. The reason could be the fact that here we are using a non-local theory and the displacement field is more enriched because of the higher-order gradients involved. Despite the wider phase-field profile, the distribution of the displacement field in x_2-direction looks the same as in the classical cases. The maximum stresses are also further reduced compared to the classical fourth-order model. The problem with the wider crack band in the second-order theory and the corresponding deviation of the strain energy density once again shows itself in the results of the effective shear stresses (S_{12}^{frac}) where the absolute value of the maximum and minimum stresses are slightly different, i.e., the stress distribution is not entirely symmetric. The problem can be seen even for non-shear components of the double-stresses. This is not the case for the results shown in Figs. 5.21 and 5.22 for the fourth-order formulation, once again showing the superiority of the fourth-order model over its second-order counterpart.

Comparing the plots for the phase-field parameter in Figs. 5.17–5.19 and 5.21, the crack front in the results shown for the strain gradient enhanced model is slightly behind the crack front of the results for the classical models. This difference between the position of the crack fronts, apart from the reasons discussed in the previous section, is due to the usage of an adaptive time stepping scheme and different time steps used in solving each model. Because of this difference, it is not possible to compare all the results at a specific time. As we want to avoid interpolating the results in time, we use the results from the closest time step after the maximum strain energy density has reached the line $x_1 = 0.65$. The difference is trivial as during crack propagation, the time step size decreases to $5\mathrm{e}{-}5\,\mathrm{s}$ and $5\mathrm{e}{-}6\,\mathrm{s}$ for the classical and gradient models, respectively (keep in mind that the total applied displacement is $0.1\,\mathrm{mm}$ making the load step size one order of magnitude smaller). An interesting observation can be made here; the results for the second-order classical model, cf. Fig. 5.17, are plotted at time $t \approx 6.18\mathrm{e}{-}2\,\mathrm{s}$, while this value is $t \approx 6.04\mathrm{e}{-}2\,\mathrm{s}$ for the fourth-order classical model,
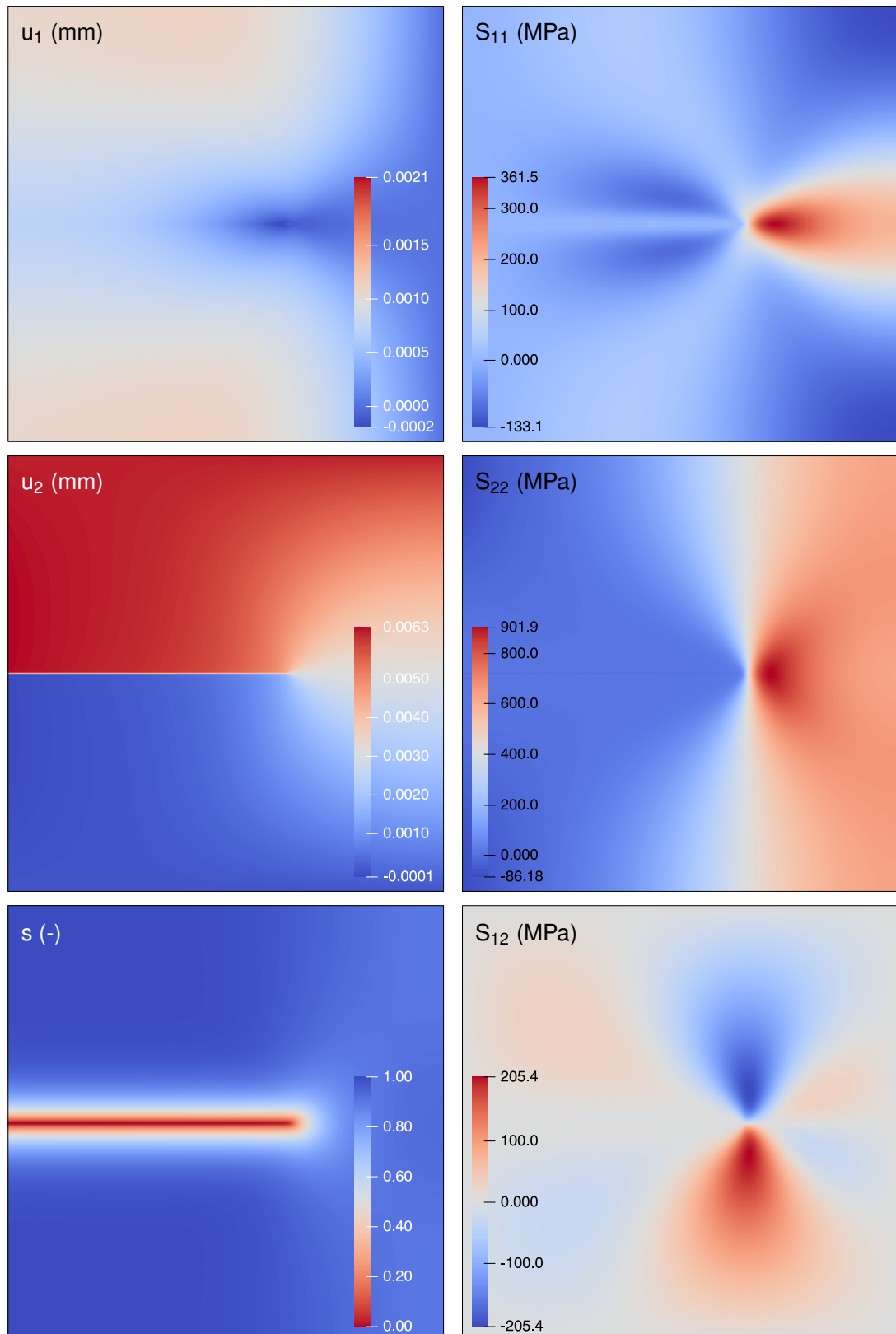
Figure 5.17: Contour plots of displacements and the phase-field variable (left), and effective stress components (right) for the classical theory ($l = 0.00$) and the second-order phase-field model. The superscript $\square^{\mathrm{frac}}$ of the effective stresses is omitted for brevity.
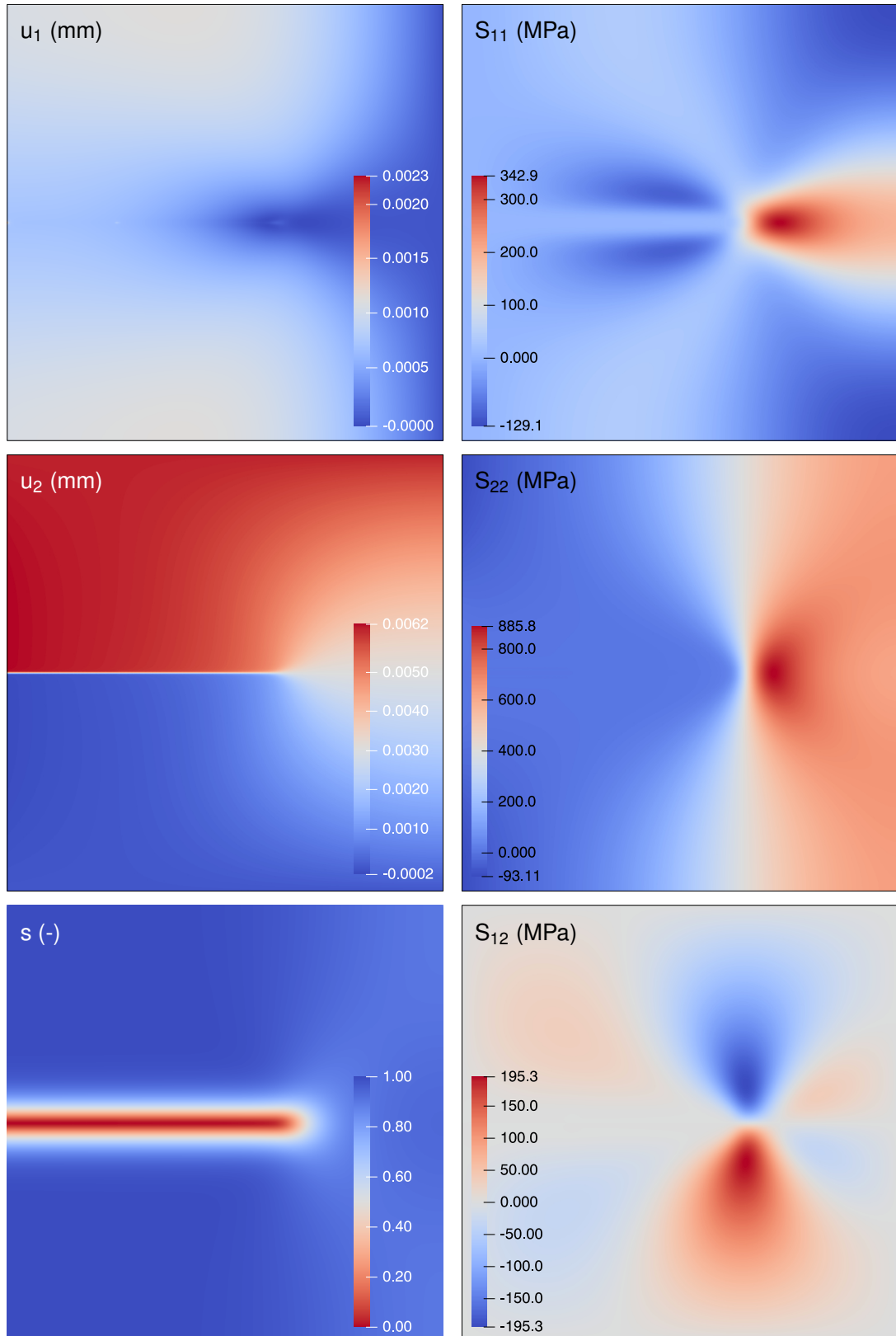
Figure 5.18: Contour plots of displacements and the phase-field variable (left), and effective stress components (right) for the classical theory ($l = 0.00$) and the fourth-order phase-field model. The superscript $\square^{\mathrm{frac}}$ of the effective stresses is omitted for brevity.
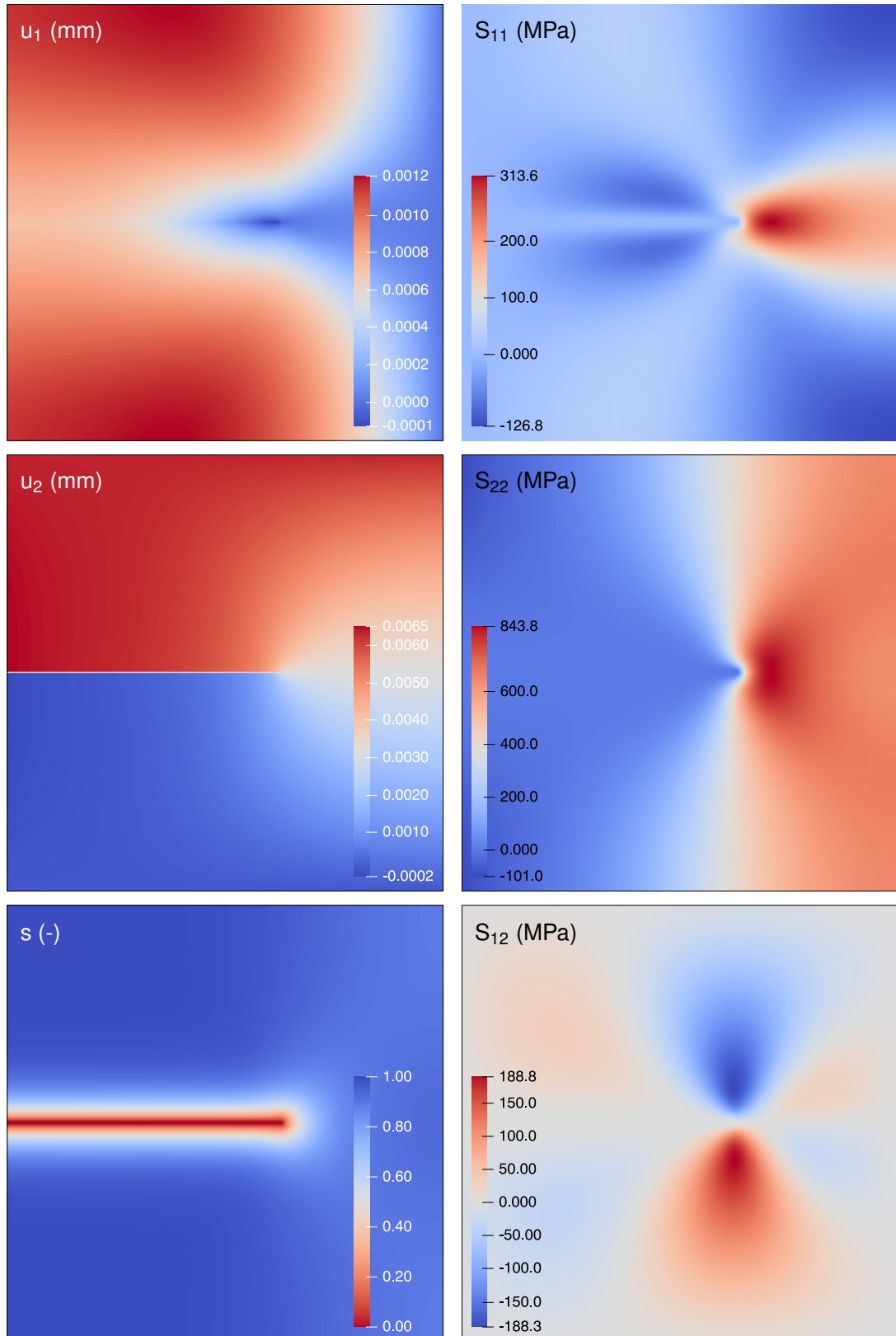
Figure 5.19: Contour plots of displacements and the phase-field variable (left), and effective stress components (right) for the gradient theory ($l = 0.02$) and the second-order phase-field model. The superscript $\square^{\text{frac}}$ of the effective stresses is omitted for brevity.
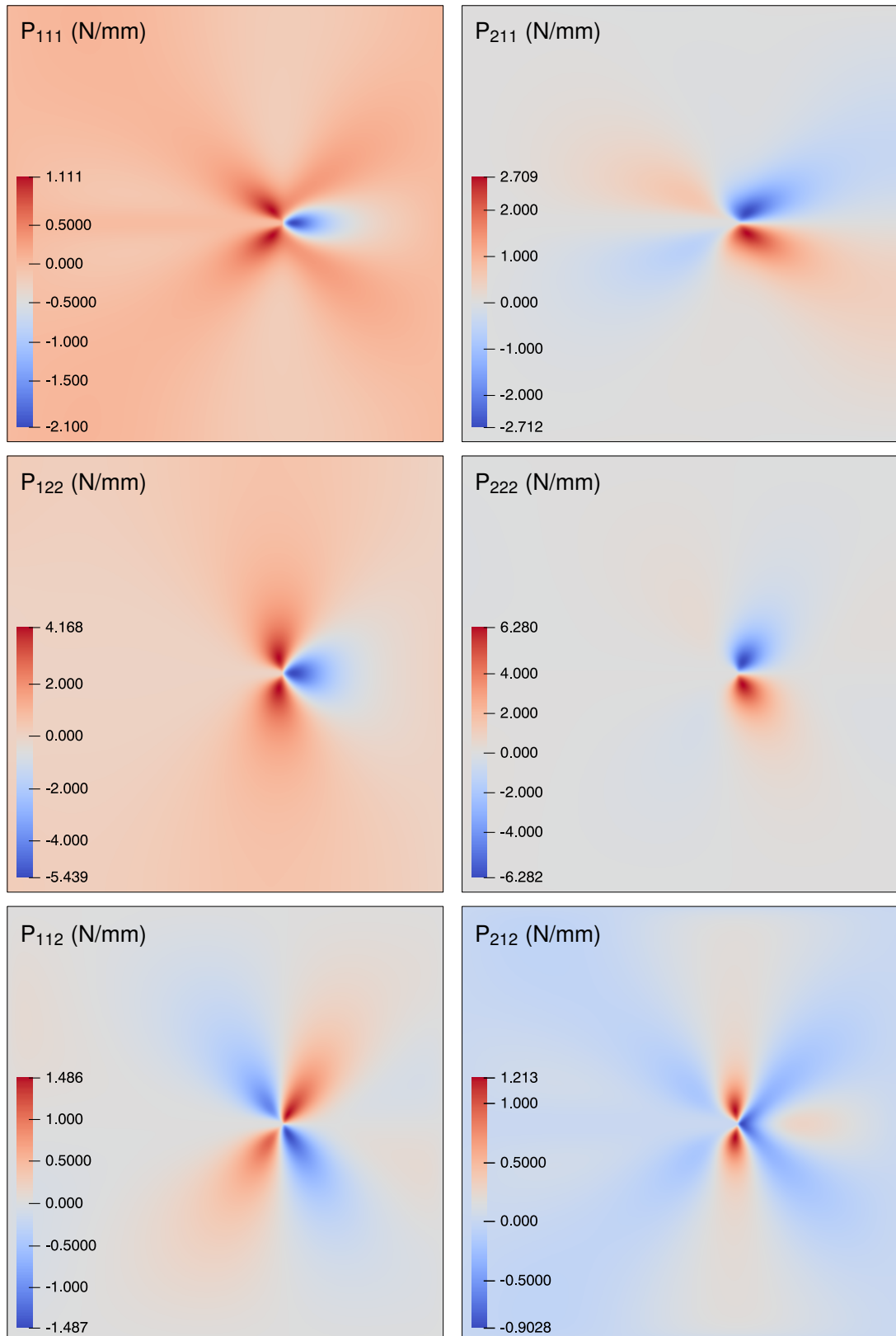
Figure 5.20: Contour plots of effective double-stress components (right) for the gradient theory ($l = 0.02$) and the second-order phase-field model. The superscript $\square^{\text{frac}}$ of the effective stresses is omitted for brevity.
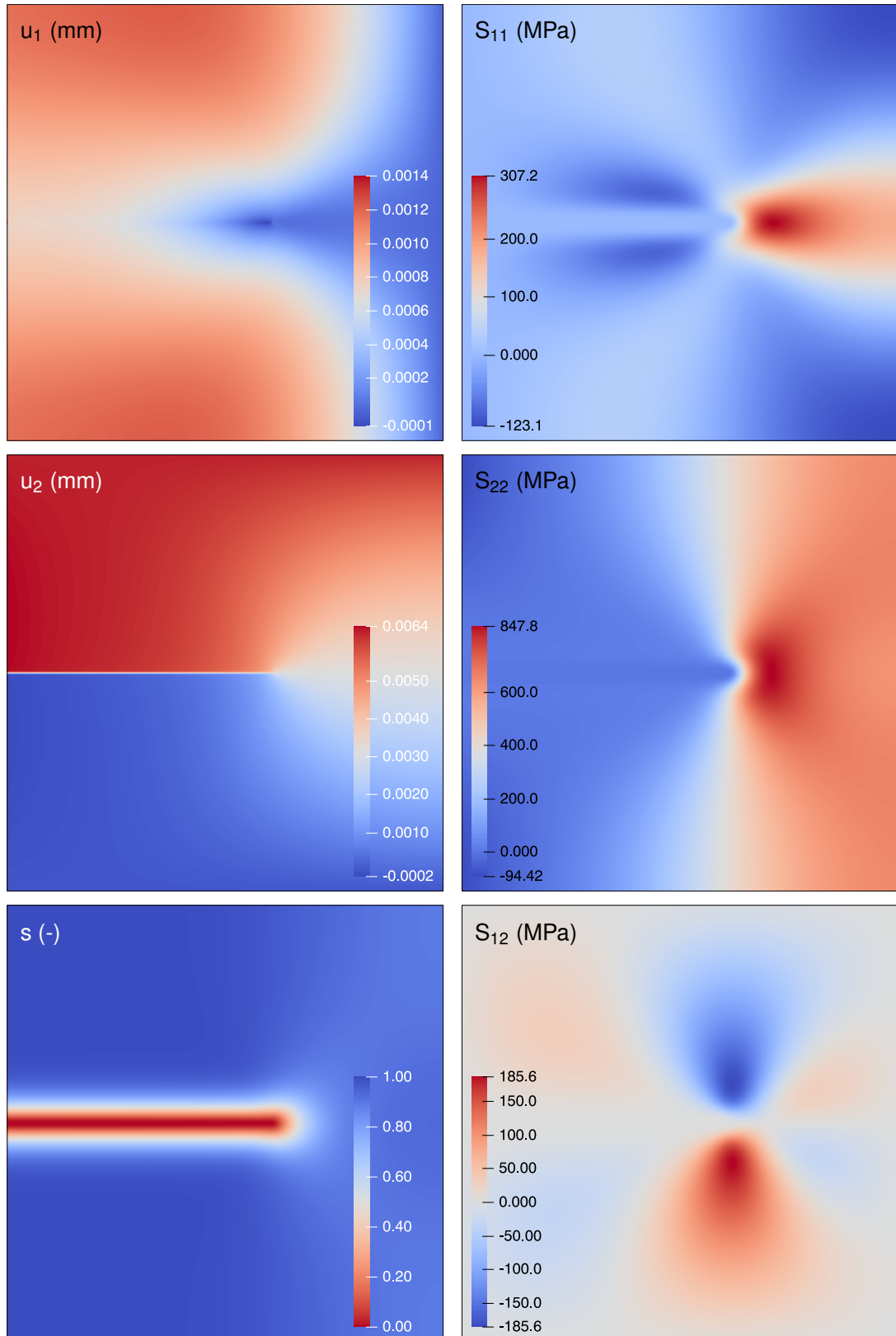
Figure 5.21: Contour plots of displacements and the phase-field variable (left), and effective stress components (right) for the classical theory ($l = 0.02$) and the fourth-order phase-field model. The superscript $\square^{\mathrm{frac}}$ of the effective stresses is omitted for brevity.
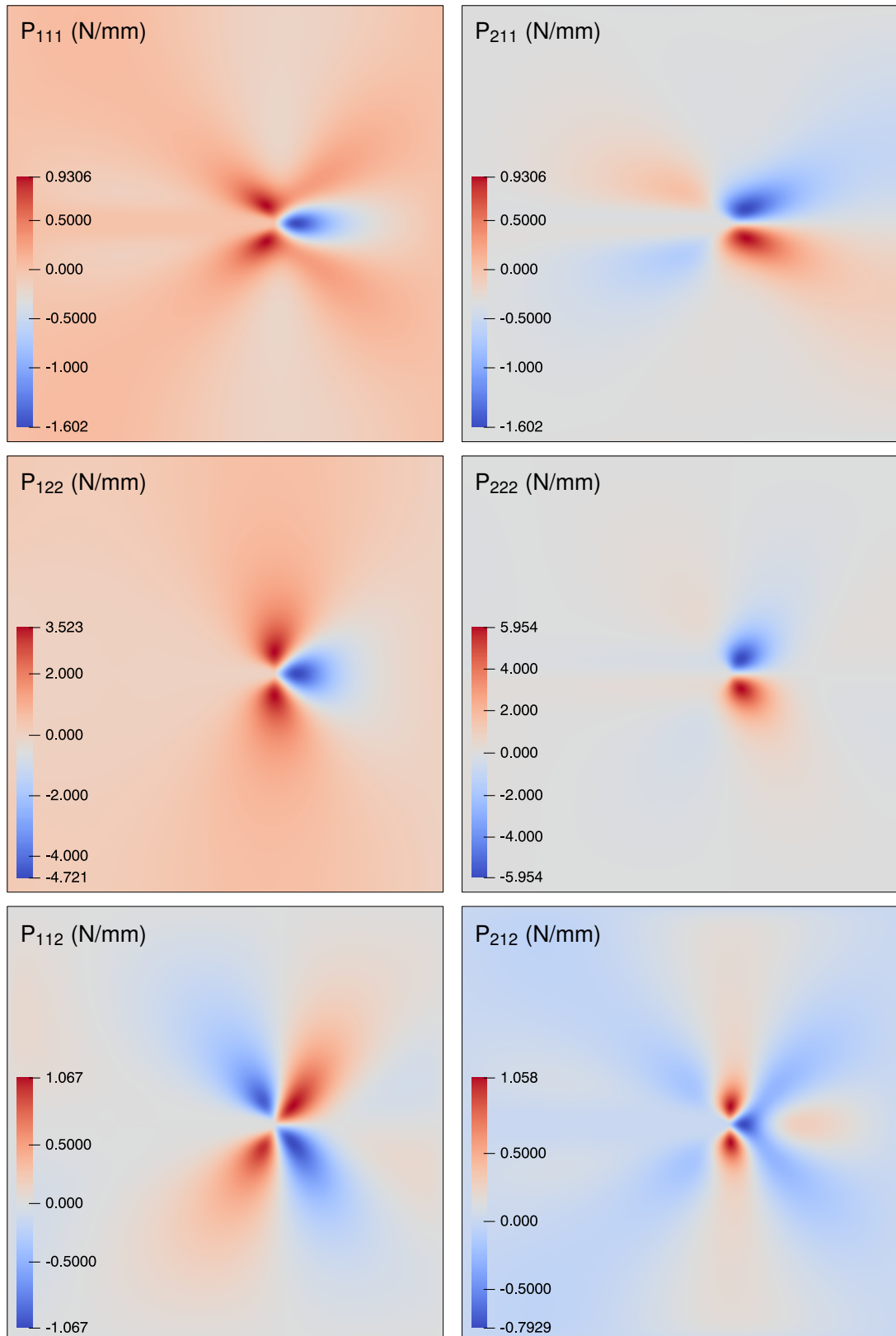
Figure 5.22: Contour plots of effective double-stress components (right) for the gradient theory ($l = 0.02$) and the fourth-order phase-field model. The superscript $\square^{\text{frac}}$ of the effective stresses is omitted for brevity.

$t \approx 6.30\mathrm{e}{-}2\,\mathrm{s}$ for the second-order gradient model and $t \approx 6.26\mathrm{e}{-}2\,\mathrm{s}$ for the fourth-order gradient model. Assuming the propagation speed of the crack, the difference between the mentioned times is noticeable. In both the classical and gradient models, the crack propagation starts earlier using the fourth-order theory, which can also be concluded from the fact that the maximum strain energy density in front of the crack tip has reached the $x_1 = 0.65\,\mathrm{mm}$ line earlier than for the second-order model. This is not surprising though since the crack density functional is different between the second-order and fourth-order formulations, cf. Eqs. (3.8) and (3.21). Moreover, comparing the results for second-order and fourth-order formulations for both the classical and strain gradient enhanced formulations, the crack starts earlier in the classical theory supporting our initial suspicions on an early start of the failure and the crack propagation phenomenon in the presence of singularities. Based on the applied boundary conditions and the chosen crack opening mode, the normal stress components are dominant in comparison to the shear stresses. Between the normal stress components, in all the plotted results, the normal component in x_2-direction, i.e, S_{22}^{frac} is almost two times larger than the stress in x_1-direction. The minimum values for S_{22} happen in the left-top and left-bottom corners of the model, while they are located at right-top and right-bottom corners for the S_{11} component. In the same way, for the gradient models, the double-stresses corresponding to the normal components and in particular to the x_2-direction (i.e., P_{211}^{frac}, P_{122}^{frac}, and P_{222}^{frac}) have higher maximum values. The double-stress components only have significant values around the crack field because of the higher stress/strain gradients in these zones. Therefore, the strain gradient contributions are trivial far away these regions which also shows why the strain energy density is similar to the values of the classical models far away from the crack front. Figures 5.23 and 5.24 further plot all the stress and double-stress components for Paths A-A′, B-B′, C-C′ introduced in the previous section for the second-order and the fourth-order formulation, respectively. All the stress components vanish smoothly in the regions where the crack exists. Interesting to note is the different behavior of the stress components between Paths B-B′ (far from the crack front) and C-C′ (closer to the crack front). The dominance of S_{22}^{frac} and its corresponding double-stress components is more obvious in the plots for Path A-A′.

5.2.3.3 Summary

Comparing the results shown in Figs. 5.23 and 5.24 for Paths B-B′ (or C-C′), between the second-order and the fourth-order models, all the classical (Cauchy) stress components have visually almost the same profiles, except for S_{22}^{frac}. It is only for this stress component that a different profile can be seen comparing the two models. Considering Path B-B′, for the second-order formulation, S_{22}^{frac} smoothly increases to zero and then decreases again once the cracked region is passed. A different behavior can be seen for the fourth-order formulation where the stress component increases up to some point close to the crack, and then decreases to zero in a small region which could correspond to the diffusive interphase of the crack, and then show a symmetric behavior after passing the crack. Before looking closer into this behavior, let us go back and study the results obtained from the classical theories ($l = 0$) with a focus on the Cauchy stress components.

Figure 5.25 summarizes all the results for the stress analysis concerning the classical components. The left column depicts the profiles for the classical and gradient second-order phase-field formulations, while the corresponding fourth-order results are shown in the right column. Let us start with the results for Path A-A′. All the results in this path seem to be conforming, specifically far from the crack front. There is not much differences between the peak values of the stress components for all the models, i.e., second-order and fourth-order
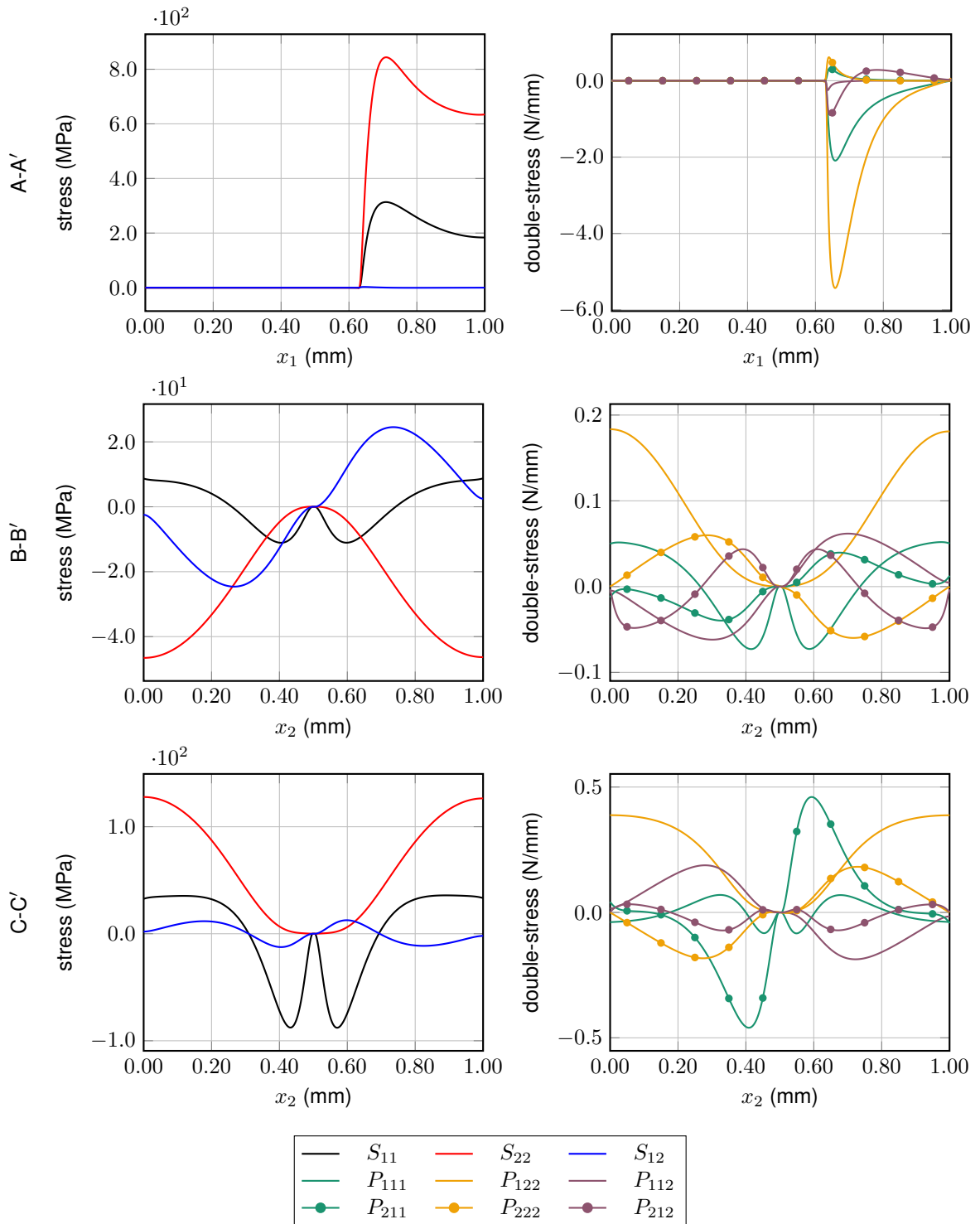
Figure 5.23: Results for the second-order formulation for $l = 0.02$ and the 408×409 mesh. Distributions of the classical Cauchy stress components (left), and the double-stress components (right) along three different cross-sections in the plane. The superscript "frac" is omitted for brevity.
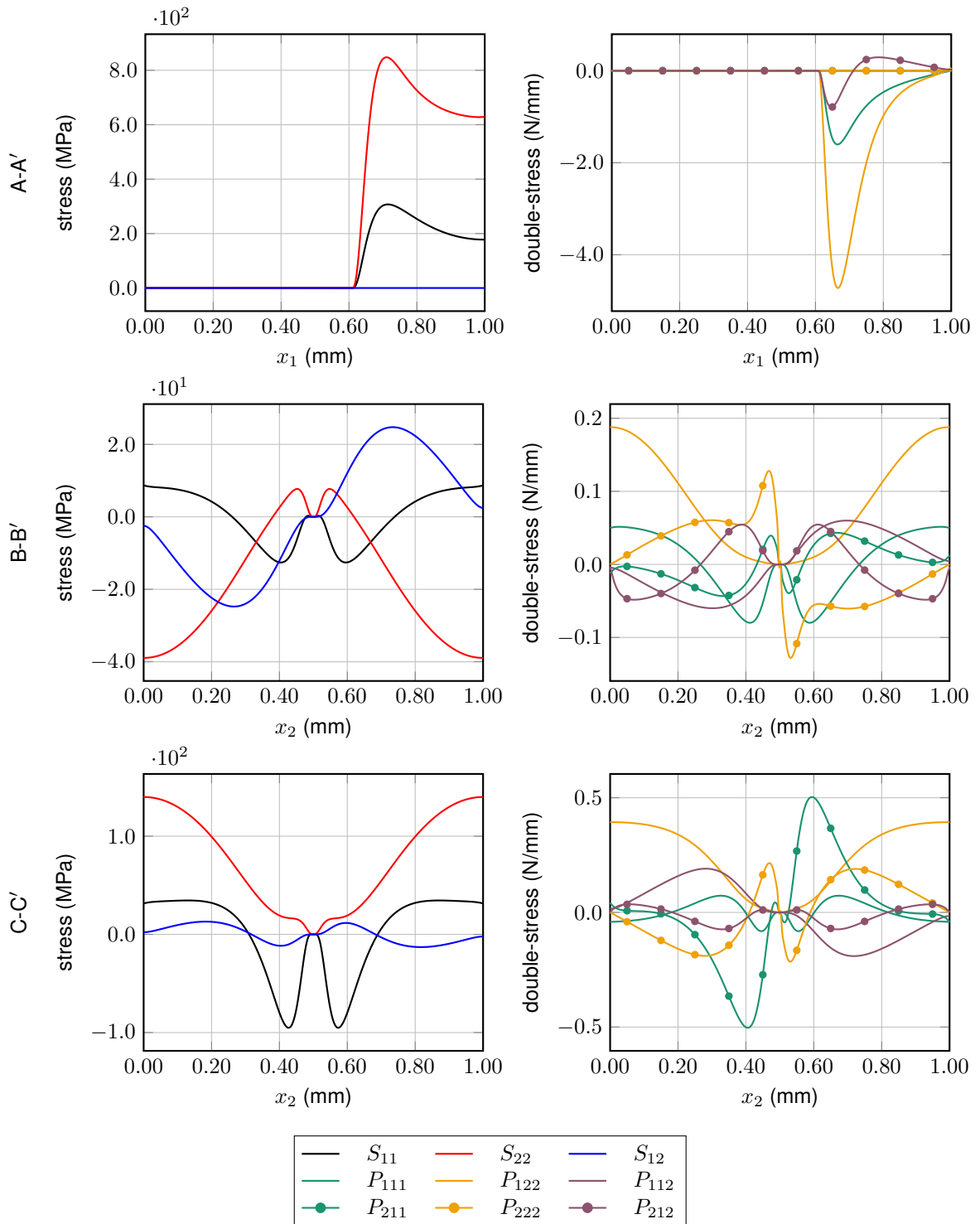
Figure 5.24: Results for the fourth-order formulation for $l = 0.02$ and the 408×409 mesh. Distributions of the classical Cauchy stress components (left), and the double-stress components (right) along three different cross-sections in the plane. The superscript "frac" is omitted for brevity.
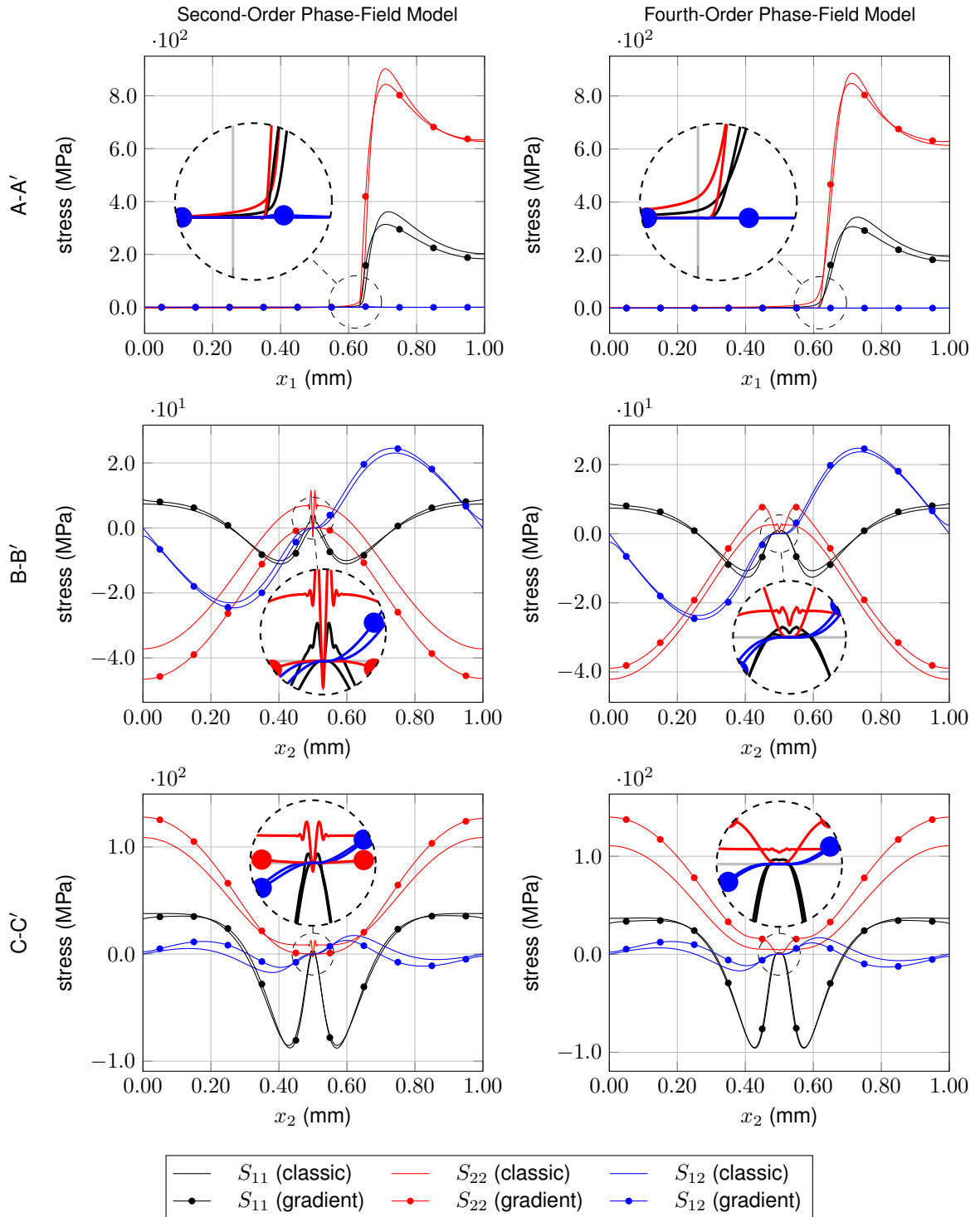
Figure 5.25: Comparison of classical Cauchy stress components between the results from the classical theory and the strain gradient enhanced phase-field models for the second-order (left) and the fourth-order (right) formulations. The superscript "frac" is omitted for brevity.

classical and gradient formulations. The same behavior is observed for the strain energy density plots, here also the gradient enhanced models produce sharper changes of the stress components, i.e., the transition (process) zone for the classical theory is wider. For Path B-B′, stress components S_{11}^{frac} and S_{12}^{frac} show a very good agreement for both second-order and fourth-order theories. Again, there are obvious differences between the profiles for the S_{22}^{frac}, the dominant stress component. Looking at the second-order formulation results, we have already mentioned the smooth behavior of the gradient enhanced model. The classical model, though, somehow follows the same behavior of the gradient enhanced fourth-order formulation in the sense that it increases smoothly up to a point very close to the crack, then an abrupt change in the value, presumably to zero, occurs causing an oscillation of the interpolated stress profile. The same situation is encountered for the second dominant stress component S_{11}^{frac}, but in a smaller scale. The trend remains the same for the fourth-order formulations where the oscillations are still obvious, although they are much less in comparison to the second-order formulation.

Now, the question is "what is the expected behavior?". Of course, in general, an abrupt change of the stress field normal to a crack is very desirable as it is a sign of a corresponding abrupt change in the displacement field which is only natural thinking of the fracture phenomenon. However, this seems not to be the expected behavior when using the phase-field method. We have a crack profile and the material is expected to get degraded in correlation with this crack phase-field parameter. Although the changes in the phase-field value and the mechanical measures are not one-by-one comparable, no sudden changes in the computational fields are expected and everything must happen in a so-called transition (interphase) zone as it is the expected behavior in general phase-field models. This brings us to the results shown in Fig. 5.26. Here a selection of the results already shown in Fig. 5.23 are plotted. We are looking at the results of Path B-B′, normal to the crack field. Only the stress component S_{22}^{frac} is plotted for both the classical and gradient enhanced second-order and fourth-order formulations. In addition to these stress profiles, the crack profile is plotted in a scaled view comparable to the stress peaks, namely all the values of the crack profile are multiplied by a factor of 20.0 for better demonstration. Two vertical lines show the borders
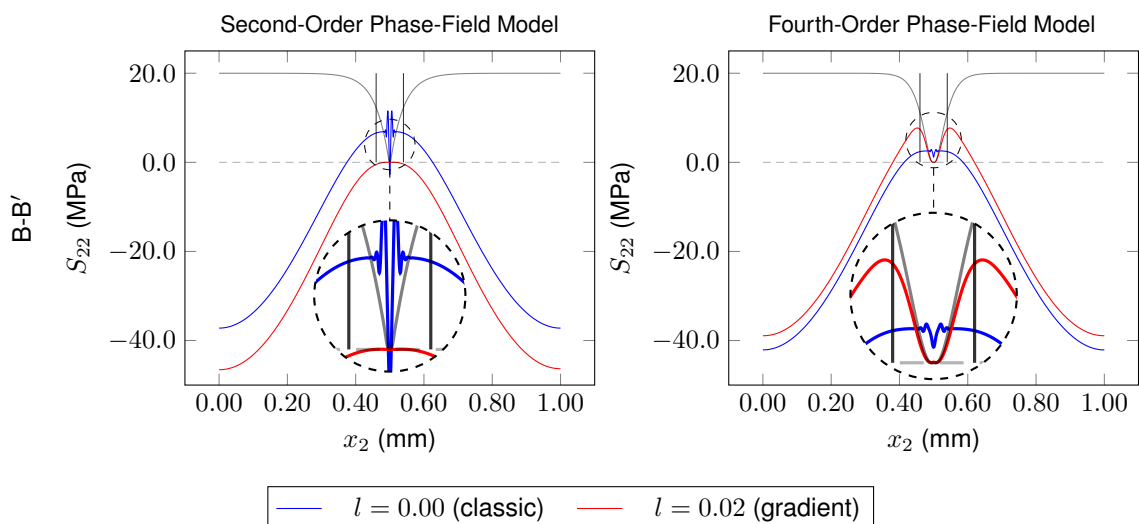
Figure 5.26: Comparison of S_{22}^{frac} stress component of the results from the classical theory and the strain gradient enhanced phase-field models for the second-order (left) and the fourth-order (right) formulations. The superscript "frac" is omitted for brevity.

of the 4ϵ zone of the crack profile. The results for the second-order and the fourth-order classical models ($l = 0$) show that the sudden change in the stress values is not directly related to the phase-field variable. The plots preserve their trend until a point very close to the cracked region and then suddenly change their value to fulfill the zero strain energy desnity requirement, resulting in an oscillation in the results. On the other hand, looking at the results for the fourth-order gradient enhanced model, the decrease in the stress component close to the cracked region follows the phase-field profile very well, not showing any sudden changes in the final plot.

6 Conclusion and Outlook

In this thesis, an integration of strain gradient elasticity into phase-field fracture mechanics is proposed. It is shown that generalized continua and in particular strain gradient theory is capable of overcoming the problems of strain energy density singularities in the presence of line and point boundary conditions. First and second strain gradient models are required to regularize the singular fields caused by these boundary conditions. Using two simplified strain gradient models, it is shown that the contributions of the second-derivatives of the displacement field in the stored energy functional are crucial in removing the effects of singularity in the strain energy density for the three-dimensional case with line loads and for the two-dimensional models with point loads. The superiority of IGA in solving partial differential equations of higher-order in comparison to the classical finite element methods is demonstrated as well. Concerning the phase-field fracture models, it is first shown that the classical Cauchy elasticity theory employed in the previous investigations results in a singular stress field, which could lead to inaccurate predictions. Therefore, the strain gradient theory is exploited, and its ability to regularize singularities is verified for these kinds of problems. That is to say, the results obtained from the proposed models meet the expectations regarding the stress distribution, i.e., the strain energy density vanishes smoothly in the broken material following the crack profile, resulting in no sudden jumps in the stress fields and consequently the strain energy density field. It has been demonstrated that the length-scale parameter of the strain gradient theory could be defined as a function of the phase-field interphase width, which makes it possible to integrate the gradient theory into the phase-field fracture formulation without introducing new parameters. Having a length-scale parameter for the microstructure seems to be a good choice as it is only through this parameter and its comparison with the length-scale parameter from the crack field that one can decide whether the crack goes through the microstructure or propagates through the boundaries of the microparticles. Two different strain gradient enhanced formulations are proposed for phase-field modelling of fracture. It is shown that both the models improve the current formulations in terms of mesh sensitivity. The fourth-order model performs better than its second-order counterpart in the sense that the results coming from this model better match the expectations.

It should be noted that this is only a preliminary investigation, and there are still various aspects that must be explored in detail. The main goal of this contribution was to create awareness in the community that stress singularities are still present in the numerical model despite employing the phase-field approach. A possible solution to this problem has been successfully proposed.

In the following, topics for further research activities are suggested:

- The gradient elasticity model used is one of the most simplified versions assuming that the higher-order stresses/strains inherit the symmetry of the classical ones making it possible to perform studies by adding a gradient length-scale parameter to the problem. More advanced versions of the theory might help improving the removal of the singularities.

- In all of the conducted simulations in this thesis, only Mode I crack propagation is considered. As discussed earlier, this choice is evident and even required if one aims to deeply study the stress and energy density fields close to the crack field. Nevertheless, the performance of the model in Mode II and III needs to be further investigated. For this, new models based on energy split of gradient materials should be derived and exploited.

- In the early chapters of this thesis, it is shown why a second strain gradient model is required to handle singularity problems related to point boundary conditions. With the same way of thinking that led us to use a first strain gradient model to overcome the singularities with the phase-field model in two dimensions, one can think of the crack tip in three dimensions to have an effect similar to a point load. For this purpose, a second-strain gradient model is needed to overcome the singularities of the classical phase-field models in three dimensions. Therefore, another potential direction for the upcoming research is to study the same phenomenon using second and higher-order strain gradient models. Our initial results in this direction suggest that unfortunately GRADELA is not performing well in three-dimensional settings. Namely, applying the same boundary conditions as shown in Fig. 5.1, results in unexpected strain energy density concentrations at the corners of the model. More sophisticated strain gradient models are therefore required to handle these problems.

- Finally, all simulations in this contribution are done based on the assumption of a pre-existing crack. In other words, only crack *propagation* is considered. The crack *nucleation* is for many applications equally important and should also be considered. Preliminary results with geometric cracks (by defining internal boundaries in the model) have shown an even more significant improvement in the outcome using the proposed model compared to the conventional ones. It can be attributed to the fact that the effect of singular points is much more pronounced when nucleation processes are studied. In these studies, the effect of using various degradation functions need to be additionally investigated.

Bibliography

[1] dell'Isola, F., Seppecher, P., and Della Corte, A. "The postulations á la D'Alembert and á la Cauchy for higher gradient continuum theories are equivalent: a review of existing results". In: *Proceedings. Mathematical, physical, and engineering sciences* 471(2183), 2015, p. 20150415. ISSN: 1364-5021. DOI: 10.1098/rspa.2015.0415.

[2] Askes, H. and Aifantis, E. C. "Gradient elasticity in statics and dynamics: An overview of formulations, length scale identification procedures, finite element implementations and new results". In: *International Journal of Solids and Structures* 48(13), 2011, pp. 1962–1990. ISSN: 00207683. DOI: 10.1016/j.ijsolstr.2011.03.006.

[3] Pideri, C. and Seppecher, P. "A second gradient material resulting from the homogenization of a heterogeneous linear elastic medium". In: *Continuum Mech Therm* 9(5), 1997, pp. 241–257.

[4] Alibert, J.-J. and Della Corte, A. "Second-gradient continua as homogenized limit of pantographic microstructured plates: a rigorous proof". In: *Z. Angew. Math. Phys.* 66(5), 2015, pp. 2855–2870.

[5] Seppecher, P., Alibert, J.-J., and dell'Isola, F. "Linear elastic trusses leading to continua with exotic mechanical interactions". In: *J Phys: Conf Ser* 319(1), 2011, p. 012018.

[6] De Felice, G. and Rizzi, N. "Homogenization for materials with microstructure". In: *ASME-PUBLICATIONS-PVP* 369, 1997, pp. 33–38.

[7] Cecchi, A. and Rizzi, N. L. "Heterogeneous elastic solids: A mixed homogenization-rigidification technique". In: *Int J Solids Struct* 38(1), 2001, pp. 29–36. DOI: 10.1016/S0020-7683(00)00018-4.

[8] Dos Reis, F. and Ganghoffer, J. F. "Construction of micropolar continua from the asymptotic homogenization of beam lattices". In: *Comput Struct* 112, 2012, pp. 354–363.

[9] Altenbach, J., Altenbach, H., and Eremeyev, V. A. "On generalized Cosserat-type theories of plates and shells: a short review and bibliography". In: *Arch Appl Mech* 80(1), 2010, pp. 73–92.

[10] Altenbach, H., Eremeyev, V. A., and Lebedev, L. P. "Micropolar Shells as Two-dimensional Generalized Continua Models". In: *Mechanics of Generalized Continua*. Springer, 2011, pp. 23–55.

[11] Federico, S. and Grillo, A. "Elasticity and Permeability of Porous Fibre-Reinforced Materials Under Large Deformations". In: *Mech Mater* 44, 2012, pp. 58–71.

[12] Tomic, A., Grillo, A., and Federico, S. "Poroelastic Materials Reinforced by Statistically Oriented Fibres - Numerical Implementation and Application to Articular Cartilage". In: *IMA J Appl Math* 79, 2014, pp. 1027–1059.

[13] Lu, Y. and Lekszycki, T. "Modeling of an initial stage of bone fracture healing". In: *Continuum Mech Therm* 27(4), 2015, pp. 851–859.

[14] Steigmann, D. J. and dell'Isola, F. "Mechanical response of fabric sheets to three-dimensional bending, twisting, and stretching". In: *Acta Mech Sinica* 31(3), 2015, pp. 373–382. ISSN: 0567-7718. DOI: 10.1007/s10409-015-0413-x.

[15] Selvadurai, A. P. S. and Nikopour, H. "Transverse elasticity of a unidirectionally reinforced composite with an irregular fibre arrangement: Experiments, theory and computations". In: *Compos Struct* 94(6), 2012, pp. 1973–1981. DOI: 10.1016/j.compstruct.2012.01.019.

[16] Goda, I., Assidi, M., and Ganghoffer, J.-F. "Equivalent mechanical properties of textile mono-layers from discrete asymptotic homogenization". In: *J Mech Phys Solids* 61(12), 2013, pp. 2537–2565.

[17] dell'Isola, F., Della Corte, A., Greco, L., and Luongo, A. "Plane bias extension test for a continuum with two inextensible families of fibers: a variational treatment with Lagrange multipliers and a perturbation solution". In: *Int J Solids Struct* 81, 2016, pp. 1–12. DOI: `10.1016/j.ijsolstr.2015.08.029`.

[18] Placidi, L., Andreaus, U., Della Corte, A., and Lekszycki, T. "Gedanken experiments for the determination of two-dimensional linear second gradient elasticity coefficients". In: *Zeitschrift für angewandte Mathematik und Physik* 66(6), 2015, pp. 3699–3725.

[19] Placidi, L., Andreaus, U., and Giorgio, I. "Identification of two-dimensional pantographic structure via a linear D4 orthotropic second gradient elastic model". In: *J Eng Math* doi: 10.1007/s10665-016-9856-8, 2016.

[20] Dietrich, L., Lekszycki, T., and Turski, K. "Problems of identification of mechanical characteristics of viscoelastic composites". In: *Acta Mech* 126(1-4), 1998, pp. 153–167.

[21] Lekszycki, T., Olhoff, N., and Pedersen, J. J. "Modelling and identification of viscoelastic properties of vibrating sandwich beams". In: *Compos Struct* 22(1), 1992, pp. 15–31.

[22] Carrella, A and Ewins, D. "Identifying and quantifying structural nonlinearities in engineering applications from measured frequency response functions". In: *Mech Syst Signal Pr* 25(3), 2011, pp. 1011–1027.

[23] Del Vescovo, D. and Fregolent, A. "Theoretical and experimental dynamic analysis aimed at the improvement of an acoustic method for fresco detachment diagnosis". In: *Mech Syst Signal Pr* 23(7), 2009, pp. 2312–2319.

[24] Javili, A., dell'Isola, F., and Steinmann, P. "Geometrically nonlinear higher-gradient elasticity with energetic boundaries". In: *Journal of the Mechanics and Physics of Solids* 61(12), 2013, pp. 2381–2401. ISSN: 00225096. DOI: `10.1016/j.jmps.2013.06.005`.

[25] Reiher, J. C., Giorgio, I., and Bertram, A. "Finite-Element Analysis of Polyhedra under Point and Line Forces in Second-Strain Gradient Elasticity". In: *Journal of Engineering Mechanics* 143(2), 2017, p. 04016112. DOI: `10.1061/(ASCE)EM.1943-7889.0001184`.

[26] Makvandi, R., Reiher, J. C., Bertram, A., and Juhre, D. "Isogeometric analysis of first and second strain gradient elasticity". In: *Computational Mechanics* 61(3), 2018, pp. 351–363. ISSN: 1432-0924. DOI: `10.1007/s00466-017-1462-8`.

[27] Reiher, J. C. "A thermodynamically consistent framework for finite third gradient elasticity and plasticity". PhD thesis. Otto-von-Guericke-Universität Magdeburg, 2017.

[28] dell'Isola, F., Cazzani, A., Andreaus, U., Placidi, L., and Barchiesi, E. "Piola, Gabrio". In: *Encyclopedia of Continuum Mechanics*. Ed. by Altenbach, H. and Öchsner, A. Berlin, Heidelberg: Springer Berlin Heidelberg, 2017, pp. 1–10. ISBN: 978-3-662-53605-6. DOI: `10.1007/978-3-662-53605-6_51-1`.

[29] dell'Isola, F., Maier, G., Perego, U., Andreaus, U., Esposito, R., and Forest, S. *The complete works of Gabrio Piola: Volume I - Commented English Translation*. Advanced Structured Materials (doi:10.1007/978-3-319-00263-7). 2014.

[30] dell'Isola, F., Andreaus, U., and Placidi, L. "At the origins and in the vanguard of peridynamics, non-local and higher-gradient continuum mechanics: An underestimated and still topical contribution of Gabrio Piola". In: *Math Mech Solids* 20(8), 2015, pp. 887–928.

[31] Cauchy, A. *Mémoire sur les systèmes isotropes de points matériels, Oeuvres complètes, 1re Série - Tome II*. pp. 351-386. Gauthier-Villars, Paris, 1850.

[32] Cauchy, A. *Mémoire sur les vibrations d'un double système de molécules et de l'éther continu dans un corps cristallisé. Oeuvres complètes, 1re Série - Tome II*. pp. 338-350. Gauthier-Villars, Paris, 1850.

[33] Cauchy, A. *Note sur l'équilibre et les mouvements vibratoires des corps solides. Oeuvres complètes, 1re Série - Tome XI*. pp. 341-346. Gauthier-Villars, Paris, 1851.

[34] Voigt, W. *Theoretische Studien über die Elasticitätsverhältnisse der Krystalle. I. Ableitung der Grundgleichungen aus der Annahme mit Polarität begabter Moleküle*. pp. 3-52. Abhandlungen der Mathematischen Classe der Königlichen Gesellschaft der Wissenschaften zu Göttingen 34, 1887.

[35] Voigt, W. *Theoretische Studien über die Elasticitätsverhältnisse der Krystalle. II. Untersuchung des elastischen Verhaltens eines Cylinders aus krystallinscher Substanz, auf dessen Mantelfläche keine Kräfte wirken, wenn die in seinem Innern wirkenden Spannungen längs der Cylinderaxe constant sind*. pp. 53-79. Abhandlungen der Mathematischen Classe der Königlichen Gesellschaft der Wissenschaften zu Göttingen 34, 1887.

[36] Voigt, W. *Theoretische Studien über die Elasticitätsverhältnisse der Krystalle. III. Untersuchung des elastischen Verhaltens eines Cylinders aus krystallinscher Substanz, auf dessen Mantelfläche keine äussern Drucke wirken, wenn die in seinem Innern wirkenden Spannungen lineäre Functionen der Axenrichtung sind*. pp. 80-100. Abhandlungen der Mathematischen Classe der Königlichen Gesellschaft der Wissenschaften zu Göttingen 34, 1887.

[37] Cosserat, E. M. P. and Cosserat, F. *Théorie des corps déformables*. Paris: A. Hermann et fils, 1909.

[38] Eringen, A. C. "Theory of Micropolar Elasticity". In: *Microcontinuum Field Theories: I. Foundations and Solids*. Ed. by Eringen, A. C. New York, NY: Springer New York, 1999, 101–248. DOI: 10.1007/978-1-4612-0555-5_5.

[39] Toupin, R. A. "Elastic materials with couple-stresses". In: *Archive for Rational Mechanics and Analysis* 11(1), 1962, pp. 385–414.

[40] Toupin, R. A. "Theories of elasticity with couple-stress". In: *Archive for Rational Mechanics and Analysis* 17(2), 1964, pp. 85–112.

[41] Mindlin, R. D. and Tiersten, H. "Effects of couple-stresses in linear elasticity". In: *Archive for Rational Mechanics and analysis* 11(1), 1962, pp. 415–448.

[42] Mindlin, R. D. "Micro-structure in linear elasticity". In: *Archive for rational mechanics and analysis* 16, 1964, pp. 51–78. DOI: 10.1007/BF00248490.

[43] Mindlin, R. D. "Second gradient of strain and surface-tension in linear elasticity". In: *International Journal of Solids and Structures* 1(4), 1965, pp. 417–438. ISSN: 00207683. DOI: 10.1016/0020-7683(65)90006-5.

[44] Gusev, A. A. and Lurie, S. A. "Symmetry conditions in strain gradient elasticity". In: *Mathematics and Mechanics of Solids* 22(4), 2015, pp. 683–691. ISSN: 1081-2865. DOI: 10.1177/1081286515606960.

[45] Polizzotto, C. "A note on the higher order strain and stress tensors within deformation gradient elasticity theories: Physical interpretations and comparisons". In: *International Journal of Solids and Structures* 90, 2016, pp. 116–121. ISSN: 00207683. DOI: 10.1016/j.ijsolstr.2016.04.001.

[46] Polizzotto, C. "A second strain gradient elasticity theory with second velocity gradient inertia – Part I: Constitutive equations and quasi-static behavior". In: *International Journal of Solids and Structures* 50(24), 2013, pp. 3749–3765. ISSN: 00207683. DOI: 10.1016/j.ijsolstr.2013.06.024.

[47] Gronwald, F. and Held, W. "Stress and hyperstress as fundamental concepts in continuum mechanics and relativistic field theories". In: *Advances in Modern Dynamics*, 1993, pp. 1–32.

[48] Jaunzemis, W. *Continuum mechanics*. New York, NY: Macmillan, 1967.

[49] Lazar, M. and Maugin, G. A. "Nonsingular stress and strain fields of dislocations and disclinations in first strain gradient elasticity". In: *International Journal of Engineering Science* 43(13-14), 2005, pp. 1157–1184. ISSN: 00207225. DOI: 10.1016/j.ijengsci.2005.01.006.

[50] Love, A. *The mathematical theory of elasticity*. 1927.

[51] Turco, E., dell'Isola, F., Cazzani, A., and Rizzi, N. L. "Hencky-type discrete model for pantographic structures: numerical comparison with second gradient continuum models". In: *Zeitschrift für angewandte Mathematik und Physik* 67(4), 2016, p. 85. ISSN: 1420-9039. DOI: 10.1007/s00033-016-0681-8.

[52] Khakalo, S., Balobanov, V., and Niiranen, J. "Modelling size-dependent bending, buckling and vibrations of 2D triangular lattices by strain gradient elasticity models: Applications to sandwich beams and auxetics". In: *International Journal of Engineering Science* 127, 2018, pp. 33–52. ISSN: 00207225. DOI: 10.1016/j.ijengsci.2018.02.004.

[53] Khakalo, S. and Niiranen, J. "Form II of Mindlin's second strain gradient theory of elasticity with a simplification: For materials and structures from nano- to macro-scales". In: *European Journal of Mechanics - A/Solids* 71, 2018, pp. 292–319. ISSN: 09977538. DOI: 10.1016/j.euromechsol.2018.02.013.

[54] Sinclair, G. B. "Stress singularities in classical elasticity–I: Removal, interpretation, and analysis". In: *Applied Mechanics Reviews* 57(4), 2004, pp. 251–298. ISSN: 0003-6900. DOI: 10.1115/1.1762503.

[55] Mousavi, S. "Dislocation-based fracture mechanics within nonlocal and gradient elasticity of bi-Helmholtz type – Part I: Antiplane analysis". In: *International Journal of Solids and Structures* 87, 2016, pp. 222–235. ISSN: 00207683. DOI: 10.1016/j.ijsolstr.2015.10.033.

[56] Karlis, G. F., Tsinopoulos, S. V., Polyzos, D., and Beskos, D. E. "Boundary element analysis of mode I and mixed mode (I and II) crack problems of 2-D gradient elasticity". In: *Computer Methods in Applied Mechanics and Engineering* 196(49), 2007, pp. 5092–5103. ISSN: 00457825. DOI: 10.1016/j.cma.2007.07.006.

[57] Jin, Y. "Atomistic Simulations of Fracture of 2d Graphene Systems and the Elastic Properties of Carbon Nanotubes". PhD Thesis. 2004.

[58] Tsai, J.-L., Tzeng, S.-H., and Tzou, Y.-J. "Characterizing the fracture parameters of a graphene sheet using atomistic simulation and continuum mechanics". In: *International Journal of Solids and Structures* 47(3), 2010, pp. 503–509. ISSN: 00207683. DOI: 10.1016/j.ijsolstr.2009.10.017.

[59] Eringen, A. C. "On differential equations of nonlocal elasticity and solutions of screw dislocation and surface waves". In: *Journal of Applied Physics* 54(9), 1983, pp. 4703–4710. ISSN: 0090-6913. DOI: 10.1063/1.332803.

[60] Gutkin, M. and Aifantis, E. C. "Dislocations in the theory of gradient elasticity". In: *Scripta Materialia* 40(5), 1999, pp. 559–566. ISSN: 13596462. DOI: 10.1016/S1359-6462(98)00424-2.

[61] Altan, S. B. and Aifantis, E. C. "On the structure of the mode III crack-tip in gradient elasticity". In: *Scripta Metallurgica et Materialia* 26(2), 1992, pp. 319–324. ISSN: 0956716X. DOI: 10.1016/0956-716X(92)90194-J.

[62] Aifantis, E. C. "On the role of gradients in the localization of deformation and fracture". In: *International Journal of Engineering Science* 30(10), 1992, pp. 1279–1299. ISSN: 00207225. DOI: 10.1016/0020-7225(92)90141-3.

[63] Niiranen, J., Khakalo, S., and Balobanov, V. "Isogeometric finite element analysis of mode I cracks within strain gradient elasticity". In: *Rakenteiden Mekaniikka* 50(3), 2017, p. 337. ISSN: 0783-6104. DOI: 10.23998/rm.65124.

[64] Aifantis, E. C. *A note on gradient elasticity and nonsingular crack fields*. 2012. DOI: 10.1515/jmbm-2012-0002.

[65] Aifantis, E. C. "Gradient Nanomechanics: Applications to Deformation, Fracture, and Diffusion in Nanopolycrystals". In: *Metallurgical and Materials Transactions A* 42(10), 2011, p. 2985. ISSN: 1543-1940. DOI: 10.1007/s11661-011-0725-9.

[66] Aifantis, E. C. "On non-singular GRADELA crack fields". In: *Theoretical and Applied Mechanics Letters* 4(5), 2014, p. 051005. ISSN: 2095-0349. DOI: 10.1063/2.1405105.

[67] Lazar, M., Maugin, G. A., and Aifantis, E. C. "Dislocations in second strain gradient elasticity". In: *International Journal of Solids and Structures* 43(6), 2006, pp. 1787 −1817. ISSN: 0020-7683. DOI: 10.1016/j.ijsolstr.2005.07.005.

[68] Aifantis, E. C. "Chapter One - Internal Length Gradient (ILG) Material Mechanics Across Scales and Disciplines". In: ed. by Bordas, S. P. and Balint, D. S. Vol. 49. Advances in Applied Mechanics. Elsevier, 2016, pp. 1 −110. DOI: 10.1016/bs.aams.2016.08.001.

[69] Ru, C. Q. and Aifantis, E. C. "A simple approach to solve boundary-value problems in gradient elasticity". In: *Acta Mechanica* 101(1), 1993, pp. 59–68. ISSN: 1619-6937. DOI: 10.1007/BF01175597.

[70] Lurie, S., Belov, P., Volkov-Bogorodsky, D., and Tuchkova, N. "Nanomechanical modeling of the nanostructures and dispersed composites". In: *Computational Materials Science* 28(3-4), 2003, pp. 529–539. ISSN: 09270256. DOI: 10.1016/j.commatsci.2003.08.010.

[71] Hughes, T., Cottrell, J., and Bazilevs, Y. "Isogeometric analysis: CAD, finite elements, NURBS, exact geometry and mesh refinement". In: *Computer Methods in Applied Mechanics and Engineering* 194(39), 2005, pp. 4135–4195. ISSN: 00457825. DOI: 10.1016/j.cma.2004.10.008.

[72] Fischer, P. "C1 Continuous Methods in Computational Gradient Elasticity". doctoralthesis. Friedrich-Alexander-Universität Erlangen-Nürnberg (FAU), 2011.

[73] Fischer, P., Klassen, M., Mergheim, J., Steinmann, P., and Müller, R. "Isogeometric analysis of 2D gradient elasticity". In: *Computational Mechanics* 47(3), 2011, pp. 325–334. ISSN: 0178-7675. DOI: 10.1007/s00466-010-0543-8.

[74] Niiranen, J., Khakalo, S., Balobanov, V., and Niemi, A. H. "Variational formulation and isogeometric analysis for fourth-order boundary value problems of gradient-elastic bar and plane strain/stress problems". In: *Computer Methods in Applied Mechanics and Engineering* 308, 2016, pp. 182–211. ISSN: 00457825. DOI: 10.1016/j.cma.2016.05.008.

[75] Jarkko Niiranen, Josef Kiendl, Antti H. Niemi, and Alessandro Reali. "Isogeometric analysis for sixth-order boundary value problems of gradient-elastic Kirchhoff plates". In: *Computer Methods in Applied Mechanics and Engineering* 316, 2017, pp. 328–348. ISSN: 00457825. DOI: 10.1016/j.cma.2016.07.008.

[76] Khakalo, S. and Niiranen, J. "Isogeometric analysis of higher-order gradient elasticity by user elements of a commercial finite element software". In: *Isogeometric Design and Analysis* 82, 2017, pp. 154–169. ISSN: 0010-4485. DOI: 10.1016/j.cad.2016.08.005.

[77] Griffith, A. A. "The Phenomena of Rupture and Flow in Solids". In: *Philosophical Transactions of the Royal Society of London. Series A, Containing Papers of a Mathematical or Physical Character* 221, 1920, pp. 163–198. ISSN: 02643952.

[78] Inglis, C. E. "Stresses in a plate due to the presence of cracks and sharp corners". In: *Transactions of the Institute of Naval Architects* 55, 1913, pp. 219–242.

[79] Irwin, G. R. "Fracture". In: *Elasticity and Plasticity / Elastizität und Plastizität*. Ed. by Flügge, S. Vol. 3 / 6. Handbuch der Physik / Encyclopedia of Physics, 0085-140X. Berlin, Heidelberg: Springer Berlin Heidelberg, 1958, pp. 551–590. ISBN: 978-3-642-45889-7. DOI: 10.1007/978-3-642-45887-3_5.

[80] Mazars, J. and Pijaudier-Cabot, G. "From damage to fracture mechanics and conversely: A combined approach". In: *International Journal of Solids and Structures* 33(20-22), 1996, pp. 3327–3342. DOI: 10.1016/0020-7683(96)00015-7.

[81] Rors, J. and Blaauwendraad, J. *Crack Models for Concrete: Discrete Or Smeared? Fixed, Multi-Directional Or Rotating?* Faculty of Civil Engineering, Delft University of Technology, 1989.

[82] Ngo, D. and Scordelis, A. "Finite element analysis of reinforced concrete beams". In: *ACI Journal Proceedings*. Vol. 64. 3. ACI. 1967.

[83] Moës, N., Dolbow, J., and Belytschko, T. "A finite element method for crack growth without remeshing". In: *International Journal for Numerical Methods in Engineering* 46(1), 1999, pp. 131–150. DOI: 10.1002/(SICI)1097-0207(19990910)46:1<131::AID-NME726>3.0.CO;2-J.

[84] Gee, B., Parchei-Esfahani, M., and Gracie, R. "XFEM simulation of a mixed-mode fracture experiment in PMMA". In: *Engineering Fracture Mechanics* 229, 2020, p. 106945. ISSN: 0013-7944. DOI: 10.1016/j.engfracmech.2020.106945.

[85] Kästner, M., Haasemann, G., and Ulbricht, V. "Multiscale XFEM-modelling and simulation of the inelastic material behaviour of textile-reinforced polymers". In: *International Journal for Numerical Methods in Engineering* 86(4-5), 2010, pp. 477–498. DOI: 10.1002/nme.3065.

[86] Haasemann, G., Kästner, M., Prüger, S., and Ulbricht, V. "Development of a quadratic finite element formulation based on the XFEM and NURBS". In: *International Journal for Numerical Methods in Engineering* 86(4-5), 2011, pp. 598–617. DOI: 10.1002/nme.3120.

[87] Melenk, J. and Babuška, I. "The partition of unity finite element method: Basic theory and applications". In: *Computer Methods in Applied Mechanics and Engineering* 139(1-4), 1996, pp. 289–314. DOI: 10.1016/s0045-7825(96)01087-0.

[88] Egger, A., Pillai, U., Agathos, K., Kakouris, E., Chatzi, E., Aschroft, I. A., and Triantafyllou, S. P. "Discrete and Phase Field Methods for Linear Elastic Fracture Mechanics: A Comparative Study and State-of-the-Art Review". In: *Applied Sciences* 9(12), 2019, p. 2436. DOI: 10.3390/app9122436.

[89] Erdogan, F. and Sih, G. C. "On the Crack Extension in Plates Under Plane Loading and Transverse Shear". In: *Journal of Basic Engineering* 85(4), 1963, pp. 519–525. DOI: 10.1115/1.3656897.

[90] Nuismer, R. J. "An energy release rate criterion for mixed mode fracture". In: *International Journal of Fracture* 11(2), 1975, pp. 245–250. DOI: 10.1007/bf00038891.

[91] Sih, G. C. "Strain-energy-density factor applied to mixed mode crack problems". In: *International Journal of Fracture* 10(3), 1974, pp. 305–321. DOI: 10.1007/bf00035493.

[92] Cheng, K. W. and Fries, T.-P. "Higher-order XFEM for curved strong and weak discontinuities". In: *International Journal for Numerical Methods in Engineering*, 2009, n/a–n/a. DOI: 10.1002/nme.2768.

[93] Sukumar, N., Moes, N., Moran, B., and Belytschko, T. "Extended finite element method for three-dimensional crack modelling". In: *International Journal for Numerical Methods in Engineering* 48(11), 2000, pp. 1549–1570. DOI: 10.1002/1097-0207(20000820)48:11<1549::aid-nme955>3.0.co;2-a.

[94] Natarajan, S., Mahapatra, D. R., and Bordas, S. P. A. "Integrating strong and weak discontinuities without integration subcells and example applications in an XFEM/GFEM framework". In: *International Journal for Numerical Methods in Engineering* 83(3), 2010, pp. 269–294. DOI: `10.1002/nme.2798`.

[95] Daux, C., Moes, N., Dolbow, J., Sukumar, N., and Belytschko, T. "Arbitrary branched and intersecting cracks with the extended finite element method". In: *International Journal for Numerical Methods in Engineering* 48(12), 2000, pp. 1741–1760. DOI: `10.1002/1097-0207(20000830)48:12<1741::aid-nme956>3.0.co;2-l`.

[96] Laborde, P., Pommier, J., Renard, Y., and Salaün, M. "High-order extended finite element method for cracked domains". In: *International Journal for Numerical Methods in Engineering* 64(3), 2005, pp. 354–381. DOI: `10.1002/nme.1370`.

[97] Menk, A. and Bordas, S. P. A. "A robust preconditioning technique for the extended finite element method". In: *International Journal for Numerical Methods in Engineering* 85(13), 2010, pp. 1609–1632. DOI: `10.1002/nme.3032`.

[98] Chevaugeon, N., Moes, N., and Minnebo, H. "Improved crack tip enrichment functions and integration for crack modeling using the extended finite element method". In: *International Journal for Multiscale Computational Engineering* 11(6), 2013, pp. 597–631. DOI: `10.1615/intjmultcompeng.2013006523`.

[99] Gupta, V., Duarte, C., Babuška, I., and Banerjee, U. "A stable and optimally convergent generalized FEM (SGFEM) for linear elastic fracture mechanics". In: *Computer Methods in Applied Mechanics and Engineering* 266, 2013, pp. 23–39. DOI: `10.1016/j.cma.2013.07.010`.

[100] Loehnert, S. "A stabilization technique for the regularization of nearly singular extended finite elements". In: *Computational Mechanics* 54(2), 2014, pp. 523–533. DOI: `10.1007/s00466-014-1003-7`.

[101] Strouboulis, T., Babuška, I., and Copps, K. "The design and analysis of the Generalized Finite Element Method". In: *Computer Methods in Applied Mechanics and Engineering* 181(1-3), 2000, pp. 43–69. DOI: `10.1016/s0045-7825(99)00072-9`.

[102] Duarte, C. and Oden, J. "An h-p adaptive method using clouds". In: *Computer Methods in Applied Mechanics and Engineering* 139(1-4), 1996, pp. 237–262. DOI: `10.1016/s0045-7825(96)01085-7`.

[103] Duarte, C., Babuška, I., and Oden, J. "Generalized finite element methods for three-dimensional structural mechanics problems". In: *Computers & Structures* 77(2), 2000, pp. 215–232. DOI: `10.1016/s0045-7949(99)00211-4`.

[104] Belytschko, T., Gracie, R., and Ventura, G. "A review of extended/generalized finite element methods for material modeling". In: *Modelling and Simulation in Materials Science and Engineering* 17(4), 2009, p. 043001. DOI: `10.1088/0965-0393/17/4/043001`.

[105] Silling, S. A. "Reformulation of elasticity theory for discontinuities and long-range forces". In: *Journal of the Mechanics and Physics of Solids* 48(1), 2000, pp. 175–209.

[106] Silling, S. A., Epton, M, Weckner, O, Xu, J., and Askari, E. "Peridynamic states and constitutive modeling". In: *Journal of Elasticity* 88(2), 2007, pp. 151–184.

[107] Macek, R. W. and Silling, S. A. "Peridynamics via finite element analysis". In: *Finite Elements in Analysis and Design* 43(15), 2007, pp. 1169–1178.

[108] Ha, Y. D. and Bobaru, F. "Studies of dynamic crack propagation and crack branching with peridynamics". In: *International Journal of Fracture* 162(1-2), 2010, pp. 229–244.

[109] Willberg, C., Wiedemann, L., and Rädel, M. "A mode-dependent energy-based damage model for peridynamics and its implementation". In: *Journal of Mechanics of Materials and Structures* 14(2), 2019, pp. 193–217.

[110] Silling, S. and Askari, E. "A meshfree method based on the peridynamic model of solid mechanics". In: *Computers & Structures* 83(17-18), 2005, pp. 1526–1535. DOI: 10.1016/j.compstruc.2004.11.026.

[111] Ganzenmüller, G., Hiermaier, S., and May, M. "On the similarity of meshless discretizations of Peridynamics and Smooth-Particle Hydrodynamics". In: *Computers & Structures* 150, 2015, pp. 71–78. DOI: 10.1016/j.compstruc.2014.12.011.

[112] Ren, H., Zhuang, X., Cai, Y., and Rabczuk, T. "Dual-horizon peridynamics". In: *International Journal for Numerical Methods in Engineering* 108(12), 2016, pp. 1451–1476. DOI: 10.1002/nme.5257.

[113] Bobaru, F., Ha, Y., and Hu, W. "Damage progression from impact in layered glass modeled with peridynamics". In: *Open Engineering* 2(4), 2012. DOI: 10.2478/s13531-012-0020-6.

[114] Ha, Y. D. "An extended ghost interlayer model in peridynamic theory for high-velocity impact fracture of laminated glass structures". In: *Computers & Mathematics with Applications* 80(5), 2020, pp. 744–761. DOI: 10.1016/j.camwa.2020.05.003.

[115] Song, J.-H., Areias, P. M. A., and Belytschko, T. "A method for dynamic crack and shear band propagation with phantom nodes". In: *International Journal for Numerical Methods in Engineering* 67(6), 2006, pp. 868–893. DOI: 10.1002/nme.1652.

[116] Hansbo, A. and Hansbo, P. "A finite element method for the simulation of strong and weak discontinuities in solid mechanics". In: *Computer Methods in Applied Mechanics and Engineering* 193(33-35), 2004, pp. 3523–3540. DOI: 10.1016/j.cma.2003.12.041.

[117] Timon Rabczuk, P. A. "A Meshfree Thin Shell for Arbitrary Evolving Cracks Based on An Extrinsic Basis". In: *Computer Modeling in Engineering & Sciences* 16(2), 2006, pp. 115–130. ISSN: 1526-1506. DOI: 10.3970/cmes.2006.016.115.

[118] Zhuang, X., Augarde, C., and Mathisen, K. "Fracture modeling using meshless methods and level sets in 3D: Framework and modeling". In: *International Journal for Numerical Methods in Engineering* 92(11), 2012, pp. 969–998. DOI: 10.1002/nme.4365.

[119] Müller, A., Wenck, J., Goswami, S., Lindemann, J., Hohe, J., and Becker, W. "The boundary finite element method for predicting directions of cracks emerging from notches at bimaterial junctions". In: *Engineering Fracture Mechanics* 72(3), 2005, pp. 373–386. DOI: 10.1016/j.engfracmech.2004.04.004.

[120] Lindemann, J. and Becker, W. In: *Mechanics of Composite Materials* 38(5), 2002, pp. 407–416. DOI: 10.1023/a:1020930125415.

[121] Yang, Z. "Fully automatic modelling of mixed-mode crack propagation using scaled boundary finite element method". In: *Engineering Fracture Mechanics* 73(12), 2006, pp. 1711–1731. DOI: 10.1016/j.engfracmech.2006.02.004.

[122] Barenblatt, G. "The Mathematical Theory of Equilibrium Cracks in Brittle Fracture". In: *Advances in Applied Mechanics*. Elsevier, 1962, pp. 55–129. DOI: 10.1016/s0065-2156(08)70121-2.

[123] Dugdale, D. "Yielding of steel sheets containing slits". In: *Journal of the Mechanics and Physics of Solids* 8(2), 1960, pp. 100–104. DOI: 10.1016/0022-5096(60)90013-2.

[124] Soparat, P. and Nanakorn, P. "Analysis of Cohesive Crack Growth by the Element-Free Galerkin Method". In: *Journal of Mechanics* 24(1), 2008, pp. 45–54. DOI: 10.1017/s1727719100001544.

[125] Steinbach, I. "Phase-field models in materials science". In: *Modelling and Simulation in Materials Science and Engineering* 17(7), 2009, p. 073001. DOI: 10.1088/0965-0393/17/7/073001.

[126] Haar, D. T. *Collected Papers of L.D. Landau*. Elsevier Science, 2013. ISBN: 9781483152707.

[127] Rowlinson, J. S. "Translation of J. D. van der Waals' "The thermodynamik theory of capillarity under the hypothesis of a continuous variation of density"". In: *Journal of Statistical Physics* 20(2), 1979, pp. 197–200. ISSN: 1572-9613. DOI: 10.1007/BF01011513.

[128] Cahn, J. W. and Hilliard, J. E. "Free Energy of a Nonuniform System. I. Interfacial Free Energy". In: *The Journal of Chemical Physics* 28(2), 1958, pp. 258–267. DOI: 10.1063/1.1744102.

[129] Cahn, J. W. and Hilliard, J. E. "Free Energy of a Nonuniform System. III. Nucleation in a Two-Component Incompressible Fluid". In: *The Journal of Chemical Physics* 31(3), 1959, pp. 688–699. DOI: 10.1063/1.1730447.

[130] Aifantis, E. C. and Serrin, J. B. "The mechanical theory of fluid interfaces and Maxwell's rule". In: *Journal of Colloid and Interface Science* 96(2), 1983, pp. 517 –529. ISSN: 0021-9797. DOI: 10.1016/0021-9797(83)90053-X.

[131] Fix, G. J., Fasano, A., and Primicerio, M. In: *Pitman, Boston*, 1983, p. 580.

[132] Langer, J. S. "Models of pattern formation in first-order phase transitions". In: *Directions in Condensed Matter Physics*. 1986, pp. 165–186. DOI: 10.1142/9789814415309_0005.

[133] Francfort, G. A. and Marigo, J.-J. "Revisiting brittle fracture as an energy minimization problem". In: *Journal of the Mechanics and Physics of Solids* 46(8), 1998, pp. 1319–1342. ISSN: 00225096. DOI: 10.1016/S0022-5096(98)00034-9.

[134] Bourdin, B., Francfort, G. A., and Marigo, J.-J. "Numerical experiments in revisited brittle fracture". In: *Journal of the Mechanics and Physics of Solids* 48(4), 2000, pp. 797–826. ISSN: 00225096. DOI: 10.1016/S0022-5096(99)00028-9.

[135] Miehe, C., Welschinger, F., and Hofacker, M. "Thermodynamically consistent phase-field models of fracture: Variational principles and multi-field FE implementations". In: *International Journal for Numerical Methods in Engineering* 83(10), 2010, pp. 1273–1311. ISSN: 1097-0207. DOI: 10.1002/nme.2861.

[136] Miehe, C., Hofacker, M., and Welschinger, F. "A phase field model for rate-independent crack propagation: Robust algorithmic implementation based on operator splits". In: *Computer Methods in Applied Mechanics and Engineering* 199(45-48), 2010, pp. 2765–2778. ISSN: 00457825. DOI: 10.1016/j.cma.2010.04.011.

[137] Ambati, M., Gerasimov, T., and Lorenzis, L. de. "A review on phase-field models of brittle fracture and a new fast hybrid formulation". In: *Computational Mechanics* 55(2), 2015, pp. 383–405. ISSN: 1432-0924. DOI: 10.1007/s00466-014-1109-y.

[138] Larsen, C. J., Ortner, C., and Süli, E. "Existence of solutions to a regularized model of dynamic fracture". In: *Mathematical Models and Methods in Applied Sciences* 20(07), 2010, pp. 1021–1048. ISSN: 0218-2025. DOI: 10.1142/S0218202510004520.

[139] Bourdin, B., Larsen, C. J., and Richardson, C. L. "A time-discrete model for dynamic fracture based on crack regularization". In: *International Journal of Fracture* 168(2), 2011, pp. 133–143. ISSN: 0376-9429. DOI: 10.1007/s10704-010-9562-x.

[140] Borden, M. J., Verhoosel, C. V., Scott, M. A., Hughes, T. J., and Landis, C. M. "A phase-field description of dynamic brittle fracture". In: *Computer Methods in Applied Mechanics and Engineering* 217-220, 2012, pp. 77–95. ISSN: 00457825. DOI: 10.1016/j.cma.2012.01.008.

[141] Miehe, C. and Schänzel, L.-M. "Phase field modeling of fracture in rubbery polymers. Part I: Finite elasticity coupled with brittle failure". In: *Journal of the Mechanics and Physics of Solids* 65, 2014, pp. 93–113. ISSN: 00225096. DOI: 10.1016/j.jmps.2013.06.007.

[142] Wilson, Z. A., Borden, M. J., and Landis, C. M. "A phase-field model for fracture in piezoelectric ceramics". In: *International Journal of Fracture* 183(2), 2013, pp. 135–153. ISSN: 1573-2673. DOI: 10.1007/s10704-013-9881-9.

[143] Miehe, C., Schänzel, L.-M., and Ulmer, H. "Phase field modeling of fracture in multi-physics problems. Part I. Balance of crack surface and failure criteria for brittle crack propagation in thermo-elastic solids". In: *Computer Methods in Applied Mechanics and Engineering* 294, 2015, pp. 449–485. ISSN: 00457825. DOI: 10.1016/j.cma.2014.11.016.

[144] Borden, M. J., Hughes, T. J., Landis, C. M., Anvari, A., and Lee, I. J. "A phase-field formulation for fracture in ductile materials: Finite deformation balance law derivation, plastic degradation, and stress triaxiality effects". In: *Computer Methods in Applied Mechanics and Engineering* 312, 2016, pp. 130–166. ISSN: 00457825. DOI: 10.1016/j.cma.2016.09.005.

[145] Weinberg, K. and Hesch, C. "A high-order finite deformation phase-field approach to fracture". In: *Continuum Mechanics and Thermodynamics* 29(4), 2017, pp. 935–945. ISSN: 1432-0959. DOI: 10.1007/s00161-015-0440-7.

[146] Ambati, M. and Lorenzis, L. de. "Phase-field modeling of brittle and ductile fracture in shells with isogeometric NURBS-based solid-shell elements". In: *Computer Methods in Applied Mechanics and Engineering* 312, 2016, pp. 351–373. ISSN: 00457825. DOI: 10.1016/j.cma.2016.02.017.

[147] Hennig, P., Müller, S., and Kästner, M. "Bézier extraction and adaptive refinement of truncated hierarchical NURBS". In: *Computer Methods in Applied Mechanics and Engineering* 305, 2016, pp. 316–339. ISSN: 00457825. DOI: 10.1016/j.cma.2016.03.009.

[148] Major, J. "7.3 Stress, Deformation, Conservation, and Rheology: A Survey of Key Concepts in Continuum Mechanics". In: *Treatise on Geomorphology*. Elsevier, 2013, pp. 20–43. DOI: 10.1016/b978-0-12-374739-6.00146-9.

[149] Malvern, L. E. "Introduction to the mechanics of a continuous medium". In: 1969.

[150] Bird, R., Stewart, W., Stewart, W., Lightfoot, E., and Lightfoot, E. *Transport Phenomena*. Wiley International edition. Wiley, 1960. ISBN: 9780471073925.

[151] Bejan, A. *Convection Heat Transfer*. Wiley, 1984. ISBN: 9780471896128.

[152] Bower, A. F. *Applied Mechanics of Solids*. CRC PR INC, Oct. 2009. 794 pp. ISBN: 1439802475.

[153] Lanczos, C. *The variational principles of mechanics*. Courier Corporation, 2012.

[154] Abali, B. E. "Revealing the physical insight of a length-scale parameter in metamaterials by exploiting the variational formulation". In: *Continuum Mechanics and Thermodynamics* 31(4), 2018, pp. 885–894. DOI: 10.1007/s00161-018-0652-8.

[155] Mittal, J. P., Kaur, I., and Sharma, R. C. *Encyclopedia of Technical Education*. Encyclopaedia of Technical Education. Mittal Publications, 2015. ISBN: 9788170994312.

[156] Altenbach, H., Altenbach, J., Kissing, W., and Altenbach, H. *Mechanics of composite structural elements*. Springer, 2004.

[157] Mindlin, R. D. and Eshel, N. N. "On first strain-gradient theories in linear elasticity". In: *International Journal of Solids and Structures* 4(1), 1968, pp. 109–124. ISSN: 00207683. DOI: 10.1016/0020-7683(68)90036-X.

[158] Lam, D., Yang, F., Chong, A., Wang, J., and Tong, P. "Experiments and theory in strain gradient elasticity". In: *Journal of the Mechanics and Physics of Solids* 51(8), 2003, pp. 1477–1508. ISSN: 00225096. DOI: 10.1016/S0022-5096(03)00053-X.

[159] Namazu, T., Isono, Y., and Tanaka, T. "Evaluation of size effect on mechanical properties of single crystal silicon by nanoscale bending test using AFM". In: *Journal of Microelectromechanical Systems* 9(4), 2000, pp. 450–459. ISSN: 1941-0158. DOI: 10.1109/84.896765.

[160] Abali, B. E., Yang, H., and Papadopoulos, P. "A Computational Approach for Determination of Parameters in Generalized Mechanics". In: *Higher gradient materials and related generalized continua*. Ed. by Altenbach, H., Müller, W. H., and Abali, B. E. Advanced Structured Materials Ser. Cham: Springer, 2019, pp. 1–18. ISBN: 978-3-030-30406-5. DOI: 10.1007/978-3-030-30406-5_1.

[161] Bertram, A. *Compendium on Gradient Materials*. 2017. DOI: 10.13140/RG.2.2.36769.51045.

[162] Gross, D. and Seelig, T. *Fracture mechanics: with an introduction to micromechanics*. Springer, 2017.

[163] Borden, M. J. "Isogeometric analysis of phase-field models for dynamic brittle and ductile fracture". PhD thesis. 2012.

[164] Amor, H., Marigo, J.-J., and Maurini, C. "Regularized formulation of the variational brittle fracture with unilateral contact: Numerical experiments". In: *Journal of the Mechanics and Physics of Solids* 57(8), 2009, pp. 1209–1229. ISSN: 00225096. DOI: 10.1016/j.jmps.2009.04.011.

[165] Nguyen, T. T., Yvonnet, J., Bornert, M., Chateau, C., Sab, K., Romani, R., and Roy, R. L. "On the choice of parameters in the phase field method for simulating crack initiation with experimental validation". In: *International Journal of Fracture* 197(2), 2016, pp. 213–226. DOI: 10.1007/s10704-016-0082-1.

[166] Tanné, E., Li, T., Bourdin, B., Marigo, J.-J., and Maurini, C. "Crack nucleation in variational phase-field models of brittle fracture". In: *Journal of the Mechanics and Physics of Solids* 110, 2018, pp. 80–99. ISSN: 00225096. DOI: 10.1016/j.jmps.2017.09.006.

[167] Wu, J.-Y., Nguyen, V. P., Nguyen, C. T., Sutula, D., Sinaie, S., and Bordas, S. P. "Phase-field modeling of fracture". In: *Advances in Applied Mechanics*. Elsevier, 2020, pp. 1–183. DOI: 10.1016/bs.aams.2019.08.001.

[168] Ginzburg, V. and Landau, L. "On the Theory of superconductivity". In: *Zh. Eksp. Teor. Fiz.* 20, 1950, pp. 1064–1082.

[169] Gurtin, M. E. "Generalized Ginzburg-Landau and Cahn-Hilliard equations based on a microforce balance". In: *Physica D: Nonlinear Phenomena* 92(3), 1996, pp. 178 –192. ISSN: 0167-2789. DOI: 10.1016/0167-2789(95)00173-5.

[170] Kuhn, C. and Müller, R. "A continuum phase field model for fracture". In: *Engineering Fracture Mechanics* 77(18), 2010, pp. 3625–3634. ISSN: 00137944. DOI: 10.1016/j.engfracmech.2010.08.009.

[171] Kuhn, C. and Müller, R. "A new finite element technique for a phase field model of brittle fracture". In: *Journal of Theoretical and Applied Mechanics* 49, 2011, pp. 1115–1133.

[172] Borden, M. J., Hughes, T. J., Landis, C. M., and Verhoosel, C. V. "A higher-order phase-field model for brittle fracture: Formulation and analysis within the isogeometric analysis framework". In: *Computer Methods in Applied Mechanics and Engineering* 273, 2014, pp. 100–118. ISSN: 00457825. DOI: 10.1016/j.cma.2014.01.016.

[173] Li, B., Peco, C., Millán, D., Arias, I., and Arroyo, M. "Phase-field modeling and simulation of fracture in brittle materials with strongly anisotropic surface energy". In: *International Journal for Numerical Methods in Engineering* 102(3-4), 2015, pp. 711–727. ISSN: 1097-0207. DOI: 10.1002/nme.4726.

[174] Sargado, J. M., Keilegavlen, E., Berre, I., and Nordbotten, J. M. "High-accuracy phase-field models for brittle fracture based on a new family of degradation functions". In: *Journal of the Mechanics and Physics of Solids* 111, 2018, pp. 458–489. ISSN: 00225096. DOI: 10.1016/j.jmps.2017.10.015.

[175] Franke, M., Hesch, C., and Dittmann, M. "Phase-field approach to fracture for finite-deformation contact problems". In: *PAMM* 16(1), 2016, pp. 123–124. DOI: `10.1002/pamm.201610050`.

[176] Dittmann, M., Aldakheel, F., Schulte, J., Wriggers, P., and Hesch, C. "Variational phase-field formulation of non-linear ductile fracture". In: *Computer Methods in Applied Mechanics and Engineering* 342, 2018, pp. 71–94. DOI: `10.1016/j.cma.2018.07.029`.

[177] Geelen, R. J., Liu, Y., Hu, T., Tupek, M. R., and Dolbow, J. E. "A phase-field formulation for dynamic cohesive fracture". In: *Computer Methods in Applied Mechanics and Engineering* 348, 2019, pp. 680–711. DOI: `10.1016/j.cma.2019.01.026`.

[178] Pham, K., Amor, H., Marigo, J.-J., and Maurini, C. "Gradient Damage Models and Their Use to Approximate Brittle Fracture". In: *International Journal of Damage Mechanics* 20(4), 2011, pp. 618–652. DOI: `10.1177/1056789510386852`.

[179] Pham, K., Amor, H., Marigo, J.-J., and Maurini, C. "Gradient Damage Models and Their Use to Approximate Brittle Fracture". In: *International Journal of Damage Mechanics* 20(4), 2011, pp. 618–652. DOI: `10.1177/1056789510386852`.

[180] Karma, A. and Rappel, W.-J. "Quantitative phase-field modeling of dendritic growth in two and three dimensions". In: *Physical Review E* 57(4), 1998, pp. 4323–4349. DOI: `10.1103/physreve.57.4323`.

[181] Karma, A., Kessler, D. A., and Levine, H. "Phase-Field Model of Mode III Dynamic Fracture". In: *Physical Review Letters* 87(4), 2001, p. 045501. DOI: `10.1103/physrevlett.87.045501`.

[182] Kuhn, C. "Numerical and Analytical Investigation of a Phase Field Model for Fracture". doctoralthesis. Technische Universität Kaiserslautern, 2013, pp. X, 143.

[183] Gerasimov, T. and Lorenzis, L. D. "On penalization in variational phase-field models of brittle fracture". In: *Computer Methods in Applied Mechanics and Engineering* 354, 2019, pp. 990–1026. DOI: `10.1016/j.cma.2019.05.038`.

[184] Geers, M., de Borst, R., Brekelmans, W., and Peerlings, R. "Strain-based transient-gradient damage model for failure analyses". In: *Computer Methods in Applied Mechanics and Engineering* 160(1), 1998, pp. 133 –153. ISSN: 0045-7825. DOI: `10.1016/S0045-7825(98)80011-X`.

[185] Ambrosio, L. and Tortorelli, V. M. *On the Approximation of Free Discontinuity Problems*. Preprints di matematica / Scuola Normale Superiore. Scuola Normale Superiore, 1990.

[186] Kuhn, C., Schlüter, A., and Müller, R. "On degradation functions in phase field fracture models". In: *Computational Materials Science* 108, 2015, pp. 374–384. ISSN: 09270256. DOI: `10.1016/j.commatsci.2015.05.034`.

[187] Karma, A. and Lobkovsky, A. E. "Unsteady Crack Motion and Branching in a Phase-Field Model of Brittle Fracture". In: *Physical Review Letters* 92(24), 2004, p. 245510. DOI: `10.1103/physrevlett.92.245510`.

[188] Henry, H. and Levine, H. "Dynamic Instabilities of Fracture under Biaxial Strain Using a Phase Field Model". In: *Phys. Rev. Lett.* 93, 10 2004, p. 105504. DOI: `10.1103/PhysRevLett.93.105504`.

[189] Kuhn, H. W. and Tucker, A. W. "Nonlinear programming". In: *Proceedings of the Second Berkeley Symposium on Mathematical Statistics and Probability, 1950*. University of California Press, Berkeley and Los Angeles, 1951, pp. 481–492.

[190] Karush, W. "Minima of functions of several variables with inequalities as side conditions." PhD thesis. Thesis (S.M.)–University of Chicago, Department of Mathematics, December 1939., 1939.

Bibliography

[191] Gerasimov, T. and De Lorenzis, L. "A line search assisted monolithic approach for phase-field computing of brittle fracture". In: *Computer Methods in Applied Mechanics and Engineering* 312, 2016. Phase Field Approaches to Fracture, pp. 276 –303. ISSN: 0045-7825. DOI: 10.1016/j.cma.2015.12.017.

[192] May, S., Vignollet, J., and Borst, R. de. "A new arc-length control method based on the rates of the internal and the dissipated energy". In: *Engineering Computations* 33(1), 2016, pp. 100–115. DOI: 10.1108/ec-02-2015-0044.

[193] Placidi, L. and Barchiesi, E. "Energy approach to brittle fracture in strain-gradient modelling". In: *Proceedings of the Royal Society A: Mathematical, Physical and Engineering Sciences* 474(2210), 2018, p. 20170878.

[194] Farrell, P. and Maurini, C. "Linear and nonlinear solvers for variational phase-field models of brittle fracture". In: *International Journal for Numerical Methods in Engineering* 109(5), 2017, pp. 648–667. DOI: 10.1002/nme.5300.

[195] Wu, J.-Y. "A unified phase-field theory for the mechanics of damage and quasi-brittle failure". In: *Journal of the Mechanics and Physics of Solids* 103, 2017, pp. 72 –99. ISSN: 0022-5096. DOI: 10.1016/j.jmps.2017.03.015.

[196] Wu, J.-Y. "Robust numerical implementation of non-standard phase-field damage models for failure in solids". In: *Computer Methods in Applied Mechanics and Engineering* 340, 2018, pp. 767 –797. ISSN: 0045-7825. DOI: doi.org/10.1016/j.cma.2018.06.007.

[197] Lancioni, G. and Royer-Carfagni, G. "The Variational Approach to Fracture Mechanics. A Practical Application to the French Panthéon in Paris". In: *Journal of Elasticity* 95(1-2), 2009, pp. 1–30. DOI: 10.1007/s10659-009-9189-1.

[198] Wu, J.-Y., Nguyen, V. P., Zhou, H., and Huang, Y. "A variationally consistent phase-field anisotropic damage model for fracture". In: *Computer Methods in Applied Mechanics and Engineering* 358, 2020, p. 112629. DOI: 10.1016/j.cma.2019.112629.

[199] Bilgen, C. and Weinberg, K. "On the crack-driving force of phase-field models in linearized and finite elasticity". In: *Computer Methods in Applied Mechanics and Engineering* 353, 2019, pp. 348–372. DOI: 10.1016/j.cma.2019.05.009.

[200] Placidi, L., Barchiesi, E., and Misra, A. "A strain gradient variational approach to damage: a comparison with damage gradient models and numerical results". In: *Mathematics and Mechanics of Complex Systems* 6(2), 2018, pp. 77–100.

[201] De Boor, C. "On calculating with B-splines". In: *Journal of Approximation theory* 6(1), 1972, pp. 50–62.

[202] Cottrell, J. A., Hughes, T. J. R., and Bazilevs, Y. "NURBS as a Pre-Analysis Tool: Geometric Design and Mesh Generation". In: *Isogeometric Analysis*. John Wiley & Sons, Ltd, 2009, pp. 19–68. ISBN: 9780470749081. DOI: 10.1002/9780470749081.ch2.

[203] Piegl, L. and Tiller, W. *The NURBS Book (2nd Ed.)* New York, NY, USA: Springer-Verlag New York, Inc., 1997. ISBN: 3-540-61545-8.

[204] Borden, M. J., Scott, M. A., Evans, J. A., and Hughes, T. J. R. "Isogeometric finite element data structures based on Bézier extraction of NURBS". In: *International Journal for Numerical Methods in Engineering* 87(1–5), 2011, pp. 15–47. ISSN: 1097-0207. DOI: 10.1002/nme.2968.

[205] D'Angella, D., Kollmannsberger, S., Rank, E., and Reali, A. "Multi-level Bézier extraction for hierarchical local refinement of Isogeometric Analysis". In: *Computer Methods in Applied Mechanics and Engineering* 328, 2018, pp. 147–174. DOI: 10.1016/j.cma.2017.08.017.

[206] Mousavi, S. M. and Paavola, J. "Analysis of plate in second strain gradient elasticity". In: *Arch Appl Mech* 84(8), 2014, pp. 1135–1143. ISSN: 1432-0681. DOI: 10.1007/s00419-014-0871-9.

[207] Taylor, R. L. *FEAP - Finite Element Analysis Program*. 2020. URL: http://projects.ce.berkeley.edu/feap.

[208] Hughes, T., Reali, A., and Sangalli, G. "Efficient quadrature for NURBS-based isogeometric analysis". In: *Comput Method Appl M* 199(5), 2010. Computational Geometry and Analysis, pp. 301 –313. ISSN: 0045-7825. DOI: 10.1016/j.cma.2008.12.004.

[209] Auricchio, F., Calabrò, F., Hughes, T., Reali, A., and Sangalli, G. "A simple algorithm for obtaining nearly optimal quadrature rules for NURBS-based isogeometric analysis". In: *Comput Method Appl M* 249, 2012. Higher Order Finite Element and Isogeometric Methods, pp. 15 –27. ISSN: 0045-7825. DOI: 10.1016/j.cma.2012.04.014.

[210] Calabrò, F., Sangalli, G., and Tani, M. "Fast formation of isogeometric Galerkin matrices by weighted quadrature". In: *Comput Method Appl M* 316, 2017. Special Issue on Isogeometric Analysis: Progress and Challenges, pp. 606 –622. ISSN: 0045-7825. DOI: 10.1016/j.cma.2016.09.013.

[211] Liu, Z.-K., Roggel, J., and Juhre, D., eds. *Simulation des Risswachstums in einer Compact Tension - Probe nach ASTM E399 mit einem spröden Phasenfeldmodell*. 2017.

[212] Richards, F. "A Gibbs phenomenon for spline functions". In: *Journal of Approximation Theory* 66(3), 1991, pp. 334–351. ISSN: 0021-9045. DOI: 10.1016/0021-9045(91)90034-8.

[213] Zhang, Z. and Martin, C. F. "Convergence and Gibbs' phenomenon in cubic spline interpolation of discontinuous functions". In: *Journal of Computational and Applied Mathematics* 87(2), 1997, pp. 359–371. ISSN: 0377-0427. DOI: 10.1016/S0377-0427(97)00199-4.

[214] Hansen, C. D. and Johnson, C. R. *The visualization handbook*. Amsterdam and London: Elsevier Butterworth-Heinemann, 2005. ISBN: 012387582X.

[215] Nguyen, V. P. and Bordas, S. "Extended Isogeometric Analysis for Strong and Weak Discontinuities". In: *Isogeometric methods for numerical simulation*. Ed. by Beer, G. and Bordas, S. P. International Centre for Mechanical Sciences. Courses and lectures, 0254-1971. Wien: Springer, 2015, pp. 21–120. ISBN: 978-3-7091-1843-6. DOI: 10.1007/978-3-7091-1843-6{_}2.

[216] Makvandi, R., Venghaus, H., and Juhre, D. *NPVI add-on for FEAP*. Version v1.4. July 2020. DOI: 10.5281/zenodo.3945132.

[217] Govindjee, S., Strain, J., Mitchell, T. J., and Taylor, R. L. "Convergence of an efficient local least-squares fitting method for bases with compact support". In: *Computer Methods in Applied Mechanics and Engineering* 213-216, 2012, pp. 84–92. ISSN: 00457825. DOI: 10.1016/j.cma.2011.11.017.

[218] Cordero, N. M., Forest, S., and Busso, E. P. "Second strain gradient elasticity of nano-objects". In: *Journal of the Mechanics and Physics of Solids* 97, 2016, pp. 92–124. ISSN: 00225096. DOI: 10.1016/j.jmps.2015.07.012.

[219] Pideri, C. and Seppecher, P. "A second gradient material resulting from the homogenization of an heterogeneous linear elastic medium". In: *Continuum Mechanics and Thermodynamics* 9(5), 1997, pp. 241–257.

[220] dell'Isola, F., Madeo, A., and Seppecher, P. "Cauchy tetrahedron argument applied to higher contact interactions". In: *Archive for Rational Mechanics and Analysis* 219(3), 2016, pp. 1305–1341.

[221] Eremeyev, V. A. "On effective properties of materials at the nano-and microscales considering surface effects". In: *Acta Mechanica* 227(1), 2016, pp. 29–42.

[222]   Mandadapu, K. K., Abali, B. E., and Papadopoulos, P. "On the Polar Nature and Invariance Properties of a Thermomechanical Theory for Continuum-on-Continuum Homogenization". In: *arXiv preprint arXiv:1808.02540*, 2018.

[223]   Turco, E., Golaszewski, M., Giorgio, I., and D'Annibale, F. "Pantographic lattices with non-orthogonal fibres: experiments and their numerical simulations". In: *Composites Part B: Engineering* 118, 2017, pp. 1–14.

[224]   Barchiesi, E., Ganzosch, G., Liebold, C., Placidi, L., Grygoruk, R., and Müller, W. H. "Out-of-plane buckling of pantographic fabrics in displacement-controlled shear tests: experimental results and model validation". In: *Continuum Mechanics and Thermodynamics*, 2018, pp. 1–13.

[225]   Ganzosch, G, Hoschke, K, Lekszycki, T, Giorgio, I, Turco, E, and Müller, W. H. "3D-Measurements of 3D-Deformations of Pantographic Structures". In: *Technische Mechanik* 38(3), 2018, pp. 233–245.

[226]   Forest, S., Dendievel, R., and Canova, G. R. "Estimating the overall properties of heterogeneous Cosserat materials". In: *Modelling and Simulation in Materials Science and Engineering* 7(5), 1999, p. 829.

[227]   Kochmann, D. M. and Venturini, G. N. "Homogenized mechanical properties of auxetic composite materials in finite-strain elasticity". In: *Smart Materials and Structures* 22(8), 2013, p. 084004.

[228]   Rahali, Y, Giorgio, I, Ganghoffer, J., and dell'Isola, F. "Homogenization à la Piola produces second gradient continuum models for linear pantographic lattices". In: *International Journal of Engineering Science* 97, 2015, pp. 148–172.

[229]   Barboura, S. and Li, J. "Establishment of strain gradient constitutive relations by using asymptotic analysis and the finite element method for complex periodic microstructures". In: *International Journal of Solids and Structures* 136, 2018, pp. 60–76.

[230]   dell'Isola, F., Seppecher, P., Spagnuolo, M., Barchiesi, E., Hild, F., Lekszycki, T., Giorgio, I., Placidi, L., Andreaus, U., Cuomo, M., Eugster, S. R., Pfaff, A., Hoschke, K., Langkemper, R., Turco, E., Sarikaya, R., Misra, A., De Angelo, M., D'Annibale, F., Bouterf, A., Pinelli, X., Misra, A., Desmorat, B., Pawlikowski, M., Dupuy, C., Scerrato, D., Peyre, P., Laudato, M., Manzari, L., Göransson, P., Hesch, C., Hesch, S., Franciosi, P., Dirrenberger, J., Maurin, F., Vangelatos, Z., Grigoropoulos, C., Melissinaki, V., Farsari, M., Muller, W., Abali, B. E., Liebold, C., Ganzosch, G., Harrison, P., Drobnicki, R., Igumnov, L., Alzahrani, F., and Hayat, T. "Advances in pantographic structures: design, manufacturing, models, experiments and image analyses". In: *Continuum Mechanics and Thermodynamics* 31(4), 2019, pp. 1231–1282.

Higher-Order Derivatives of Shape Functions

A1 Global First and Second Derivatives

Here, we will show the process to transform the local derivatives of the shape functions (derivatives with respect to the parametric coordinates) to their global (spatial) counterparts. We will use the same approach employed by R. L. Taylor's team in nurbFEAP/igaFEAP [207] for the implementation of two-dimensional global second-derivatives and will expand it to three dimensions and global third-derivatives.

The calculations here are independent of the shape function nature and demonstrate merely the mapping from local to global coordinates. For the calculations related to deriving the NURBS shape functions, we refer the reader to [202]. We will do the calculations for the most general case, i.e., $\partial^3 N_a/\partial\xi\partial\eta\partial\zeta$, all the other third derivatives are in fact parts of this one (e.g. replacing η with ξ results in $\partial^3 N_a/\partial\xi^2\partial\zeta$).

First, we need to find the relation between the local and global first derivatives (i.e., $\partial N_a/\partial\xi$ in terms of $\partial N_a/\partial x_1$, $\frac{\partial N_a}{\partial x_2}$ and $\partial N_a/\partial x_3$). Using the chain rule,

$$\frac{\partial N_a}{\partial \xi} = \frac{\partial x_1}{\partial \xi} \cdot \frac{\partial N_a}{\partial x_1} + \frac{\partial x_2}{\partial \xi} \cdot \frac{\partial N_a}{\partial x_2} + \frac{\partial x_3}{\partial \xi} \cdot \frac{\partial N_a}{\partial x_3}, \tag{A.1}$$

where $(\partial x_1/\partial\xi)$ are components of the Jacobian matrix. Deriving the relation for all the parametric directions (ξ, η, and ζ), solving the following system of equations gives us the global first derivatives:

$$\left\{ \begin{array}{c} \dfrac{\partial N_a}{\partial \xi} \\[2mm] \dfrac{\partial N_a}{\partial \eta} \\[2mm] \dfrac{\partial N_a}{\partial \zeta} \end{array} \right\} = \left[\begin{array}{ccc} \dfrac{\partial x_1}{\partial \xi} & \dfrac{\partial x_2}{\partial \xi} & \dfrac{\partial x_3}{\partial \xi} \\[2mm] \dfrac{\partial x_1}{\partial \eta} & \dfrac{\partial x_2}{\partial \eta} & \dfrac{\partial x_3}{\partial \eta} \\[2mm] \dfrac{\partial x_1}{\partial \zeta} & \dfrac{\partial x_2}{\partial \zeta} & \dfrac{\partial x_3}{\partial \zeta} \end{array} \right] \cdot \left\{ \begin{array}{c} \dfrac{\partial N_a}{\partial x_1} \\[2mm] \dfrac{\partial N_a}{\partial x_2} \\[2mm] \dfrac{\partial N_a}{\partial x_3} \end{array} \right\}, \tag{A.2}$$

$$\left\{ \begin{array}{c} \dfrac{\partial N_a}{\partial x_1} \\[2mm] \dfrac{\partial N_a}{\partial x_2} \\[2mm] \dfrac{\partial N_a}{\partial x_3} \end{array} \right\} = \left[\begin{array}{ccc} \dfrac{\partial x_1}{\partial \xi} & \dfrac{\partial x_2}{\partial \xi} & \dfrac{\partial x_3}{\partial \xi} \\[2mm] \dfrac{\partial x_1}{\partial \eta} & \dfrac{\partial x_2}{\partial \eta} & \dfrac{\partial x_3}{\partial \eta} \\[2mm] \dfrac{\partial x_1}{\partial \zeta} & \dfrac{\partial x_2}{\partial \zeta} & \dfrac{\partial x_3}{\partial \zeta} \end{array} \right]^{-1} \cdot \left\{ \begin{array}{c} \dfrac{\partial N_a}{\partial \xi} \\[2mm] \dfrac{\partial N_a}{\partial \eta} \\[2mm] \dfrac{\partial N_a}{\partial \zeta} \end{array} \right\}. \tag{A.3}$$

The next step is to find the relation between second order derivatives,

$$\frac{\partial^2 N_a}{\partial \xi \partial \eta} = \frac{\partial}{\partial \eta} \left(\frac{\partial N_a}{\partial \xi} \right) = \frac{\partial}{\partial \eta} \left(\frac{\partial x_1}{\partial \xi} \cdot \frac{\partial N_a}{\partial x_1} + \frac{\partial x_2}{\partial \xi} \cdot \frac{\partial N_a}{\partial x_2} + \frac{\partial x_3}{\partial \xi} \cdot \frac{\partial N_a}{\partial x_3} \right). \tag{A.4}$$

Applying the product rule, Eq. (A.4) becomes

$$\frac{\partial^2 N_a}{\partial \xi \partial \eta} = \frac{\partial^2 x}{\partial \xi \partial \eta} \cdot \frac{\partial N_a}{\partial x_1} + \frac{\partial x_1}{\partial \xi} \cdot \frac{\partial}{\partial \eta} \left(\frac{\partial N_a}{\partial x_1} \right) + \frac{\partial^2 y}{\partial \xi \partial \eta} \cdot \frac{\partial N_a}{\partial x_2} + \frac{\partial x_2}{\partial \xi} \cdot \frac{\partial}{\partial \eta} \left(\frac{\partial N_a}{\partial x_2} \right)$$
$$+ \frac{\partial^2 z}{\partial \xi \partial \eta} \cdot \frac{\partial N_a}{\partial x_3} + \frac{\partial x_3}{\partial \xi} \cdot \frac{\partial}{\partial \eta} \left(\frac{\partial N_a}{\partial x_3} \right). \tag{A.5}$$

In Eq. (A.5), there are four new kinds of components. First, $\frac{\partial^2 N_a}{\partial \xi \partial \eta}$ which is the local derivative and is known. The second type includes the elements like $\frac{\partial^2 x}{\partial \xi \partial \eta}$ which can be calculated using the same procedure as the Jacobian matrix (only this time with second order derivatives). Components like $\frac{\partial N_a}{\partial x_1}$ represent the global first derivatives. Finally there are $\frac{\partial}{\partial \eta} \left(\frac{\partial N_a}{\partial x_1} \right)$ kind of components, which need special treatment. Using the chain rule yields

$$\frac{\partial}{\partial \eta} \left(\frac{\partial N_a}{\partial x_1} \right) = \frac{\partial x_1}{\partial \eta} \cdot \frac{\partial^2 N_a}{\partial x_1^2} + \frac{\partial x_2}{\partial \eta} \cdot \frac{\partial^2 N_a}{\partial x_2^2} + \frac{\partial x_3}{\partial \eta} \cdot \frac{\partial^2 N_a}{\partial x_3^2}. \tag{A.6}$$

Doing the same procedure for all the similar elements and replacing them in Eq. (A.5), after re-ordering, Eq. (A.5) becomes

$$\frac{\partial^2 N_a}{\partial \xi \partial \eta} = \left(\frac{\partial^2 x}{\partial \xi \partial \eta} \right) \frac{\partial N_a}{\partial x_1} + \left(\frac{\partial^2 y}{\partial \xi \partial \eta} \right) \frac{\partial N_a}{\partial x_2} + \left(\frac{\partial^2 z}{\partial \xi \partial \eta} \right) \frac{\partial N_a}{\partial x_3}$$
$$+ \left(\frac{\partial x_1}{\partial \xi} \cdot \frac{\partial x_1}{\partial \eta} \right) \frac{\partial^2 N_a}{\partial x_1^2} + \left(\frac{\partial x_2}{\partial \xi} \cdot \frac{\partial x_2}{\partial \eta} \right) \frac{\partial^2 N_a}{\partial x_2^2} + \left(\frac{\partial x_3}{\partial \xi} \cdot \frac{\partial x_3}{\partial \eta} \right) \frac{\partial^2 N_a}{\partial x_3^2}$$
$$+ \left(\frac{\partial x_1}{\partial \xi} \cdot \frac{\partial x_2}{\partial \eta} + \frac{\partial x_1}{\partial \eta} \cdot \frac{\partial x_2}{\partial \xi} \right) \frac{\partial^2 N_a}{\partial x_1 \partial x_2} \tag{A.7}$$
$$+ \left(\frac{\partial x_1}{\partial \xi} \cdot \frac{\partial x_3}{\partial \eta} + \frac{\partial x_1}{\partial \eta} \cdot \frac{\partial x_3}{\partial \xi} \right) \frac{\partial^2 N_a}{\partial x_1 \partial x_3}$$
$$+ \left(\frac{\partial x_2}{\partial \xi} \cdot \frac{\partial x_3}{\partial \eta} + \frac{\partial x_2}{\partial \eta} \cdot \frac{\partial x_3}{\partial \xi} \right) \frac{\partial^2 N_a}{\partial x_2 \partial x_3}.$$

The same applies for other second-derivatives. Now, to calculate the unknowns, the following system of equations must be solved (see Eq. (A1)).

$$
\underbrace{\begin{Bmatrix} \dfrac{\partial^2 N_a}{\partial \xi^2} \\[4pt] \dfrac{\partial^2 N_a}{\partial \eta^2} \\[4pt] \dfrac{\partial^2 N_a}{\partial \zeta^2} \\[4pt] \dfrac{\partial^2 N_a}{\partial \xi \partial \eta} \\[4pt] \dfrac{\partial^2 N_a}{\partial \xi \partial \zeta} \\[4pt] \dfrac{\partial^2 N_a}{\partial \eta \partial \zeta} \end{Bmatrix}}_{\text{known}}
=
\underbrace{\begin{bmatrix}
\left(\dfrac{\partial x_1}{\partial \xi}\right)^2 & \left(\dfrac{\partial x_2}{\partial \xi}\right)^2 & \left(\dfrac{\partial x_3}{\partial \xi}\right)^2 & 2\dfrac{\partial x_1}{\partial \xi}\dfrac{\partial x_2}{\partial \xi} & 2\dfrac{\partial x_1}{\partial \xi}\dfrac{\partial x_3}{\partial \xi} & 2\dfrac{\partial x_2}{\partial \xi}\dfrac{\partial x_3}{\partial \xi} \\[8pt]
\left(\dfrac{\partial x_1}{\partial \eta}\right)^2 & \left(\dfrac{\partial x_2}{\partial \eta}\right)^2 & \left(\dfrac{\partial x_3}{\partial \eta}\right)^2 & 2\dfrac{\partial x_1}{\partial \eta}\dfrac{\partial x_2}{\partial \eta} & 2\dfrac{\partial x_1}{\partial \eta}\dfrac{\partial x_3}{\partial \eta} & 2\dfrac{\partial x_2}{\partial \eta}\dfrac{\partial x_3}{\partial \eta} \\[8pt]
\left(\dfrac{\partial x_1}{\partial \zeta}\right)^2 & \left(\dfrac{\partial x_2}{\partial \zeta}\right)^2 & \left(\dfrac{\partial x_3}{\partial \zeta}\right)^2 & 2\dfrac{\partial x_1}{\partial \zeta}\dfrac{\partial x_2}{\partial \zeta} & 2\dfrac{\partial x_1}{\partial \zeta}\dfrac{\partial x_3}{\partial \zeta} & 2\dfrac{\partial x_2}{\partial \zeta}\dfrac{\partial x_3}{\partial \zeta} \\[8pt]
\dfrac{\partial x_1}{\partial \xi}\dfrac{\partial x_1}{\partial \eta} & \dfrac{\partial x_2}{\partial \xi}\dfrac{\partial x_2}{\partial \eta} & \dfrac{\partial x_3}{\partial \xi}\dfrac{\partial x_3}{\partial \eta} & \left(\dfrac{\partial x_1}{\partial \xi}\dfrac{\partial x_2}{\partial \eta}+\dfrac{\partial x_1}{\partial \eta}\dfrac{\partial x_2}{\partial \xi}\right) & \left(\dfrac{\partial x_1}{\partial \xi}\dfrac{\partial x_3}{\partial \eta}+\dfrac{\partial x_1}{\partial \eta}\dfrac{\partial x_3}{\partial \xi}\right) & \left(\dfrac{\partial x_2}{\partial \xi}\dfrac{\partial x_3}{\partial \eta}+\dfrac{\partial x_2}{\partial \eta}\dfrac{\partial x_3}{\partial \xi}\right) \\[8pt]
\dfrac{\partial x_1}{\partial \xi}\dfrac{\partial x_1}{\partial \zeta} & \dfrac{\partial x_2}{\partial \xi}\dfrac{\partial x_2}{\partial \zeta} & \dfrac{\partial x_3}{\partial \xi}\dfrac{\partial x_3}{\partial \zeta} & \left(\dfrac{\partial x_1}{\partial \xi}\dfrac{\partial x_2}{\partial \zeta}+\dfrac{\partial x_1}{\partial \zeta}\dfrac{\partial x_2}{\partial \xi}\right) & \left(\dfrac{\partial x_1}{\partial \xi}\dfrac{\partial x_3}{\partial \zeta}+\dfrac{\partial x_1}{\partial \zeta}\dfrac{\partial x_3}{\partial \xi}\right) & \left(\dfrac{\partial x_2}{\partial \xi}\dfrac{\partial x_3}{\partial \zeta}+\dfrac{\partial x_2}{\partial \zeta}\dfrac{\partial x_3}{\partial \xi}\right) \\[8pt]
\dfrac{\partial x_1}{\partial \eta}\dfrac{\partial x_1}{\partial \zeta} & \dfrac{\partial x_2}{\partial \eta}\dfrac{\partial x_2}{\partial \zeta} & \dfrac{\partial x_3}{\partial \eta}\dfrac{\partial x_3}{\partial \zeta} & \left(\dfrac{\partial x_1}{\partial \eta}\dfrac{\partial x_2}{\partial \zeta}+\dfrac{\partial x_1}{\partial \zeta}\dfrac{\partial x_2}{\partial \eta}\right) & \left(\dfrac{\partial x_1}{\partial \eta}\dfrac{\partial x_3}{\partial \zeta}+\dfrac{\partial x_1}{\partial \zeta}\dfrac{\partial x_3}{\partial \eta}\right) & \left(\dfrac{\partial x_2}{\partial \eta}\dfrac{\partial x_3}{\partial \zeta}+\dfrac{\partial x_2}{\partial \zeta}\dfrac{\partial x_3}{\partial \eta}\right)
\end{bmatrix}}_{\text{known}}
\cdot
\underbrace{\begin{Bmatrix} \dfrac{\partial^2 N_a}{\partial x_1^2} \\[4pt] \dfrac{\partial^2 N_a}{\partial x_2^2} \\[4pt] \dfrac{\partial^2 N_a}{\partial x_3^2} \\[4pt] \dfrac{\partial^2 N_a}{\partial x_1 \partial x_2} \\[4pt] \dfrac{\partial^2 N_a}{\partial x_1 \partial x_3} \\[4pt] \dfrac{\partial^2 N_a}{\partial x_2 \partial x_3} \end{Bmatrix}}_{\text{unknown}}
$$

$$
+
\underbrace{\begin{bmatrix}
\dfrac{\partial^2 x}{\partial \xi^2} & \dfrac{\partial^2 y}{\partial \xi^2} & \dfrac{\partial^2 z}{\partial \xi^2} \\[6pt]
\dfrac{\partial^2 x}{\partial \eta^2} & \dfrac{\partial^2 y}{\partial \eta^2} & \dfrac{\partial^2 z}{\partial \eta^2} \\[6pt]
\dfrac{\partial^2 x}{\partial \zeta^2} & \dfrac{\partial^2 y}{\partial \zeta^2} & \dfrac{\partial^2 z}{\partial \zeta^2} \\[6pt]
\dfrac{\partial^2 x}{\partial \xi \partial \eta} & \dfrac{\partial^2 y}{\partial \xi \partial \eta} & \dfrac{\partial^2 z}{\partial \xi \partial \eta} \\[6pt]
\dfrac{\partial^2 x}{\partial \xi \partial \zeta} & \dfrac{\partial^2 y}{\partial \xi \partial \zeta} & \dfrac{\partial^2 z}{\partial \xi \partial \zeta} \\[6pt]
\dfrac{\partial^2 x}{\partial \eta \partial \zeta} & \dfrac{\partial^2 y}{\partial \eta \partial \zeta} & \dfrac{\partial^2 z}{\partial \eta \partial \zeta}
\end{bmatrix}}_{\text{known}}
\cdot
\underbrace{\begin{Bmatrix} \dfrac{\partial N_a}{\partial x_1} \\[4pt] \dfrac{\partial N_a}{\partial x_2} \\[4pt] \dfrac{\partial N_a}{\partial x_3} \end{Bmatrix}}_{\text{known from Eq. (A.3)}}
$$

Moving the second part of Eq. (A1) RHS to left,

$$
\begin{Bmatrix}
\dfrac{\partial^2 \bar{N}_a}{\partial \xi^2} \\[2mm]
\dfrac{\partial^2 \bar{N}_a}{\partial \eta^2} \\[2mm]
\dfrac{\partial^2 \bar{N}_a}{\partial \zeta^2} \\[2mm]
\dfrac{\partial^2 \bar{N}_a}{\partial \xi \partial \eta} \\[2mm]
\dfrac{\partial^2 \bar{N}_a}{\partial \xi \partial \zeta} \\[2mm]
\dfrac{\partial^2 \bar{N}_a}{\partial \eta \partial \zeta}
\end{Bmatrix}
=
\begin{Bmatrix}
\dfrac{\partial^2 N_a}{\partial \xi^2} \\[2mm]
\dfrac{\partial^2 N_a}{\partial \eta^2} \\[2mm]
\dfrac{\partial^2 N_a}{\partial \zeta^2} \\[2mm]
\dfrac{\partial^2 N_a}{\partial \xi \partial \eta} \\[2mm]
\dfrac{\partial^2 N_a}{\partial \xi \partial \zeta} \\[2mm]
\dfrac{\partial^2 N_a}{\partial \eta \partial \zeta}
\end{Bmatrix}
-
\begin{bmatrix}
\dfrac{\partial^2 x}{\partial \xi^2} & \dfrac{\partial^2 y}{\partial \xi^2} & \dfrac{\partial^2 z}{\partial \xi^2} \\[2mm]
\dfrac{\partial^2 x}{\partial \eta^2} & \dfrac{\partial^2 y}{\partial \eta^2} & \dfrac{\partial^2 z}{\partial \eta^2} \\[2mm]
\dfrac{\partial^2 x}{\partial \zeta^2} & \dfrac{\partial^2 y}{\partial \zeta^2} & \dfrac{\partial^2 z}{\partial \zeta^2} \\[2mm]
\dfrac{\partial^2 x}{\partial \xi \partial \eta} & \dfrac{\partial^2 y}{\partial \xi \partial \eta} & \dfrac{\partial^2 z}{\partial \xi \partial \eta} \\[2mm]
\dfrac{\partial^2 x}{\partial \xi \partial \zeta} & \dfrac{\partial^2 y}{\partial \xi \partial \zeta} & \dfrac{\partial^2 z}{\partial \xi \partial \zeta} \\[2mm]
\dfrac{\partial^2 x}{\partial \eta \partial \zeta} & \dfrac{\partial^2 y}{\partial \eta \partial \zeta} & \dfrac{\partial^2 z}{\partial \eta \partial \zeta}
\end{bmatrix}
\begin{Bmatrix}
\dfrac{\partial N_a}{\partial x_1} \\[2mm]
\dfrac{\partial N_a}{\partial x_2} \\[2mm]
\dfrac{\partial N_a}{\partial x_3}
\end{Bmatrix} .
\tag{A.8}
$$

Finally, the global derivatives can be calculated using Eq. (A.9).

$$
\begin{bmatrix}
\dfrac{\partial^2 N_a}{\partial x_1^2}\\[4pt]
\dfrac{\partial^2 N_a}{\partial x_2^2}\\[4pt]
\dfrac{\partial^2 N_a}{\partial x_3^2}\\[4pt]
\dfrac{\partial^2 N_a}{\partial x_1 \partial x_2}\\[4pt]
\dfrac{\partial^2 N_a}{\partial x_1 \partial x_3}\\[4pt]
\dfrac{\partial^2 N_a}{\partial x_2 \partial x_3}
\end{bmatrix}
=
\left[\,M\,\right]^{-1}
\begin{bmatrix}
\dfrac{\partial^2 \bar N_a}{\partial \xi^2}\\[4pt]
\dfrac{\partial^2 \bar N_a}{\partial \eta^2}\\[4pt]
\dfrac{\partial^2 \bar N_a}{\partial \zeta^2}\\[4pt]
\dfrac{\partial^2 \bar N_a}{\partial \xi \partial \eta}\\[4pt]
\dfrac{\partial^2 \bar N_a}{\partial \xi \partial \zeta}\\[4pt]
\dfrac{\partial^2 \bar N_a}{\partial \eta \partial \zeta}
\end{bmatrix}
\tag{A.9}
$$

where

$$
\left[\,M\,\right]=
$$

$$
\begin{bmatrix}
\left(\dfrac{\partial x_1}{\partial \xi}\right)^2 &
\left(\dfrac{\partial x_2}{\partial \xi}\right)^2 &
\left(\dfrac{\partial x_3}{\partial \xi}\right)^2 &
2\,\dfrac{\partial x_1}{\partial \xi}\dfrac{\partial x_2}{\partial \xi} &
2\,\dfrac{\partial x_1}{\partial \xi}\dfrac{\partial x_3}{\partial \xi} &
2\,\dfrac{\partial x_2}{\partial \xi}\dfrac{\partial x_3}{\partial \xi} \\[8pt]

\left(\dfrac{\partial x_1}{\partial \eta}\right)^2 &
\left(\dfrac{\partial x_2}{\partial \eta}\right)^2 &
\left(\dfrac{\partial x_3}{\partial \eta}\right)^2 &
2\,\dfrac{\partial x_1}{\partial \eta}\dfrac{\partial x_2}{\partial \eta} &
2\,\dfrac{\partial x_1}{\partial \eta}\dfrac{\partial x_3}{\partial \eta} &
2\,\dfrac{\partial x_2}{\partial \eta}\dfrac{\partial x_3}{\partial \eta} \\[8pt]

\left(\dfrac{\partial x_1}{\partial \zeta}\right)^2 &
\left(\dfrac{\partial x_2}{\partial \zeta}\right)^2 &
\left(\dfrac{\partial x_3}{\partial \zeta}\right)^2 &
2\,\dfrac{\partial x_1}{\partial \zeta}\dfrac{\partial x_2}{\partial \zeta} &
2\,\dfrac{\partial x_1}{\partial \zeta}\dfrac{\partial x_3}{\partial \zeta} &
2\,\dfrac{\partial x_2}{\partial \zeta}\dfrac{\partial x_3}{\partial \zeta} \\[8pt]

\dfrac{\partial x_1}{\partial \xi}\dfrac{\partial x_1}{\partial \eta} &
\dfrac{\partial x_2}{\partial \xi}\dfrac{\partial x_2}{\partial \eta} &
\dfrac{\partial x_3}{\partial \xi}\dfrac{\partial x_3}{\partial \eta} &
\left(\dfrac{\partial x_1}{\partial \xi}\dfrac{\partial x_2}{\partial \eta}+\dfrac{\partial x_1}{\partial \eta}\dfrac{\partial x_2}{\partial \xi}\right) &
\left(\dfrac{\partial x_1}{\partial \xi}\dfrac{\partial x_3}{\partial \eta}+\dfrac{\partial x_1}{\partial \eta}\dfrac{\partial x_3}{\partial \xi}\right) &
\left(\dfrac{\partial x_2}{\partial \xi}\dfrac{\partial x_3}{\partial \eta}+\dfrac{\partial x_2}{\partial \eta}\dfrac{\partial x_3}{\partial \xi}\right) \\[8pt]

\dfrac{\partial x_1}{\partial \xi}\dfrac{\partial x_1}{\partial \zeta} &
\dfrac{\partial x_2}{\partial \xi}\dfrac{\partial x_2}{\partial \zeta} &
\dfrac{\partial x_3}{\partial \xi}\dfrac{\partial x_3}{\partial \zeta} &
\left(\dfrac{\partial x_1}{\partial \xi}\dfrac{\partial x_2}{\partial \zeta}+\dfrac{\partial x_1}{\partial \zeta}\dfrac{\partial x_2}{\partial \xi}\right) &
\left(\dfrac{\partial x_1}{\partial \xi}\dfrac{\partial x_3}{\partial \zeta}+\dfrac{\partial x_1}{\partial \zeta}\dfrac{\partial x_3}{\partial \xi}\right) &
\left(\dfrac{\partial x_2}{\partial \xi}\dfrac{\partial x_3}{\partial \zeta}+\dfrac{\partial x_2}{\partial \zeta}\dfrac{\partial x_3}{\partial \xi}\right) \\[8pt]

\dfrac{\partial x_1}{\partial \eta}\dfrac{\partial x_1}{\partial \zeta} &
\dfrac{\partial x_2}{\partial \eta}\dfrac{\partial x_2}{\partial \zeta} &
\dfrac{\partial x_3}{\partial \eta}\dfrac{\partial x_3}{\partial \zeta} &
\left(\dfrac{\partial x_1}{\partial \zeta}\dfrac{\partial x_2}{\partial \eta}+\dfrac{\partial x_1}{\partial \eta}\dfrac{\partial x_2}{\partial \zeta}\right) &
\left(\dfrac{\partial x_1}{\partial \zeta}\dfrac{\partial x_3}{\partial \eta}+\dfrac{\partial x_1}{\partial \eta}\dfrac{\partial x_3}{\partial \zeta}\right) &
\left(\dfrac{\partial x_2}{\partial \zeta}\dfrac{\partial x_3}{\partial \eta}+\dfrac{\partial x_2}{\partial \eta}\dfrac{\partial x_3}{\partial \zeta}\right)
\end{bmatrix}
$$

A2 Global Third Derivatives

The same procedure applies for the third-derivatives. Here, to avoid tremendous matrix representations, a summary of the necessary steps to derive the unknowns is presented. The Eq. (A.7) counterpart for the third-derivatives is

$$
\begin{aligned}
\frac{\partial^3 N_a}{\partial \xi \partial \eta \partial \zeta} =\ & \frac{\partial x_1}{\partial \xi} \cdot \frac{\partial x_1}{\partial \eta} \cdot \frac{\partial x_1}{\partial \zeta} \cdot \frac{\partial^3 N_a}{\partial x_1^3} + \frac{\partial x_2}{\partial \xi} \cdot \frac{\partial x_2}{\partial \eta} \cdot \frac{\partial x_2}{\partial \zeta} \cdot \frac{\partial^3 N_a}{\partial x_2^3} + \frac{\partial x_3}{\partial \xi} \cdot \frac{\partial x_3}{\partial \eta} \cdot \frac{\partial x_3}{\partial \zeta} \cdot \frac{\partial^3 N_a}{\partial x_3^3} \\
& + \left[\frac{\partial x_1}{\partial \xi} \cdot \frac{\partial x_1}{\partial \eta} \cdot \frac{\partial x_2}{\partial \zeta} + \left(\frac{\partial x_1}{\partial \xi} \cdot \frac{\partial x_2}{\partial \eta} + \frac{\partial x_1}{\partial \eta} \cdot \frac{\partial x_2}{\partial \xi} \right) \frac{\partial x_1}{\partial \zeta} \right] \cdot \frac{\partial^3 N_a}{\partial x_1^2 \partial x_2} \\
& + \left[\frac{\partial x_1}{\partial \xi} \cdot \frac{\partial x_1}{\partial \eta} \cdot \frac{\partial x_3}{\partial \zeta} + \left(\frac{\partial x_1}{\partial \xi} \cdot \frac{\partial x_3}{\partial \eta} + \frac{\partial x_1}{\partial \eta} \cdot \frac{\partial x_3}{\partial \xi} \right) \frac{\partial x_1}{\partial \zeta} \right] \cdot \frac{\partial^3 N_a}{\partial x_1^2 \partial x_3} \\
& + \left[\frac{\partial x_2}{\partial \xi} \cdot \frac{\partial x_2}{\partial \eta} \cdot \frac{\partial x_1}{\partial \zeta} + \left(\frac{\partial x_1}{\partial \xi} \cdot \frac{\partial x_2}{\partial \eta} + \frac{\partial x_1}{\partial \eta} \cdot \frac{\partial x_2}{\partial \xi} \right) \frac{\partial x_2}{\partial \zeta} \right] \cdot \frac{\partial^3 N_a}{\partial x_1 \partial x_2^2} \\
& + \left[\frac{\partial x_2}{\partial \xi} \cdot \frac{\partial x_2}{\partial \eta} \cdot \frac{\partial x_3}{\partial \zeta} + \left(\frac{\partial x_2}{\partial \xi} \cdot \frac{\partial x_3}{\partial \eta} + \frac{\partial x_2}{\partial \eta} \cdot \frac{\partial x_3}{\partial \xi} \right) \frac{\partial x_2}{\partial \zeta} \right] \cdot \frac{\partial^3 N_a}{\partial x_2^2 \partial x_3} \\
& + \left[\frac{\partial x_3}{\partial \xi} \cdot \frac{\partial x_3}{\partial \eta} \cdot \frac{\partial x_1}{\partial \zeta} + \left(\frac{\partial x_1}{\partial \xi} \cdot \frac{\partial x_3}{\partial \eta} + \frac{\partial x_1}{\partial \eta} \cdot \frac{\partial x_3}{\partial \xi} \right) \frac{\partial x_3}{\partial \zeta} \right] \cdot \frac{\partial^3 N_a}{\partial x_1 \partial x_3^2} \\
& + \left[\frac{\partial x_3}{\partial \xi} \cdot \frac{\partial x_3}{\partial \eta} \cdot \frac{\partial x_2}{\partial \zeta} + \left(\frac{\partial x_2}{\partial \xi} \cdot \frac{\partial x_3}{\partial \eta} + \frac{\partial x_2}{\partial \eta} \cdot \frac{\partial x_3}{\partial \xi} \right) \frac{\partial x_3}{\partial \zeta} \right] \cdot \frac{\partial^3 N_a}{\partial x_2 \partial x_3^2} \\
& + \left[\left(\frac{\partial x_1}{\partial \xi} \cdot \frac{\partial x_2}{\partial \eta} + \frac{\partial x_1}{\partial \eta} \cdot \frac{\partial x_2}{\partial \xi} \right) \frac{\partial x_3}{\partial \zeta} + \left(\frac{\partial x_1}{\partial \xi} \cdot \frac{\partial x_3}{\partial \eta} + \frac{\partial x_1}{\partial \eta} \cdot \frac{\partial x_3}{\partial \xi} \right) \frac{\partial x_2}{\partial \zeta} \right. \\
& \left. + \left(\frac{\partial x_2}{\partial \xi} \cdot \frac{\partial x_3}{\partial \eta} + \frac{\partial x_2}{\partial \eta} \cdot \frac{\partial x_3}{\partial \xi} \right) \frac{\partial x_1}{\partial \zeta} \right] \cdot \frac{\partial^3 N_a}{\partial x_1 \partial x_2 \partial x_3} \\
& + \left(\frac{\partial^2 x}{\partial \xi \partial \zeta} \cdot \frac{\partial x_1}{\partial \eta} + \frac{\partial x_1}{\partial \xi} \cdot \frac{\partial^2 x}{\partial \eta \partial \zeta} + \frac{\partial^2 x}{\partial \xi \partial \eta} \cdot \frac{\partial x_1}{\partial \zeta} \right) \cdot \frac{\partial^2 N_a}{\partial x_1^2} \\
& + \left(\frac{\partial^2 y}{\partial \xi \partial \zeta} \cdot \frac{\partial x_2}{\partial \eta} + \frac{\partial x_2}{\partial \xi} \cdot \frac{\partial^2 y}{\partial \eta \partial \zeta} + \frac{\partial^2 y}{\partial \xi \partial \eta} \cdot \frac{\partial x_2}{\partial \zeta} \right) \cdot \frac{\partial^2 N_a}{\partial x_2^2} \\
& + \left(\frac{\partial^2 z}{\partial \xi \partial \zeta} \cdot \frac{\partial x_3}{\partial \eta} + \frac{\partial x_3}{\partial \xi} \cdot \frac{\partial^2 z}{\partial \eta \partial \zeta} + \frac{\partial^2 z}{\partial \xi \partial \eta} \cdot \frac{\partial x_3}{\partial \zeta} \right) \cdot \frac{\partial^2 N_a}{\partial x_3^2} \\
& + \left(\frac{\partial^2 x}{\partial \xi \partial \zeta} \cdot \frac{\partial x_2}{\partial \eta} + \frac{\partial x_1}{\partial \xi} \cdot \frac{\partial^2 y}{\partial \eta \partial \zeta} + \frac{\partial^2 x}{\partial \eta \partial \zeta} \cdot \frac{\partial x_2}{\partial \xi} + \frac{\partial x_1}{\partial \eta} \cdot \frac{\partial^2 y}{\partial \xi \partial \zeta} \right. \\
& \left. + \frac{\partial^2 x}{\partial \xi \partial \eta} \cdot \frac{\partial x_2}{\partial \zeta} + \frac{\partial^2 y}{\partial \xi \partial \eta} \cdot \frac{\partial x_1}{\partial \zeta} \right) \cdot \frac{\partial^2 N_a}{\partial x_1 \partial x_2} \\
& + \left(\frac{\partial^2 x}{\partial \xi \partial \zeta} \cdot \frac{\partial x_3}{\partial \eta} + \frac{\partial x_1}{\partial \xi} \cdot \frac{\partial^2 z}{\partial \eta \partial \zeta} + \frac{\partial^2 x}{\partial \eta \partial \zeta} \cdot \frac{\partial x_3}{\partial \xi} + \frac{\partial x_1}{\partial \eta} \cdot \frac{\partial^2 z}{\partial \xi \partial \zeta} \right. \\
& \left. + \frac{\partial^2 x}{\partial \xi \partial \eta} \cdot \frac{\partial x_3}{\partial \zeta} + \frac{\partial^2 z}{\partial \xi \partial \eta} \cdot \frac{\partial x_1}{\partial \zeta} \right) \cdot \frac{\partial^2 N_a}{\partial x_1 \partial x_3} \\
& + \left(\frac{\partial^2 y}{\partial \xi \partial \zeta} \cdot \frac{\partial x_3}{\partial \eta} + \frac{\partial x_2}{\partial \xi} \cdot \frac{\partial^2 z}{\partial \eta \partial \zeta} + \frac{\partial^2 y}{\partial \eta \partial \zeta} \cdot \frac{\partial x_3}{\partial \xi} + \frac{\partial x_2}{\partial \eta} \cdot \frac{\partial^2 z}{\partial \xi \partial \zeta} \right. \\
& \left. + \frac{\partial^2 y}{\partial \xi \partial \eta} \cdot \frac{\partial x_3}{\partial \zeta} + \frac{\partial^2 z}{\partial \xi \partial \eta} \cdot \frac{\partial x_2}{\partial \zeta} \right) \cdot \frac{\partial^2 N_a}{\partial x_2 \partial x_3} \\
& + \frac{\partial^3 x}{\partial \xi \partial \eta \partial \zeta} \cdot \frac{\partial N_a}{\partial x_1} + \frac{\partial^3 y}{\partial \xi \partial \eta \partial \zeta} \cdot \frac{\partial N_a}{\partial x_2} + \frac{\partial^3 z}{\partial \xi \partial \eta \partial \zeta} \cdot \frac{\partial N_a}{\partial x_3}.
\end{aligned}
\tag{A.10}
$$

After doing the same calculations for all the third-derivatives and re-ordering, this results to a system of equations which looks similar to Eq. (A1),

$$\mathbf{a}_{10\times1} = \mathbf{B}_{10\times10}\cdot\mathbf{c}_{10\times1} + \mathbf{D}_{10\times6}\cdot\mathbf{e}_{6\times1} + \mathbf{F}_{10\times3}\cdot\mathbf{g}_{3\times1}, \tag{A.11}$$

where the subscripts denote the dimensions. In Eq. (A.11), $\mathbf{a}$ is the vector of local third-derivatives (known), $\mathbf{c}$ represents the unknown vector of global third-derivatives, $\mathbf{e}$ is the vector of global second-derivatives (known from Eq. (A.9)), $\mathbf{g}$ denotes the vector of global first-derivatives (known from Eq. (A.3)), and $\mathbf{B}$, $\mathbf{D}$ and $\mathbf{F}$ (all known) are coefficient matrices. At last, defining

$$\mathbf{h}_{10\times1} = \mathbf{a}_{10\times1} - \mathbf{D}_{10\times6}\cdot\mathbf{e}_{6\times1} - \mathbf{F}_{10\times3}\cdot\mathbf{g}_{3\times1}, \tag{A.12}$$

the global third-derivatives vector, $\mathbf{c}$, can be calculated from,

$$\mathbf{c}_{10\times1} = \mathbf{B}_{10\times10}^{-1}\cdot\mathbf{h}_{10\times1}. \tag{A.13}$$

A full representation of the above matrices can be found in [26].

Phase-Field Fracture and Mindlin's Theory

In this section, a complete representation of the residual and tangent matrices for the Mindlin's Form II formulation (Sec. 2.2.3) integrated with the phase-field fracture model in the framework of isogeometric analysis is provided. Most of the variables are already defined in the previous chapters.

B1 Second-Order Phase-Field Fracture Model

The quadratic stored elastic energy is given by, cf. Eq. (2.61)

$$\Psi_{\text{grad}}^{\text{SGE}} := \int_{\Omega} \psi_{\text{grad}}^{\text{SGE}} \mathrm{d}V = \int_{\Omega} \left(\frac{1}{2} E_{ij} C_{ijkl} E_{kl} + \frac{1}{2} H_{ijk} D_{ijklmn} H_{lmn} \right) \mathrm{d}V, \tag{B.1}$$

where the material stiffness D_{ijklmn} can be defined as

$$\begin{aligned}
D_{ijklmn} &= c_1 \left(\delta_{ij}\delta_{kl}\delta_{mn} + \delta_{in}\delta_{jk}\delta_{lm} + \delta_{ij}\delta_{km}\delta_{ln} + \delta_{ik}\delta_{jn}\delta_{lm} \right) + c_2\delta_{ij}\delta_{kn}\delta_{ml} \\
&\quad + c_3 \left(\delta_{ik}\delta_{jl}\delta_{mn} + \delta_{im}\delta_{jk}\delta_{ln} + \delta_{ik}\delta_{jm}\delta_{ln} + \delta_{il}\delta_{jk}\delta_{mn} \right) \\
&\quad + c_4 \left(\delta_{il}\delta_{jm}\delta_{kn} + \delta_{im}\delta_{jl}\delta_{kn} \right) \\
&\quad + c_5 \left(\delta_{il}\delta_{jn}\delta_{mk} + \delta_{im}\delta_{jn}\delta_{lk} + \delta_{in}\delta_{jl}\delta_{km} + \delta_{in}\delta_{jm}\delta_{kl} \right),
\end{aligned} \tag{B.2}$$

where $c_1 - c_5$ are the gradient material parameters. Note that in contrast to the Lamé constants (λ, μ) which are of unit pressure, the gradient material parameters in Eq. (B.2) are of unit force. Their physical meaning ([18, 219–222]), experimental determination ([158, 223–225]), and numerical homogenization ([226–229]) are heavily discussed in the literature; we refer to [230] for a recent review.

The total energy of fracture is given by

$$\Psi_{\text{grad}}^{\text{frac}}(\mathbf{E}, \mathbf{H}, s) = \int_{\Omega} \left[s^2\, \psi_{\text{grad}}^{\text{SGE}} + \mathcal{G}_c \left(\frac{(1-s)^2}{4\epsilon} + \epsilon |\nabla s|^2 \right) \right] \mathrm{d}V - \int_{\Omega} \mathbf{b} \cdot \mathbf{u} \, \mathrm{d}V. \tag{B.3}$$

The effective classical stresses are given by Eq. (3.43),

$$S_{ij}^{\text{frac}} := s^2\, C_{ijkl} E_{kl} = s^2 \left(\lambda E_{pp}\delta_{ij} + 2\mu E_{ij} \right) \tag{B.4}$$

For the effective double stresses, we have

$$\begin{aligned}
P_{ijk}^{\text{frac}} := s^2\, D_{ijklmn} H_{lmn} = s^2 \big(&c_1 \left(2\delta_{ij}H_{kll} + \delta_{ik}H_{llj} + \delta_{jk}H_{lli} \right) + c_2\delta_{ij}H_{llk} \\
&+ c_3 \left(2\delta_{ik}H_{jll} + 2\delta_{jk}H_{ill} \right) + 2c_4 H_{ijk} + c_5 \left(2H_{ijk} + 2H_{jki} \right) \big).
\end{aligned} \tag{B.5}$$

Note that, here, the gradient of the strain tensor is defined by

$$H_{ijk} := E_{ij,k} = \frac{u_{i,jk} + u_{j,ik}}{2}.$$
(B.6)

For the displacement degrees of freedom (the mechanical part), we have

$$\int_\Omega \left(\mathbf{S}^{\text{frac}} : \delta\mathbf{E} + \mathbf{P}^{\text{frac}} \vdots \delta\mathbf{H} \right) dV$$
$$= \int_\Omega \mathbf{b} \cdot \delta\mathbf{u} \, dV + \int_{\Gamma_1} \bar{\mathbf{t}}^1 \cdot \delta\mathbf{u} \, dA + \int_{\Gamma_1} \bar{\mathbf{t}}^2 \cdot \delta\nabla_{\mathbf{n}} \mathbf{u} \, dA, + \int_\Xi \bar{\mathbf{t}}^3 \cdot \delta\mathbf{u} \, dL,$$
(B.7)

as the weak form. The relation for the second-order phase-field model becomes

$$\int_\Omega \left[\frac{\dot{s}}{M} \delta s + 2\, \mathcal{G}_c \epsilon \, \nabla s \, \delta\nabla s + \left(2s\, \psi_{\text{grad}}^{\text{SGE}} + \frac{\mathcal{G}_c(s-1)}{2\epsilon} \right) \delta s \right] dV = \int_{\Gamma_2} q_n \, \delta s \, dA,$$
(B.8)

For the second-order phase-field model, in the absence of external forces, the residual matrix for the control point I, derived from Eqs. (B.7) and (B.8), is (the superscript "frac" is omitted from S and P)

$$\left[\hat{\mathbf{P}}^I \right] = \begin{bmatrix} \hat{P}^I_{u_1} \\ \hat{P}^I_{u_2} \\ \hat{P}^I_{u_3} \\ \hat{P}^I_s \end{bmatrix}$$
(B.9)

with,

$$\hat{P}^I_{u_1} = s^2 \left[\left(S_{11} R^I_{,1} + S_{12} R^I_{,2} + S_{13} R^I_{,3} \right) + \left(P_{111} R^I_{,11} + P_{112} R^I_{,12} + P_{113} R^I_{,13} \right. \right.$$
$$\left. \left. + P_{211} R^I_{,12} + P_{212} R^I_{,22} + P_{213} R^I_{,23} + P_{311} R^I_{,13} + P_{312} R^I_{,23} + P_{313} R^I_{,33} \right) \right],$$
(B.10)

$$\hat{P}^I_{u_2} = s^2 \left[\left(S_{22} R^I_{,2} + S_{12} R^I_{,1} + S_{2,3} R^I_{,3} \right) + \left(P_{211} R^I_{,11} + P_{212} R^I_{,12} + P_{213} R^I_{,13} \right. \right.$$
$$\left. \left. + P_{221} R^I_{,12} + P_{222} R^I_{,22} + P_{223} R^I_{,23} + P_{321} R^I_{,13} + P_{322} R^I_{,23} + P_{323} R^I_{,33} \right) \right],$$
(B.11)

$$\hat{P}^I_{u_3} = s^2 \left[\left(S_{33} R^I_{,3} + S_{13} R^I_{,1} + S_{2,3} R^I_{,2} \right) + \left(P_{311} R^I_{,11} + P_{312} R^I_{,12} + P_{313} R^I_{,13} \right. \right.$$
$$\left. \left. + P_{321} R^I_{,12} + P_{322} R^I_{,22} + P_{323} R^I_{,23} + P_{331} R^I_{,13} + P_{332} R^I_{,23} + P_{333} R^I_{,33} \right) \right],$$
(B.12)

and,

$$\hat{P}^I_s = R^I \frac{1}{M} \frac{\partial s}{\partial t} + 2\mathcal{G}_c \epsilon \left(R^I_{,1} s_{,1} + R^I_{,2} s_{,2} + R^I_{,3} s_{,3} \right) + R^I \left(2s\psi_{\text{grad}}^{\text{SGE}} + \frac{\mathcal{G}_c(s-1)}{2\epsilon} \right).$$
(B.13)

Consequently, the stiffness matrix can be written as

$$\left[\hat{\mathbf{K}}^{IJ} \right] = \int_\Omega \begin{bmatrix} \hat{K}^{IJ}_{u_1 u_1} & \hat{K}^{IJ}_{u_1 u_2} & \hat{K}^{IJ}_{u_1 u_3} & \hat{K}^{IJ}_{u_1 s} \\ & \hat{K}^{IJ}_{u_2 u_2} & \hat{K}^{IJ}_{u_2 u_3} & \hat{K}^{IJ}_{u_2 s} \\ & & \hat{K}^{IJ}_{u_3 u_3} & \hat{K}^{IJ}_{u_3 s} \\ symm. & & & \hat{K}^{IJ}_{ss} \end{bmatrix} dV$$
(B.14)

with

$$
\begin{aligned}
\hat{K}^{IJ}_{u_1 u_1} = s^2 \big[&\lambda R^I_{,1} R^J_{,1} + \mu \left(2R^I_{,1} R^J_{,1} + R^I_{,2} R^J_{,2} + R^I_{,3} R^J_{,3} \right) \\
&+ c_1 \big(R^I_{,11} R^J_{,33} + R^J_{,11} R^I_{,33} + R^I_{,11} R^J_{,22} + R^J_{,11} R^I_{,22} \\
&\qquad + 2R^I_{,13} R^J_{,13} + 2R^I_{,12} R^J_{,12} + 4R^I_{,11} R^J_{,11} \big) \\
&+ c_2 \big(R^I_{,13} R^J_{,13} + R^I_{,12} R^J_{,12} + R^I_{,11} R^J_{,11} \big) \\
&+ c_3 \big(\left(R^I_{,33} + R^I_{,22} + 2R^I_{,11} \right) R^J_{,33} + \left(R^J_{,22} + 2R^J_{,11} \right) R^I_{,33} \\
&\qquad + \left(R^I_{,22} + 2R^I_{,11} \right) R^J_{,22} + 2R^J_{,11} R^I_{,22} \\
&\qquad + R^I_{,13} R^J_{,13} + R^I_{,12} R^J_{,12} + 4R^I_{,11} R^J_{,11} \big) \\
&+ c_4 \big(R^I_{,33} R^J_{,33} + 2R^I_{,23} R^J_{,23} + R^I_{,22} R^J_{,22} \\
&\qquad + 3R^I_{,13} R^J_{,13} + 3R^I_{,12} R^J_{,12} + 2R^I_{,11} R^J_{,11} \big) \\
&+ c_5 \big(R^I_{,33} R^J_{,33} + 2R^I_{,23} R^J_{,23} + R^I_{,22} R^J_{,22} \\
&\qquad + 5R^I_{,13} R^J_{,13} + 5R^I_{,12} R^J_{,12} + 4R^I_{,11} R^J_{,11} \big) \big],
\end{aligned}
\tag{B.15}
$$

$$
\begin{aligned}
\hat{K}^{IJ}_{u_1 u_2} = s^2 \big[&\lambda R^I_{,1} R^J_{,2} + \mu R^I_{,2} R^J_{,1} \\
&+ c_3 \big(R^I_{,12} R^J_{,33} + R^J_{,12} R^I_{,33} + 2R^I_{,13} R^J_{,23} + 3R^I_{,12} R^J_{,22} \\
&\qquad + R^J_{,12} R^I_{,22} + 3R^I_{,11} R^J_{,12} + R^J_{,11} R^I_{,12} \big) \\
&+ c_4 \big(R^I_{,13} R^J_{,23} + R^I_{,12} R^J_{,22} + R^I_{,11} R^J_{,12} \big) \\
&+ c_5 \big(R^I_{,12} R^J_{,33} + R^J_{,12} R^I_{,33} + R^I_{,13} R^J_{,23} + 2R^I_{,12} R^J_{,22} \\
&\qquad + R^J_{,12} R^I_{,22} + 2R^I_{,11} R^J_{,12} + R^J_{,11} R^I_{,12} \big) \\
&+ c_6 \big(R^J_{,13} R^I_{,23} + R^J_{,12} R^I_{,22} + R^J_{,11} R^I_{,12} \big) \\
&+ c_7 \big(3R^J_{,13} R^I_{,23} + 3R^J_{,12} R^I_{,22} + 3R^J_{,11} R^I_{,12} \big) \big],
\end{aligned}
\tag{B.16}
$$

$$
\begin{aligned}
\hat{K}^{IJ}_{u_1 u_3} = s^2 \big[&\lambda R^I_{,1} R^J_{,3} + \mu R^I_{,3} R^J_{,1} \\
&+ c_1 \big(3R^I_{,13} R^J_{,33} + R^J_{,13} R^I_{,33} + 2R^I_{,12} R^J_{,23} + R^I_{,13} R^J_{,22} \\
&\qquad + R^J_{,13} R^I_{,22} + 3R^I_{,11} R^J_{,13} + R^J_{,11} R^I_{,13} \big) \\
&+ c_2 \big(R^I_{,13} R^J_{,33} + R^I_{,12} R^J_{,23} + R^I_{,11} R^J_{,13} \big) \\
&+ c_3 \big(2R^I_{,13} R^J_{,33} + R^J_{,13} R^I_{,33} + R^I_{,12} R^J_{,23} + R^I_{,13} R^J_{,22} \\
&\qquad + R^J_{,13} R^I_{,22} + 2R^I_{,11} R^J_{,13} + R^J_{,11} R^I_{,13} \big) \\
&+ c_4 \big(R^J_{,13} R^I_{,33} + R^J_{,12} R^I_{,23} + R^J_{,11} R^I_{,13} \big) \\
&+ c_5 \big(3R^J_{,13} R^I_{,33} + 3R^J_{,12} R^I_{,23} + 3R^J_{,11} R^I_{,13} \big) \big],
\end{aligned}
\tag{B.17}
$$

$$
\begin{aligned}
\hat{K}^{IJ}_{u_1 s} = 2s \big[&\left(S_{11} R^I_{,1} + S_{12} R^I_{,2} + S_{13} R^I_{,3} \right) \\
&+ \big(P_{111} R^I_{,11} + P_{112} R^I_{,12} + P_{113} R^I_{,13} + P_{211} R^I_{,12} + P_{212} R^I_{,22} \\
&\qquad + P_{213} R^I_{,23} + P_{311} R^I_{,13} + P_{312} R^I_{,23} + P_{313} R^I_{,33} \big) \big] R^J,
\end{aligned}
\tag{B.18}
$$

$$
\begin{aligned}
\hat{K}^{IJ}_{u_2 u_2} = s^2 \Big[&\lambda R^I_{,2} R^J_{,2} + \mu \left(R^I_{,1} R^J_{,1} + 2 R^I_{,2} R^J_{,2} + R^I_{,3} R^J_{,3} \right) \\
&+ c_1 \left(R^I_{,22} R^J_{,33} + R^J_{,22} R^I_{,33} + 2 R^I_{,23} R^J_{,23} + \left(4 R^I_{,22} + R^I_{,11} \right) R^J_{,22} \right. \\
&\qquad \left. + R^J_{,11} R^I_{,22} + 2 R^I_{,12} R^J_{,12} \right) \\
&+ c_2 \left(R^I_{,23} R^J_{,23} + R^I_{,22} R^J_{,22} + R^I_{,12} R^J_{,12} \right) \\
&+ c_3 \left(\left(R^I_{,33} + 2 R^I_{,22} + R^I_{,11} \right) R^J_{,33} + \left(2 R^J_{,22} + R^J_{,11} \right) R^I_{,33} \right. \\
&\qquad + R^I_{,23} R^J_{,23} + \left(4 R^I_{,22} + 2 R^I_{,11} \right) R^J_{,22} \\
&\qquad \left. + 2 R^J_{,11} R^I_{,22} + R^I_{,12} R^J_{,12} + R^I_{,11} R^J_{,11} \right) \\
&+ c_4 \left(R^I_{,33} R^J_{,33} + 3 R^I_{,23} R^J_{,23} + 2 R^I_{,22} R^J_{,22} + 2 R^I_{,13} R^J_{,13} \right. \\
&\qquad \left. + 3 R^I_{,12} R^J_{,12} + R^I_{,11} R^J_{,11} \right) \\
&+ c_5 \left(R^I_{,33} R^J_{,33} + 5 R^I_{,23} R^J_{,23} + 4 R^I_{,22} R^J_{,22} + 2 R^I_{,13} R^J_{,13} \right. \\
&\qquad \left. + 5 R^I_{,12} R^J_{,12} + R^I_{,11} R^J_{,11} \right) \Big] ,
\end{aligned}
\tag{B.19}
$$

$$
\begin{aligned}
\hat{K}^{IJ}_{u_2 u_3} = s^2 \Big[&\lambda R^I_{,2} R^J_{,3} + \mu R^I_{,3} R^J_{,2} \\
&+ c_1 \left(3 R^I_{,23} R^J_{,33} + R^J_{,23} R^I_{,33} + \left(3 R^I_{,22} + R^I_{,11} \right) R^J_{,23} \right. \\
&\qquad \left. + \left(R^J_{,22} + R^J_{,11} \right) R^I_{,23} + 2 R^I_{,12} R^J_{,13} \right) \\
&+ c_2 \left(R^I_{,23} R^J_{,33} + R^I_{,22} R^J_{,23} + R^I_{,12} R^J_{,13} \right) \\
&+ c_3 \left(2 R^I_{,23} R^J_{,33} + R^J_{,23} R^I_{,33} + \left(2 R^I_{,22} + R^I_{,11} \right) R^J_{,23} \right. \\
&\qquad \left. + \left(R^J_{,22} + R^J_{,11} \right) R^I_{,23} + R^I_{,12} R^J_{,13} \right) \\
&+ c_4 \left(R^J_{,23} R^I_{,33} + R^J_{,22} R^I_{,23} + R^J_{,12} R^I_{,13} \right) \\
&+ c_5 \left(3 R^J_{,23} R^I_{,33} + 3 R^J_{,22} R^I_{,23} + 3 R^J_{,12} R^I_{,13} \right) \Big] ,
\end{aligned}
\tag{B.20}
$$

$$
\begin{aligned}
\hat{K}^{IJ}_{u_2 s} = 2s \Big[&\left(S_{22} R^I_{,2} + S_{12} R^I_{,1} + S_{2,3} R^I_{,3} \right) \\
&+ \left(P_{211} R^I_{,11} + P_{212} R^I_{,12} + P_{213} R^I_{,13} + P_{221} R^I_{,12} + P_{222} R^I_{,22} \right. \\
&\qquad \left. + P_{223} R^I_{,23} + P_{321} R^I_{,13} + P_{322} R^I_{,23} + P_{323} R^I_{,33} \right) \Big] R^J ,
\end{aligned}
\tag{B.21}
$$

$$
\begin{aligned}
\hat{K}^{IJ}_{u_3u_3} = s^2 \Big[& \lambda R^I_{,3} R^J_{,3} \mu \left(R^I_{,1} R^J_{,1} + R^I_{,2} R^J_{,2} + 2 R^I_{,3} R^J_{,3} \right) \\
& + c_1 \left(\left(4 R^I_{,33} + R^I_{,22} + R^I_{,11} \right) R^J_{,33} + \left(R^J_{,22} + R^J_{,11} \right) R^I_{,33} \right. \\
& \qquad \left. + 2 R^I_{,23} R^J_{,23} + 2 R^I_{,13} R^J_{,13} \right) \\
& + c_2 \left(R^I_{,33} R^J_{,33} + R^I_{,23} R^J_{,23} + R^I_{,13} R^J_{,13} \right) \\
& + c_3 \left(\left(4 R^I_{,33} + 2 R^I_{,22} + 2 R^I_{,11} \right) R^J_{,33} \right. \\
& \qquad + \left(2 R^J_{,22} + 2 R^J_{,11} \right) R^I_{,33} + R^I_{,23} R^J_{,23} + \left(R^I_{,22} + R^I_{,11} \right) R^J_{,22} \\
& \qquad \left. + R^J_{,11} R^I_{,22} + R^I_{,13} R^J_{,13} + R^I_{,11} R^J_{,11} \right) \\
& + c_4 \left(2 R^I_{,33} R^J_{,33} + 3 R^I_{,23} R^J_{,23} + R^I_{,22} R^J_{,22} + 3 R^I_{,13} R^J_{,13} \right. \\
& \qquad \left. + 2 R^I_{,12} R^J_{,12} + R^I_{,11} R^J_{,11} \right) \\
& + c_5 \left(4 R^I_{,33} R^J_{,33} + 5 R^I_{,23} R^J_{,23} + R^I_{,22} R^J_{,22} + 5 R^I_{,13} R^J_{,13} \right. \\
& \qquad \left. + 2 R^I_{,12} R^J_{,12} + R^I_{,11} R^J_{,11} \right) \Big] ,
\end{aligned}
\tag{B.22}
$$

$$
\begin{aligned}
\hat{K}^{IJ}_{u_3s} = 2s \Big[& \left(S_{33} R^I_{,3} + S_{13} R^I_{,1} + S_{2,3} R^I_{,2} \right) \\
& + \left(P_{311} R^I_{,11} + P_{312} R^I_{,12} + P_{313} R^I_{,13} + P_{321} R^I_{,12} + P_{322} R^I_{,22} \right. \\
& \left. + P_{323} R^I_{,23} + P_{331} R^I_{,13} + P_{332} R^I_{,23} + P_{333} R^I_{,33} \right) \Big] R^J ,
\end{aligned}
\tag{B.23}
$$

$$
\hat{K}^{IJ}_{ss} = 2 \mathcal{G}_c \epsilon \left[R^I_{,1} R^J_{,1} + R^I_{,2} R^J_{,2} + R^I_{,3} R^J_{,3} \right] + R_I \left(2 \psi^{\mathrm{SGE}}_{\mathrm{grad}} + \frac{\mathcal{G}_c}{2\epsilon} \right) R_J .
\tag{B.24}
$$

Finally, the damping matrix has the form

$$
\left[\hat{\mathbf{D}}^{IJ} \right] = \int_\Omega
\begin{bmatrix}
0 & 0 & 0 & 0 \\
0 & 0 & 0 & 0 \\
0 & 0 & 0 & 0 \\
0 & 0 & 0 & \frac{1}{M} R^I R^J
\end{bmatrix}
\mathrm{d}V .
\tag{B.25}
$$

B2 Fourth-Order Phase-Field Fracture Model

The same matrices can be obtained for the fourth-order phase-field formulation from Eqs. (B.7) and the weak form of the fourth-order phase-field model,

$$
\int_\Omega \left[\frac{\dot{s}}{M} \delta s + \mathcal{G}_c \left(\epsilon \, \nabla s \, \delta \nabla s + \frac{\epsilon^3}{2} \Delta s \, \delta \Delta s \right) + \left(2s \, \psi^{\mathrm{SGE}}_{\mathrm{grad}} + \frac{\mathcal{G}_c (s-1)}{2\epsilon} \right) \delta s \right] \mathrm{d}V = \int_{\Gamma_2} q_n \, \delta s \, \mathrm{d}A ,
$$

with the only differences being the $\hat{P}^I_s$ component of the residual matrix, and the $\hat{K}^{IJ}_{ss}$ component of the stiffness matrix

$$
\begin{aligned}
\hat{P}^I_s = {} & R^I \frac{1}{M} \frac{\partial s}{\partial t} + \mathcal{G}_c \left(\epsilon \left(R^I_{,1} s_{,1} + R^I_{,2} s_{,2} + R^I_{,3} s_{,3} \right) \right. \\
& \left. + \frac{\epsilon^3}{2} \left(R^I_{,11} + R^I_{,22} + R^I_{,33} \right) \left(s_{,11} + s_{,22} + s_{,33} \right) \right) + R^I \left(2s \psi^{\mathrm{SGE}}_{\mathrm{grad}} + \frac{\mathcal{G}_c (s-1)}{2\epsilon} \right) ,
\end{aligned}
\tag{B.26}
$$

and,

$$
\begin{aligned}
\hat{K}_{ss}^{IJ} = \mathcal{G}_c \Big(&\epsilon \left[R_{,1}^I R_{,1}^J + R_{,2}^I R_{,2}^J + R_{,3}^I R_{,3}^J \right] \\
&+ \frac{\epsilon^3}{2} \left(R_{,11}^I + R_{,22}^I + R_{,33}^I \right) \left(R_{,11}^J + R_{,22}^J + R_{,33}^J \right) \Big) + R_I \left(2\psi_{\text{grad}}^{\text{SGE}} + \frac{\mathcal{G}_c}{2\epsilon} \right) R_J \, .
\end{aligned}
$$

(B.27)

Mesh Convergence Study (Strain Gradient Elasticity Enhanced Models)

In the following, the results of the mesh convergence study for the second-order and the fourth-order formulations for different values of the length-scale parameter l are provided. Figure C.1 represents the results for the second-order formulation with $l = \epsilon$. The convergence trend can be seen clearly in the results both for the phase-field and the strain energy density values. The energy density completely vanishes in the crack zone for path B-B′ in a sufficiently refined mesh. Here, the previously mentioned deviation of the phase-field and the energy density plots is easier to observe (cf. Sect. 5.2.2.2). The same results are depicted in Fig. C.2 for the case $l = 2\epsilon$.

Figures C.3 and C.4 illustrate the mesh convergence study results for the fourth-order formulation with $l = \epsilon$ and $l = 2\epsilon$, respectively. Again, the convergence trend of the phase-field and the strain energy density values is obvious. The symmetric distribution of the phase-field and the energy density is preserved for both the results. In this context, acceptable results are already obtained for a normal mesh with 192×193 control points.
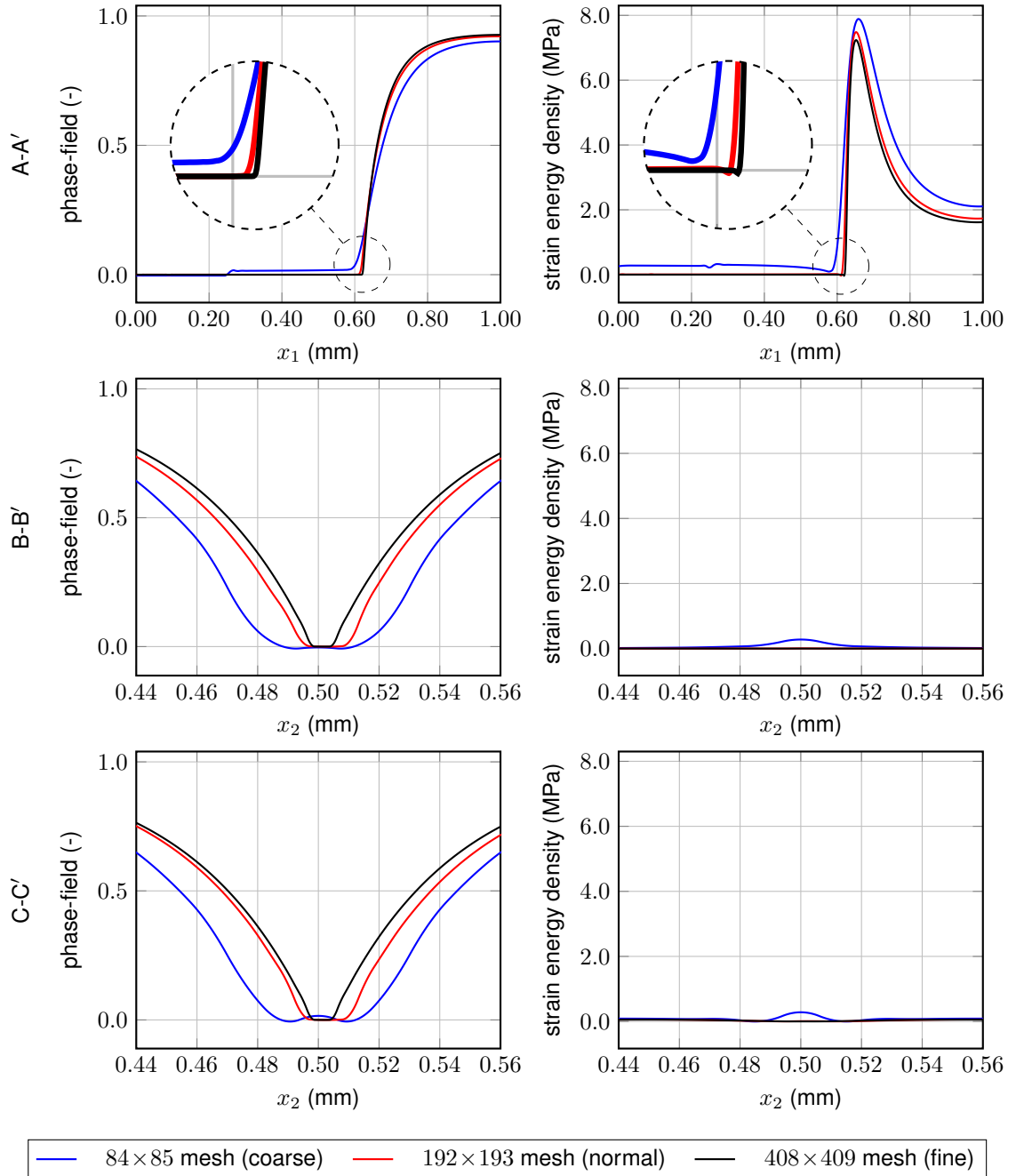
Figure C.1: Results for the second-order formulation for $l = \epsilon = 0.02$ for different mesh sizes. Distributions of the phase-field (left), and the strain energy density (right) along three different cross-sections in the plane
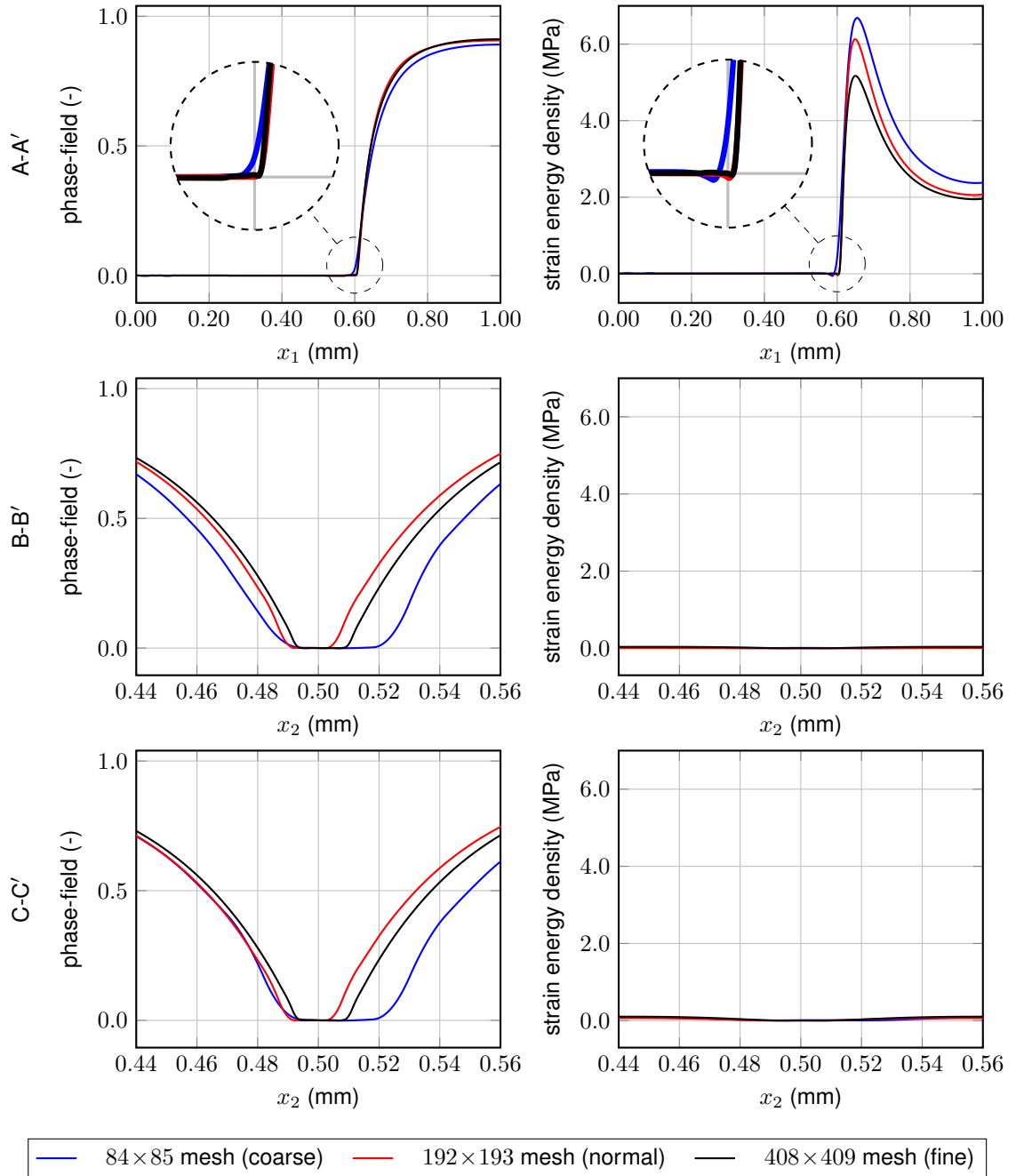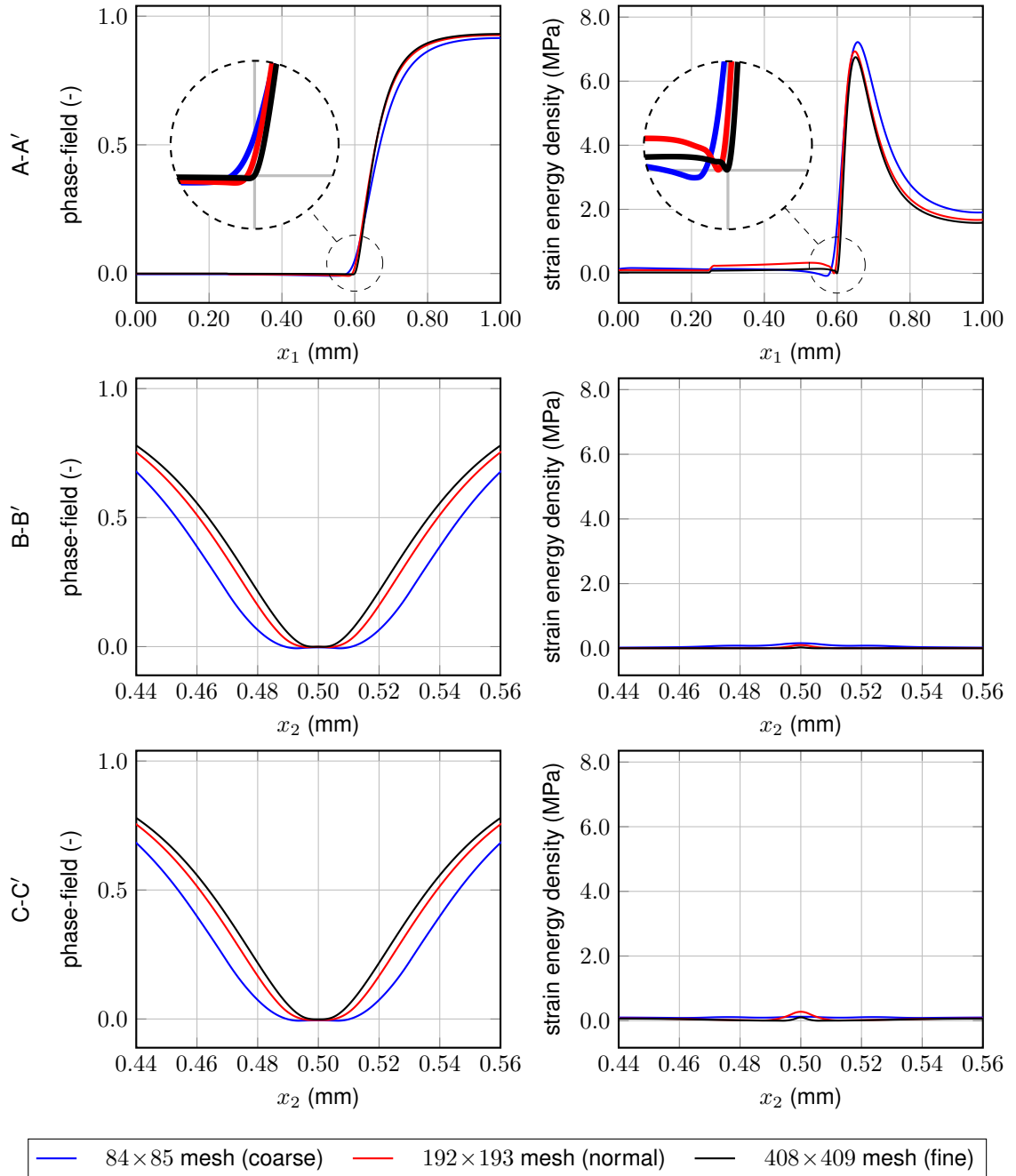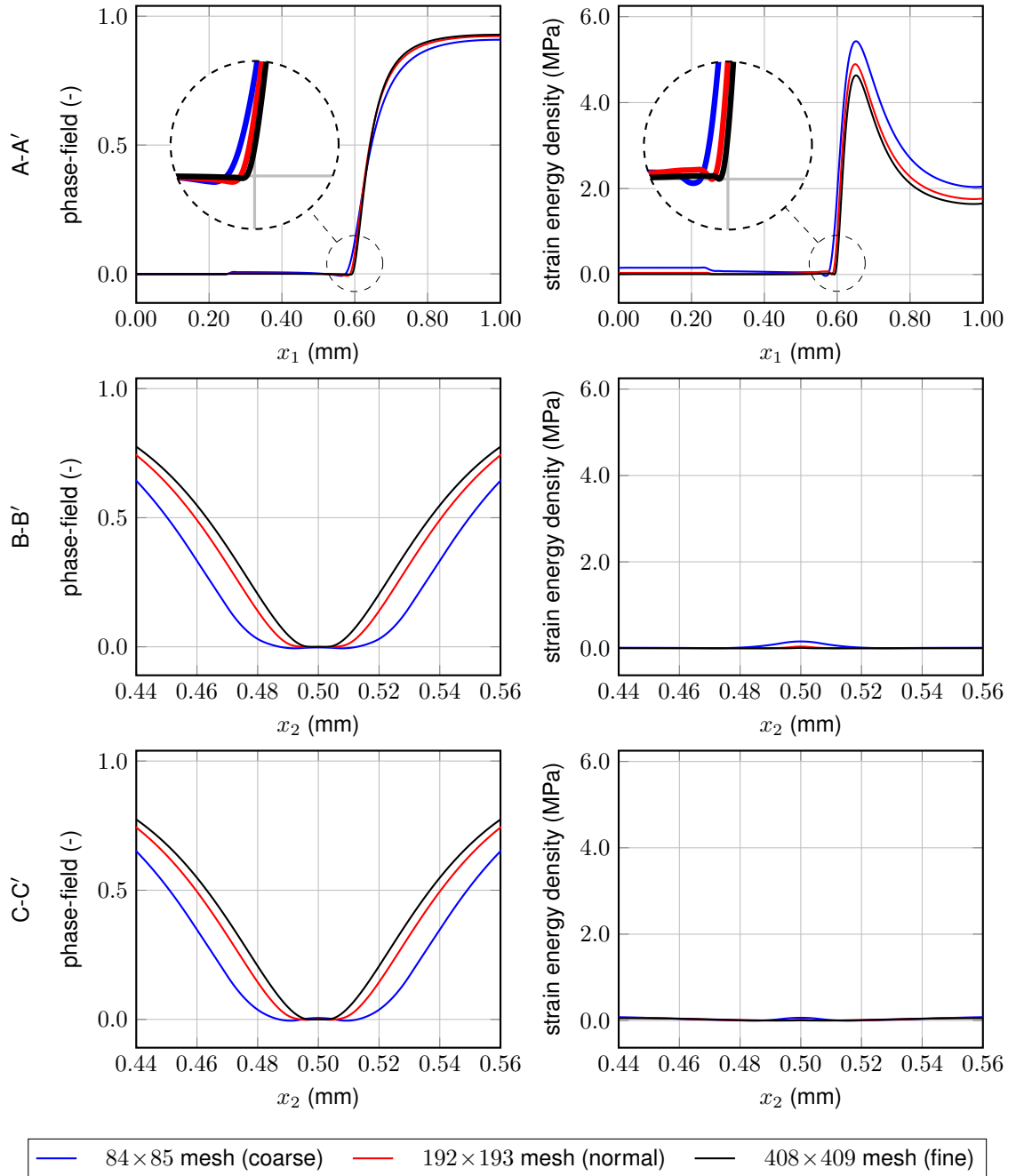
Figure C.2: Results for the second-order formulation for $l = 2\epsilon = 0.04$ for different mesh sizes. Distributions of the phase-field (left), and the strain energy density (right) along three different cross-sections in the plane
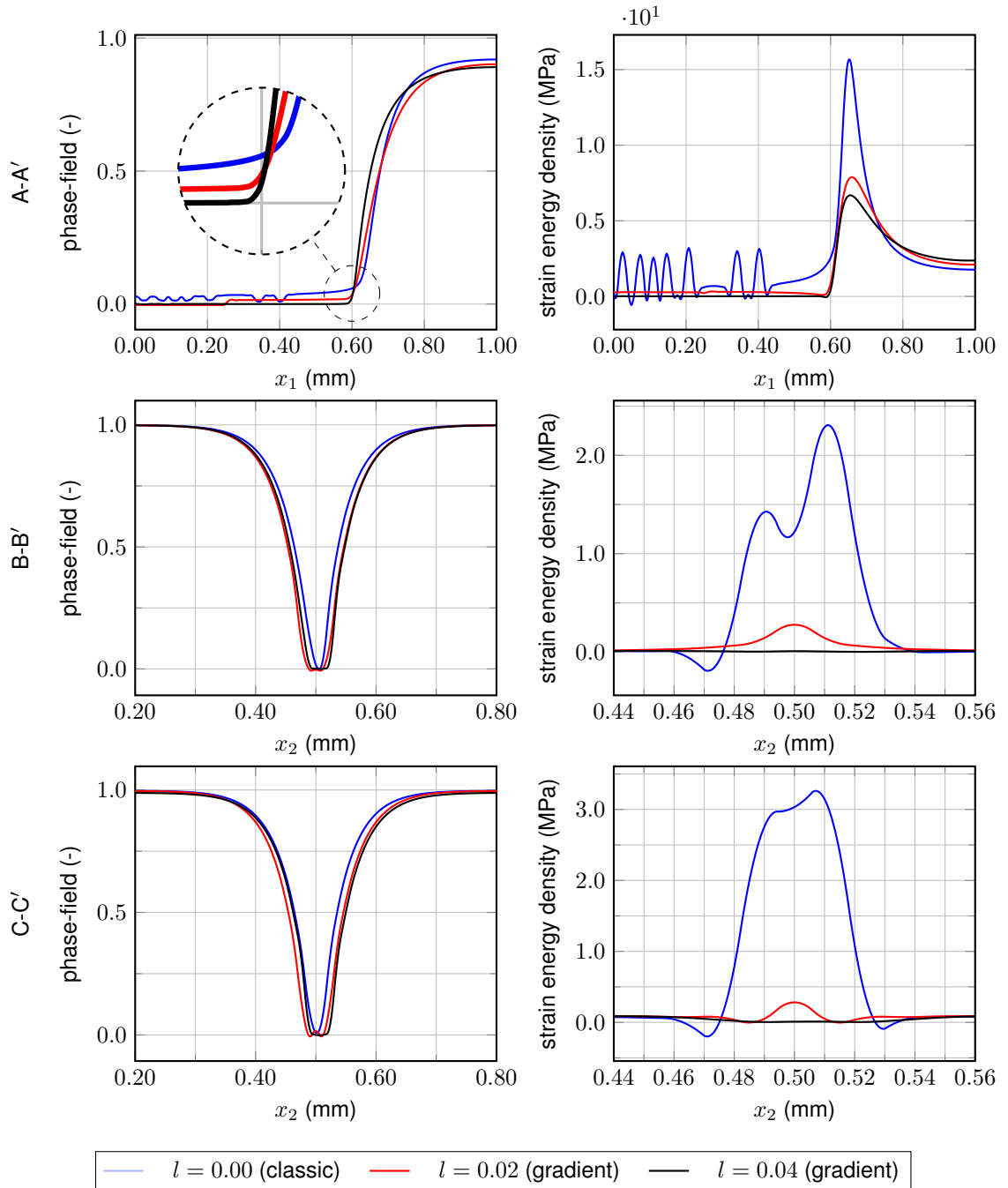
Figure C.3: Results for the fourth-order formulation for $l = \epsilon = 0.02$ for different mesh sizes. Distributions of the phase-field (left), and the strain energy density (right) along three different cross-sections in the plane

Figure C.4: Results for the fourth-order formulation for $l = 2\epsilon = 0.04$ for different mesh sizes. Distributions of the phase-field (left), and the strain energy density (right) along three different cross-sections in the plane

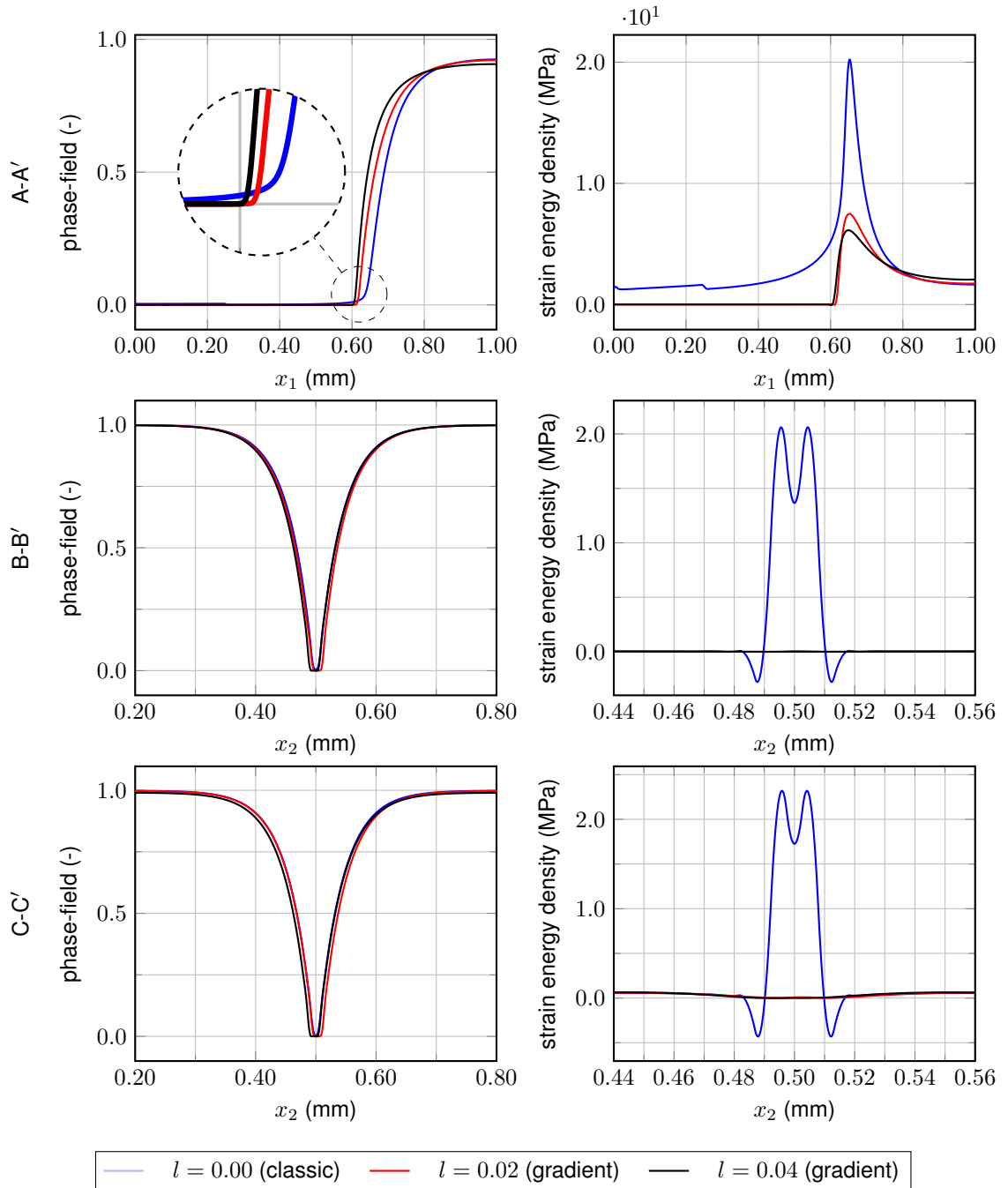Figure C.5: Results for the second-order formulation for different values of l and the 84×85 mesh. Distributions of the phase-field (left), and the strain energy density (right) along three different cross-sections in the plane
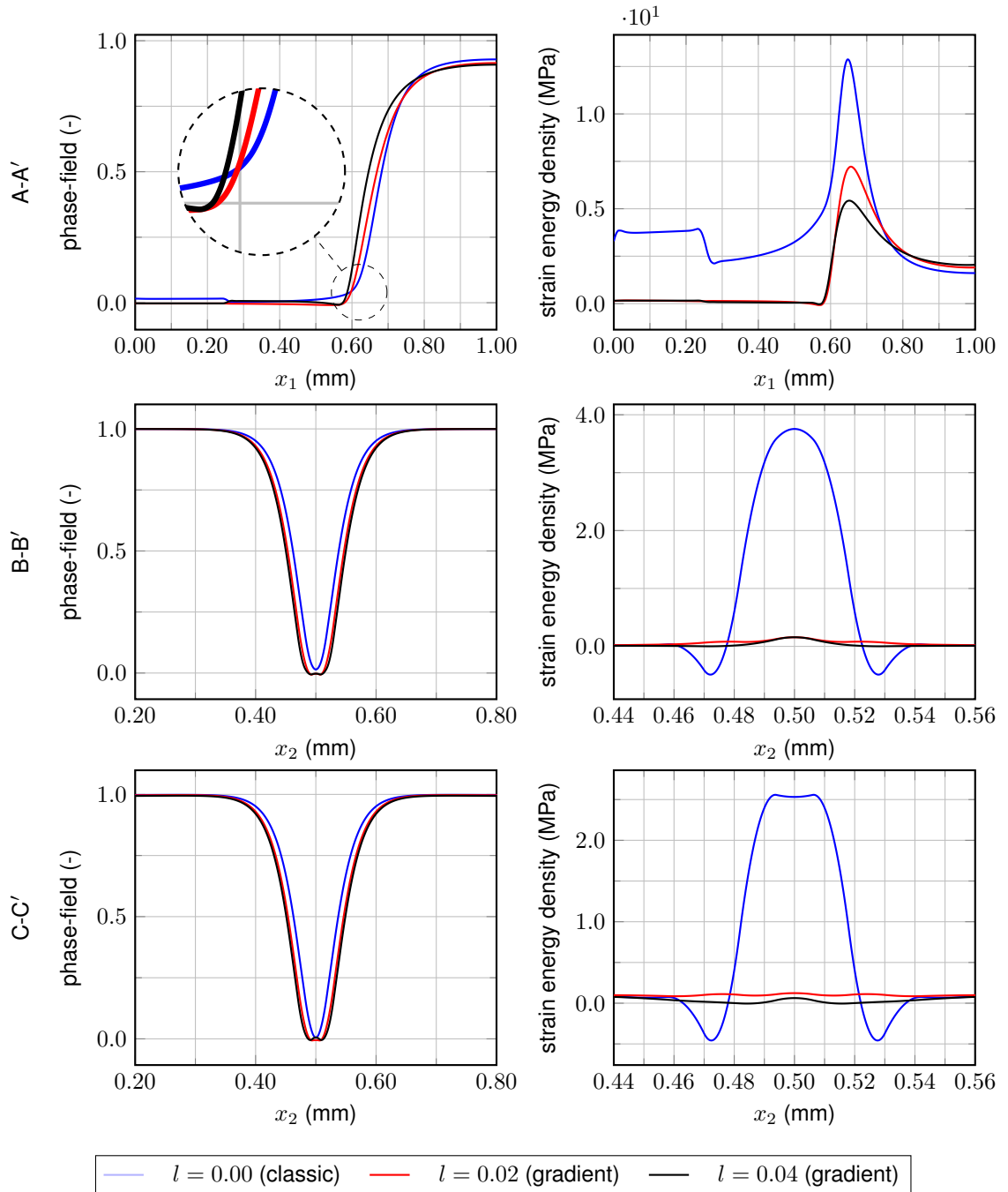
Figure C.6: Results for the second-order formulation for different values of l and the 192×193 mesh. Distributions of the phase-field (left), and the strain energy density (right) along three different cross-sections in the plane

Figure C.7: Results for the fourth-order formulation for different values of l and the 84×85 mesh. Distributions of the phase-field (left), and the strain energy density (right) along three different cross-sections in the plane
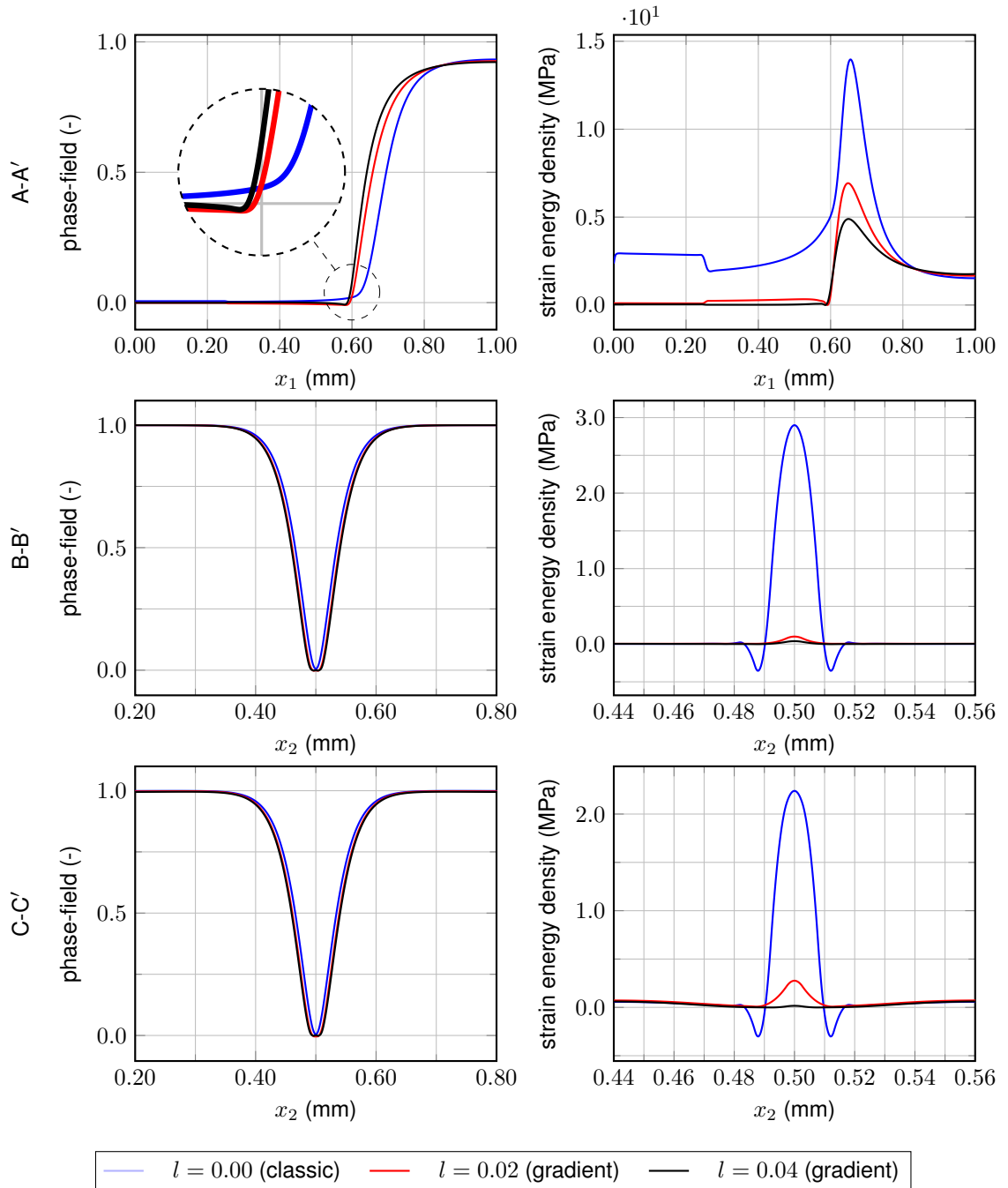
Figure C.8: Results for the fourth-order formulation for different values of l and the 192×193 mesh. Distributions of the phase-field (left), and the strain energy density (right) along three different cross-sections in the plane